Development of a multimodal imaging probe for detecting aggressive

prostate cancer

Thesis submitted for the degree of doctor of philosophy at the University

of Hull

By

Mitchell Thomas Clarke MChem (Hull)

Department of Biomedical Sciences

University of Hull

March 2020

Abstract

This thesis reports on the synthesis, development and validation of a novel, non-toxic dual modal bio-imaging probe that targets a conformational molecular switch and relocalisation of cell surface Endo180 into endosomes that occurs during the early stages of aggressive prostate cancer.

InP/ZnS quantum dots were synthesised using a successive heating methodology following the introduction of a cooling phase between the addition of 'shelling' precursors. Photoluminescent quantum yields following the synthesis of **InP/ZnS (2)** quantum dots are reported at 85.30% in hexane and 57% in water (following phase transfer).

An OI/MR dual-modal imaging probe was successfully synthesised following the surface modification of **InP/ZnS (2) – TGA** with Ln(III) DOTA chelate derivative (Ln = Gd, Eu and Tb). Up to 190 Gd(III) chelates were added to the surface of **InP/ZnS (2) – TGA** resulting in a combined r_1 value of 1609.94 mM^{-1}s^{-1} (**InP/ZnS (2) – Gd.5a**) when **InP/ZnS (2)** is synthesised with InI$_3$. High values of photoluminescent quantum yield were achieved of up to 19.9% (**InP/ZnS (2) – Gd.5.b**) with no shift in emission properties observed following surface functionalisation when compared to **InP/ZnS (2) – TGA**.

A targeted dual modal OI/MR imaging probe for the early detection of aggressive prostate cancer has been developed, *via* a two-step surface modification of **InP/ZnS (2) – TGA** with Endo180 conformational specific antibodies (A5.158, 39.10) and Gd(III) chelate (**Gd.5a**).

Bouillard, J.-S. G.; Tamang, S.; Stasiuk, G. J. Near Unity Quantum Yield in InP Based Quantum Dots through Thermal Diffusion. *Commun. Chem.* **2019**, *2*.

Acknowledgements

Abbreviations

Å - Angstrom

ADT – Androgen Deprivation Therapy

a.u. – Arbitrary Units

AuNP – Gold Nanoparticles

B_0 – External magnetic field

BBB – Blood Brain Barrier

BPH – Benign Prostate Hyperplasia

CA – Contrast Agent

Calc – Calculated

CCK-8 – Cell Counting Kit-8

CD147 – Cluster of Differentiation 147

CN – Coordination Number

CRD – Cysteine Rich Domain

cRGD – Cyclic-Arginine-Glycine-Aspartic Peptide

CTLD – C-type Lectin Domain

CS – Core/Shell

CZ – Central Zone

δ – Delta (NMR chemical shift)

Δ – Delta (Change in)

DCM – Dichloromethane

DDT – Dodecanethiol

DFT – Density Functional Theory

D_h – Hydrodynamic diameter

DLS – Dynamic light Scattering

DMAP - Dimethylaminopyridine

DO3A – 1,4,7 – tris(carboxymethyl) – 1,4,7,10 – tetraazacyclododecane

DOTA – 1,4,7,10 – tetraazacyclododecane - 1,4,7,10 – tetraacetic acid

DTC – Dithiocarbamates

DTPA – Diethylenetriamine pentaacetic acid

ECM – Extracellular Matrix

EDC – 1-Ethyl-3-(3-Dimethylaminopropyl)carbodiimide

EDX – Energy Dispersive X-Ray Spectroscopy

e.g. – exempli gratia (For Example)

EtOH – Ethanol

EMA – European Medical Agency

EMT – Epithelial-to-Mesenchymal

ESMS – Electrospray Mass Spectrometry

eV – Electrovolts

FACS – Fluorescent-Activated Cell Sorting

^{18}F-FDG - ^{18}F-labelled fluorodeoxyglucose

FI – Fluorescent Imaging

FNII – Fibronectin Type-II

FWHM – Full Width Half Maximum

GdCA – Gadolinium (III) based Contrast Agent

GRP – Gastric Releasing Peptide

GRPr – Gastric Releasing Peptide Receptor

ɣ - Gyroscopic Ratio

HAADF – High Angular Dark Field

HOPO - Hydroxypyridinone

HRTEM – High Resolution Transmission Electron Microscopy

HRMS – High Resolution Mass Spectroscopy

HSA – Human Serum Albumin

Hz - Hertz

I – Spin Quantum Number (nucleus)

in vitro – in an artificial environment outside of a living organism

in vivo – inside a living organism

ISC – Intersystem Crossing

ISUP – International Society of Urological Pathologists

k – Rate Constant

k_{ex} – Water Exchange Rate

$k_{H2O/D2O}$ – Rate constants in H_2O/D_2O

λ_{ex} – Wavelength of Excitation

λ_{em} – Wavelength of Emission

K – Kelvin

Da – Dalton

M – Molar Concentration

MMP – Matrix Metalloproteinase

MNPs – Metallic Nanoparticles

$mM^{-1}s^{-1}$ – per millimolar per second (units of relaxivity)

ms^{-1} – per millisecond

MR – Magnetic Resonance

MRI – Magnetic Resonance Imaging

mpMRI – Multiparamagnetic Magnetic Resonance Imaging

mpUS – Multiparamagnetic Ultrasound

NaOH – Sodium Hydroxide

NCs - Nanocrystals

NIR – Near Infrared

nm - Nanometre

NMR – Nuclear Magnetic Resonance

NMV – Net Magnetisation Vector

NP - Nanoparticles

ns – Nanoseconds

NSF – Nephrogenic Systemic Fibrosis

OATPs – Organic-Anion Transporting Peptides

OI – Optical Imaging

PASP – Polyaspartic Acid

PBS - Phosphate Buffered Saline

PCa – Prostate Cancer

$P(DMA)_3$ – Tris(dimethylamino) Phosphine

PET – Positron Emission Tomography

PEG – Polyethylene Glycol

PI – Post Injection

PLQY – Photoluminescent Quantum Yield

Pro-UPA – Pro-Urokinase Plasminogen Activator

PSA – Prostate Specific Antigen

PSMA – Prostate Specific Membrane Antigen

$P(TMS)_3$ – Tris(trimethylsilyl)Phosphine

PXRD – Powder X-ray Diffraction

PZ – Peripheral Zone

q – Inner Sphere Hydration State

QDs – Quantum Dots

r_1 – Relaxivity

RF – Radio Frequency

S – Singlet Electronic State

SAP – Square Antiprismatic

SPECT – Single Photon Emission Computed Tomography

SPIONs – Super Paramagnetic Iron Oxide Nanoparticles

T – Tesla

T_1 – Triplet Electronic State

T_1 – Longitudinal Relaxation Time

T_2 – Transverse Relaxation Time

τ_m – Water Exchange Lifetime

τ_R – Rotational Correlation Time

Tau – Delay increments

TCEP – Tris(2-carboxyethyl)phosphine

TEM – Transmission Electron Microscopy

TGA – Thioglycolic Acid

TMAOH – Tetramethyl Ammonia Hydroxide

TNM – Tumour Node Metastasis

TOP – Trioctyl Phosphine

TOPO – Trioctylphosphine Oxide

TOP-S – Trioctylphosphine Saturated with Sulphur

TSAP – Twisted Square Antiprismatic

TZ – Transitional Zone

UPAR – Urokinase Plasminogen Activator Receptor

UPARAP - Urokinase Plasminogen Activator Receptor Associated Protein

V – Volume

V_C – Core Volume

V_{CS} – Core/shell Volume

Z_{eff} – Effective Nuclear Charge

ω_0 – Angular Frequency

<u>**Contents**</u>

Chapter 1: Introduction

1.1 The prostate and prostate cancer

1.1.1 Function, anatomy and histology of the prostate

The prostate gland is an organ present in human males and consists of fibro muscular tissue, with its primary role within the body being to produce components of the seminal fluid.[1] In humans, approximately 20-30% of the seminal fluids are provided by the prostate gland (specifically from the luminal cells within the prostate).[2] The prostate contributes several components to the seminal plasma (such as Prostate Specific Antigen (PSA) and zinc) which are of large biological importance, such as improving sperm viability by increasing basicity of seminal fluid.[2] The prostate is a 'donut shaped' gland which in young males weighs approximately 40 g with an approximate area of 30 cm^3, with age however, the prostate grows in size resulting in a 50 year old male having a prostate with an approximate weight of anywhere in the region of 100-150 g.[1]

The prostate gland can be categorized into 3 distinguishably different sections, both by anatomical and histological differences. These regions being the central, transition and peripheral zones (figure 1.1). The central zone (approximately 30% of total volume) surrounds only the ejaculatory ducts. The transition zone (approximately 5% of total volume) surrounds the prostatic urethra, with both the central and transition zones being found in the peripheral zone (65 – 70% in volume approximately).[1] The 3 different zones have been shown by McNeal *et al.* to play different roles in the formation of

different disease types ranging from benign prostate hyperplasia (BPH) to

different prostate cancer disease states.[3] BPH has been shown to arise in the

transitional zone despite only accounting for 5% of the overall volume of the

prostate, whereas carcinomas were shown to originate specifically within the

peripheral zone with the central zone showing no origins in disease states.
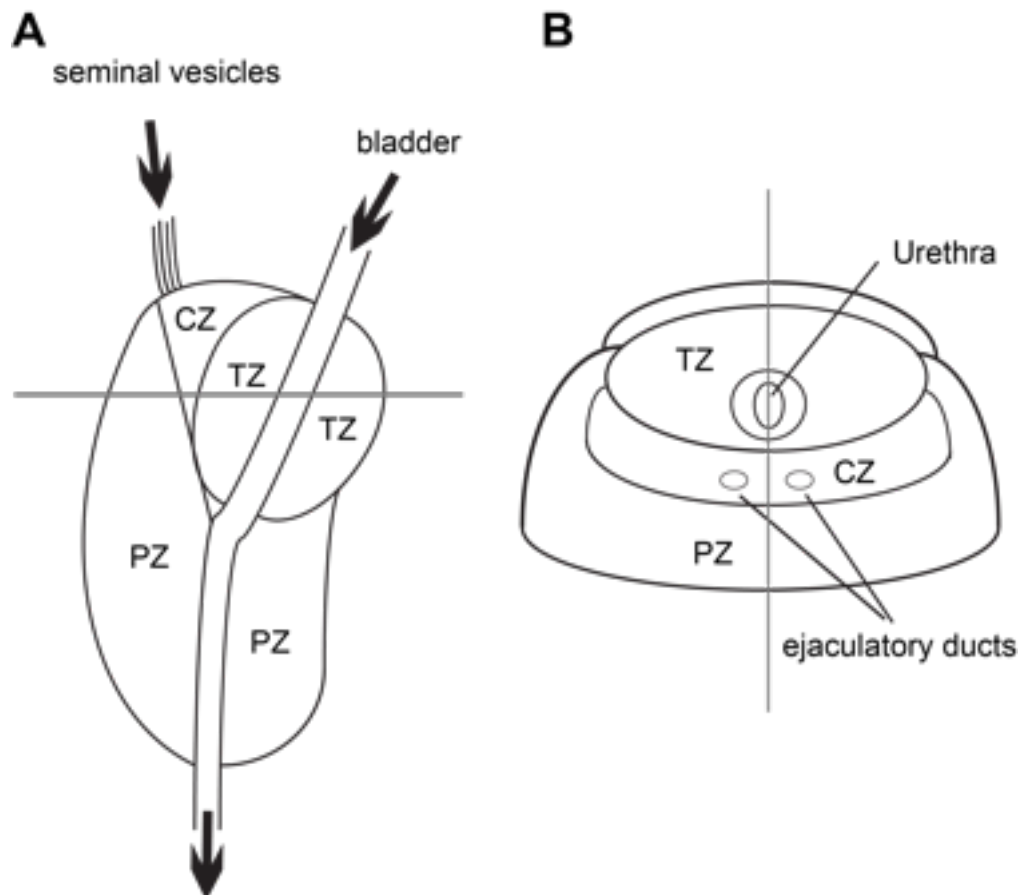
Figure 1.1. Image showing the three distinct regions within the prostate gland. The Central Cone (CZ), the Transition Zone (TZ) and Peripheral Zone (PZ).[4]

The gland itself consists of two distinct cell layers, a basal layer that is in direct

contact with the basal lamina as well as luminal cells that produce the seminal

fluid associated with the prostate. Both cell layers however are in contact on

one side.

1.1.2 Prostate cancer overview

Prostate cancer (PCa) is the most common non-cutaneous cancer in men within the western world. In 2019, 174,650 new incidences of PCa were diagnosed, this will only add to the 3.3 million already existing cases worldwide.[5,6] PCa is generally associated as a slow growing malignancy once formed however, PCa can still have adverse effects on the human life. A recent study looking at the mortality rates of new incidences compared to mortality rates of cancer cases in North America, showed PCa accounted for one fifth of all new cases (174,650/870,970). However, the number of deaths associated to PCa was less than one tenth when considering overall mortality rate (31,620/321,670).[6] These numbers published in the American Cancer Journal For Clinicians elegantly show that the high incident rate of PCa does not necessarily lead to a high mortality rate for those diagnosed. A mortality rate for incidences in 2019 in America can be estimated at 18.1%, with this number being in part due to the fact that initially PCa is a disease which presents asymptomatically, diagnosis therefore, is usually complete as part of a preventative medicine plan with active surveillance methods usually prescribed.[7-8]

Prostate Specific Antigen (PSA), a glycoprotein which is expressed within both normal and diseased prostate tissue, is used within the clinical setting as a biomarker for PCa. When an abnormal event such as cancer occurs within the prostate an overabundance of cells, overproduction of PSA and the resultant increase of PSA in the bloodstream, results in a measurable difference within PSA within the blood indicating an issue within the prostate. In general

PSA concentrations of 4ng/ml within the blood are considered normal, with men showing concentration in excess of 10ng/ml are considered high and in need of further testing. Patients which have PSA concentrations within the range of 4-10nm/ml may undergo a digital rectal examination before undergoing further examination to assess the prostates condition. However, care must be taken when interpreting PSA results as elevated PSA levels indicate greater than normal PSA production whilst having limited specificity to PCa as other illness such as infection within the prostate or benign prostate hyperplasia can cause elevated PSA within the blood. As PSA levels can often be so difficult to interpret as a one-off test, routine screening is often used to follow disease progress as part of an active surveillance plan. The transition towards an aggressive form of the disease is often when the first symptoms of PCa are observed, and also when secondary metastatic disease sites are detected within the patient. Distant metastatic sites for PCa are skeletal bone, lymph nodes, lungs, liver and brain. Local invasion close to the diseased prostate gland can lead to invasion of the nearby vessels as well as the bladder and rectum.[9]

1.1.3 Prostate cancer disease staging and grading

On the assumption of a patient having PCa following increasing levels of PSA within a preventative medical care plan, a positive diagnosis has to be confirmed based on microscopic evaluation of prostate tissue obtained *via* needle biopsy. This is complete with 10-12 cores being taken by trans-rectal ultrasound in a grid like pattern.[8] Following successful tissue biopsy a clinical

cancer disease staging is able to be determined from the tissue samples. Two crucial pieces of information are able to be determined from this;

- Firstly, it is able to describe in what state the immediate area around the prostate is in and whether the disease is contained to a specific area (determine the spread of disease)

- Second, histological grading reflecting the differentiation of affected tissue.

However, both of these scoring systems require different methods of grading (TNM and Gleason).

Clinical staging of tumour progression using the 'Tumour Node Metastasis' (TNM) model has long been used within clinical practice.[10] The use of the TNM method is able to yield an arbitrary score resulting in the clarification of the disease state as either low-, intermediate- or high- risk, which ultimately determine the course of treatment for the patient. Clinical staging (T) is able to be determined using prostate core samples and gives an idea of the extent of the disease. The lymph node (N) viability and the extent of metastatic activity (M) are also taken into account. The current TNM guidelines used for prostate cancer were revised in 2010 and an overall score being derived from the values below.[10]

- Tx – Primary tumour cannot be assessed

- T0 – Primary tumour not visible

- T1 – Primary tumour not palpable nor visible by imaging

  o T1a – Tumour histology found in less than 5% of tissue resected

  o T1b – Tumour histology found in more than 5% of tissue resected

  o T1c – Tumour found by needle biopsy (following elevated PSA

    screening)

- T2 - Tumour confined within the prostate

  o T2a – Tumour invades one half of one lobe or less

  o T2b – Tumour invades more than one half of one lobe but not

    both

  o T2c – Tumour invades both lobes

- T3 – Tumour extends out of the prostate capsule

  o T3a – Extracapsular (unilaterally or bilaterally)

  o T3b – Tumour invades seminal vessels

- T4 – Fixed or invades adjacent structures

- Nx – Nodes not assessed

- N0 – no regional metastasis

- N1 – Metastasis found (regionally)

- M0 – No distant metastasis

- M1 – Distant metastasis

  o M1a – Non-regional lymph node(s)

  o M1b – Bone(s)

  o M1c – Other sites with or without bone(s)

Accompanying the TNM grading system, the Gleason grading system was developed in 1966 by its namesake specifically for the differentiation of diseased prostate tissue.[11] Gleason's grading system reflects the histological differences within the prostate and had stood the test of time for nearly 4 decades, until Gleason himself updated his own system in 1992 to improve accuracy following improvements in technology.[12] With this update, the International Society of Urological Pathologists (ISUP) revised the Gleason grading in attempt to modernise the histological grading of prostate tissue.[13,14] Revision of the grading system in 2005 occurred due to the evolution of screening techniques over the past 4 decades such as the advent of serum PSA, immunohistochemistry staining and thin 18-gauge needle biopsy.[13] Following the ISUP recommendation the histological tissue grading scale of 1 to 5 give definitions for each grades, which are as follows;

- Grade/Pattern 1: Individual discrete, well-formed glands

- Grade/Pattern 2: Predominantly well-formed glands with lesser component or poorly formed cribriform glands

- Grade/Pattern 3: Predominantly poorly formed cribriform glands with a lesser component of well-formed glands

- Grade/Pattern 4: Only poorly formed glands.

- Grade/Pattern 5: No gland formation, with signs of necrosis. May or may not show signs of cribriform glands.

Along with the definitions that were determined *via* consensus at the ISUP

conference in 2005, an accompanying diagram (figure 1.2) outlaying the

updated histological patterns from 1-5 was also given.
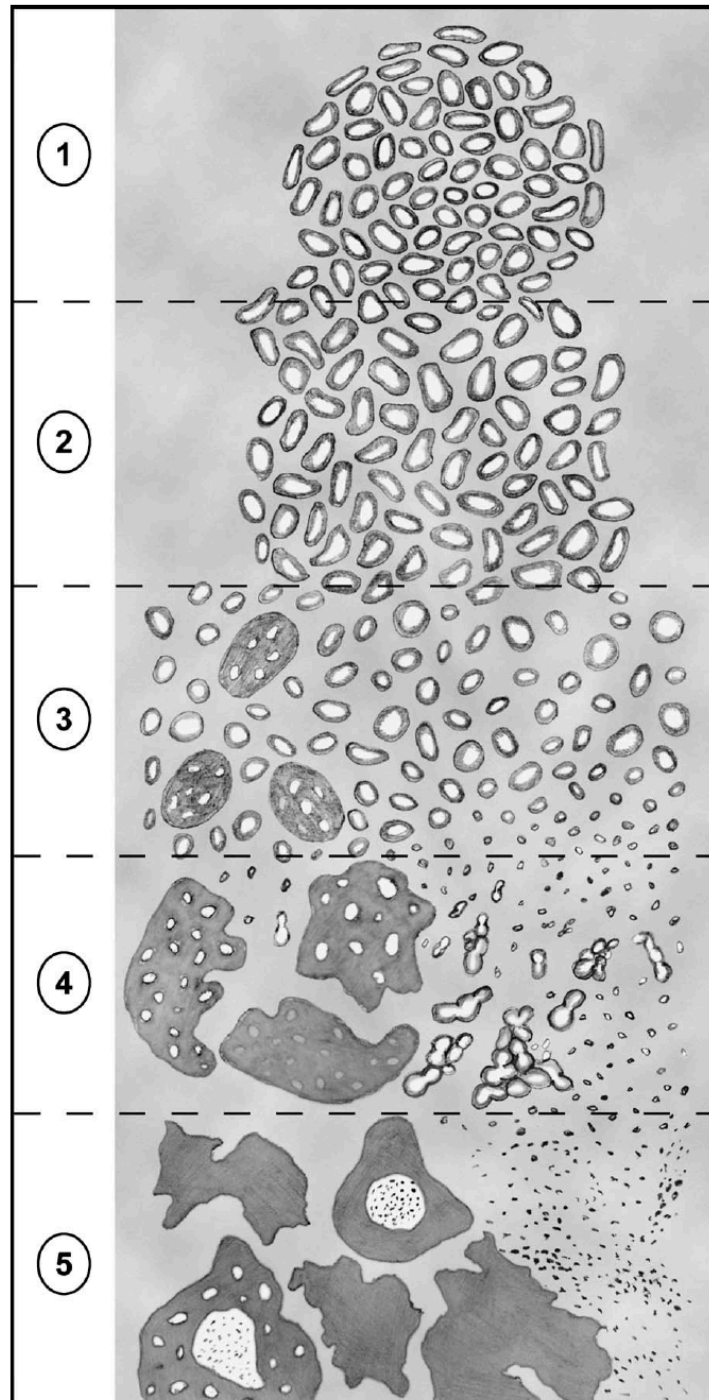
Figure 1.2. Gleason grading system for the histology of diseased tissue on a scale
of 1-5.[15]

In addition to defining the five different patterns, the Gleason system gives guidance to the pathologist on how to categorise tumours that display more than one pattern. The pathologist reports grades in the format Y+Z where Y is the dominant pattern and Z is the minor pattern present within the tissue sample. Using this system will result in Gleason score ranging from 2 (low risk) through to 10 (high risk). However, in 2014, the ISUP consensus conferences revised the above grading, resulting in a new framework for pathologists to work from when grading cancerous tissue.[14,16] These findings are able to more precisely determine tumour behaviour by grading tissue on a scale of 1 – 5 using Gleason's original pattern. These grading's are shown below.

Grade 1: 3 + 3 = 6

Grade 2: 3 + 4 = 7

Grade 3: 4 + 3 = 7

Grade 4: 4 + 4, 3 + 5, 5 + 3 = 8

Grade 5: 4 + 5, 5 + 4, 5 + 5 = 9/10

This system was able to be prognostically validated on over 25,000 men and had a greater prognostic discrimination than the tradition Gleason grading system (Gleason score 6, 7, 8 –10) when diagnosing low, intermediate and high-risk cancers.

1.1.4 Course of disease and treatment

1.1.4.1 Genetic mutations within prostate cancer

Prostate cancer is a genetic disease state formed via the mutation of key regulatory genes, resulting in their inactivation (suppression) or increased activation/amplification (oncogene). Risk factors including age, ethnicity and family history, as well as environmental factors such as lifestyle and sexual history have influence over increased rates of genomic mutation. In a recent study published by Rubin and Demicheilis, several important genomic mutations within PCa were outlined including mutations within the androgen receptor (AR), PTEN and cellular tumour antigen P53 (TP53), with all playing a role in the development of PCa.[17]

Since the pioneering work of Huggins and Hodges in 1941 in which the relationship between androgens and PCa progression was first discovered, were patient tumour progression was seen to slow and even regress following the removal of the testes which resulted in the stemming of testosterone and downstream androgens. Further work later revealed PCa progression was largely driven by the AR, whilst showing that the AR is present in some degree within all PCa tumours.[18,19] The AR (figure 1.3.B) belongs to the steroid hormone group of nuclear receptors and is a ligand-dependent transcription factor that controls the expression of specific genes. AR cell signalling occurs following the binding of native androgen ligand 5α-dihydrotestosterone (DHT), a metabolite of testosterone after it has undergone conversion *via* cytochrome

P450, 5α-reductase (figure 1.3.A) promoting the growth and survival of

prostate cells.[20]
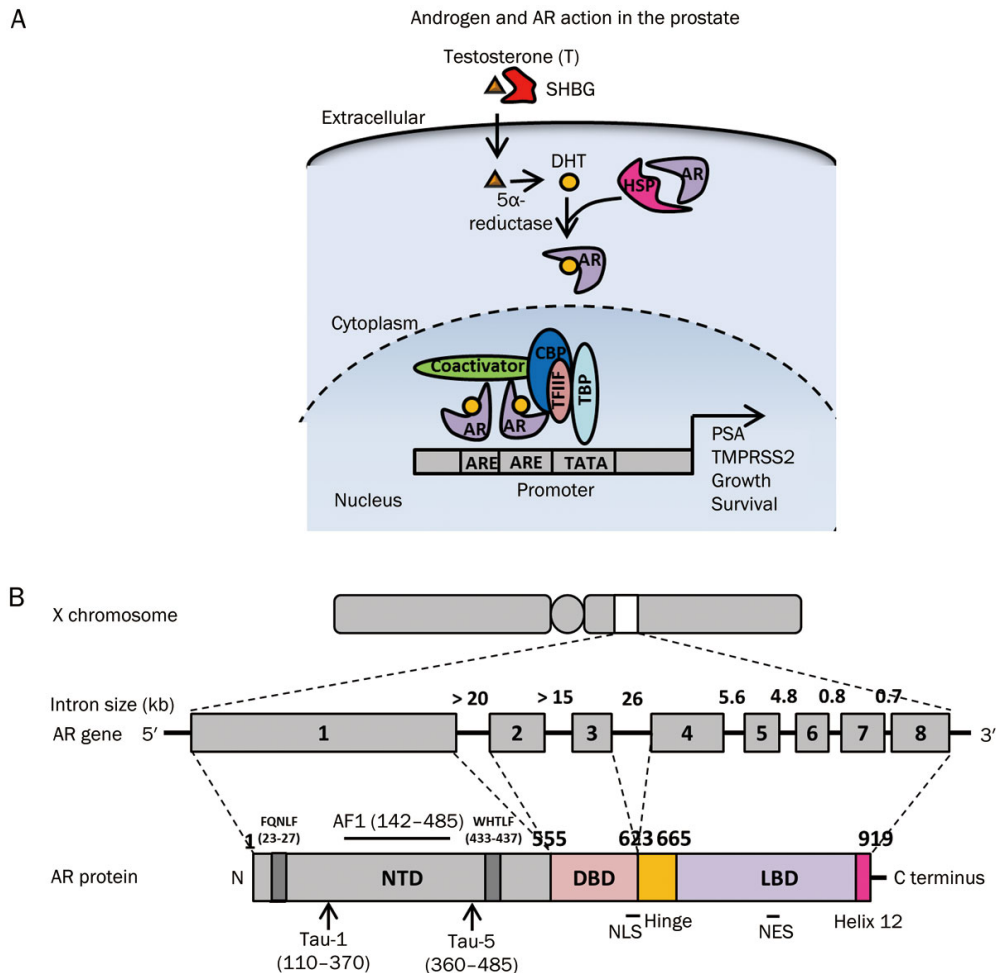
Figure 1.3. (A) Summary of the major androgen receptor signalling pathways in prostate cancer. Upon binding to dihydrotestosterone, androgen receptor translocates to the nucleus, binds to its target genes and regulates their expression. (B). Schematic representation of the androgen receptor gene and protein, with indications of its specific motifs and domains.[21]

The binding of DHT to AR displaces heat-shock protein due to its high affinity

for AR and drives interaction between the N and C termini within the AR whilst

binding importin-α, thus allowing for translocation of AR from cytoplasm into

the nucleus. When in the nucleus, receptor dimers bind to androgen receptor elements (AREs) available in the promoter regions of target genes (such as PSA, TMPRSS2).[21] Responses such as growth and survival are then therefore able to be triggered due to the recruitment of various coregulatory genes which facilitates transcription.

ARs play a pivotal role in prostate carcinogenesis and therefore a range of hormone therapies (known as androgen deprivation therapy (ADT) section 1.1.4.2) depriving tumours of androgens such as testosterone and DHT have been developed to treat hormone-naïve PCa. However, a major complication within PCa is the development of castrate-resistent prostate cancer (CRPC), a much more lethal phenotype of the disease. The development and forthcoming evolution from clinically hormone-naïve PCa to CRPC can be shown to be due to androgenic stimulation leading to downstream effects including but not limited to; AR amplification/overexpression, gain of function within the receptor, intercrine androgen production, overexpression of AR cofactor and ligand independent AR activation by growth factors.[22–26] Due to this, traditional methods for the treatment of PCa including the depriving of androgens to the tumour *via* androgen deprivation therapy (ADT) is often unable to be used. Treatment options for differing forms of PCa are discussed in further detail in section 1.1.4.2.

1.1.4.2 Treatment of disease

Following a new PCa diagnosis, both the extent of the PCa to which the patient has in combination with their individual circumstances are taken into account before considering treatment options, in which a system that encourages shared decision making between patient and treatment team is used. In the case of very early stage PCa, (Gleason 6, PSA <4 mg/l) active monitoring is often utilised, with this method justifiable since this approach is associated with a 99% disease-specific 8-year survival rate as well as being a non-intrusive treatment method offering little discomfort to patients.[27] On the progression of PCa to one which can be diagnosed as low risk cancer (Gleason 6-7, PSA 4-10 mg/l, where the tumour is localised to the prostate and has not yet broken out of the capsule surrounding the prostate gland), three main treatment options are given to the patient (active surveillance, radical prostatectomy and intense radiation therapy). The three main treatment options outlined above are compared for the treatment of early PCa in the ProtecT trial, in which all three treatment modalities are shown to reduce the risk of clinical progression within the disease state.[8] However, following the move to a more aggressive form of the disease (>10 mg/l, positive nodule diagnosis on DRE Gleason >7), active surveillance is no longer an option as a management method, with the surgical and radiation methodologies for its treatment being favored.

As discussed previously in section 1.1.4.1, PCa growth is driven by androgens (specifically testosterone and DHT), therefore, the use of ADT can be used as either a stand-alone treatment or in combination with other treatment modalities in hormone-naïve PCa with this coming in a variety of forms

(orchiectomy, Luteinizing hormone-releasing hormone (LHRH) agonists and LHRH antagonists) all of which designed to lower androgen levels and slow tumour progression.[28] The combination of ADT and surgery in order to shrink patients PCa tumors prior to radical prostatectomy is used to make the surgery more manageable, with patients who are at risk of PCa reoccurrence being treated with simultaneous radiation and ADT. These therapeutic options came off the back of several random trials which suggested improved cancer survival rates when patients are treated in this manner.[29–31] Once the disease has progressed further, often it becomes resistant to hormone therapy, however, the course of treatment usually follows the path of intermitted ADT as it has been shown to give patients a better quality of life with limited side effect. This treatment option has shown no overall improvement in cancer survival rates when compared to continuous ADT.[32] Recently the CHAARTED trial looked at the survival rates of men treated with ADT compared to those treated with ADT and docetaxel. Men showed 33.3% longer life expectancy when treated with both ADT and docetaxel simultaneously compared to being treated with just ADT.[33]

1.1.5 The search for new prostate cancer biomarkers

The use of PSA serum levels in the detection of PCa has been used clinically since its introduction in 1989.[34] Since its introduction a dramatic increase in the PCa incidence rate has been seen (figure 1.4). However, the increase in incidence in PCa can partially be attributed to the high rate of false-positive and false-negative results that the PSA-test gives when used as a stand-

alone diagnostic tool. Ultimately, putting patients through unnecessary downstream procedures and anxiety.[34] For this reason, several improvements to the PSA-test along with the search for new PCa biomarkers has become a rapidly developing area of research. For example there are attempts to increase the selectivity and specificity of the PSA screening tests *via* derivations on the original tests including; the use of percentage free PSA,[35] age specific PSA ranges,[36] and PSA velocity. However, the majority have proved largely ineffective due to the conditions such as BPH effecting selectivity for PCa alone being very difficult to achieve. Percentage free-PSA however, can be utilised as a more selective biomarker for PCa when compared to PSA testing alone as it is able to distinguish a PCa disease state from other prostate associated conditions. This is due to the method using a ratio of active-PSA against free-PSA within the bloodstream. Under normal conditions, PSA is produced by acini within the prostate in the active form which is free to diffuse into the bloodstream where it is rapidly bound by proteinase inhibitors such as alpha-1-antichymotrypsin (ACT) and alpha-2-macroglobulin. A percentage of active-PSA will also undergo proteolysis generating inactive-PSA which is able to enter the bloodstream as free-PSA. The percentage of active-PSA/free-PSA is seen to be higher in men with PCa when compared to those with normal prostate or BPH, as a decrease in free-PSA internal proteolytic cleavage within prostate cells is observes. Resulting in a measurable change in the percentage free-PSA being recorded when measured.

The search therefore for new molecular biomarker for the diagnosis of PCa has recently resulted in the advent of commercially available diagnostic

from companies such as Decipher, Prolaris and Oncotype DX.[37–39] The major

advantage that new biomarkers have over PSA testing is the ability to

prognostically distinguish between indolent and aggressive PCa tumours. These

prognostic methods offer additional information on treatment options before a

plan is determined by the patient and treatment team.
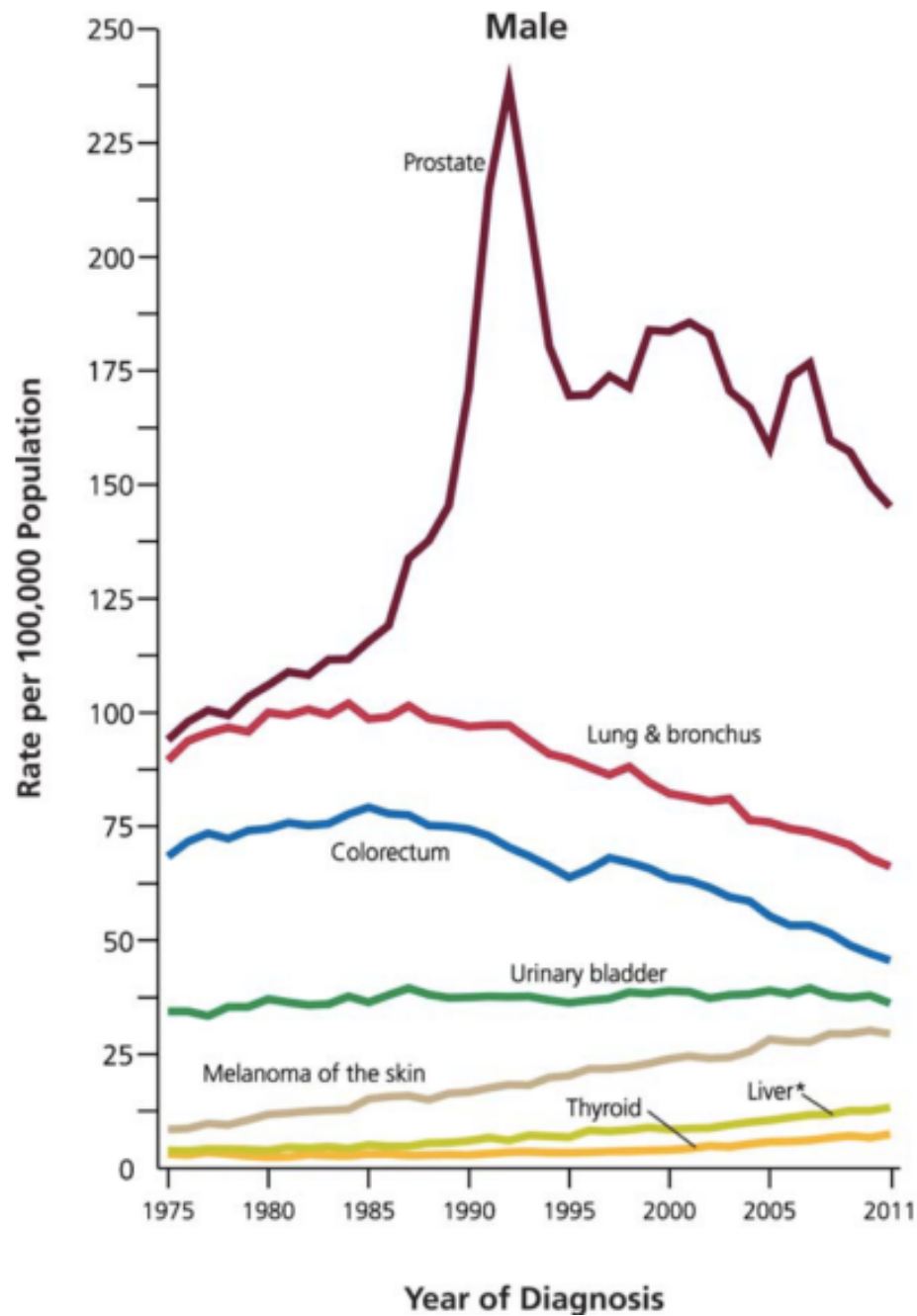
Figure 1.4. Cancer incidence rates against the year of diagnosis for a range of male cancers. As can be seen for PCa after PSA test has been introduced in the early 1980's a large peak is seen for cases of incidences.[40]

Work carried out over recent years by Sturge *et al.* has investigated an alternative biomarker for the detection of PCa. The work within the Sturge lab has looked at the strong positive correlation between the expression and

function of tumour-cell associated Endo180 (which is present in ~75% of PCa cases), Gleason sum score and PCa patient survival.[41,42] This strong correlation between associated Endo180 and PCa forms the basis for the work within this research thesis, with Endo180 being used as a biomarker used in the development of the multimodal bio-imaging platform under development within this body of work. The bio-imaging probes discussed within this work are designed to be used to detect invasive epithelial cells in the prostate gland, using fluorescent/Magnetic Resonance Imaging (MRI) based diagnostic medical imaging methods in the hope of delivering a novel diagnostic/imaging probe for earlier detection of aggressive PCa.

1.2 Endo180

1.2.1 Overview

Synonyms: Endocytic Receptor 180 (Endo180, used throughout the thesis); Macrophage Mannose Receptor, C-type 2 (MRC2); Urokinase-type Plasminogen Activator Receptor Associated Protein (uPARAP).

Endo180 was first identified by the Isacke group in the early 1990's, initially Endo180 was described as a 180 kDa endocytic receptor (initially given the name p180 in literature) in the early 90's.[43] In 1996 however, this work was expanded on by Wu *et al.* who were able to show that Endo180 was in fact a macrophage mannose receptor, belonging to a wider ranging family which included mannose receptor (CD206), the m-type phospholipase A_2 receptor (PLA$_2$R) and DEC-205[44,45]. In 2000, Behrendt was able to coin a new name for

Endo180 by identifying it as urokinase plasminogen activator receptor associated protein (uPARAP).[46] This name was given due to the ability of being able to from a molecular complex with pro-urokinase plasminogen activator (Pro-uPA) and urokinase plasminogen activator receptor (uPAR) at the same time (figure 1.5). Many reviews have been published since the identification of Endo180, demonstrating Endo180 as a endocytic collagen receptor playing a major role within the tissue remodelling process *via* the delivery of collagen to areas of lysosomal degradation through collagen internalisation. [45,47,48]

1.2.2 Structure of Endo180

Endo180, much like the other members of the mannose receptor family can be subdivided into four different structural components.[44,45] Endo180 is able to be characterised by the terminal cysteine-rich domain (CRD) which is immediately followed by a fibronectin type II (FNII) domain. These two constituent parts play a crucial role in the binding of some sulphate sugars (CRD) as well as the binding of collagen (FNII).[45] Eight C-type lectin domains (CTLD) arranged in series form a chain like structure giving Endo180 a single polypeptide backbone. These three components (CRD, FNII and 8-CTLD's) all terminate in a short cytoplasmic tail which has numerous sites for phosphorylation, with the cytoplasmic tail playing a role in allowing the extracellular collagen ligands into the cell.[43,45]
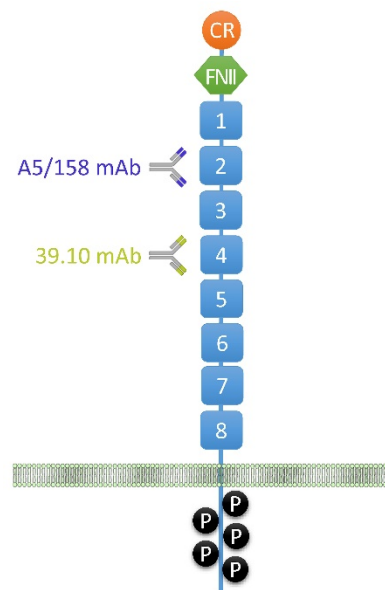
Figure 1.5. Structure of Endo180. Four main components: a cysteine rich (CR) domain, fibronectin type II (FNII) domain, eight C-type lectin domains (CTLDs) capable of selective binding to specific mAb's (shown above in figure) as well as a cytoplasmic tail capable of phosphorylation and generating intracellular signals.[49]

1.2.3 Endo180 and mAb specific binding

Work by Rivera-Calzada *et al.* in 2003 was able to show that the CRD and FNII domain can form a loop like structure with CTLD-1, this is possible due to the CRD being able bind to CTLD-1.[50] However, it was postulated that this loop like structure opened with changes in environment as well as ligand binding. Several in-house antibodies under study within the Sturge lab are capable of binding to different domains in human Endo180. Mouse anti-human antibodies (mAb) E1/183 bind selectively to CRD domain, while mAb A5/158 binds

selectively to CTLD-2, as does mAb 39.10 to CTLD-4 (figure 1.5).[51] Engelholm *et al.* have been able to show with work published in 2015 that an anti-mouse Endo180 antibody can be used to treat primary bone cancer.[52] Within the work presented by Engelholm and team, Endo180 was identified as a therapeutic target for the treatment of osteolytic (bone-degrading) osteosarcoma. This was postulated to be possible considering the high expression of Endo180-positive osteosarcoma cells present at bone lesion sites. Endo180 expression was silenced in a mouse xenograft model that comprised of NCTC-2472 cells (an osteosarcoma cell line) being injected into the femurs of mice. Engelholm also observed high levels of Endo180-positive osteosarcoma cells in human tissue samples, validating their choice of *in vivo* model as clinically relevant. In their study, the treatment of mice with osteolytic osteosarcoma using the monoclonal antibody (mAb) 5f4 led to silencing of Endo180 protein expression through recognition of the first three N-terminal domains (CRD, FNII and CTLD-1), but this silencing effect involved an unknown molecular mechanism.[53,54] Alongside the work by Engelholm, the Sturge group have shown that targeting of Endo180 with silencing mAb 39.10 and A5.158 can be used to block the migratory behaviour of a range of invasive tumour cell types,[55,56] including cells found in aggressive PCa. Sturge and team were first able to show that mAb 39.10 can be used for epitope-specific targeting of CTLD-4 within the Endo180 backbone. Moreover, binding of mAb 39.10 to CTLD-4 was found to result in the induction of invasive behaviour by normal epithelial cells. This effect was found to be downstream effect of the disruption of an epithelial-to-mesenchymal (EMT) suppressor molecular complex formed between CTLD-4 in Endo180 and the extracellular matrix metalloproteinase (MMP) inducer CD147, with this

discussed further in section 1.2.3.1.[42] In contrast, mAb A5.158 was found to function in a similar manor to mAb 5f4 in the work presented by Engelholm. The epitope binding of mAb A5.158 to CTLD-2 resulted in blockade of the invasive properties of PCa cells.[41] Figure 1.6 depicts the signalling pathways of Endo180 which involves members of the Rho GTPase family, RhoA, Cdc42 and Rac1, all of which Sturge has shown to regulate intracellular actin dynamics.[56] The rapid activation of Cdc42 and Rac signalling pathways leading to promotion of chemotactic tumour cell migration was shown in breast cancer cells expressing Endo180, due to Endo180 enhancing uPa-mediated filopodia production.[55] Sturge was also able to connect Endo180 with cell motility *via* Endo180 mediating the activation of the RhoA pathway, ultimately leading to the activation of Rho Kinase (ROCK) before the phosphorylation of myosin light chani-2 (MLC-2).[56]

        The work presented by both Engelholm and Sturge form the basis for work outlined within this body of work. Specifically, the aim of this thesis was to design and synthesise a specific antibody based diagnostic tool with the unique capability of medically imaging malignant prostate tumours in a non-invasive manner.
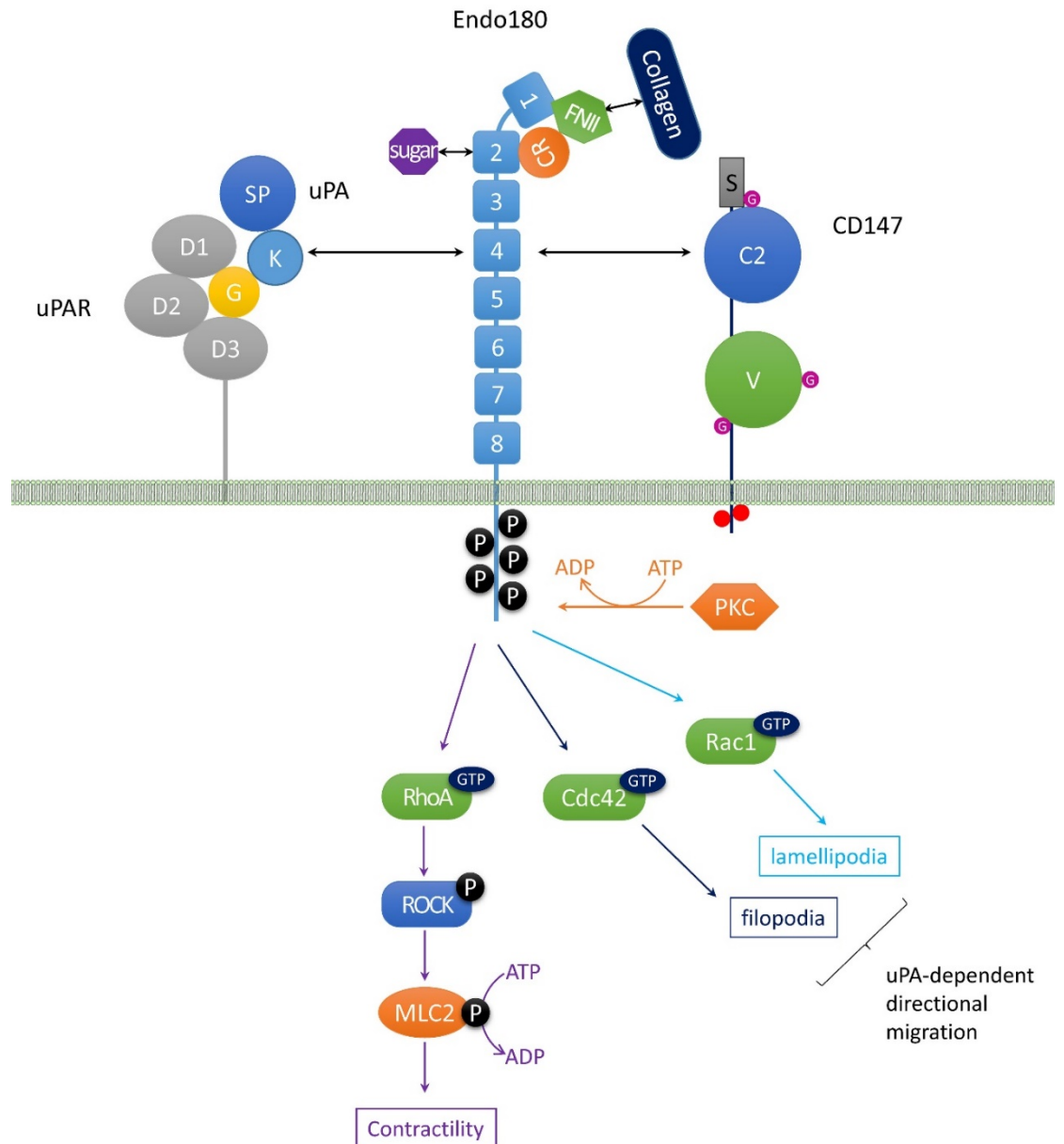
Figure 1.6. Endo180 binding partners as well as downstream signalling pathways which are influenced by endo180. Where CRD – cysteine-rich domain, FNII – fibronectin type II-like domain, 1-8 – eight C-type lectin domains (CTLD 1-8), P – phosphorylation sites. uPA: SP – serine protease domain, K – kringle domain, G – growth factor domain. uPAR: D1-3 – three lymphocyte antigen-6/uPAR domains (LU domains). CD147: S – signal peptide, C2 – immunoglobulin (Ig)-like C2-type domain, V – Ig-like V-type domain, G – N-Glycosylation sites, red cycle – hypoxia-inducible factor (HIF) binding sites.[49]

1.2.3.1 Endo180 and cluster of differentiation 147 (CD147) role in supressing EMT

Epithelial-to-mesenchymal transition (EMT) is a reversible trans differentiation program involving a switch from apical-to-basal polarization of epithelial cells, which are adherent to each other and a basement membrane, to a detached mesenchymal-like phenotype that is highly motile and invasive.[57] Type-III EMT is linked to early stage tumour development and progression with tumour cells obtaining mesenchymal-like properties, with Endo180 playing a crucial role in cell migration and adhesion in early stage PCa. As explained previously in section 1.2.3, Endo180 is linked to the RhoA, Cdc42 and Rac1 signalling pathways (figure 1.6), regulating cell motility and adhesion to one another.[55] The importance of Endo180 as a EMT suppressor was shown by Sturge *et al.* in a recent study, where it was shown that CTLD-4 within the Endo180 backbone formed a complex with cluster of differentiation 147 (CD147) known as a extracellular matrix metalloproteinase inducer (EMMPRIN). The complex of Endo180-CD147 was shown within the work to act as a novel EMT suppressor due to do its ability to modulate cell adhesion, however, the disruption of complex Endo180-CD147 was attributed to the marked decrease in 5 year survival outcome in PCa patients with Endo180 expressing low-to-intermediate grade PCa (Gleason score 5-7) (figure 1.7).[42]
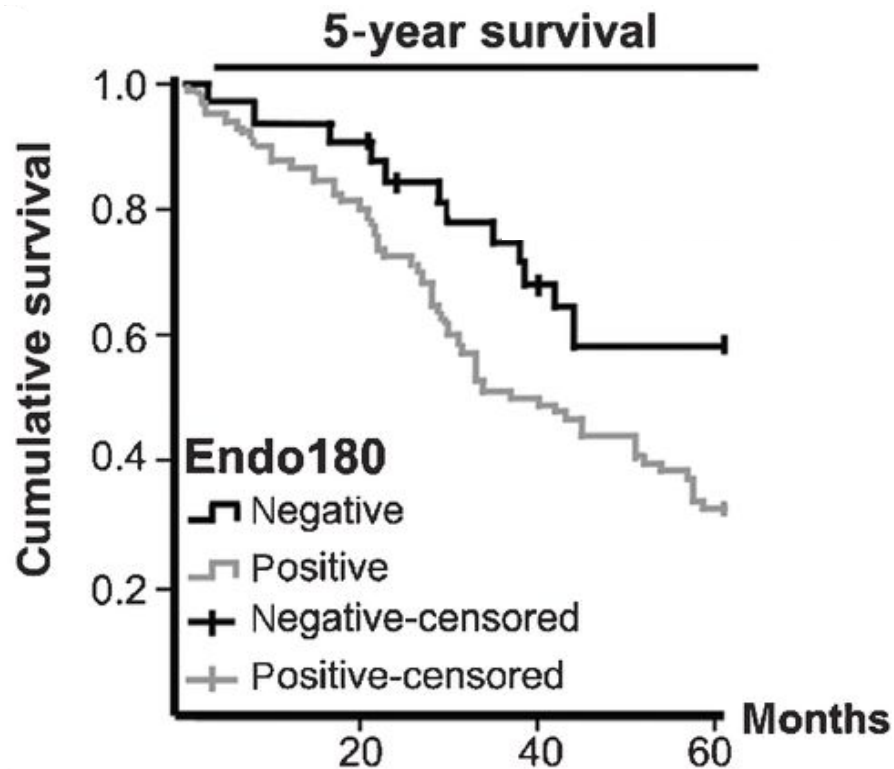
Figure 1.7. Difference in 5-year survival rate of PCa patients based only on Endo180 expression within the tumour.

Following the breakdown of complex Endo180-CD147, Endo180 plays a role in PCa tumour progression *via* its role in EMT (promoting the disassembly of cell-cell junctions).[56,58] Kogianni *et al.* showed further that PCa tumour progression is effected by Endo180 as it has an ability to drive an EMT-like phenotype *via* contractile signals promoting the disassembly of cell-cell adhesions and increasing cell migration, whilst up regulating EMT-promoting factor TGF-β_1.[51] The team were also able to show within the study that Endo180 expression was highly expressed with a EMT-like phenotype, with this correlating with Gleason score in PCa. Furthermore, the Endo180-CD147 complex is shown by Sturge *et al.* to be integral in an epithelial phenotype of prostate cells, with this in mind Endo180 has become a new biomarker for imaging PCa progression and is used as such within this body of work.

1.3 Molecular & Medical Imaging

Molecular imaging is a rapidly developing discipline which sees the combining of both molecular biology with a medical imaging technique. The advances over the last decade within both cell and molecular biology have led to an enhancement in the understanding of cancer biology as well as cell behaviour. Medical imaging techniques allow for the visualisation of pathophysiological processes non-invasively in a real-time environment, whilst also offering the doctor-patient team the possibility for serial monitoring whilst providing information on disease state. This allows for specific alterations to be made to a patient treatment plan.[59] These modifications to patient treatment plans are made available through longitudinal, non-invasive, quantitative and repetitive imaging of targeted biological processes at both molecular and anatomical levels. In recent years, molecular and medical imaging has played an important role in the field of diagnostic medicine, particularly within the field of oncology. Medical imaging methods can be seen to be used at the forefront of diagnostic medical research in a bid to develop new tumour-targeting therapies as well as novel approaches for the early detection and monitoring of previously diagnosed malignancies.[60] The techniques for the imaging of cancer include optical imaging (bioluminescence and fluorescence), Positron Emission Tomography (PET), Single Photon Emission Computed Tomography (SPECT) and Magnetic Resonance Imaging (MRI).[60]

1.3.1 Magnetic resonance Imaging (MRI)

Magnetic Resonance Imaging (MRI) is a non-invasive diagnostic medical imaging technique developed over 50 years ago and is used daily by clinical teams to evaluate multiple disease states.[61] MRI is capable of producing highly detailed three-dimensional images of anatomical features such as organs, tissue and blood flow within the human body. The technique utilises the high abundance of water molecules (specifically the ^{1}H nuclei present) within the human body, to give detailed images of organs. This results in a low signal to noise ratio, producing a technique which offers a sensitivity range for the spatial resolution within the mm. In the instances where MRI is to be used to aid in the detection of disease states such as cancer, contrast agents consisting of paramagnetic metal complexes are widely used to overcome sensitivity issues (discussed in section 1.4). MRI was first developed within the University of Nottingham by Sir Peter Mansfield, alongside the efforts of Paul Lauterbur at the University of Illinois with both works coinciding in 1972. The efforts of both can be seen in the joint award of the Nobel prize in medicine in 2003.[62,63]

1.3.1.1 Principles of Magnetic Resonance Imaging

MRI can be described as a complex proton nuclear magnetic resonance (NMR) experiment and is based upon the interaction between an applied static magnetic field (β_0) and a nucleus that possess spin.[64] Nuclear spin angular momentum is a property that is dependent on the exact composition of the atom, every element within the periodic table (with exception to argon and

cerium) will produce at least one isotope that will have spin. Due to this, nearly

all elements in the periodic table can be studied using MRI due to its reliance on

the spinning motion of specific nuclei present in biological tissues. MRI is an

imaging modality based upon spin active nuclei which are present within the

body, such as protons, all of which have a spin quantum number I = ½.

Electromagnetic induction law states, that nuclei which have a net

charge and are precessing acquire a net magnetic moment (or net magnetic

vector) and are able to align with an external magnetic field.[65] This will only

occur within an element if the mass number is odd giving the nucleus a value of

I = ½, and this process is called angular momentum or spin. When a nucleus has

angular momentum, it is to be considered constantly spinning about its own

axis perpendicular to the direction of rotation. With this being present in all

elements with I = ½ (figure 1.8).
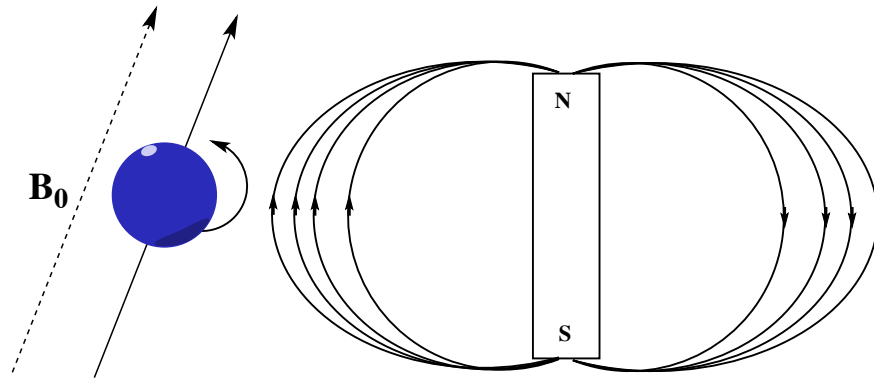
Figure 1.8. shows a ^{1}H nucleus spinning about its own perpendicular axis. This creates a magnetic field which is parallel to its own axis (left hand side). This is analogues of a bar magnet which has a magnetic field flowing from north to south poles.

To perform an MRI scan, the patient's body which contains tissue with an abundance of MRI active nuclei (due to the body being made of mostly water and fatty tissue) are placed into a strong, static external magnetic field (β_0). Once exposed to β_0 the spins within the protons will all align either parallel or anti-parallel with the external magnetic field. The distribution between parallel and anti-parallel spins is described by the Boltzmann equation, with distribution being determined by energy difference between the two states. With the strength of β_0 also playing a role in overall distributuion. The distribution will then result in a net spin in one direction (usually parallel to β_0 as this is the lowest energy state). As the spins try to align themselves with β_0 they will begin to precess perpendicular to the magnetic field in which their being exposed to. This produces a constant speed of rotation with this known as the Larmor frequency around the axis of β_0 with the z-axis of rotation being parallel (figure 1.9).
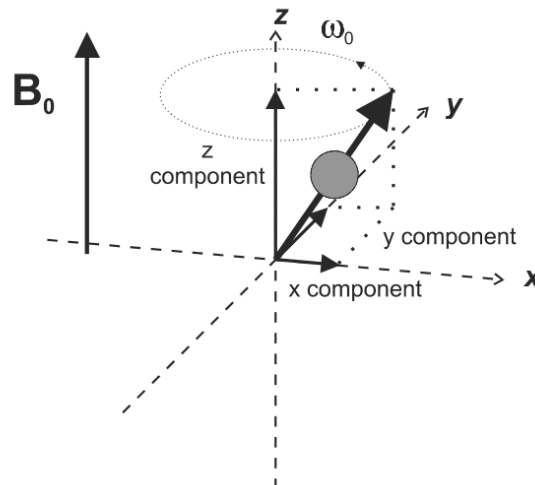
Figure 1.9. Depicting proton motion in an external magnetic field β_0 where a proton will process about the z-axis of rotation parallel to that of the external magnetic field β_0 with a frequency proportional to β_0. Known as the Larmor frequency ω_0.

The frequency of precession ω_0 is determined by and proportional to β_0 which is shown by the Larmor equation.[66] This is shown in equation 1.1;

$$\omega_0 = \gamma\beta_0 \qquad\qquad\qquad (1.1)$$

Where ω_0 is the Larmor frequency in megahertz (MHz), β_0 is the magnetic field strength in tesla (T) and γ is the gyromagnetic ratio (constant) in $s^{-1}T^{-1}$. The net magnetisation vector (NMV) is the summation of all the magnetic moment vectors produced by ^1H hydrogen nuclei within a MRI. The sum of the magnetisation vector differs when inside and outside of an β_0. In the absence of an β_0 the individual magnetic moments are randomly orientated and oppose each other resulting in zero net magnetization.[67] When an β_0 is applied, the

hydrogen nuclei will align within the field in one of two directions parallel to the direction of β_0 (spin-up or spin-down) and this phenomena is known as the Zeeman effect. Whilst exposed to an β_0 both parallel and antiparallel hydrogen nuclei which will be present, with more parallel spin nuclei being observed. This gives rise to a NMV whilst in a magnetic field and is given the term M_0. The orientation of M_0 will be in the direction parallel to β_0 and will be constant with respect to time, this is shown in equation 1.2.[64]

$$M_0 = \chi\beta_0 \tag{1.2}$$

Where χ is the magnetic susceptibility.

Resonance occurs when an object is perturbed by an oscillation close to its own natural frequency. In the case of MRI, a radiofrequency (RF) pulse at the Larmor frequency of hydrogen nuclei (42.5 MHz for a 1T instrument) is used to excite spin up hydrogen nuclei as to increase the population of spin down nuclei.[65] The energy required to induce resonance within hydrogen nuclei at clinical magnetic field strength corresponds to the RF band in the electromagnetic spectrum. On excitation of spin up nuclei states with an RF pulse, the NMV will move out of alignment with β_0. The angle in which the NMV has distorted is called the 'flip angle' and is determined by the amplitude and duration of the RF pulse. The most commonly used flip angles are $\pi/2$ (90º) or π (180º) and these are shown in Figure 1.10.[68]
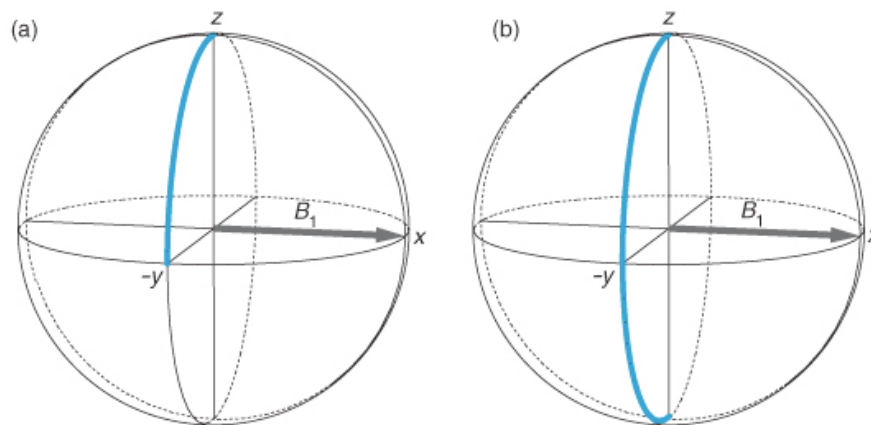
Figure 1.10 3-D images of the effect on the NMV when a RF pulse β1 is used to induce a flip angle of (a) $\pi/2$ (90º) and (b) π (180º). The blue line in the diagram is assumed to be the tip of the NMV as the RF pulse is applied.[65]

After the removal of an RF pulse the NMV is again under the influence of β_0 and will try to realign itself. As this process occurs excited hydrogen nuclei will lose energy and relaxation of the NMV is observed. During this relaxation process, high energy spin-down nuclei return to their lower energy state spin-up configuration parallel to β_0. This can be seen to happen in two distinct methods; a longitudinal relaxation which allows for recovery of longitudinal magnetization (T_1 recovery), and a decay process of transverse magnetisation (T_2 decay).

1.3.1.2 T_1 weighted imaging

When a temporary magnetic field is applied (RF or β_1) to a nucleus with a NMV it will temporary align in the x direction until the external magnetic field is removed. On removal of β_1 the NMV will attempt to re-align itself with β_0, in

an attempt to re-align with the y-axis. The relaxation of the NMV following the removal of β_1 is able to be expressed in equation 1.3 which links longitudinal relation (T_1) with net magnitisation (M_0).[69]

$$M_z = M_0 \left(1 - e^{-t/T_1}\right) \tag{1.3}$$

where M_0 is the net magnetisation, t is the time after the RF pulse and T_1 is a time constant of longitudinal relaxation which is tissue dependent. T_1 relaxation/recovery time is a measurement of the lattice parameters around the spin and can be expressed as a function of the rotational correlation time.[70]

1.3.1.3 $T_2/T_2{}^*$

T_2 relaxation otherwise known as the transverse or spin-spin relaxation time is the time taken for nuclear spins to move out of phase with one another. T_2 determines the rate at which the signal can be seen to be extinguished. T_2 relaxation occurs along the transverse plane and is produced by tilting the longitudinal magnetisation into the transverse plane using an external RF pulse. The newly produced transverse magnetisation which precesses about the z-axis at the Larmor frequency initially has a magnitude as the spins are all in alignment (in phase).[71] Following the removal of the external RF pulse, the spins will fall out of alignment (decay) along the transverse plane and return to an equilibrium position. T_2 decay is defined as the time taken for 37% of the excited net magnetisation along the transverse plane to return to the equilibrium position.

In principle, once an external RF pulse is applied, excitation of protons

forces spin coherence which over time diminishes back to the equilibrium

position. Once excited, all individual magnetic spins will precess with the same

Larmor frequency, however over time each individual spin will begin to precess

at their own Larmor frequency removing any coherence between the net

magnetisation.[69,72] This can be shown in equation 1.4

$$M_{XZ} = M_{XZ}(0)e^{-t/T_2} \qquad\qquad (1.4)$$

Where $M_{XZ}(0)$ is the net magnetisation in the xz axis, $M_{XZ}(0)$ is the

transverse magnetisation, t is time taken and T_2 is the transverse relaxation and

defined as the time taken for 37% of the net magnetisation after an external RF

has been recovered. T_2 relaxation is primarily caused by the intrinsic field of

adjacent protons (spin) and is therefore denoted as spin-spin relaxation.

Transverse relaxation will cause dephasing of the coherent transverse

magnetization resulting in a completely out of phase sample. Also observed is a

reversible bulk dephasing effect caused by the inhomogeneity within the

magnetic field, the difference in magnetic susceptibility of different tissues and

gradients applied for spatial encoding, this is given the relaxation time T_2*.[71]

Due to the inhomogeneity of the magnet, a true T_2 value therefore will not be

obtained, rather a shorter signal decay will be observed T_2*. In order to achieve

a true reading for a T_2 relaxation and to eliminate inhomogeneity within the

magnetic field, a 180º RF pulse must be used. This is called a spin-echo

sequence and will give a true T_2 relaxation.

Tissues within the body have different T_2 relaxations, this allows for an image with different pathologies being shown in greyscale. For example water protons within tissue have a T_2 relaxation of 40-200 ms.[69] Longitudinal and transverse relaxation and recovery work in parallel with each other to result in an image being produced, due to the longitudinal relaxation having a much greater effect than the transverse relaxation (or at least equal effect) contrast agents are developed in order to change T_1 relaxation times. This therefore will allow for images of disease states such as cancer to be both diagnosed and monitored whilst using MRI.

1.4 Contrast agents for MRI

1.4.1 First generation gadolinium contrast agents

The ongoing evolution of technologies within MRI has had an influential role in making it one of the most frequently used modalities for diagnosis and management of disease states such as liver disease and PCa.[73-75] Contrast agents (CA), have been developed at a rate in line with that of technology as so to allow for better contrast within images between healthy and diseased tissue. CA have been developed using many different paramagnetic metal ions due to their innate ability to accelerate relaxation rates of water protons within the body.[76] Many examples of T_1 CAs with unpaired electrons are within the transition metal and lanthanide series, for example manganese(II)[77], iron(III) and gadolinium(III) have all been used to create CA for MRI.[78] gadolinium(III) based contrasted agents (GdCA) fall into the category of T_1 contrast agents, due to their innate ability to increase signal intensity by lowering the T_1 of bound water protons by increasing water exchange rates of said proton (rates in excess of 10^6 s^{-1}). This increase in signal can then be passed on to surrounding water molecules.[79] Gd(III) is chosen due to its near perfect properties for use within CA design, its seven unpaired electrons, slow electron relaxation rate and large effective magnetic moment, μ_{eff} = 7.94 B.M, result in a metal that has appeared to be built for CA design.[76,80]

First generation GdCAs centred around the complexation of Gd(III) with simple derivatives of either diethylenetriamine pentaacetic acid (DTPA)[20,21] or 1,4,7,10-tetra-azacyclododecane-1,4,7,10-tetraacetic acid (DOTA).[22] This work

lead to the production of GdCAs which were approved for clinical use from the

early 1990s, with these designs being shown in figure 1.11.
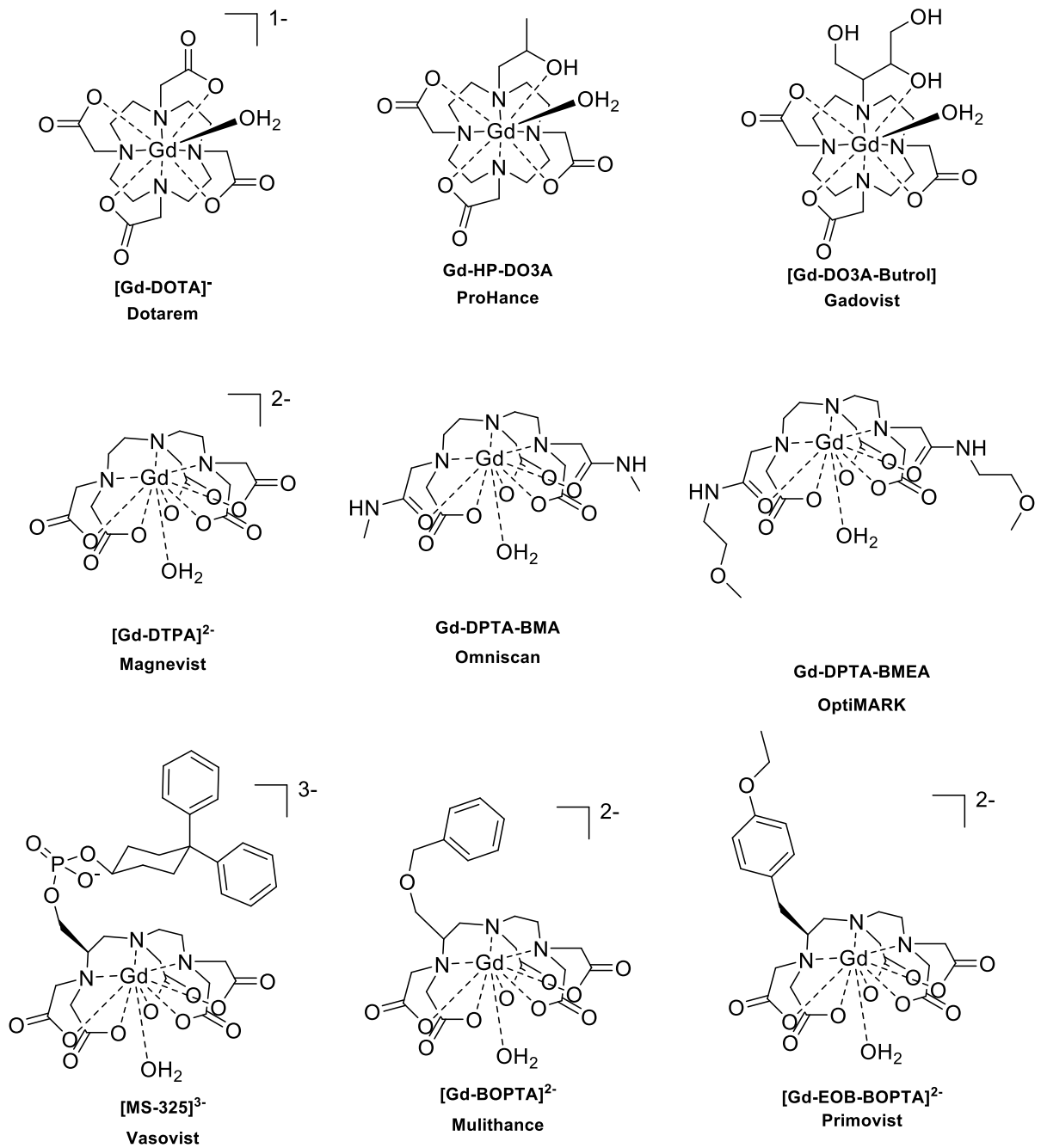
Figure 1.11. First generation GdCAs as well as their clinically used name.

Following their introduction into a clinical environment, both clinicians and researchers alike have had fears over the stability of first generation GdCA.[81] This due to the removal of the Gd(III) metal under some biological conditions, such as an increase in patient cases of nephrogenic systemic fibrosis (NSF) in patients with pre-existing kidney problems with this attributed to a combination of acidosis and slow clearance of GdCA; Patients have also been seen to exhibit gadolinium deposits within the brain following the increased use of GdCAs within clinical practice.[81] Therefore, regulations have since been put in place to restrict the use of clinically approved GdCAs based on their kinetic inertness. This in 2017 lead to the EMA restricting all use of non-linear GdCA. A common feature which is observed within all of the first generation GdCAs is their high level of kinetic stability (table 1.1). This results in each ligand forming a highly stable 8-member complex with the Gd(III) ion, with one free coordination site for the binding of water to the metal centre.[82,83]

Contrast Agent	Chemical Name	$\log K_{ML}$	k_{obs} (10^3s^{-1})
Magnevist®	[Gd-DTPA]$^{2-}$	22.46	1.2
Omniscan®	Gd-DTPA-BMA	16.85	> 20
2ptiMARK®	Gd-DTPA-BMEA	16.84	-
Dotarem®	[Gd-DOTA]$^-$	25.30	0.021
Gadovist®	[Gd-DO3A-butrol]$^{2-}$	21.80	-
Prohance®	Gd-HP-DO3A	23.80	0.064

Table 1.1. showing a list of association constants, $\log K_{ML}$, and acid dissociation rate constants, k_{obs}, for commercially available GdCAs.

Following binding of a water molecule to the Gd(III) metal centre, properties

such as water proton relaxivity and inner sphere water relaxation can be tuned

in order to increase the observed r_1 value.

1.4.1.1 Water proton relaxivity (r_1)

The enhancement of both longitudinal and transverse relaxation rate

(specifically longitudinal relaxation when using GdCAs) to increase the signal to

noise ratio allowing for an improved image within MRI is complete with the use

of GdCAs. The longitudal relaxation rate of free water protons, R_{1p}, can be

shown to be made of two contributions, from both inner and outer sphere.

Inner sphere (R_{1p}^{IS}) arise from water molecules bound directly to the metal

centre, whereas, outer sphere (R_{1p}^{OS}) contributions come from the bulk water

(equation 1.5). CA efficiency is shown in terms of relaxivity, r_1, this is related to

R_{1p} as shown by equation 1.6 below with r_1 expressed in mM^{-1}s^{-1}.[84]

$$R_{1p} = R_{1p}^{IS} + R_{1p}^{OS} \tag{1.5}$$

$$R_1 = R_{1p}/[Gd] \tag{1.6}$$

The design of the CA ligand dictates that the major contributor for relaxation is

the inner sphere contribution of R_{1p}. Ligands therefore are designed with at

least one space for a water molecule to bind to the metal centre in order to have

an effect on R_{1p}^{IS}, with this being shown in equation 1.7.[84]

$$r_1 = \frac{cq}{55.5}\left(\frac{1}{T_{1m}+\tau_m}\right)$$ (1.7)

Where q is the number of coordinated water molecules, c is the concentration of paramagnetic ion, T_{1M} is the longitudinal relaxation time of the inner sphere waters and τ_m is the water exchange lifetime.

1.4.2 Increase in (r_1) through contrast agent design.

The use of strategic contrast agent (CA) design has become an integral part within optimisation relaxation rates, allowing for CAs to have their capabilities fully unlocked. CA design is able to dictate the complex distribution, localisation and behaviour in a dynamic system all with intricate ligand design. Due to the low sensitivity MRI suffers as an imaging technique, often large quantities of CA (often on the gram scale) are needed to be administered to render a usable image. Therefore, a desire to reduce the amount of CA used by increasing relaxivity is greatly desired within the field. Relaxivity (r_1), as described above is the relaxation rate per unit concentration of contrast agent (section 1.4.1.1). This is able to be controlled by a number of controlling factors including, hydration state (q), water exchange lifetime (τ_m) and rotational correlation time (τ_R). With some controlling factors being seen to be linked by equation 1.3.

1.4.2.1 Hydration state

  The hydration state of GdCAs, such as those shown in figure 1.11 is 1.

The $q = 1$ is due to the octadentate ligand backbone within the GdCAs in figure

1.11 forming a complex with a trivalent gadolinium ion which possess a

coordination number of 9, allowing for 1 available inner sphere water molecule

to bind to the metal centre. Following coordination of water to the metal centre,

an increase in r_1 is seen. From equation 1.3, it is evident that an increase in

hydration state ($q>1$) will lead to an increase in relaxivity. In general, increased

relaxivity can be achieved by decreasing available coordination sites within the

ligand, therefore offering more coordinating sites for inner sphere water to bind

to the metal centre. However, on increasing q a decrease in thermodynamic

stability is often observed due to innate susceptibility to phosphate or

bicarbonate substitution. Leading to metal decomplexation and toxicity issues

which are associated. This is seen for example when one acetate arm is

removed from $[Gd(DOTA)(H_2O)]^-$ to form $[Gd(DO3A)(H_2O)_2]$. Overall, q is seen

to double however, the stability of the complex lowers due to the water

molecules being able to be displaced *via* anion binding. Raymond and co-

workers were able to show a GdCA with $q = 2$ was able to be

thermodynamically stable as well as resistant to anion coordination with the

use of hydroxypyridinone (HOPO) group of compounds.[85] As GdCA with a $q > 1$

have been shown to have problems with thermodynamic stability within a

biological environment, all currently used GdCA in the clinic can be seen to be

$q=1$. This leads to other methods for the increasing of relaxivity which are seen

in figure 1.12.
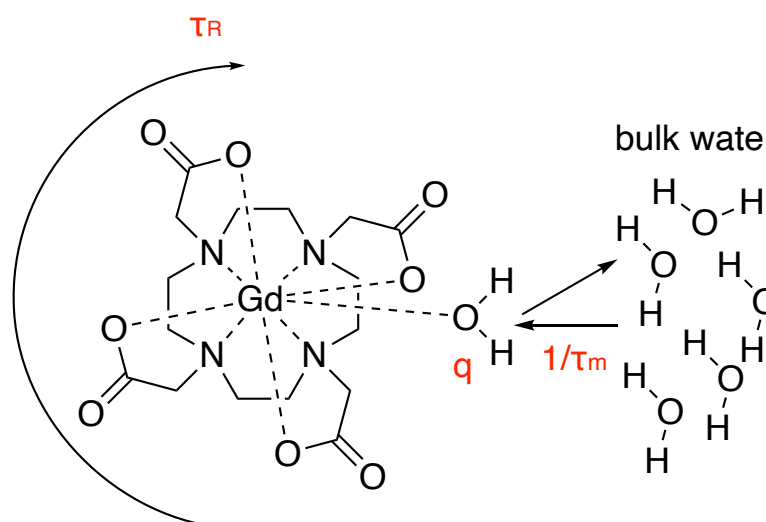
Figure 1.12 shows the parameters which influence relaxivity of a gadolinium based contrast agent [Gd(HP-DO3A)(H$_2$O)]. q (hydration state) the number of water molecules coordinated the metal centre in the inner-sphere. τ_m represents the water exchange lifetime and τ_R represents the rotational correlation time of the GdCAs.

1.4.2.2 Water exchange lifetime (τ_m)

Water exchange lifetime, τ_m ($k_{ex} = \frac{1}{\tau_m}$) plays an integral role within determining relaxivity of a GdCAs. This parameter represents the time an inner-sphere water molecule spends coordinated to the Gd(III) metal centre before exchanging back into the bulk water (depicted in figure 1.12), resulting in relaxation being transmitted back to the bulk water protons. Water exchange lifetime has also been shown to influence the rotational correlation time (τ_R), with an increase τ_R resulting in increased relaxivity. The relaxivity enhancement seen by increasing τ_R is only able to be made possible by the optimisation of τ_m (τ_m = 40 – 100 ns).[86] Water exchanging at the coordinated metal centre occurs *via* a water molecule leaving the coordinated inner-sphere,

forcing a change of shape and geometry within the complex. On the detachment

of the inner-sphere water molecule, an octadentate complex is formed with an

8-coordinate metal centre. Thus, allowing another water molecule from the

outer (second) coordination sphere to bind to the Gd(III) metal centre.

Therefore, restoring the 9-coordinate geometry around the Gd(III) metal.

During this process of exchange to and from the bulk water however, the water

molecules must have sufficient residency time on the Gd(III) ion before

dissociating back to the second coordination sphere. If too short a time is spent

on the metal, its protons will not be efficiently relaxed. However, too much time

spent on the metal is unnecessary, as this occupies the first coordination sphere

and delays proton relaxation further.[86,87] Within the majority of GdCAs which

are have been reported, most have shown a slow water exchange rate. The

optimisation of which would go a long way in to optimizing relaxivity

measurements within GdCAs.[88]

1.4.2.3 Rotational correlation time (τ_R)

As shown in equation 1.3, inner-sphere relaxation is dictated by the

relaxation time of bound water, T_{1m}, as well as water residency time, τ_m. These

two parameters are to be kept as short as possible for relaxivity of GdCAs to

increase. However, for the first-generation contrast agents $T_{1m} > \tau_m$ therefore,

T_{1m} limits relaxivity in these cases. T_{1m} is able to be shown in equation 1.8

below.

$$\frac{1}{T_{1m}} = \frac{2}{15} \frac{\gamma_H^2 g_e^2 \mu_B^2 S(S+1)}{r_{GdH}^6} \left[\frac{7\tau_{c2}}{1+\omega_S^2\tau_{c2}^2} + \frac{3\tau_{c1}}{1+\omega_H^2\tau_{c1}^2} \right]$$ (1.8)

Where γ_H is the proton gyromagnetic ratio, g_e is the electron g-factor, μ_B is the

Bohr magneton and S is the spin quantum number (7/2 for Gd(III)). Equation

1.8 shows that relaxation is therefore dependent on 4 contributing factors; the

Gd-H distance (r_{GdH}), the proton Larmor frequency, ω_H (in rad/s), the electron

Larmor frequency, ω_S (ω_S = 658 ω_H), and the correlation times τ_{c1} and τ_{c2}. With

correlation times being composed of 3 contributing factors shown in equation

1.9.

$$\frac{1}{\tau_{ci}} = \frac{1}{\tau_m} + \frac{1}{\tau_R} + \frac{1}{T_{1e}} \text{ i: } 1,2$$ (1.9)

where τ_{ci} is the correlation time, τ_m is the water residency time, τ_R is the

rotational correlation time and T_{ie} is the electronic relaxation time of the

metal.[87] Overall, correlation time will be dominated by the shortest of the three

within equation 1.9. Within clinical imaging the most common field strengths to

be used are between 0.5 and 1.5 T, at this field strength range the dominant

correlation time will always be τ_R.[80,86–88] Therefore, slowing the tumbling rate of

GdCAs will increase T_{1m} by increasing τ_R. A variety of approaches have been

utilised to increase τ_R with the most common to combine a GdCAs with a large

macromolecule, lengthening τ_R significantly (section 1.4.3.2). However, on the

combining of a GdCAs with a large macromolecule there is a possibility that

water residency times may be affected following the binding to a larger

molecule.[86]

Rotational correlation time at frequencies used within clinical MRI scanners is the determining factor that governs relaxivity. Therefore, it is imperative to optimize τ_R to achieve the greatest enhancement to relaxivity possible.[88] The majority of clinical MRI scans are undertaken at a magnetic field strength of 1.5 T (64 MHz proton frequency). At this field strength, a decrease in the tumbling rate of GdCAs would result in a large enhancement. However, when moving to frequencies within the range of 100-400 MHz (2.35-9.4 T field strength) if the rotation of the GdCAs is decreased to the point where $\omega_s^2 \tau_c^2 > 1$ then longitudinal relaxivity will decrease with increase τ_R. With this in mind, the decreasing of τ_R for the enhancement of relaxivity should only be used when MRI scans are to be complete at low field (1.5 T). Whereas, at high, τ_R values should remain within an intermediate value.

1.4.3 Enhancement of relaxation rate (r_1)

In recent years, a drive to improve longitudinal relaxivity of GdCAs has centred around two of the three parameters discussed above. First, the manipulation of water exchange lifetime to optimise the water exchange dynamics. Second, the decreasing tumbling rate of GdCAs to enhance relaxivity through increased rotational correlation time. With this in mind, recent efforts have resulted in the design of GdCAs with both short τ_m as well as a long τ_R, thus allowing for greater longitudinal relaxation rates to be achieved. The methods used to achieve higher r_1 values *via* the manipulation of both τ_m and τ_R are discussed in further detail in sections 1.4.3.1/2 and have been reviewed

extensively with the findings published in a review by Siriwardena-Mahanama and Allen.[89]

1.4.3.1 Enhancement through manipulation of water exchange rate (τ_m)

The manipulation of τ_m observed at a gadolinium metal centre within a GdCA can be used as an important tool for the optimisation of longitudinal relaxation rates. As previously discussed, at the currently used magnetic fields within clinical imaging (60 MHz/1.5 T), short τ_m values (10-30 ns) are desirable when using large molecular weight GdCAs, with this value shortening (1-10 ns) when larger magnetic fields are used. There are many factors which contribute to the overall τ_m value achieved by GdCAs, these include; complex charge, solvent accessibility, steric hindrance of the water binding site (with the site being the gadolinium metal centre) and also the water exchange mechanism being used.[86] The exploitation of charge was used by Sherry and co-workers to demonstrate the effect which it has on τ_m values. The group showed that by increasing the number of anionic groups within a complex, the τ_m values obtained would significantly shorten. Neutral amide ligating donors were used alongside anionic acetate donors. This resulted in a τ_m change from 0.24 µs when 4 acetate ligands were present to 26 µs when 0 were present.[90] Alternative approaches to optimize τ_m *via* the increase of steric bulk around the gadolinium metal centre, such as that reported by Merbach and team who showed an increase in $-CH_2$ units within the macrocycle leads to an increase seen in water exchange rate.[91] Within the work undertaken by Merbach, one or two of the ethylene bridges within the backbone of DOTA[4-] and DTPA[5-] were

replaced a propylene bridge. Alternatively, within the same work acetate arms were replaced with propionate coordinate groups, in both cases however, thermodynamic stability was seen to drop with their stability being comparable to GdCAs used within clinical imaging.[91]

A further point of consideration when designing a GdCAs with ligands derived from DOTA (such as those within this body of work), is that τ_m is dictated by the ratio of square anti-prismatic (SAP) to twisted square anti-prismatic (TSAP) isomers within solution. It is known that [Ln(dota)]⁻ complexes in solution are able to form four different stereoisomers, comprised of two pairs of distereoisomers (SAP/TSAP). This arises from the orientation of a five-membered coordination metallacycles formed with ethylene bridges in the macrocycle ($\lambda\,\lambda\,\lambda\,\lambda$ or $\delta\,\delta\,\delta\,\delta$) and pendent arms on the macrocycle (Λ or Δ).[89,92] With λ and δ relating to ring inversion and Λ and Δ relating to arm rotation, this is shown in figure 1.13.
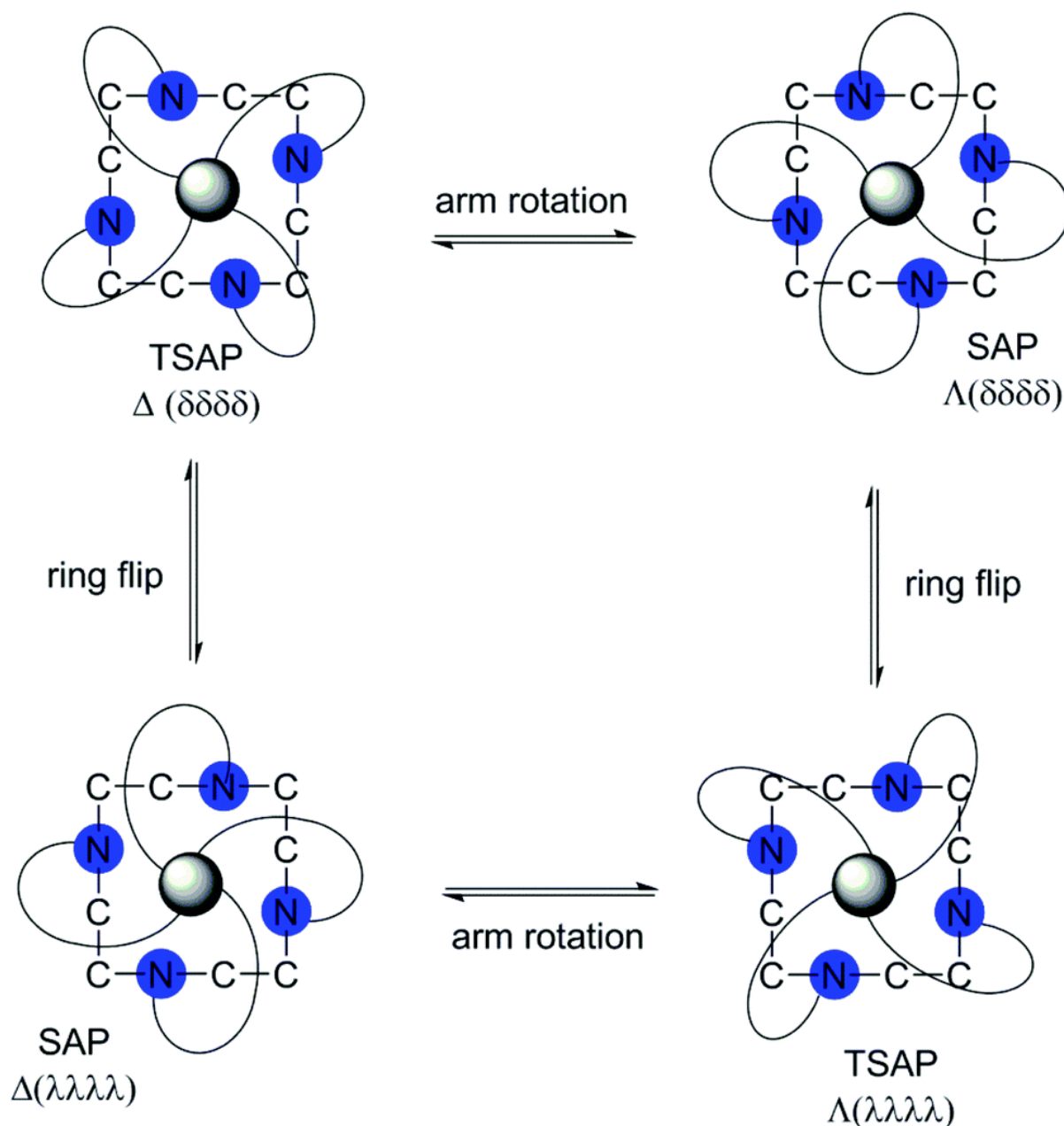
Figure 1.13. Showing [Ln(dota)]⁻ stereoisomers in solution.[93]

SAP and TSAP isomers can be characterised *via* their twist angles which are observed between nitrogen and oxygen donor atom planes, θ.[94] Typically, the angle observed for Gd(III) structure is 40° for SAP structures and between −20° and −30° for TSAP geometries.[80,94] Due to the added steric hindrance at the water coordination site observed within the SAP isomer, the TSAP form can have up to 200 times faster water exchange rate. As there are differences in τ_m

between SAP and TSAP isomers, the tuning of SAP/TSAP ratio *via* coordination

chemistry-based strategies allows for sterically bulky groups to be added to

macrocyclic compounds resulting in a favouring of TSAP isomer. The Parker lab

were able to show this manipulation of the TSAP/SAP ratio for decrease of τ_m

via adding steric bulk. Within the work presented by the group, propionate

groups were added at the α-positions of the pendent arms allowing for three

analogue complexes to be formed. In the series, the water exchange rates

increase with increasing TSAP/SAP ratio.[95] The work reports water exchange

rates of up to 10.3 times higher following the addition of propionate at the α-

positions of the pendent arms. This as explained, due to the bulky group

blocking both ring inversion as well as arm rotation thus increasing TSAP/SAP

ratio. However, it is important to note that relative abundance of the two

isomers also depends on other factors including ionic radius, solvent, ionic

strength of the solution, and salt composition.[89]

1.4.3.2 Enhancement through manipulation of rotational correlation time (tumbling rate)

As discussed in section 1.4.2.3, at commonly used clinical MR imaging

frequencies high longitudinal relativities are able to be achieved *via* the slowing

of τ_R to match nuclear and electron spin coupling. Therefore, the coupling of

Gd(III) chelating agents through both covalent and non-covalent methodologies

presented within the literature result in GdCAs with longer τ_R and ultimately

increased longitudinal relaxivity.

The covalent addition of either a natural or synthetic polymer to increase the size of a DOTA based ligand with these systems shows good potential to increase relaxivity with increased size. Ye *et al.* synthesised a large molecular weight GdCAs by introducing a large polysulfide on one of the acetate arms. The increase in steric bulk following the addition of the long chain polymer saw an increase in both transverse and longitudinal relaxation with values of 7.20 mM^{-1}s^{-1} and 9.70 mM^{-1}s^{-1} respectively. This is a 2-fold increase in r_1 when compared to the r_1 of Gd(DOTA) – 4.1 mM^{-1}s^{-1}.[96] The same group also reported the formation of two further DOTA based ligand systems which incorporated polymers ((N6-lysyl) lysine DOTA monoamine and 3-(2-carboxyethyldisulfanyl) propanoic acid copolymers (GODC)). The molecular weight of GODC was able to be determined at 26.4 KDa and had a recorded r_1 value of 8.251 mM^{-1}s^{-1}, again 2-fold greater than that of Gd(DO3A) at the same temperature and field strength.[97] Casali and co-workers also used this method to increase τ_R *via* the formation of a Gd(III) containing DO3A-monoamide coupled to a modified dextran polymer. [98] The increase in size of ligand was able to be seen to be dramatic as the average size of ligand was recorded at 52.1 KDa, this therefore having an effect on r_1 which was recorded at 10.59 mM^{-1}s^{-1} (at pH 7.4, 37 °C, 20 MHz).[98]

An alternative method for the increase of τ_R was shown by Aime and co-workers, their method utilized the entrapment of GdCAs within protein (apoferritin). Aime and team initially dissociated the apoferritin protein at a pH of 2, before allowing the subunits to assemble around a GdCA (GdHPDO$_3$A) at a pH of 7.[99] Aime was able to show that after extensive dialysis, the GdHPDO$_3$A

had been encapsulated within the apoferritin, with at least 10 GdHPDO$_3$A molecules being held. A large increase in relaxivity measurement of up to 20x following encapsulation when compared to that of free GdHPDO$_3$A in water, with a value of 80 mM^{-1}s^{-1} for GdHPDO$_3$A in apoferritin when compared to 4.2 mM^{-1}s^{-1} when free in water.[99]

1.4.4 Second generation MRI contrast agents

MRI in general, has the capability to produce high detail images (when looking at a large-scale image such as a whole-body scan) with good resolution, however, issues still remain within the technique regarding its sensitivity. The lack of sensitivity within MRI often hinders the detection of processes occurring on the cellular and molecular level. At present, first generation contrast agents (section 1.4.1) are used at a dosage of 0.1 mmol kg^{-1} in order to overcome the sensitivity issues. However, other methods of overcoming the inherent insensitivity associated within MRI are of current research interest to develop second generation contrast agents. The methods currently being used include - but are not limited to - targeted, responsive, metal and multimeric and multimodal contrast agent.[7, 76, 86–91]

Banerjee *et al.* were able to show an example of a prostate-specific membrane antigen (PSMA) targeted DOTA based GdCA.[107] Within the work outline by Banerjee, PSMA was able to be conjugated to mono, di and trimeric systems. All of which had nM affinities for PSMA, following this the team was also able to show a specific uptake in tumours bearing PSMA compared to

tumours which are non-PSMA expressing *in vivo.*[107] Meade *et al.* also used a

targeted approach by conjugating Gd(III)-DO3A with progesterone in order to

target the progesterone receptor status in hormone-dependent disease (figure

1.14).[108]
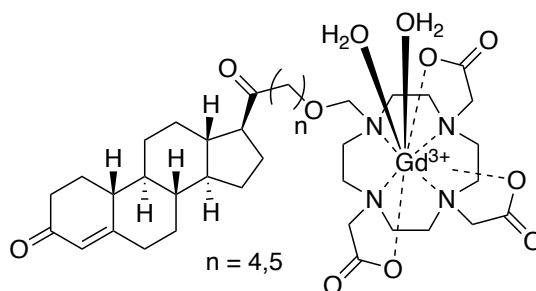
Figure 1.14. Image showing progesterone targeted GdCAs developed by Meade
and co-workers.[108]

Within the study Meade was able to show that the increase linker length

increases both toxicity and lipophilicity, whilst also increasing binding to

progesterone receptor. The *in vivo* studies carried out within the work showed

a large uptake within tumour expressing the progesterone receptor with r_1

values ranging between the values of 5.2 to 6.9 mM^{-1}s^{-1}.[108] An underlying issue

with targeted MRI contrast agents is the low signal to noise ratio which is often

associated with this style of second generation contrast agent, due to ratio of

Gd(III) chelate to receptor.

A favoured approach for increase in signal to noise ratio is the use of

multimeric contrast agents. Multimeric contrast agents increase sensitivity by

increasing the payload of GdCAs within the molecule, creating a large molecular

weight contrast agent. Their construction is able to be complete via three distinct methods; covalently *via* organic molecules, inorganic complexes and self-assembly systems. All of which are able to lead to an increase in r_1 due to the increase seen in t_R due to the increase in size of GdCAs. Tóth and coworkers were able to show that the use of an inorganic complex can increase r_1 values when incorporated with a Gd(III) ion forming a GdCAs. The team designed a metallostar structure which used iron bipyridine (Fe(bpy)$_3$) ligands bearing pendant Gd(III)DTTA chelates. This was found to have an r_1 value of 20.2 mM^{1}s^1 (60 MHz, 25°C).[109] Furthermore, it was found that on changing the central metal ion, no change was seen for the recorded r_1 value.

Despite the promise showed by the metallostar system, as for the primary contrast agents it also has limits to its potential, due mainly in part to it being bound by the amount coordinate bonds the central metal iron can hold. This being a restricting factor in the number of Gd(III) chelates which can be added. Due to this, the surface functionalisation and modification of metallic nanoparticles (MNPs) has had increased research interest, as it offers the possibility of a surface payload of GdCAs in the hundreds. Within the current research, the MNPs used have been of a non-toxic nature such as gold (AuNP) and InP/ZnS core/shell quantum dots and well as iron oxide (SPIONS) nanoparticles. Meade *et al.* were able to demonstrate the use of surface functionalised AuNP for the *in vivo* imaging of the pancreas.[110] Citrate stabilised AuNPs of approximately 17nm were surface loaded with a thiolic derivative of either Gd(III) DO3A/DTPA to form lip-DO3a@AuNP or lip-DTPA@AuNP, with a maximum loading of 2375 ± 81 chelates (lip-DO3A@AuNP). The r_1 value were

reported at 7T at 4.0 and 4.7 mM^{-1}s^{-1} respectively, resulting in an overall r_1 per AuNP of up to 9500 mM^{-1}s^{-1} (lip-DO3A@AuNP). The surface functionalisation of AuNPs has also been completed in the Wilton-Ely group in which dithiolcarbamates (DTC), have been added to the N10 position on the DO3A macrocycle. The DTC functional group is then used in a surface functionalisation reaction with AuNP (ca.18 nm in diameter).[111] The work shows that the DTC group used in the functionalisation of the surface of AuNP pull electrons towards it, the N10 donating pair of electrons do not coordinate the Gd(III) metal centre. Therefore, producing a Au@DTC-DO3A-Gd system with a q=3. Au@DTC-DO3A-Gd produces an obtained r_1 value of 1500 mM^{-1}s^{-1} (400 MHz), a value of 4.7 mM^{-1}s^{-1} per chelate. A low r_1 value for a q=3 complex. In an attempt to improve both q and possibly stability issues, Wilton-Ely and co-workers have developed this previous work, producing a Gd(III) AuNP system with a q=1. This improvement was based on one-pot synthesis of an 8-coordinate Gd(III) DOTA chelator which still featured a DTC at the N10 position, whilst also being able to add targeting (FA-SH), biocompatibility (PEG-SH), uptake (thioglucose) and optical imaging (BODIPY-SH) properties to the surface.[112] The mono aqua complex in the unbound form was shown to have a r_1 value of 4.0 mM^{-1}s^{-1}, however, on bonding to AuNP this rose to 34.3 mM^{-1}s^{-1} (10 MHz, 37 °C). This give a r_1 per object of 4203 mM^{-1} s^{-1} (at 10 MHz, 37 °C) when only the Gd(III) was tethered to the surface through the DTC linker.[112]

1.5 Optical Imaging

1.5.1 Introduction

The ability to visualize the inner workings of biological systems is crucial in order to gain an understanding of basic mechanistic processes within the body, optical imaging (OI) methodologies (in particular fluorescence imaging (FI)) allow for this to be complete at relatively low risk to patients. While some clinically used imaging modalities use ionising radiation generating potential negative side effects, OI utilizes the use of a non-ionizing source ranging from ultraviolet to infrared light.[113] The lower risk commonly associated with OI, therefore allows for the patients disease progression/regression to be monitored over a long time frame.[114] The OI methods used can commonly be seen to centre around FI with its prevalence seen to increase over recent years with FI discussed in further detail in section 1.5.2.

1.5.2 Fluorescence and Fluorescence Imaging (FI)

Fluorescence is a form of luminescence in which light is emitted from a source following its excitation, with the emission wavelength (λ_{em}) in general, being longer than that of the excitation wavelength (λ_{ex}). The process involves the excitation of electrons within the ground energy state (S_0) into an excited electronic state (S_n were n>0) *via* photon absorption at a specific λ_{ex}. Following excitation of electrons into an excited vibrational state, relaxation of electrons with high vibrational energy will occur to the lowest available vibrational level of the electronic excited state S_1. On returning to S_0 from S_1, the excited electron

within the electronic excited state will emit light at a specific λ_{em} *whilst relaxing*

back to the ground state. This process of fluorescence emission can be seen in

figure 1.15 along with other relaxation pathways available for electrons in the

S_n vibrational energy level.
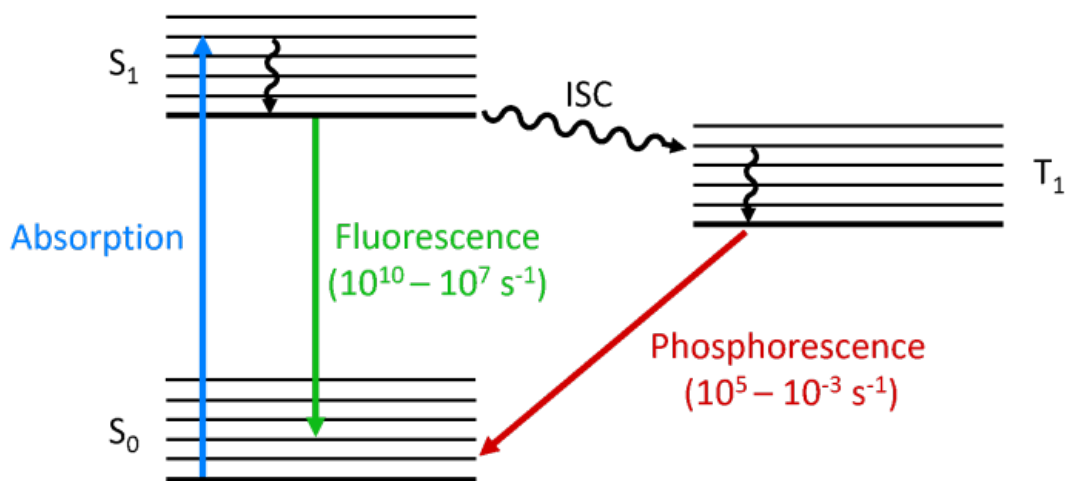
Figure 1.15. Fluorescence and phosphorescence processes shown with typical rate constants depicted. Excitation of electron *via* photon absorption (blue line) from ground single state (S_0) to excited vibrational singlet state (S_1). Short lived fluorescent decay (green line) *via* relaxation from S_1 to S_0. Inter-system crossing (ISC) from (S_1) to excited triplet state (T_1) is seen before relaxation to ground state (S_0) via long lived phosphorescence decay (red line).

On return to S_0 from S_n, photon emission at specific λ_{em} is observed *via*

visualisation of either short (fluorescence) or long lived (phosphorescence)

non-radiative decay. These two pathways are shown in figure 1.15, with the

long-lived phosphorescence decay attributed to the time taken for decay from

an excited T_n state to a S_0 state following intersystem crossing of a S_n to T_n. As

appose to singlet-singlet decay in the case of fluorescence.

The ability to visualise the decay process associated with fluorescence therefore allows for the utilisation of fluorescence probes such as; quantum dots (section 1.5.3), fluorescent dyes, fluorescent proteins and metallic nanoparticle (doped with lanthanides) to be used within the clinical setting, with recent literature suggesting a use for fluorescence within image guided surgery being a future possibility. [61,102-107] However, fluorescent emission in the visible region (450 – 600 nm) can have limited scope for use within *in vivo* applications due to the attenuation and scattering of light, due to the auto fluorescence emitted from endogenous substances such as water and haemoglobin.[121] The limitations associated with FI, when used as a singular imaging modality, have resulted in a surge of research activity (including this body of work) into the development of a multi-modal imaging probe which incorporates a fluorescent reporting group such as those mentioned above. These methods of combining two or more modalities have been reviewed in detail by Zhao *et al.* and are discussed in further detail in section 3.1.[121]

1.5.3 Quantum Dots

1.5.3.1 Overview

Colloidal semiconductor nanocrystals (NCs), known as quantum dots (QDs) have been brought to the forefront of modern research focus following the seminal work of Efros, Ekimov, Brus, Henglein.[122-125] In which the dependence of their optical and electronic properties was shown to be dependent on their core size. This phenomena as well as other mesoscopic properties of QDs including their stability, broad excitation spectra and narrow

emission spectra all arising as they are subject to the quantum confinement effect.[123,126–128] QDs are NCs made of semiconducting material with diameters that range in the small nanometre range, in which quantum confinement effects lead to a widening band gap within the nanoparticle (NP). Due to this, a state of free charge carries within the dot leading to discrete energy levels. With these levels being linked to the overall size of the QDs.[129–131] Therefore, λ_{em} and subsequent colour can be dictated by size of synthesised QDs following an informed choice of core material. This is shown in figure 1.16.
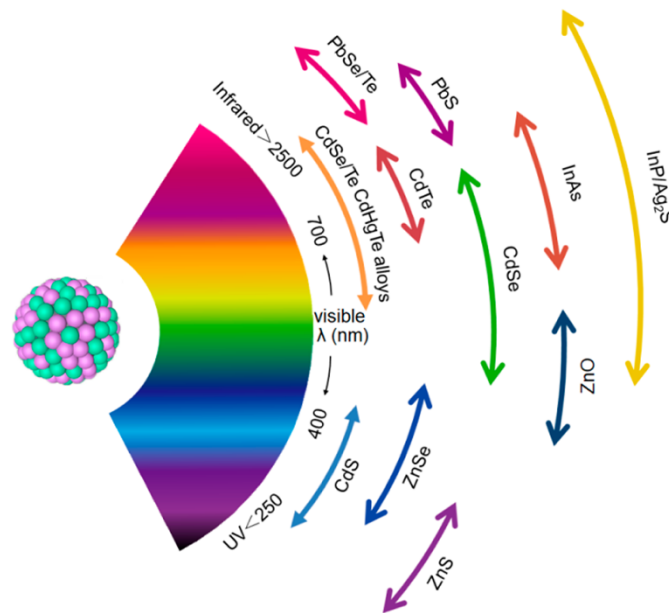
Figure 1.16. Image showing how changing semiconductor material during the synthesis of QD cores leads to changes within their emission properties (specifically λ_{em})

As shown by Tamang *et al.* core only QDs will suffer from low photoluminescent quantum yields (PLQY) in some cases can as low as 1% due to problems associated with photodegredation.[132] With many if not all of the potential applications for QDs relying on the PLQY, the overcoating or shelling

of core only QDs with a secondary semiconductor material with a larger

bandgap now common practice. Thus, creating core/shell (CS) QDs.

   As stated above, CS QDs are synthesised by the overcoating of core only

QDs with a secondary semiconductor nanomaterials with a large bandgap of

that of the core material. These nanomaterials are often comprised of atoms

from groups II-IV, III-V or II-VI within the periodic table, have a large offset

within their relative valence and conduction bands, have a shell material with a

significantly larger band gap than that of the core material (in the case of

InP/ZnS the band gap is 1.35 eV) and are defined as particles with a size which

is smaller than that of the Bohr radius(for InP/ZnS it is to be below 10

nm).[132,133] As QDs have the ability to be charge carriers (due to their ability to

have both electrons and holes thus creating charge), they are often referred to

as artificial atoms due to their ability to occupy discreet energy levels. This is a

direct effect of the quantum confinement effect mentioned above. On excitation

of an electron from the ground state in the valence band to the conductance

band a hole with a net positive charge will be created, within CS QDs this can be

done in two distinct paths dependent on the type of QD. These paths are

outlined in figure 1.17 below.
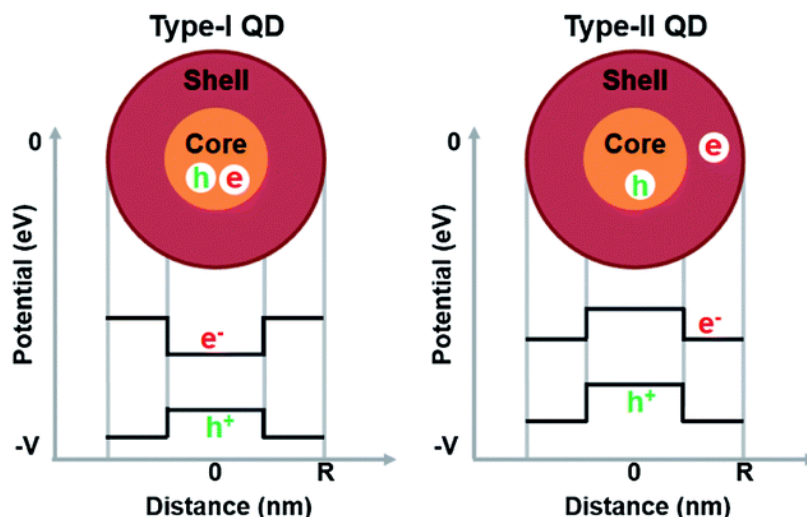
Figure 1.17. Image showing both a type-I Core/shell QD (left) and a type-II QD (right). In a type-I QD both the hole and electron are kept within the core, whereas in type-II the electron is promoted into the shell crossing the core/shell interface.[134]

CS QDs will exhibit a structure which is dependent largely on that of the secondary shelling material, as show in in figure 1.17 if the band gap of the shell material is larger than that of the core, the hole-electron pair will be confined in the core yielding a type-I CS QD. With InP/ZnS CS QDs being a good example of a commonly synthesized type-I CS QD due to its ability to produce large PLQY when synthesised in this way.[127,135,136] In contrast to type-I, type-II CS QDs have a shell material with a smaller band gap than that of the core, leading to hole/electron confinement in the core and shell respectively. Due to the difference in confinement material, emission wavelength exhibits a bathochromic shift offering much higher emission profiles that that of type-I QDs.[137] Examples of type-II CS QDs have been around in the literature for many years with many of them having a heavy metal core such as Se, Cd or Te making

them highly toxic.[138–140] Recently however, type-II InP core QDs have been

synthesised.[141]

1.5.3.2 Stability and cytotoxicity of Quantum dot systems in biomedical applications

When compared to tradition organic fluorophores such as Rhodamine,

fluorescein and tetramethylrhodaminisothocyanate (TRITC), QDs can be seen to

offer a range of benefits for use within a biological system; two of these benefits

include the increased stability offered (resistance to photobleaching), as well as

increased PLQY and optical properties associated with QDs.[142,143] Traditional

fluorophores will lose photostability resulting in a diminished overall PLQY for

use within bioimaging following repeated excitation events. However, in

contrast due to the much larger stability of the QDs they will undergo multiple

excitation events whilst retaining both photostability and also their high level of

QY.[142,143] Jaiswal *et al.* first showed that QDs have the ability to resist photo

bleaching as well as presenting work showing the ability of CS QDs to resist

both metabolic and chemical degradation. Both key in biomedical imaging

applications. Following increased stability, CS QDs were able to be used as a

method of *in vivo* imaging both in short and long-time frames. This was shown

by Yamamoto *et al.* when CdSe/ZnS CS were used for long life fluorescent

imaging of T-lymphoma blood cells within a mouse over a period of 24 h.[144] A

study by Ballou *et al.* again in 2004 showed again the used of CdSe/ZnS CS QDs

for a long-term imaging study within mice. The team were able to show that the

QDs remained fluorescently active *in vivo* for a time period of up to at least 4

months.[145] Due to the known cytotoxic materials used within QDs such as the

heavy metals of Cd, Se and Te, it is integral to design a QD nanoparticle which will not allow the cytotoxic material to leak/leach into the surrounding area within the body. The leaching effect can occur due to many internal and external factors including, Illumination, oxidation and the coating of the core/shell NP with cytotoxic ligands.[146]

Cytotoxic effects which are related to differing QD systems can often be eliminated by their preparation, particularly by the preparation of a known passivating surface layer or shell. CdSe core QDs are believed to pose cytotoxic effect within the body (differing effect within the body due to difference of cell lines, animal species), however when correctly shelled using ZnS or many layers of ZnS/SiO the property can be alleviated due to the removal of leakage from the QDs into the surrounding area. In recent years, a switch to non-cytotoxic materials has been seen with alternatives to classical core NPs being used. III-V group QDs such as InP or InGaP have been used rather than the traditional QDs due to a reduction in cytotoxicity, however this comes with the drawbacks of long production times combined with a lower PLQY when compared to the CdSe core.[147] In 2015 G. Lin *et al.* ran a cytotoxic study using single shelled InP QDs, using a shell of ZnS. They found that fluorescence from the QDs was able to be observed up to 12 weeks post injection in the liver and spleen on BALc mice,[148] alongside this Choi *et al.* showed that there was no detectable uptake in the liver or kidneys of Sprague–Dawley (SD) male rats and CD-1 male mice post injection. Choi has suggested that the uptake in the liver is due to the large size of QDs being used in other studies, in their study QDs with a hydrodynamic size of 5.5 nm were used. It was suggested that this was small enough to be renal

execration as the size was small enough to be within the kidney filtration limit.[149] This was backed up by work completed by Su *et al.,* who state that the bio-distribution of QDs is size dependent with uptake of large QDs being seen in the spleen and not in the kidney. [150] However, the study is able to demonstrate the QDs lack of toxicity following examination of tissue (figure 1.18) from the heart (He), liver (Li), spleen (Sp), lungs (Lu) and kidneys (Ki).
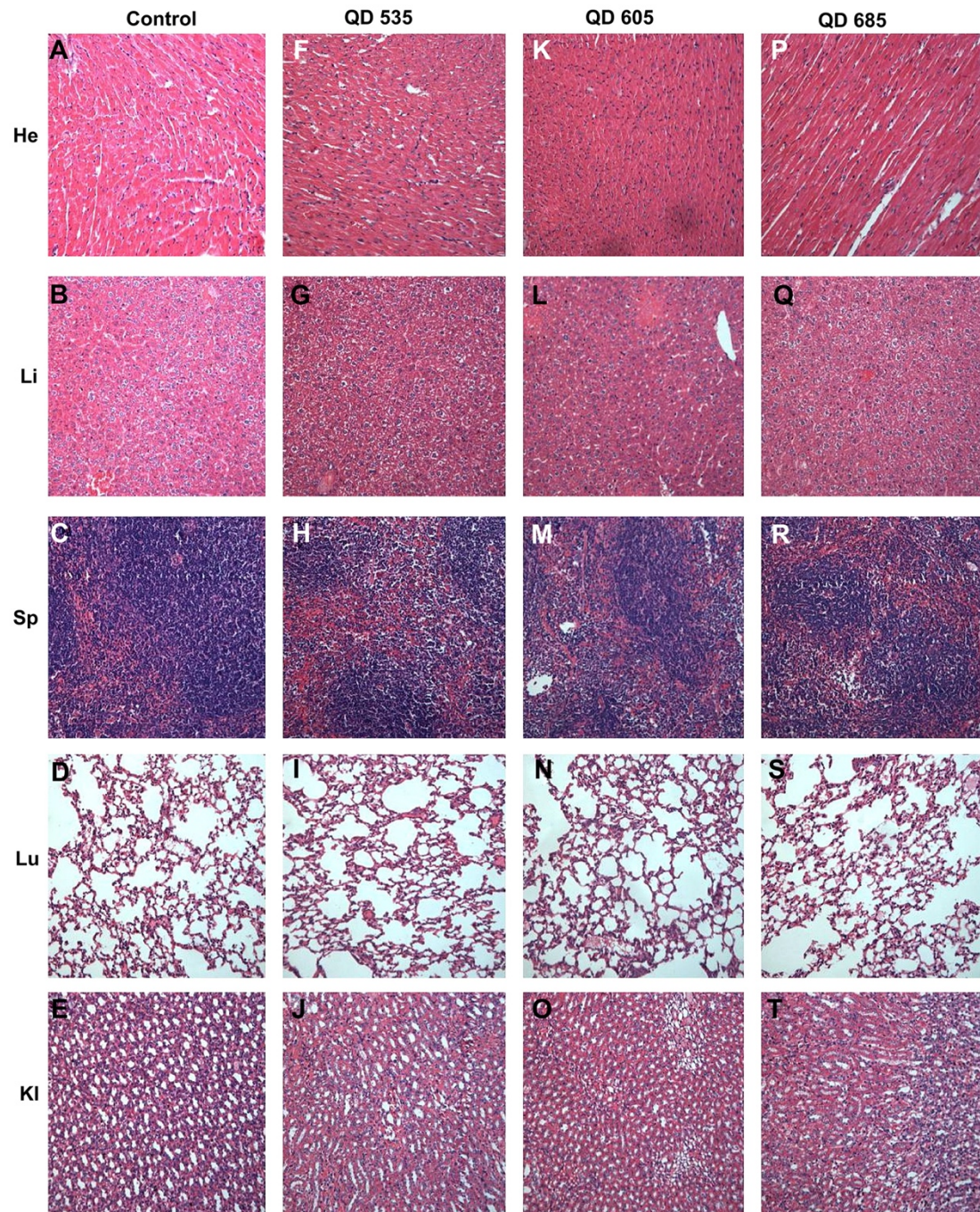
Figure 1.18. Representative organ histology for control and treated animals. For control (A–E) and injected with aqQD535 (F–J), aqQD605 (K–O) and aqQD685 (P–T) animals, heart (He), liver (Li), spleen (Sp), lung (Lu) and kidney (Ki) are shown.[150]

There are also many other factors which can affect the bio-distribution and ultimately the cytotoxic effects which QDs will have when inside of the body. This can be a factor for QDs which have been produced with large charge on the surface and can effect blood serum components due to the large opposing charge observed.[148]

1.6 Lanthanides

1.6.1 Properties of lanthanides

The lanthanides are a series of electropositive, metals found to lie between the s- and d- blocks. The series is made up of elements ranging from Ce – Lu; All elements within the series comprise a Xenon core electron configuration (La [Xe] $6s^2$ $5d^1$) followed by the periodic filling of the $4f$-orbitals. As more protons as added to the nucleus, the $4f$ orbitals contract more rapidly and increase in stability when compared to the $5s$, due to better penetration of the Xenon core. This added stability results in the $4f$ orbitals filling preferentially across the series and electron configurations for all lanthanide elements are shown below in table 1.2.

| Physical properties | | |
Ln(III)	Valence Shell	Effective Ionic Radii (pm) M(III)
La(III)	[Xe] $4f^0$	116
Ce(III)	[Xe] $4f^1$	114.3
Pr(III)	[Xe] $4f^2$	112.6
Nd(III)	[Xe] $4f^3$	110.9
Pm(III)	[Xe] $4f^4$	109.3
Sm(III)	[Xe] $4f^5$	107.3
Eu(III)	[Xe] $4f^6$	106.6
Gd(III)	[Xe] $4f^7$	105.3
Tb(III)	[Xe] $4f^8$	104
Dy(III)	[Xe] $4f^9$	102.7
Ho(III)	[Xe] $4f^{10}$	101.5
Er(III)	[Xe] $4f^{11}$	100.4
Tm(III)	[Xe] $4f^{12}$	99.4
Yb(III)	[Xe] $4f^{13}$	98.5
Lu(III)	[Xe] $4f^{14}$	97.7

Table 1.2. Table showing physical properties of lanthanide M(III) ions. Valence shell electron configuration shown as well as effective ionic radius shown (pm) for CN 8 complexes.

Unlike the *d*-block elements, the lanthanides can be seen to traverse across the series with decreases in both atomic and ionic radii within the Ln(III) ions, known as lanthanide contraction. This creates a remarkable uniformity across the series. The uniform nature can be shown in ionic state with the most common being Ln(III) within aqueous solution, however, instances of both Ln(II) and Ln(IV) oxidation states have been reported.[151] The trivalent nature is a direct result of the periodic loss of the $5d^1\ 6s^2$ electrons within the [Xe] $4f^n\ 5d^1\ 6s^2$. The uniform Ln(III) state *via* the removal of $5d^1\ 6s^2$ is able to be

demonstrated by the similarity in combined ionisation energies as you move across the group. The ionic radii of Ln(III) exhibits a smooth decrease across the series (with exception of Eu and Yb). This is attributed to the poor screening ability of the *f*-orbital electrons, therefore on moving across the series an increased nuclear charge (Z_{eff}) is observed. As there is no compensation by increased shielding from *f*-orbitals the ionic radii decrease on moving across the series.

1.6.2 Coordination chemistry of lanthanide ions

Forty years ago, very little was understood with regard to the coordination chemistry of lanthanide complexes when compared to the *d*-block metals. Since then however, greater understanding has shown that lanthanides exhibit a variety of coordination numbers (CN) and geometries when compared to *d*-block metals. Reasons for their apparent CN have also been brought to light. In general, Ln(III) ions prefer to bind to hard donors such as O and F as appose to soft donors (P and S), with nitrogen donors being a slight anomaly with apparent high basicity of ligands leading to the increased formation of hydroxide complexes.

Ionic radii across the lanthanide of Ln(III) ions range from $1.032\,\text{Å}$ to $0.861\,\text{Å}$ (La(III) and Lu(III) respectively with 6-coordinate radii values given). When these ionic radii are compared with the largest M(III) ion of the transition metal Ti(III) recorded at $0.670\,\text{Å}$ (6-coordinate radii), it is clear to see based

purely on steric grounds why the Ln(III) ions would be able to accommodate a CN greater than 6. Furthermore, the $4f$-orbitals within the lanthanide series are shielded by the 5s and 5p electrons there is little in the way of covalent bonding available, resulting in CN being solely dependent on how many ligands can be packed around a Ln(III) ion, with CN observed from 2 to 12 within lanthanide complexes. Most commonly the Ln(III) ions adopt a CN of 8 or 9 with the determination being dependent on ionic radii. This is able to be shown with Ln(III) ions in aqueous solution.

In aqueous solution, the CN of $[Ln(H_2O)_n]^{3+}$ is 9 for early lanthanides (La-Eu) due to lack of steric restriction observed within early series lanthanide M(III) ions having larger ionic radii. While the later series Ln(III) ions (Dy-Lu) have a CN of 8. Nine-coordinate species are assigned tricapped prismatic structure with CN 8 having a square anti-prismatic coordination.

1.6.3 Lanthanide luminescence

1.6.3.1 Introduction to lanthanide luminescence

Within the lanthanide series, many of the Ln(III) ions are capable of exhibiting a form of luminescence, with this luminescence process is summarised in figure 1.19.
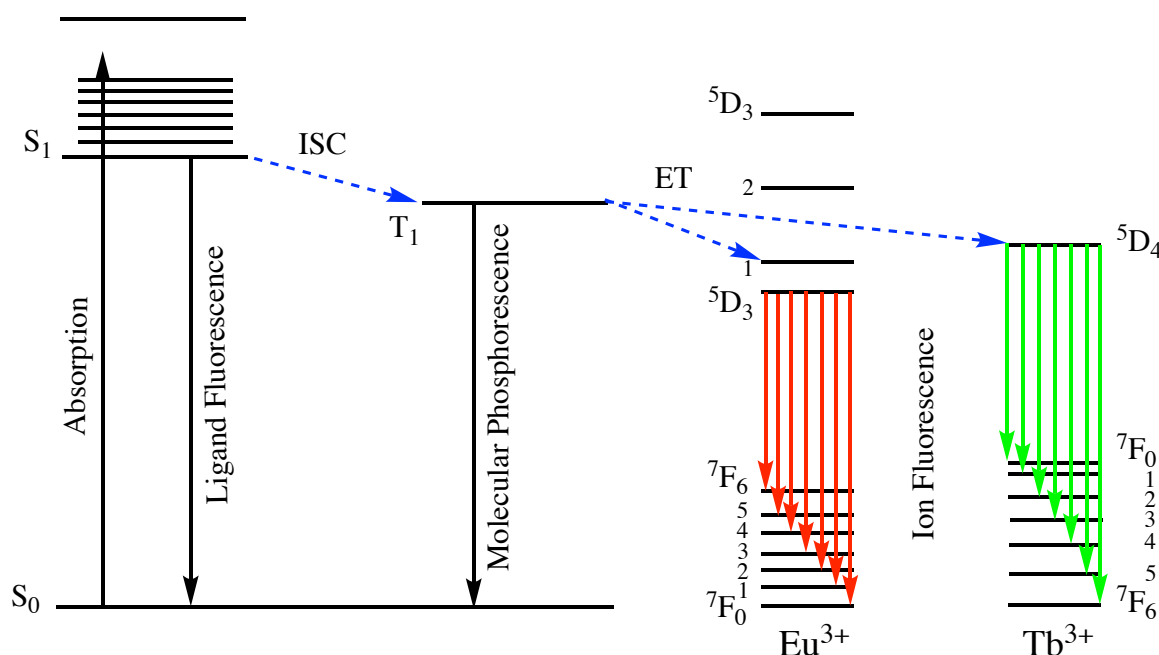
Figure 1.19. showing a summarisation of the process required for lanthanide luminescence to occur.[152] Where S_0 - ground vibrational state, S_1 – excited vibrational state, T_1 – Excited triplet state, ISC – intersystem crossing and ET is radiation less energy transfer (dashed blue line) from excited triplet state to lanthanide excide states $^5D_0$ (Eu(III)) and $^5D_4$ (Tb(III)).[152]

As with fluorescent imaging above in section 1.5.2, luminescence occurs following the promotion of an electron from S_0 to the excited S_1 state, following the absorption of a quantum of energy (ultraviolet light source). However, following the relaxation to the lowest available S_1 vibrational state, a non-

radiative decay path (intersystem crossing) to a T_1 state of the ligand is taken. Figure 1.19 shows a non-radiative energy transfer can then be undertaken by the excited electron to a nearby Ln(III) excited state. From there it can return to a ground state either by non-radiative emission or by metal-ion fluorescence (involving *f-f* transitions).

Two of the most useful Ln(III) ion for use within lanthanide luminescence studies are Tb(III) and Eu(III) which luminesce with green and red colour, respectfully. In the case of Tb(III), emission is observed primarily due to transitions between the $^5D_4$ and ^7F_n (where n = 6-0). Typically, a ΔJ=1 ($^5D_4$ and $^7F_5$) transition offering the strongest emission. However, Eu(III) emits using transitions observed from $^5D_0$ to ^7F_n (where n = 4-0). Unlike Tb(III) however, transition to $^7F_0$, $^7F_1$, and $^7F_2$ are more useful as they are able to be used for both qualitative and quantitative analysis of Eu compounds.

1.6.3.2 Solvent quenching of lanthanide luminescence

A common problem observed within lanthanide luminescence, specifically when using Eu(III) and Tb(III) is the phenomena of luminescent quenching when in aqueous solutions. When in aqueous solution a secondary pathway becomes available for competition with radiative decay transitions. Resulting in a loss of luminescence due to the deactivation of the excited lanthanide state through a non-radiative decay pathway. The use of a deactivation pathway is possible due to the vibrational energy levels of H_2O

being close enough to that of the excited state of both Eu(III) and Tb(III). This is

seen in figure 1.20 below.
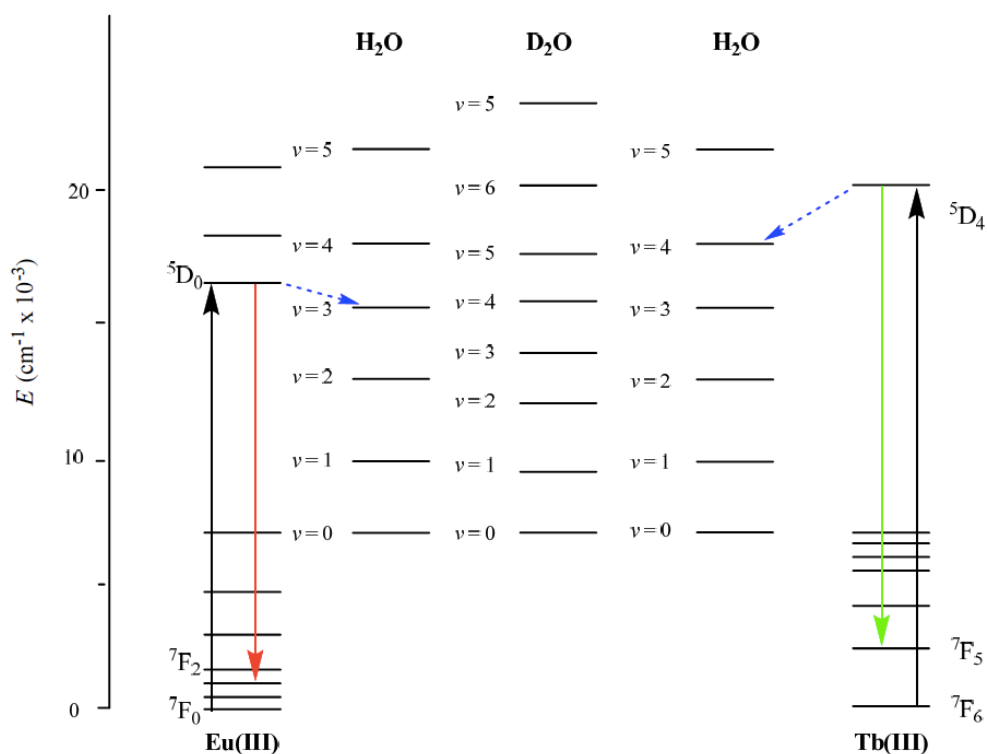
Figure 1.20. showing the vibrational quenching of Eu(III) and Tb(III) excited states. Excitation (black arrow) occurs from the ground to excited state ($^7F_0$ to $^5D_0$ for Eu(III) and $^7F_6$ to $^5D_4$ for Tb(III)) followed by emission, showing the $\Delta J = 2$ transition for Eu(III) (red arrow, $^5D_0$ to $^7F_2 \sim 615$ nm) and $\Delta J = 1$ for Tb(III) (green arrow, $^5D_4$ to $^7F_5 \sim 545$ nm). Overlap of the $v = 3$ vibrational level of H_2O with the $_5D_0$ excited state of Eu(III) is greater than with the $_5D_4$ excited state of Tb(III), thus, resulting in greater quenching effects and shorter lifetime of Eu(III) emission. Following radiation less energy transfer (blue arrow).[153]

The energy transfer between the lowest excited states in both Eu(III) and

Tb(III) ($^5D_0$ and $^5D_4$) to vibrational energy level within H_2O ($v = 3, 4$

respectively) occurs due to the efficient overlap of the two energy states. Thus,

vibrational quenching of the Eu(III) and Tb(III) excited states manifests,

resulting in a less than optimal luminescence output. In order to

alleviate/minimalize quenching of lanthanide luminescence, the Ln(III) ion is

able to be either complexed or encapsulated by a ligand system. Therefore,

removing water from the coordination sphere of the lanthanide. The distancing

of water from the metal centre results in a reduction in non-radiative decay

pathways available for excited state Ln(III) ions to relax through, resulting in

luminescence being preserved. In the presence of D_2O however, vibrational

quenching can be seen to be lower in both Eu(III) and Tb(III) complexes, due to

the reduced rate of energy transfer seen when D_2O is used as a solvent when

compared to H_2O with this shown in figure 1.20.[154] Resulting in O-H oscillators

have a better overlap with excited vibrational states than that of the O-D

oscillators as of their higher vibrational energy. As the rates of decay in H_2O and

D_2O (k_{H2O} , k_{D2O}) can be determined when measuring emission intensity vs time

(resulting in a first order decay constants) in both H_2O and D_2O. Following this,

hydration state, q, is able to be determined using equations 1.11 and 1.12

below.

$$q_{Eu} = 1.2 \left[\left(k_{H_2O} - k_{D_2O} \right) - 0.25 \right] \qquad\qquad 1.11$$

$$q_{Tb} = 5 \left[\left(k_{H_2O} - k_{D_2O} \right) - 0.06 \right] \qquad\qquad 1.12$$

1.7 Aims and Thesis Outline

The work described throughout this thesis looks at developing a targeted multimodal bio-imaging tool for the enhanced early detection of metastatic PCa, building upon work previously reported by Sturge and Stasiuk.[155,156] Within the work, synthesis of both MRI (Gd(III)) and optical imaging (QDs) agents are described before the addition of prostate specific targeting agents (Endo180 mAbs) is added. Furthermore, the optical properties of QDs as well as the luminescent properties of chemically similar lanthanide ions are reported. Chapter two focuses of the development of a novel method for the synthesis of highly fluorescent non-toxic InP/ZnS core/shell QDs. Within the chapter, a novel synthetic method is presented resulting in InP/ZnS QDs in organic solution. The chapter also looks at the phase transfer of QDs from organic to aqueous solution whilst preserving photoluminescent quantum yield. Discussions about both the synthetic methods and also issues faced are also within this body of work. Chapter three first outlines the design and synthesis of a Gd(III) chelating ligand. This work is then used as a basis to design a small catalogue of thiol derivatives of gadolinium chelates for the surface modification of previously synthesised InP/ZnS core/shell QDs. Later in the chapter, the surface functionalisation and characterisation of InP/ZnS QDs with newly synthesised Gd(III) chelates is undertaken. This chapter also uses other lanthanide complexes (specifically Eu and Tb) to determine the hydration states of all complexes formed. Chapter four details the formation of a targeted dual-modal bio-imaging probe. This is able to be complete by the introduction of a prostate specific targeting antibody to the dual modal probe formed in chapter

three. Following the formation of an OI/MR targeted imaging probe, validation

studies within a range of prostate and PCa cell lines (RWPE-1, RWPE-2, PC-3) as

well as cell lines where endo180 is both under (MCF-7) and overexpressed

(MCF7-E) are undertaken. Chapter five looks at both the conclusions which can

be drawn from the thesis, as well as any suggested future work. Chapter six

describes the experimental work carried out.

Chapter 2: Near unity quantum yield in InP based quantum dots through thermal diffusion.

2.1 Introduction

Colloidal semiconductor nanoparticles (known as quantum dots (QDs)) have seen an astronomical increase in use over the last 30 years spanning a range of applications, including but not limited to photo-voltamics, solid state labelling and biological imaging.[117,157,158] The use of group III-V QDs, such as those based around InP have gained increased interest following the seminal work established by Wells *et al.* Wells and team were the first to demonstrate a synthetic method for the synthesis of III-V QDs such as InAs and GaAs, this was complete using a dehalosilyation reaction (scheme 2.1).[159]

$$(Me_3Si)_3As + MX_3 \rightarrow MAs + 3Me_3SiX$$

$$M = Ga \text{ or } In, \ \ X = Cl \text{ or } Br$$
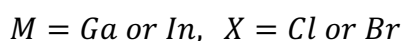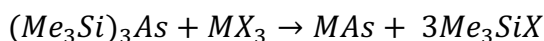
Scheme 2.1. Proposed dehalosilyation reaction mechanism P(TMS)$_3$

Since Wells however, there has been an increased drive to create QDs which exhibit non-toxic properties, as well as having the ability to be physiologically stable. These two properties combined with the photophysical properties associated with QDs can be used within the bio-medical imaging field safely and efficiently to produce a safe long-lived bio-imaging probe. With this in mind, InP based QDs have seen a large increase in research activity within recent years.[132]

InP based QDs are seen as a good alternative when looking into applications within the biomedical field when compared to more traditional II-VI QD systems. These contain heavy metals such as cadmium and have long been connected to toxicity concerns, thus resulting in the II-VI group of QDs being rendered not viable for biomedical imaging.

2.1.1 Evolution and synthesis of InP Core Quantum dots

As discussed previously, the increase in research interest within QDs is in part due to their potential ability to be used in applications such as biomedical imaging, due to their unique photoluminescent properties attributed to the onset of the effects of quantum confinement. Allowing for the photophysical properties of QDs to be adjusted with changes to a range of physical properties such as size, shape, composition and surface state.[160] The phenomena of quantum confinement therefore opens QDs research interests into both the fundamental and technical applications as their properties are dramatically affected by the overall size of the nanoparticle.[157,161–164] Over recent years, InP based QDs have become one of the most widely studied QDs belonging to the III-V semiconductor family for two reasons. First, the synthetic method is one which is reliable as well as cost effective (due to the use of cost effective precursors) and second, there are no heavy metal elements used within the synthesis of InP based QDs allowing for their use within a wide range of applications (such as biomedical imaging).

The synthesis of InP based QDs is one that has slowly evolved with time, building on the discovery of the dehalosilyation reaction by Wells (scheme 2.1). A review showing the majority of breakthroughs within the field was published by Tamang *et al.*[132] Following the pioneering work by Wells, a team of Healy, Wells and their co-workers built upon the early dehalosilyation reaction to show InP NCs were able to be formed *via* the use of adduct complexes, before the elimination of Me₃SiCl (scheme 2.2).[165,166]

$$InCl_3 + P(SiMe_3)_3 \rightleftharpoons Cl_3InP(SiMe_3)_3 \rightleftharpoons$$

$$\downarrow \; - Me_3SiCl$$

$$InP \xleftarrow{- 2 \, Me_3SiCl} Cl_2InP(SiMe_3)_3$$
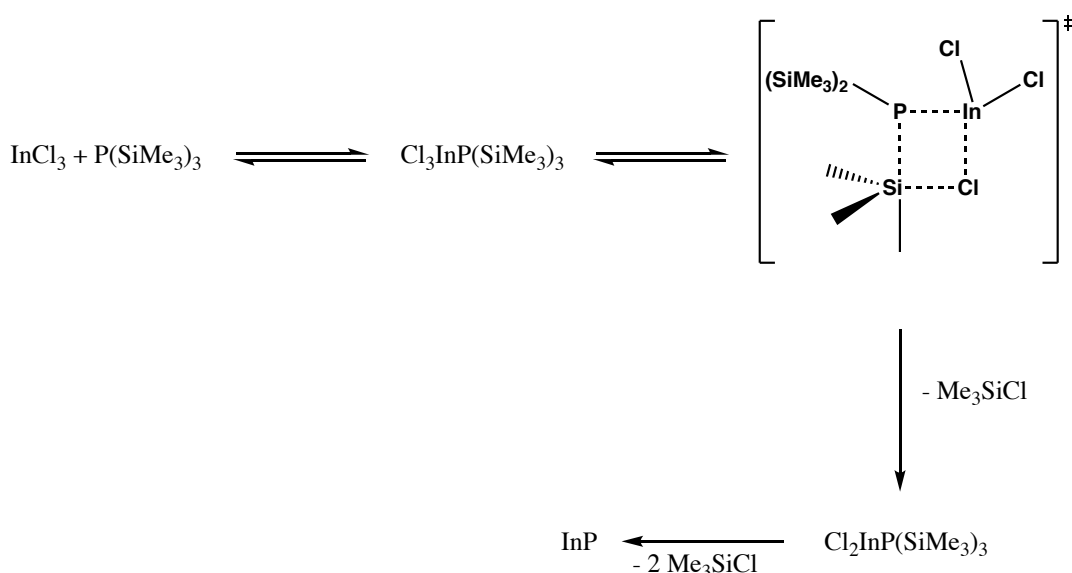
Scheme 2.2. Proposed dehalosilyation reaction mechanism P(TMS)₃.[165]

The method outlined in scheme 2.2 required the final equivalent of Me₃SiCl to be removed at very high temperature (650°C) whilst under vacuum for 1 hour, which can prove to be problematic with such high temperatures being used. This use of high temperature ultimately leads to the development of a new method which didn't require its use. Mićić *et al.* were able to improve on the original dehalosilyation reaction by reducing the reaction temperature by more than 2-fold with the use of Tris(trimethylsilyl)phosphine (P(Me₃Si)₃)

(P(TMS)$_3$) in trioctylphosphine oxide (TOPO). The reaction could be carried out at the lower temperature of 270°C for 3 days;[167] however, problems within monodispersity in size still arose when using the method outlined by Mićić, attributed to the long reaction times. Heath and co-workers looked to improve size distribution of synthesised InP NCs using a size-selection precipitation method, thus proving the InP NCs which can exhibit the size-dependent optical properties which are seen within modern day InP based QDs.[168] Although the team were able to improve on the size distribution of synthesised InP NCs, the synthetic method which had been produced was still a lengthy procedure, reliant on the slow precipitation of InP NCs.

A turning point within the synthesis of high quality InP NCs can be seen within the work of Peng *et al.,* who were able to reduce the very long reaction times commonly associated with the synthesis of InP NCs to date. The teams approach utilised 1-octadecene as a non-coordinating solvent in combination with a fatty acid stabilising ligand.[169] The team were able to synthesise both InP and InAs without the use of any size sorting methods by strictly controlling the reaction parameters. This resulted in the formation of nearly monodisperse InP and InAs NCs at a reduced reaction time compared to reaction methods previously reported. Similar chemical approaches have also been used within the synthesis of monodisperse CdS QDs as well as others within the II-VI semiconductor family, with the use of a coordinating solvent first being demonstrated within the synthesis of II-VI semiconductors.[139] Following on from the work from Peng, Bawendi and co-workers showed the increased working temperatures that the presence of a coordinating solvents offer within

the synthetic reaction. Due to the advantages that coordinating solvents offer within the synthesis of InP NCs, all InP synthetic reactions are now carried out in their presence.

The phosphorus precursor used within the synthesis of InP NCs has also undergone investigation in order to produce nanoparticles of a higher optical purity. Allen *et al.* were able to show that the most commonly used phosphorus precursor $P(TMS)_3$ used within the production of InP NCs depleted at a very high rate when reacted at the high temperatures commonly associated within InP NCs synthesis.[170] It is suggested that the depletion in $P(TMS)_3$ precursor and the resultant lack in elemental phosphorus will result in the growth of the InP NCs by Oswald ripening, this in turn leading to a more monodisperse nanoparticle of lesser optical purity. As well as problems observed within the depletion of phosphorus precursor, a move to a more non-toxic, cost-efficient synthesis method has resulted in a move away from $P(TMS)_3$ precursor being used. Many Phosphorus precursors have been evaluated including P_4, $In(tBu_2P)_3$, Na_2P, PCl_3 and PH_3 gas all with mixed success.[171–174] However, Yang and co-workers developed a synthetic method using the cheaper and easy to handle (due to stability in the presence of air) aminophosphine precursor, Tris(dimethylamino) phosphine $(P(DMA)_3)$.[175] The method used by Yang and team showed $P(DMA)_3$ in combination with $InCl_3$ (as the indium precursor), dissolved in oleylamine (coordination solvent) with $ZnCl_2$ to increase the optical purity of the synthesised NCs. This work paved the way for increases in PLQY which will be discussed in section 2.3.[115,175]

2.1.2 InP/ZnS core/shell synthesis methods

InP core only NCs synthesised in the manor above will typically exhibit a PLQY of less than 1% in organic solvent, the low PLQY can be attributed to surface oxidation and photo-degradation of the InP QDs.[132] To overcome this, Type-I InP based core/shell QDs have been produced by the overcoating of the InP core NCs with a secondary semiconductor material which has a larger bandgap than that of the core, resulting in an increased PLQY whilst also adding to both the photo and chemical stability on the overall nanoparticle.[176]

As for InP NCs, Type-I InP based core/shell QDs synthetic methods have evolved over time with a variety of techniques which include a range of semiconductor coatings to forego the degradation to the core, which can result in poor PLQY. The most widely studied shell material used in combination with an InP NCs can be seen to be zinc sulphide (ZnS), due to the combination of low toxicity, chemical stability, low cost and high band gap (3.6 eV) produced between the core and shelling semiconducting materials to form InP/ZnS.[132] The synthesis of core/shell QDs requires the epitaxial growth of the shelling material on the surface of the core, as opposed to the formation of separate NCs being formed within the reaction solvent. Haubald et $al.$ were the first to successful achieve the synthesis of core/shell InP/ZnS by depositing crystalline ZnS onto the surface of synthesised InP NCs in trioctyl phosphine (TOP).[177] The highly reactive organometallic precursors diethyl zinc (Et_2Zn) and bis(trimethylsilyl)sulfide ($S(SiMe_3)_2$) were used to deposit ZnS onto the surface of InP. However, to avoid Oswald ripening of the InP cores, heating within the

reaction had to be kept to short intervals, leading to a long reaction time.

Following a reaction time of 3 days, an increase within PLQY of 15% was

observed. However, the reaction was able to be continued and showed a

maximum increase in PLQY of 23% after a reaction time of 3 weeks.[177]

However, the maximum PLQY achieved of 23% still falls short of core/shell QDs

which have a core which contain heavy metal elements such as Cd, having PLQY

in excess of 65%. Xie *et al.* used a low temperature reaction method to improve

the PLQY in organic solvents to up to 40%, by producing high-quality InP NCs

before the addition of a ZnS shell. It was shown that the overnight addition of

ZnS precursors leads to the 0production of optically pure InP/ZnS core/shell

QDs in a reduced time frame.[178] Nann and co-workers presented a synthetic

reaction method which was able to increase the PLQY whilst simultaneously

decreased the reaction time, thus improving on previously reported methods.

[147,179] InP/ZnS were therefore able to be synthesised with PLQY of up to 60%

within a time of 20 minutes following the production of InP cores.

One common feature of all previously discussed synthetic methods for

the synthesis of InP/ZnS core/shell QDs is the use of $P(TMS)_3$ as the phosphorus

precursor within the initial InP NCs synthesis step. However, due to the

shortcomings discussed above the synthesis of InP QDs using non-toxic

precursor $P(DMA)_3$ is desirable. Tessier *et al.* were able to use $P(DMA)_3$ within

their synthetic method to produce an InP/ZnS core/shell QD with a PLQY of up

to 70%. This synthetic method also offers a degree of tunablility within the

specific emission profiles dependent on both reaction times and precursors

used within the reaction.[115] As well as tunablility, the QDs produced by Tessier

and team showed a very high optical purity with the monodispercity in the FWHM ranging between 46-64 nm, because of these qualities, a modified method is used to produce InP/ZnS core/shell QDs within this body of work.

2.1.3 Methods for phase transfer for hydrophilic InP/ZnS QDs

InP/ZnS core/Shell QDs have long been used as an optical imaging agent for both *in vitro* and *in vivo* biomedical applications.[156,180] In order for this to become a possibility QDs which have been synthesised typically in organic solvents, have to undergo a surface modification reaction (known as a phase transfer reaction) producing QDs with a hydrophilic surface. Generally, preparation of hydrophilic QDs can be achieved in 3 different ways: First, QDs can be prepared in bulk aqueous phase;[138] Second, QDs can undergo post synthetic ligand exchange, where QDs will be initially prepared in organic phase and undergo surface modification with hydrophilic ligands (with this method used within this body of work).[181] The third method involves the use of encapsulating the hydrophobic QDs in different hydrophilic carrier vehicles, thus allowing transfer of hydrophobic QDs into the aqueous phase.[182]

Ligand exchange on the surface of core/shell QDs prepared in organic phase using mono and bidentate thiolic ligands has proved very popular in creating water soluble QDs. Aldana *et al.* used QDs which had undergone a phase transfer by changing surface ligands using 3-mercapto-1-propanol (MPOH) in order to form hydrophilic QDs.[183] This reaction was shown to be pH dependent requiring a pH of 10 for MPOH to bind to the surface of the Cd based

QDs. Moloney *et al.* used the monodentate thiolic ligand penicilamine as a surface ligand to form a range of chiral QDs with potential applications in drug-delivery systems.[184] Tamang *et al.* outlined the use of a range of thiolic ligands which are able to be used for the phase transfer of InP based QDs.[181] Tamang *et al.* were able to demonstrate the use of both mono and bidentate thiolic ligands for the use within surface modification reactions, they also observed a differing amount of PLQY loss dependent on the ligand used. pH is also shown to play a vital role within the reaction as each thiolic acid used for surface modification requires a different pH conditions to form a thiol bond on the surface of the QD as appose to the thiolate by product. With control of pH improving transfer yields within the reaction.[181]

The evolution within the synthesis techniques seen over recent years within the group III-V QDs, coupled with the abundance of techniques available for the solubilisation of QDs in water have allowed for InP based QDs to be viewed as viable options as biomedical imaging agents. One drawback observed however, are the low photo luminescent quantum yields (PLQY) or quantum efficiencies which are often associated with InP based QDs when in aqueous solvents. The issues previously mentioned regarding InP based QDs are challenged within the presented body of work with the following;

- A novel synthetic method for the synthesis of ultra-bright InP/ZnS core/shell QDs
- The synthetic method used for phase transfer of novel InP/ZnS QDs

The work looks to address the low PLQY in aqueous media and tries to explain

how it is circumvented with the synthetic method used.

2.2 Synthesis and characterisation of tunable InP core only Quantum dots

2.2.1 Synthesis of InP core QDs

The synthesis method used for the production of InP core only quantum dots was based on the previously published work by Tessier *et al.*[115] The method requires the use of both a Zn(II) metal salt ($ZnCl_2$) and an In(III) halide precursor, with the reaction taking place within a primary amine (oleylamine) acting as a coordinating solvent. The interchangeable nature of In(III) halide used gives access to size tuning of the synthesised InP core with the inter-changing of In(III) halide (X = I, Cl) (discussed in more detail below). Finally, the injection of a phosphine precursor ($P(DMA)_3$) at elevated temperature results in the formation of InP core only QDs with specific emission properties. A simplified schematic of the core synthesis can be see below in scheme 2.3.

$$In(X)_3 + ZnCl_2 + oleylamine \xrightarrow[\substack{180°C \\ 30\ minutes}]{P(DMA)_3} InP\ cores$$

$$X = Cl, I$$
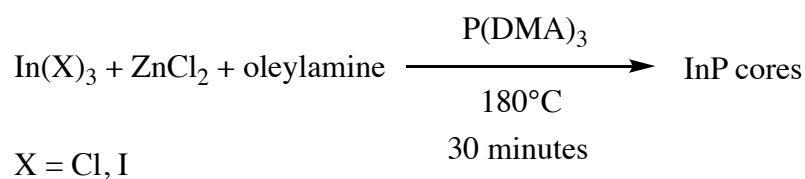
Scheme 2.3. Simplified schematic diagram of the formation of InP core only QDs in the presence of a phosphorus precursor.

As seen in scheme 2.3, InP cores are formed *via* a one-pot, hot injection method within a 30-minute time scale. One feature of this reaction is its ability to be carried out using schlenk line techniques rather than the traditionally

used glove box methods often associated with the production of high purity InP

QDs. Schlenk line techniques are able to be used within this synthetic method

due to the phosphorus precursor used P(DMA)$_3$. P(DMA)$_3$ is used as the

phosphine precursor within the synthetic method as an alternative to

traditional air sensitive phosphorus precursors such as (P(TMS)$_3$). The reaction

therefore, is able to be carried out following a degassing procedure with use of a

schlenk line providing the stringent oxygen free environment required for the

successful synthesis of InP core only QDs.

Initially, both In(III) halide and Zn(II) metal salt precursors (1:1 ratio)

are loaded into a 100 ml three-neck round bottom flask along with the primary

amine before undergoing degassing followed by argon being flowed through the

reaction, an example of this set up can be seen in figure 2.1 below. At this point,

it is important to note the large significance in the resultant overall size profiles

for InP QDs which will be synthesised depended on the In(III) halide precursor

used within this initial step. On the alteration of In(III) halide from InI$_3$ to InCl$_3$ a

change in the specific emission profiles can be seen, with the tunable range

from 525 – 630 nm (observed as green and red emission respectively). The

change occurs due to the observed change within the bandgap of InP QD cores

when the In(III) halide is changed. When synthesise of InP cores occurs using

the lighter of the two halides (Cl), the resultant bandgap can be seen to be

smaller. This results in a nanoparticle of larger size.[115,132] This opens up the

possibility of a synthetic route to tuneable InP QDs with specific emission

profiles following the alteration of In(III) used within the synthetic process.
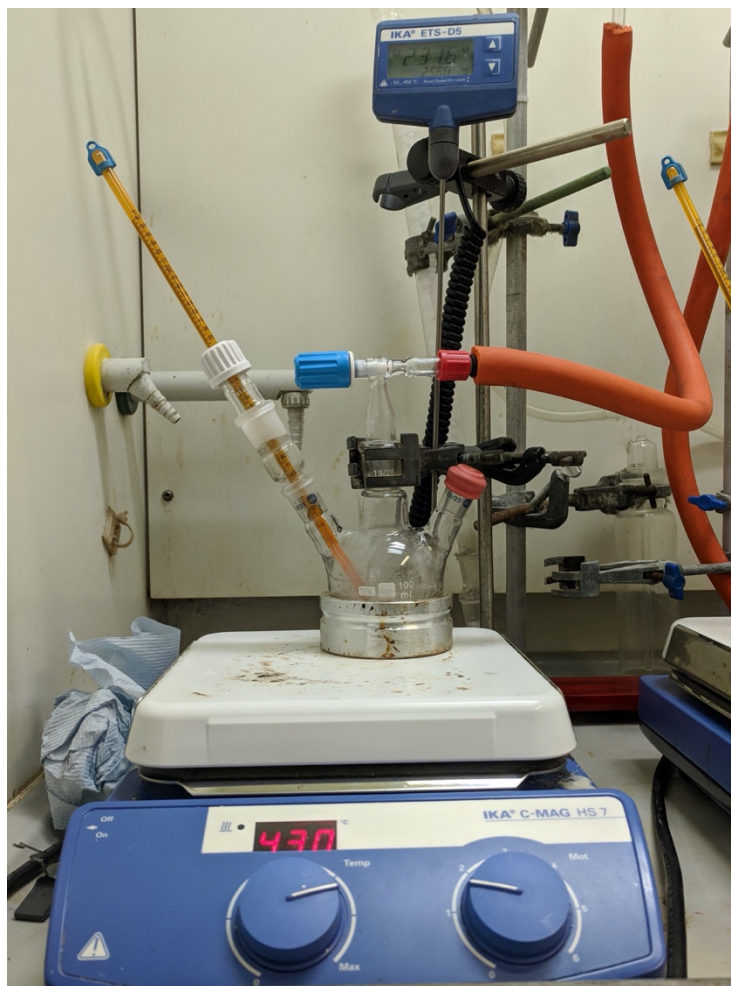
Figure 2.1. Image showing the experimental set up for the synthesis of InP cores.

The use of a primary amine within the reaction as both non-coordinating solvent and surface capping ligand can be seen. Oleylamine is used as it allows for reaction temperatures in excess of 300°C without decomposition. The Zn(II) precursor (ZnCl₂) is used in the initial reaction to efficiently passivate both surface defects and trap states during InP core growth.[175] The passivation of both surface defects and trap states from the addition of Zn(II) precursor leads to a reduction in the number of non-radiative recombination pathways through defect states in the core once a shelling material is added at a later stage, resulting in a QD of improved optical quality and with larger PLQY.[185] It is important to note, adding Zn(II) salts at this initial stage of the reaction does not

automatically dictate the formation of In(Zn)P alloyed QDs within the reaction. However, the formation of the alloy can only be ruled out following the evaluation of synthesised InP cores using powder X-ray diffraction techniques.[175,186]

The addition of a phosphine precursor at an elevated temperature (180°C) is required to initiate the growth of InP cores, this is achieved by the use of a rapid hot injection method under the flow of argon. The rapid injection of $P(DMA)_3$ is complete at a molar ration of 3.6:1 with respect to the In(III) halide. The ratio of 3.6:1 is used to drive the reaction towards a chemical yield of up to 80% as opposed to 30% yield which is observed when a yield of 1:1 ratio is used.[115] The use of $P(DMA)_3$ also reduces the experimental cost when compared to traditional phosphine precursors ($P(TMS)_3$), whilst also being safer and easier to handle as there is a reduced need for air sensitive handling techniques.[116] On the addition of $P(DMA)_3$ the colourless solution undergoes an almost immediate colour change, with the colour change being dependent on the In(III) halide used during the initial synthesis. The colour change observed tends towards a deep green or red colour for InI_3 and $InCl_3$ respectively. InP cores will continue to grow steadily in size until the reaction has come to completion (30 minutes) regardless of In(III) precursor used. On completion, the reaction is quenched with the use of chloroform, followed by the precipitation of InP QDs in excess ethanol. The prepared QDs are then able to be re-suspended in an organic solvent such as hexane to allow their physical properties to be analysed (section 2.2.2.)

2.2.2. Analysis of prepared InP core only QDs

The synthesis of InP cores (referred to throughout this thesis as core only QDs) reaches completion within a reaction time of 30 minutes, their growth is found to be proportional to the time of the reaction. The growth of InP QDs can be followed using UV-vis spectroscopy (Figure 2.2), as the first excitonic peak within InP QDs can be seen within the UV-Vis spectrum. During the 30-minute growth period, InP core only QDs can be seen to grow in size, the first excitonic peak undergoes a bathochromic shift with respect to time. The shift to a longer wavelength can be attributed to the steady growth of the InP cores during the reaction. Figure 2.2 shows the bathochromic shift of the first excitonic peak for InP cores synthesised with both InI_3 and $InCl_3$ (top and bottom respectively). One point of note in figure 2.2 is the difference in wavelength ranges which is able to be achieved with the same synthetic method with only In(III) halides differing. The tunablility within the wavelength range observed is a factor governed by the size of the synthesised InP NPs, the interchanging of In(III) halide allows for the alteration in size of InP cores which lead to differences within their emissive properties, which is depended on growth time.
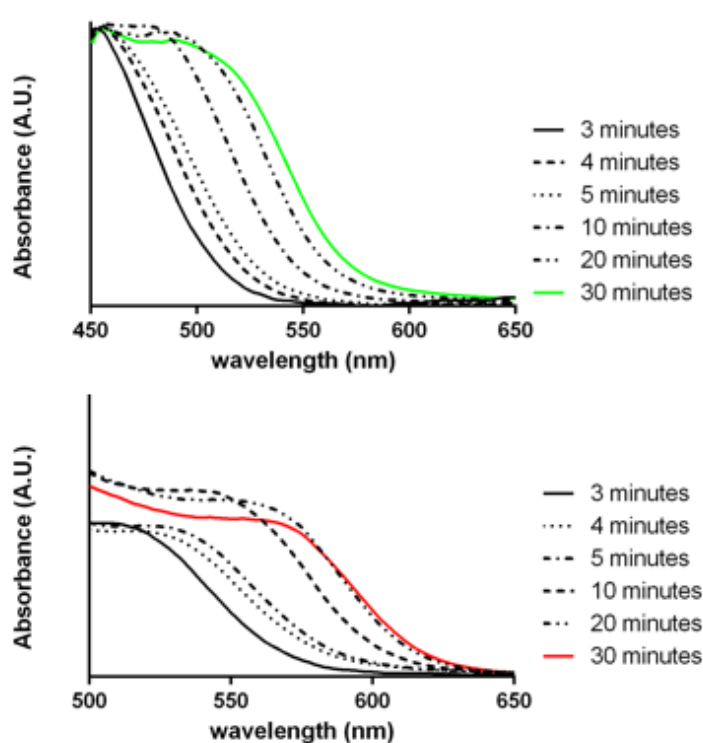
Figure 2.2. Electronic absorption spectra showing the bathochromic shift observed by the first excitonic peak within the InP cores synthesised. (top - InI_3, bottom – $InCl_3$, Hexane, 298k).

The average nanoparticle size as well as the difference in size of the synthesised InP cores synthesised using different indium halides has been investigated using transmission electron microscopy (TEM). The average particle sizing of synthesised InP cores was achieved by measuring a range of individual QDs using scanning transmission electron microscopy (STEM) data shown in figure 2.3.
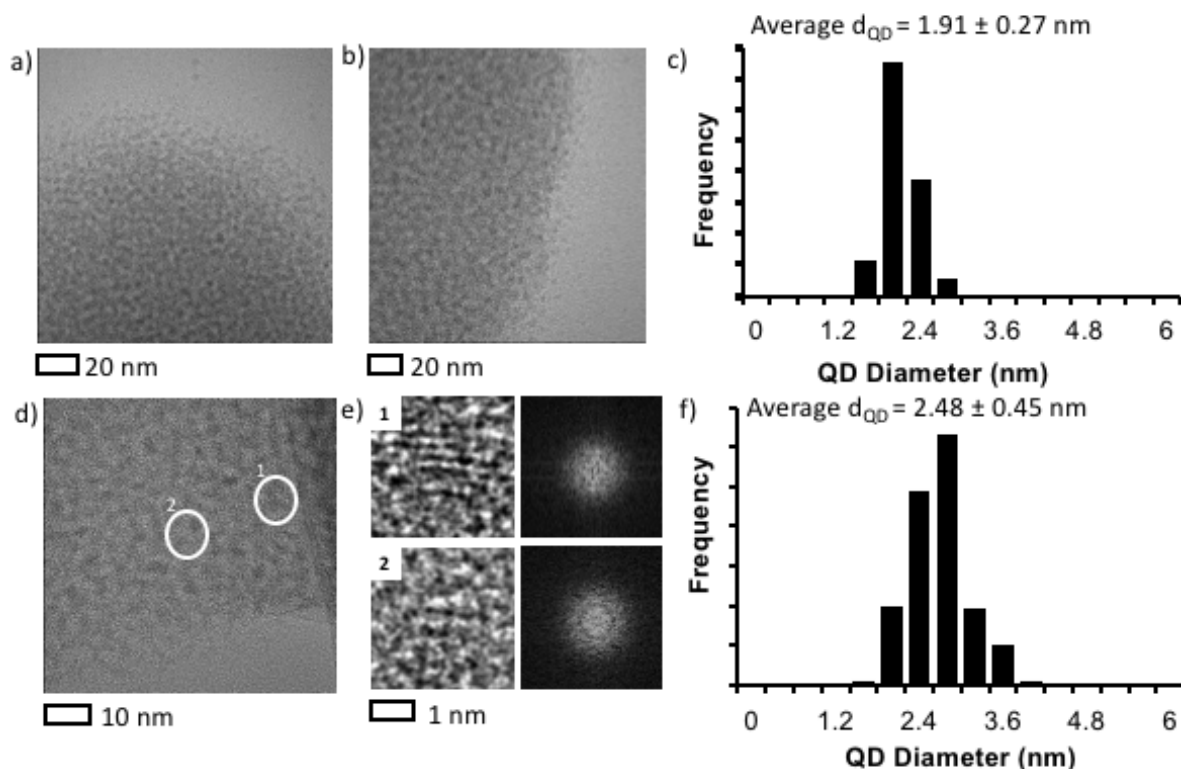
Figure 2.3. Physical properties of InP cores shown. a,b,d show HRTEM images (a,b – red, d – green), e – magnified HRTEM images of singular InP core QDs from d. c,f show size distribution for as-synthesised InP core only QDs (green and red respectively).

High resolution TEM (HRTEM) is able to show an increase in overall size of synthesised InP QDs from 1.91 ± 0.27 nm to 2.48 ± 0.45 nm (InI_3 and $InCl_3$ in hexane respectively) when a change in In(III) halide is used during the synthesis. As can be seen from figure 2.3.c/f, QDs prepared using $InCl_3$ (2.3.f) as opposed to InI_3 (2.3.c) yielded an NP of larger average size. The larger size is attributed to the smaller bandgap produced within the red emissive QDs (section 2.2.1). HRTEM, STEM, high angle annular dark field (HAADF) and energy-dispersive X-ray spectroscopy (EDX) were used in conjunction to determine the In:Zn ratio within the InP cores as well as also trying to identify

the level of free Zn on the surface of the InP core QDs. One limitation with using

these methods for evaluation of InP cores was that only the levels of Zn(II)

metal on the surface could be analysed, this was due to the limitations within

the analytical techniques. Therefore, further evaluation has to be undertaken to

determine whether In(Zn)P alloys have formed within the synthesis procedure.

This is complete in the form of powder X-ray diffraction methods which are

detailed further below. In:Zn ratios of up to 3:1 were observed (table 2.1) with

the InP cores for both the synthesised NPs irrespective of the In(III) halide

which was used during the synthesis.

	In:Zn Ratio	
Indium halide	In(III)	Zn(II)
InI_3	75.00 ± 0.4	25.00 ± 0.4
$InCl_3$	62.92 ± 1.27	37.08 ± 1.27

Table 2.1. In:Zn ratios found within synthesised InP cores using different In(III) halides.

STEM imaging (figure 2.4) has been used to give an indication into the location

of the Zn(II) metal within the formed InP cores. As can be seen in figure 2.4,

Zn(II) metal is present on the surface of newly formed InP NPs. The presence of

Zn(II) metal on the surface has been shown to play a critical role in the addition

of a secondary shelling material (such as ZnS or ZnSe) and how its formation around the surface of the core is initiated.[115]
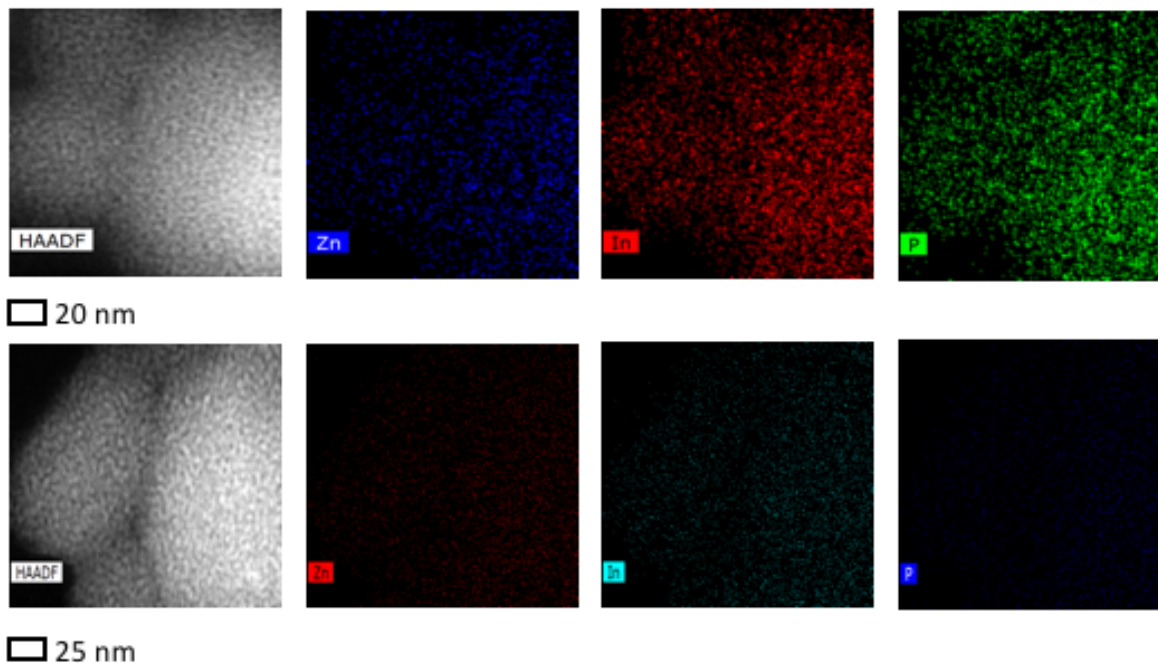
Figure 2.4. STEM panel images for InP cores synthesised with InI3 (top) and InCl3 (bottom) show the presence of Zn(II) metal on the surface of InP core only QDs.

The confirmation of the formation of InP cores as opposed to the formation of In(Zn)P alloys was determined by the use of powder X-ray diffraction (PXRD) techniques. PXRD confirmed that the nano-materials which were synthesised were made solely of InP semiconductor material, with no alloyed material being present (figure 2.5). PXRD results showed that the material synthesised had a cubic structure comparable to InP.
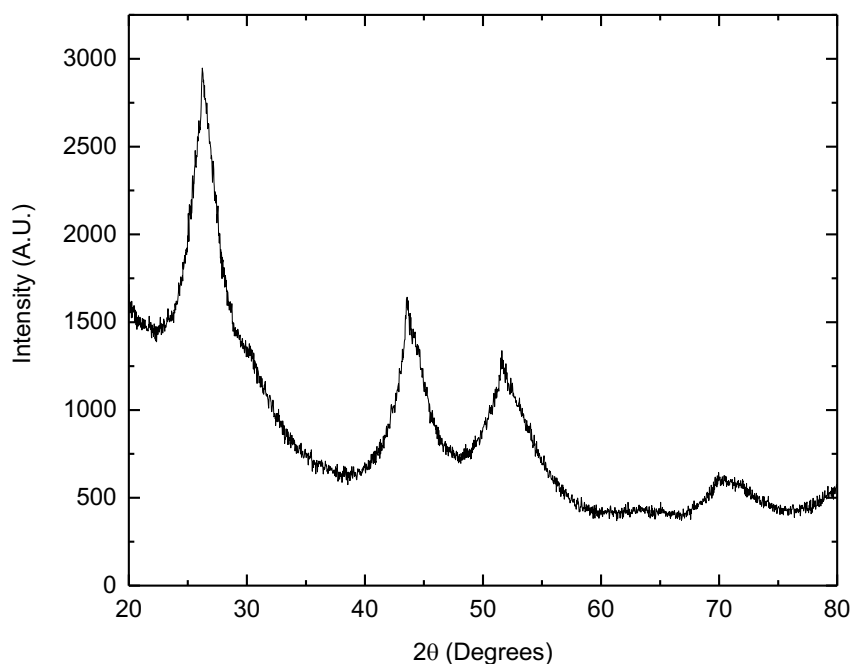
Figure 2.5. PXRD InP cores after 30 minutes of growth time. InP cores shown to be of cubic structure with A=B=C and a,b,c=90*

As-prepared InP cores show a very limited luminescent potential when in organic solvents before the addition of a secondary shelling material, this is attributed to the abundance of surface trap states present within the InP core despite the use of Zn(II) metal in the initial synthesis steps. Trap states result in the non-radiative decay of the exciton leading to a poor PLQY which is seen in core only InP QDs.[177] In order for InP based QDs to be used within a biological setting a secondary layer (shell) needs to be added, this has been shown by multiple academic research teams to increase PLQY dramatically due to the reduction in surface trap states and non-radiative-recombination available to the InP core.[177] Resulting in a core/shell QDs which have a vastly improved PLQY which have potential applications within the world of biomedical imaging.

2.3 Synthesis and evaluation of InP/ZnS (1) core/shell Quantum Dots

2.3.1 Synthesis of InP/ZnS (1) core/shell Quantum Dots

Due to the lack of luminescent properties observed within as-synthesised InP core only QDs discussed above in section 2.2.2, InP QDs on their own would make for a very poor optical imaging agent due to their low photoluminescent properties. The overcoating of the InP QDs with a secondary shelling material of larger band gap semiconductor material is one of the most common methods for the improvement of both the photo and chemical stability of InP based QDs. The epitaxial growth of zinc sulfide (ZnS) through the addition of a chalcogen precursor will give rise to a type-I InP/ZnS core/shell QD with a lattice mismatch of 7.7%. This lattice mismatch between InP core and ZnS shelling material is small enough to allow for the direct growth of ZnS on the surface of InP core without the separate formation of ZnS NPs within the reaction solvent.[176]

The hot-injection of ZnS shell precursors into the InP core reaction following a growth time of 20 minutes results in the production of **InP/ZnS (1)**. Two pre-made precursors are used in tandem to yield a shell of ZnS around an InP core. Initially, trioctylphosphine saturated with sulphur (TOP-S) is injected and allowed to stir at an increased temperature (200°C) for 1 h before the further addition of a Zn(II) metal precursor. TOP-S is used as the chalcogen precursor in place of dodecanethiol (DDT), a commonly used precursor for monolayer growth, as no hypsochromic shift within emission maxima

measurements are observed. The shift observed when using DDT is attributed to surface etching of the InP core.[175] Following the addition of a chalcogenic precursor, the further addition of Zn(II) metal precursor (Zn-stearate) in 1-octadecane also has to be added. This secondary addition of Zn(II) metal is required due to the limiting amount of Zn(II) metal which is initially added during the core synthesis step. Again, following the addition, the temperature is increased and further additions of both precursors are added incrementally with additional temperature increased to yield **InP/ZnS (1)**.

Following the formation of **InP/ZnS (1)** from the subsequent shelling procedure, **InP/ZnS (1)** QDs are able to be isolated first by quenching of the reaction using a small amount of chloroform followed by precipitation in ethanol. **InP/ZnS (1)** can then be re-suspended in organic solvent following the centrifugation of the sample. One point of note is the excess stearate which is involved within the reaction. Following re-suspension in hexane, **InP/ZnS (1)** are to be left overnight to allow excess stearate to precipitate out of solution. This can then later be removed by centrifugation of the **InP/ZnS (1)** samples at high speed (above 10000 rpm).

2.3.2 Physical studies of InP/ZnS (1) Core/Shell Quantum Dots

Following the epitaxial growth of a secondary semiconductor shelling material (ZnS) onto the surface of InP core only QDs resulting in the formation of **InP/ZnS (1),** an overall increase in average particle size is expected. The evaluation in the observed change with the average particle size between InP

cores and **InP/ZnS (1)** is able to be complete using HRTEM imaging.

Comparisons between InP core only QDs and **InP/ZnS (1)** QDs synthesised

with both In(III) halide precursors show that the average particle size increases

as expected following the epitaxial growth of a ZnS shell on the surface of InP,

resulting in the formation of a core/shell QD. Increase in particle sizes of 1.91 ±

0.27 nm to 2.28 ± 0.37 nm and 2.48 ± 0.45 nm to 2.67 ± 0.48 nm for InI_3 and

$InCl_3$ respectively which are shown in figure 2.6.
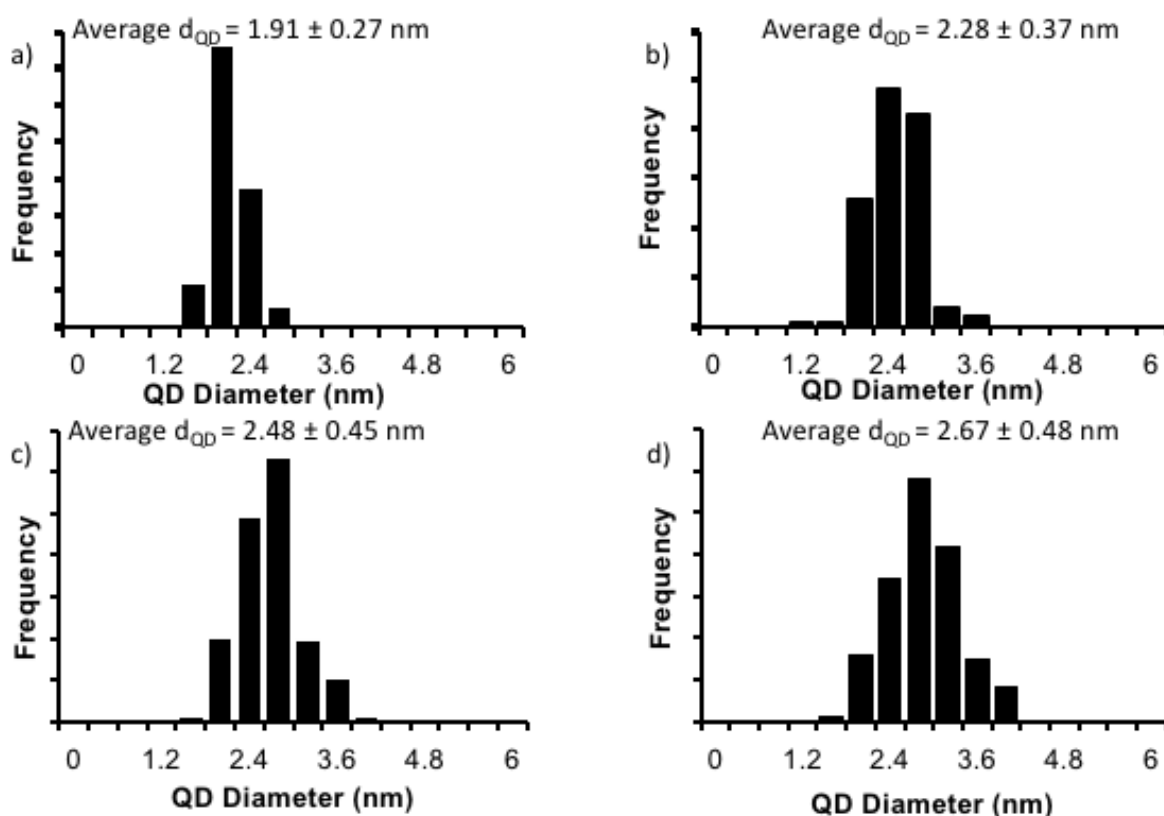
Figure 2.6. Comparison of size distribution graphs obtained through HRTEM of synthesised InP and InP/ZnS (1) QDs. a – green InP, b – green InP/ZnS (1), c – red InP, d – red InP/ZnS (1).

In addition to the increase in size observed when **InP/ZnS (1)** are synthesised from as-prepared InP QDs, a change in physical shape is also able to be seen within the HRTEM images (figure 2.7). HRTEM images of InP core only QDs are able to show that a NP described as quasi-spherical in nature is produced. This is due to there being no visible distortions between atomic planes observed around the extreme edge of the InP QDs. This therefore, results in a NP of spherical like shape (figure 2.7a).
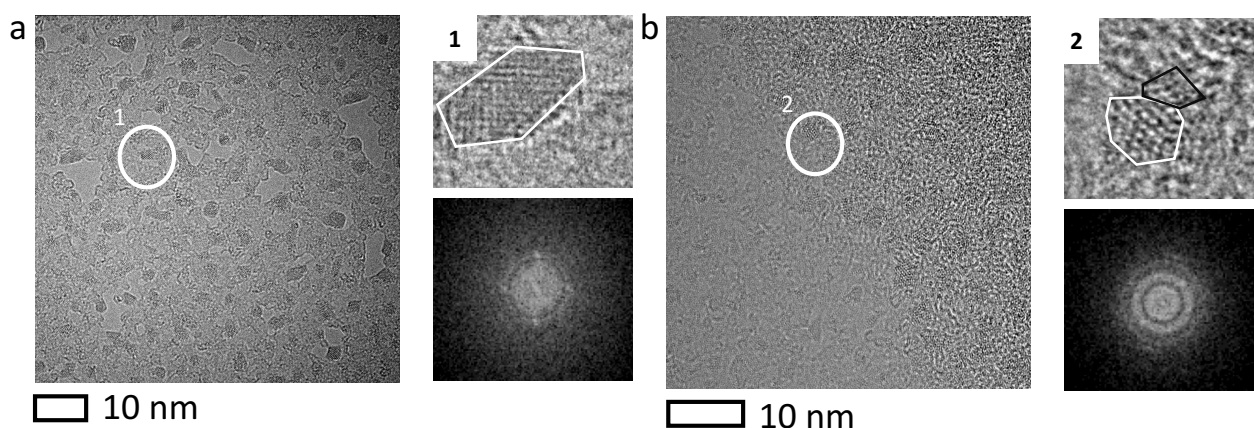
Figure 2.7. HRTEM images showing the quasi-spherical nature of InP core only QDs (a)(InP core outlined in white), compared with the irregular shaped InP/ZnS (1) QDs (b) (InP core outlined in white with ZnS epitaxial shell growth outlined in black).

Following the epitaxial growth of ZnS on the surface of InP cores to form **InP/ZnS (1)** core/shell QDs, atomic line breaks within the atomic planes between the core and shell materials are able to be seen within the HRTEM images (Figure 2.7b). The line breaks within the atomic planes are attributed to the change in semiconductor material at the boundary edge of the InP cores which results in the growth of ZnS islands on the surface of InP, as opposed to

an even coverage distributed across the surface. The addition of ZnS islands to

the surface of InP cores leads to the formation of **InP/ZnS (1)** QDs which are no

longer quasi-spherical in nature, instead forming irregular shaped

nanoparticles. The preferential formation of ZnS islands on the surface of InP

cores as oppose to the addition of an even monolayer has been investigated

further later within the chapter and is explained in more detail in section 2.4.4.

Investigations into the In:Zn ratios for synthesised **InP/ZnS (1)** QDs

were also undertaken as the ratio previously obtained for InP core only QDs

was expected to have changed significantly following the addition of a

secondary shelling material rich in Zn. With an expected increase in Zn(II) from

results previously recorded in section 2.2.2. EDX spectroscopy was able to be

used to show an increase in the ratio of Zn(II) following the addition of a ZnS

shell onto the InP core NP. The exact values for the In:Zn ratio for InP cores and

InP/ZnS (1) can be seen in table 2.2. The increase which is observed is

accredited to the ZnS island formation on the surface of InP cores.

QD	Indium halide	In:Zn Ratio	
		In(III)	Zn(II)
InP	InI_3	75.00 ± 0.4	25.00 ± 0.4
	$InCl_3$	62.92 ± 1.27	37.08 ± 1.27
InP/ZnS (1)	InI_3	24.00 ± 0.45	76.00 ± 0.45
	$InCl_3$	42.77 ± 1.36	57.23 ± 1.36

Table 2.2. In:Zn ratios of InP and InP/ZnS (1) determined using EDX
spectroscopy.

The crystalline nature of the **InP/ZnS (1)** QDs was able to be confirmed by Fast

Fourier transforms (FFTs) of the lattice images obtained from the HRTEM.

From the nature of the diffraction pattern, InP and **InP/ZnS (1)** are consistent

with that of cubic zinc blende structure (figure 2.7).[164] STEM imaging has been

used to show the increased level of Zn(II) metal on the surface of synthesised

InP/ZnS (1) when compared to InP core only NPs, this is shown in figure 2.8.

The STEM images show an increase of Zn(II) metal on the surface of **InP/ZnS

(1)** QDs when compared with InP QDs. The increased Zn(II) metal observed

within figure 2.8 on the surface of **InP/ZnS (1)** when compared to InP core only

QDs is represented of the epitaxial growth of the shelling material and

furthermore, the ZnS island formation on the surface of InP core only QDs.
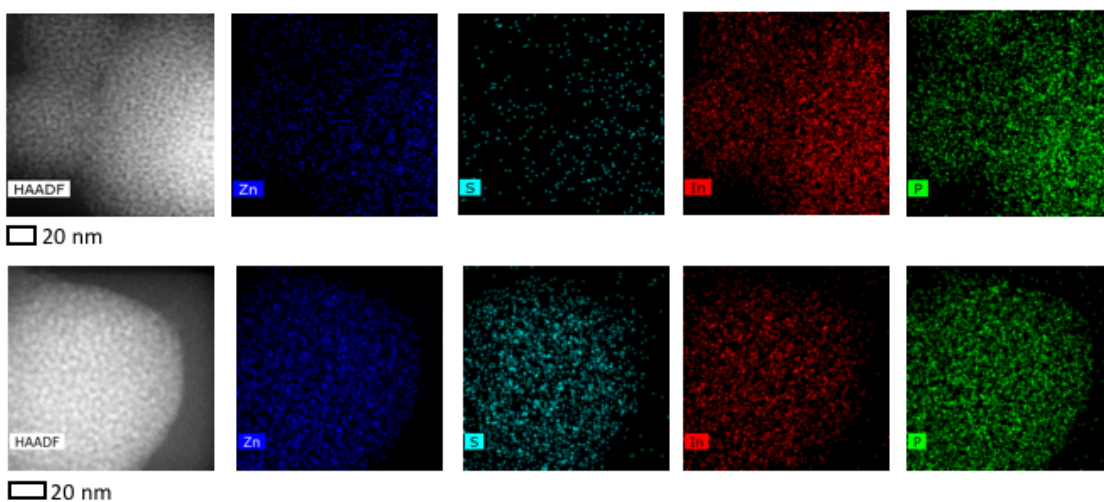
Figure 2.8. Comparison of STEM images to show Zn(II) metal on the surface of as prepared InP and InP/ZnS (1). InP core only QDs– top, InP/ZnS (1) – bottom, both synthesised with InI_3 as the Indium halide.

The addition of a shelling material to the surface of InP QDs resulting in the formation of a type-I **InP/ZnS (1)** core/shell QD is expected to lead to a NP of increased photoluminescent capability, which has a greater capacity to be used within a biological setting. The evaluation of photoluminescent properties of **InP/ZnS (1)** are discussed below in section 2.3.3.

2.3.3 Luminescent studies of InP/ZnS (1) Core/Shell Quantum Dots

As discussed earlier in section 2.2, InP QDs synthesised without the use of a secondary shelling material such as ZnS exhibit a very poor PLQY in the range of less than 1%. This is due in part to the multitude of non-radiative decay pathways available for the relaxation of the exciton back down to the ground state, which is the preferred relaxation method when compared to radiative recombination resulting in a low PLQY. Following the epitaxial growth of a ZnS shell onto the surface of InP core only QDs forming a type-I InP/ZnS core/shell QD, a reduction in both the non-radiative decay pathways and surface trap states available for the relaxing exciton can be seen to be observed.[127,179,187] This reduction therefore, results in an increase within photoluminescent potential of **InP/ZnS (1)** core/shell QDs and this is discussed below.

On the evaluation of **InP/ZnS (1)** with the use of UV-Vis spectroscopic methods to identify the maxima observed for the first excitonic peak following the shelling procedure, it can be shown that there is no observable shift in wavelength when compared to that of the first excitonic peak of InP cores. This

can be seen regardless of indium halide used within the initial synthesis step (figure 2.9.a/b). There is no observed shift in wavelength of the first excitonic peak due to the shelling procedure having no impact on InP core size, this in turn allows for any resultant change in size which was determined to be solely attributed to the addition of ZnS onto the surface of InP cores to form **InP/ZnS (1)**. InP core size dictates the photoluminescent properties which are associated with **InP/ZnS (1)**, this is due to the quantum confinement effect. The fluorescent emission profiles which are observed for the **InP/ZnS (1)** (figure 2.9.a/b) therefore are subject to change, dependent on the size of the synthesised InP cores. InP core sizes of 1.91 ± 0.27 nm and 2.48 ± 0.45 for InI_3 and $InCl_3$ respectively, result in an emission peak with an approximate red shift of ~75 nm. This shift can be seen in both the 2D and 3D emission plots in figure 2.9 below.
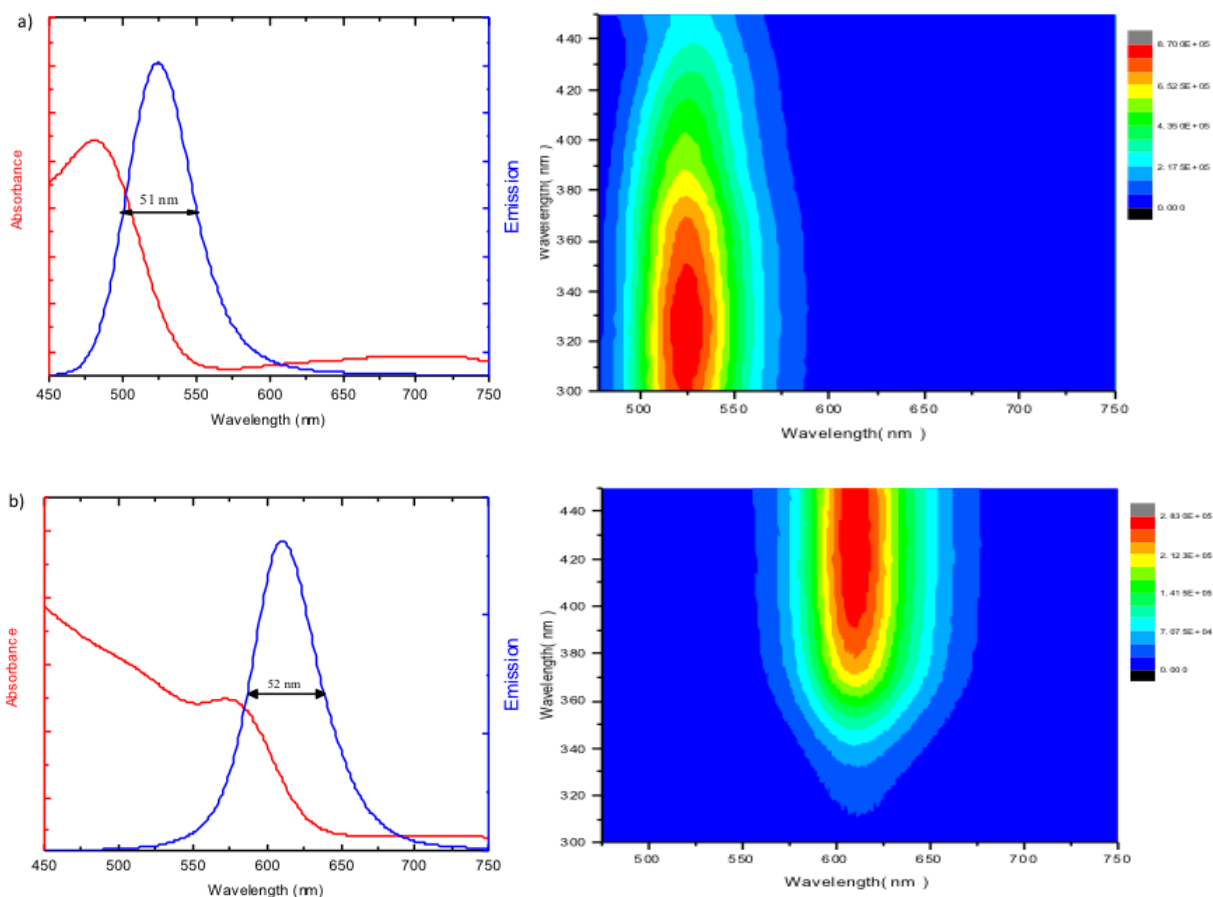
Figure 2.9. 2D and 3D photoluminescent properties of InP/ZnS (1). a,b showing first exciton peak and emission profiles for InP/ZnS (1). c,d showing 3D excitation/emission profiles following synthesis of InP/ZnS (1). a-c are formed using InI$_3$ with b-d being formed using InCl$_3$.

The emission maxima (λ_{em}) for **InP/ZnS (1)** were recorded at an excitation wavelength (λ_{ex}) = 405 nm. The λ_{em} was found to be 534 and 611 nm for **InP/ZnS (1)** QDs synthesised with InI$_3$ and InCl$_3$ respectively (figure 2.9.a/b). The bathochromic shift in λ_{em} from 534 nm to 611 nm is attributed to a 0.57 nm increase in InP core size, with the increase in core size resulting in a longer λ_{em}. This increase in core size accounts for the colour change observed when the **InP/ZnS (1)** samples in hexane are observed under a UV-light, a colour change

from green to red can be seen by eye. The monodisperse nature of **InP/ZnS (1)**

QDs can be determined using the full width half maximum (FWHM) of the

obtained emission spectra in figure 2.9.a/b-blue. The FWHM can determine

how monodisperse the synthesised **InP/ZnS (1)** QDs are with the larger FWHM

showing a more polydisperse sample. FWHM of 51 and 52 nm were recorded

for synthesised **InP/ZnS (1)** (synthesis used InI_3 and $InCl_3$ respectively). These

values were seen to be comparable with other synthetic methods using the less

cost effective and less stable phosphine precursor $P(TMS)_3$ which has a FWHM

range of 40-60 nm.[127]

3D emission/excitation plots for **InP/ZnS (1)** synthesised with both

In(III) halides allow the visualisation of the broad excitation wavelengths which

are commonly associated within InP based QDs (figure 2.9.c/d). This quality of

having a broad λ_{ex} as well as small emission maxima makes QDs a desirable

platform for imaging purposes. One common feature which is observed within

the 3D emission/excitation plots is the consistent Stokes shift which can see to

remains consistent at ca 200 nm regardless of In(III) halide used within the

synthesis method. This can be shown as InI_3 shows a Stokes shift λ_{ex} = 320 nm

to λ_{em} = 524 nm with $InCl_3$ having an λ_{ex} = 425 nm giving an λ_{em} = 611 nm.

On the formation of a type-I core/shell QD the reduction within the non-

radiative decay pathways as well as the passivation of surface trap states sees

an increase in PLQY for both as-prepare InP based core/shell QD with a

fluorescent emission observed as expected. Due to this reduction, an increase in

PLQY is observed within both **InP/ZnS (1)** samples. The PLQY increases to 39

and 49% for InI$_3$ and InCl$_3$ respectively. The PLQY values which were obtained

for **InP/ZnS (1)** were in the range expected (40 – 60%) and rival those values

obtained using the more volatile phosphorus precursors (P(TMS)$_3$). Fluorescent

lifetime measurements of **InP/ZnS (1)** can be used to investigate the

differences which are seen in the PLQY between **InP/ZnS (1)** synthesised with

InI$_3$ and InCl$_3$. This relationship between the PLQY and fluorescent lifetime is

dictated by the difference in radiative and non-radiative decay pathways which

are available to the exciton after excitation from an outside light source.

Fluorescent lifetimes were taken at an excitation wavelength of 405 nm with

InP/ZnS (1) dissolved in organic solvent (hexane). The fluorescent lifetimes

which were found can be seen in table 2.3 below.

QD	Zn:In ratio[a] / atomic %	Diameter[b] (nm)	λ_{em} (nm)	PLQY Φ	Lifetime (ns)	Γ_{rad} (ns^{-1})	$\Gamma_{non\ rad}$ (ns^{-1})
InP	25:75 (± 0.4)	1.91 ± 0.27	-	-	-	-	-
InP	37:63 (± 1.27)	2.42 ± 0.45	-	-	-	-	-
InP/ZnS (1)	76:24 (± 0.45)	2.28 ± 0.37	534	39%	21.65	0.0166	0.0296
InP/ZnS (1)	57:33 (± 1.36)	2.67 ± 0.48	613	49%	19.70	0.0249	0.0259

Table 2.3. Physical and photophysical properties of InP emitting QDs in hexane.

The fluorescent lifetimes observed for the as-prepared **InP/ZnS (1)**

core/shell QDs in hexane showed a single exponential decay corresponding to a

fluorescent lifetime of around 20 ns with exact values being shown in table 2.3.

Using these attained values the difference in PLQY between **InP/ZnS (1)**

synthesised with different In(III) halides can start to be explained *via* the

difference in radiative and non-radiative decay pathways. The relationship

between PLQY and lifetime can be shown in equation 2.1.

$$PLQY = \frac{\Gamma_{RAD}}{\Gamma_{RAD} + \Gamma_{NON-RAD}}$$

(2.1)

Where Γ_{RAD} is the decay constant for the radiative decay pathway and $\Gamma_{NON-RAD}$ is

the decay constant for non-radiative decay pathways.[188] Despite the similarity

in fluorescent lifetime ($\approx$20 ns) there is a notable difference within the observed

PLQY of 10% and this is due to difference in the amount of radiative and non-

radiative decay channels available for exciton decay. **InP/ZnS (1)** synthesised

using $InCl_3$ have a PLQY of 49%, this is coupled with a Γ_{RAD} = 0.0249 ns^{-1}.

Alternatively, **InP/ZnS (1)** synthesised with InI_3 have a PLQY of 39% and a Γ_{RAD}

= 0.0166 ns^{-1}. The lower Γ_{RAD} value which is seen for the **InP/ZnS (1)**

synthesised with InI_3 as compared to that of $InCl_3$ indicated a lesser amount of

available radiative decay pathways which are accessible for the exciton to decay

through. This lower number of radiative decay pathways as well as an increased

number of $\Gamma_{NON-RAD}$ ($InCl_3$ - 0.0259 ns^{-1}, InI_3 0.0296 ns^{-1}) results in a lower

observed PLQY for **InP/ZnS (1)** synthesised using InI_3. It is therefore of great

importance to increase the number of available radiative decay pathways in

order to increase the PLQY of InP/ZnS core/shell QDs. In order to do this, the

increasing of surface coverage of InP cores with the shelling material (ZnS) can

increase the amount of radiative decay pathways and thus increase the PLQY of

type-I InP/ZnS QDs. With the improved PLQY being of great importance within

biomedical imaging applications. The values obtained for PLQY of **InP/ZnS (1)**

in hexane can be seen to be comparable to values which have been previously

reported within literature. For example, Tessier reports that InP/ZnS QDs

which are prepared in a similar way usually exhibit a PLQY within a range of

40-60%.[115]

2.4 Synthesis and evaluation of InP/ZnS (2) core/shell quantum dots.

2.4.1 Synthesis of InP/ZnS (2) core/Shell quantum Dots

The synthesis of **InP/ZnS (1)** previously discussed follows what can be

described as a traditional one-pot hot-injection synthesis method. The synthesis

which is described in section 2.3.1 first sees the production of InP core only QDs

using an In(III) halide precursor and the non-toxic air stable phosphorus

precursor P(DMA)$_3$. Once complete, the epitaxial growth of a secondary shelling

material in the form of a ZnS shell yields **InP/ZnS (1)** core/shell QDs with

tunable emission profiles within the visible emission spectra (525 – 625 nm).

The introduction of a thermally controlled cooling phase on completion of the

synthesis of **InP/ZnS (1)** QDs followed by a second successive heating stage

with the introduction of further ZnS shelling precursors leads to the production

of **InP/ZnS (2)**. This methodology (termed the successive heating method

throughout) involves cooling newly synthesised **InP/ZnS (1)** QDs to 180°C

under argon flow for 30 minutes on completion of the first ZnS precursor

injection. Then, immediately following the 30-minute cooling phase, the

addition of addition ZnS precursors is again added as in the synthesis of

InP/ZnS (1). A scheme for the successive heating methodology used for the

formation of **InP/ZnS (2)** can be seen in scheme 2.3.

In(X)$_3$ + ZnCl$_2$ + oleylamine $\xrightarrow[\substack{180°C \\ 30 \text{ minutes}}]{\text{P(DMA)}_3}$ **InP cores** $\xrightarrow[\substack{180°C \text{ - } 260°C}]{\text{ZnS shelling Precursors}}$ **InP/ZnS (1)**

X = Cl, I

Temperature controlled cooling step (180°C)   30 minutes

ZnS shelling Precursors

InP/ZnS (2) $\xleftarrow[\substack{180°C \text{ - } 260°C}]{}$ **InP/ZnS (1)**
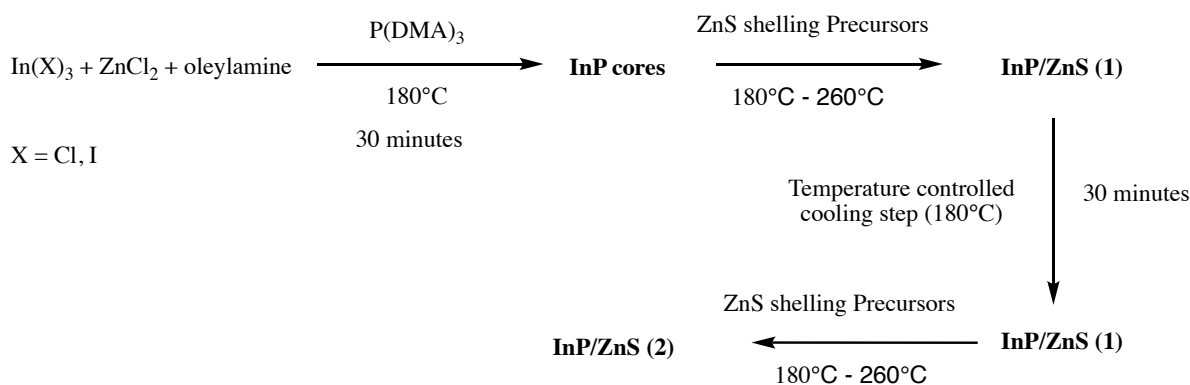
Scheme 2.3. Reaction scheme showing the successive heating methodology for the synthesis of InP/ZnS (2).

Interestingly, **InP/ZnS (2)** core/shell QDs formed using the successive heating

method showed both chemical and photophysical changes which would see

InP/ZnS (2) become a more applicable synthesis method for InP based QDs

which are to be used in a biomedical setting. These improvements are evaluated

and discussed further below.

2.4.2 Physical properties of InP/ZnS (2) Core/Shell Quantum dots

To investigate as to whether a change in overall size of InP/ZnS QDs can

be seen when altering the synthesis method from a traditional (**InP/ZnS (1)**) to

a successive (**InP/ZnS (2)**) heating method, HRTEM imaging was used. The use

of a successive heating method resulted in the increase in size for the **InP/ZnS**

(2) when compared to a tradition heating method. An overall increase size distribution of 2.28 ± 0.37 nm to 2.76 ± 0.37 nm and 2.67 ± 0.48 nm to 2.75 ± 0.45 nm was observed for **InP/ZnS (2)** synthesised using InI_3 and $InCl_3$ respectively (figure 2.10), with the increase in size being attributed to the addition of further ZnS to the surface of **InP/ZnS (1)**. This theory for the increase in size is further supported by the change to the In:Zn ratio.
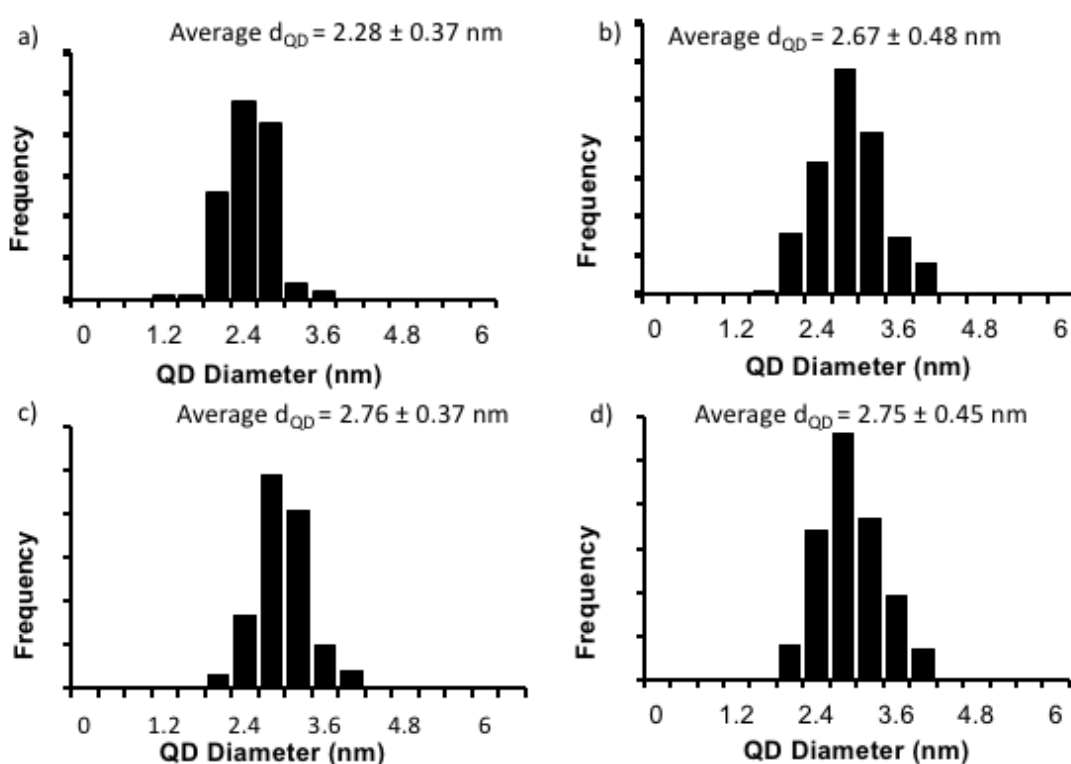
Figure 2.10. Size distribution comparison between InP/ZnS (1) (a-b) and InP/ZnS (2) (c-d). a-c show QDs Synthesised with InI_3 with b-d showing QDs synthesised with $InCl_3$.

QD	Indium Halide	In:Zn Ratio	
		In(III)	Zn(II)
InP	InI_3	75.00 ± 0.40	25.00 ± 0.40
	$InCl_3$	62.92 ± 1.27	37.08 ± 1.27
InP/ZnS (1)	InI_3	24.00 ± 0.45	76.00 ± 0.45
	$InCl_3$	42.77 ± 1.36	57.23 ± 1.36
InP/ZnS (2)	InI_3	15.00 ± 0.13	85.00 ± 0.13
	$InCl_3$	26.51 ± 0.28	73.49 ±0.28

Table 2.4. In:Zn ratio showing the increasing value of Zn from cores to (1)/(2).

EDX spectroscopy was used to show a definitive increase of Zn(II) within the

InP/ZnS (2) QDs when compared to that of those QDs synthesized *via* a

traditional synthesis method. Zn:In ratios increased further to values of 85:15 ±

0.13 and 73:27 ± 0.28 for **InP/ZnS (2)** synthesised with InI_3 and $InCl_3$

respectively, with exact values being shown in table 2.4.

Following the increase observed in Zn(II) metal on the surface as a result

of EDX spectroscopy shown in table 2.4, STEM imaging methods were also used

to visualise the increase in Zn(II) metal on the surface following the change of

synthesis technique. As can be seen in figure 2.11 an increase in Zn(II) metal on

the surface of synthesised QDs can be observed when moving from InP cores

(figure 2.11.top) through to **InP/ZnS (1)** (figure 2.11. middle) and is seen again

to increase on the surface of **InP/ZnS (2)** (figure 2.11.bottom).
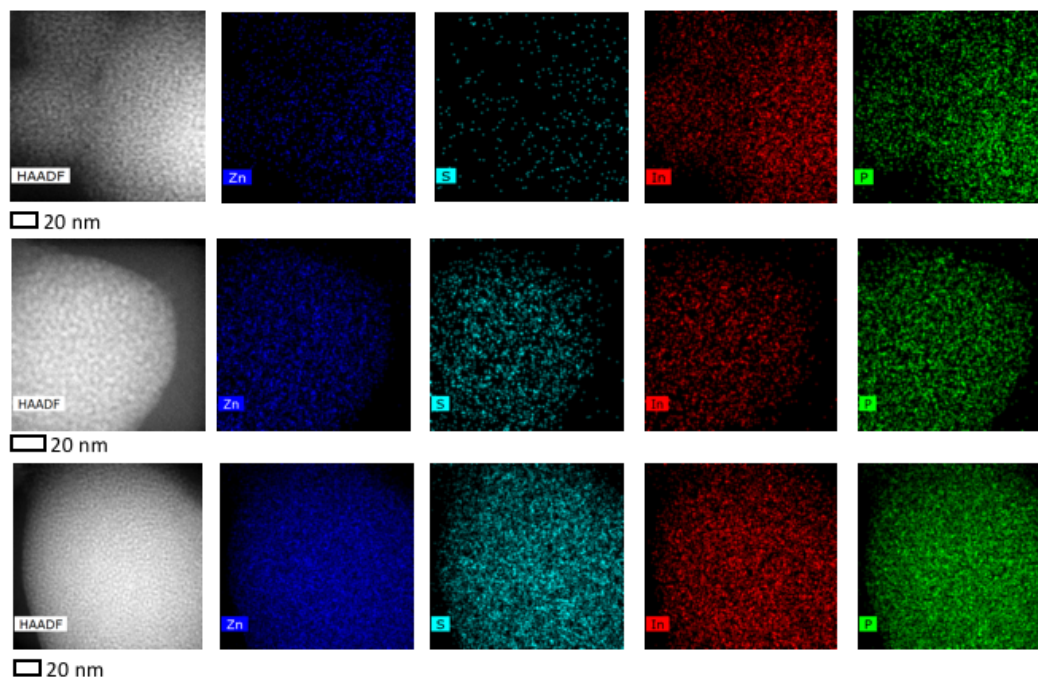
Figure 2.11. STEM images showing the increase in Zn(II) metal on the surface of InP based QDs synthesised with InI_3 depended on synthesis method. Top panel – InP cores, middle panel – InP/ZnS (1), bottom panel – InP/ZnS (2).

The use of a successive heating method to synthesise **InP/ZnS (2)** also sees a regression within the shape of the synthesised nanoparticle to a shape which is similar to those observed for InP core only QDs seen in figure 2.3.

As discussed above in section 2.3.2, **InP/ZnS (1)** core/shell QDs are able to be formed *via* the formation of ZnS islands on the surface of InP cores, rather than a gradual even monolayer of ZnS shelling material being deposited onto the surface of the InP core. This results in atomic line breaks being visible within the HRTEM images in figure 2.7. When InP/ZnS QDs are prepared using the successive heating synthesis method, no visible atomic line breaks between the InP core and ZnS shelling material can be seen figure 2.12.

111
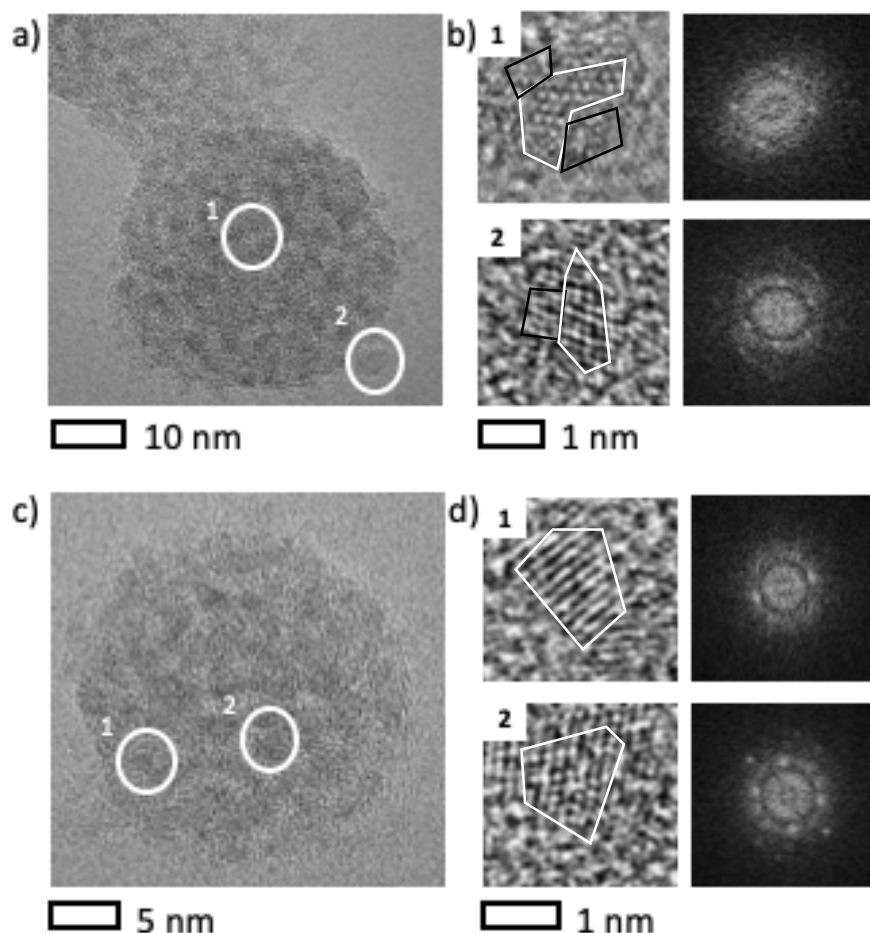
Figure 2.12. HRTEM images depicting the differences in shape of synthesised InP/ZnS core/shell QDs using traditional synthetic method (a-b) (showing island formation- black on InP cores - white) and successive heating method (c-d) forming quasi-spherical core/shell InP/ZnS QDs with no ZnS island formation.

The absence of atomic line breaks within the **InP/ZnS (2)** HRTEM images, result in the formation of InP/ZnS core/shell QDs which have a quasi-spherical shape (figure 2.12). On the further addition of ZnS shelling precursors following a temperature controlled cooling phase within the synthesis of **InP/ZnS (2)** QDs, a shape change within the synthesised InP/ZnS core/shell QDs was

observed and the reasons for this are discussed in further detail below in section 2.4.4.

2.4.3 Fluorescent properties of InP/ZnS (2) core/shell quantum Dots

As previously discussed in section 2.3.3, the addition of a secondary shelling material (ZnS) to the surface of InP core only QDs results in an increased PLQY when InP/ZnS core/shell QDs are dispersed within organic solvents. The increase in PLQY is attributed to the reduction within the non-radiative pathways which are available for the relaxation of the exciton within the newly formed type-I core/shell QDs. However, it is hoped that the addition of a temperature controlled cooling phase within the synthesis will further reduce the available non-radiative decay pathways by increasing surface coverage of InP cores with ZnS shelling material. With this in turn dramatically increasing the PLQY which can be achieved by InP based QDs. **InP/ZnS (2)** core/shell QDs exhibited similar photoluminescent properties to them observed for the QDs synthesised formed using a traditional synthesis method. As previously seen, a shift in emission maxima can be forced with the change in In(III) halide used within the initial InP core synthesis. On completion of **InP/ZnS (2)**, λ_{em} of 530 nm and 617 nm (InI$_3$ and InCl$_3$ respectively) (figure 2.13 and 2.14) were found. On comparing of the λ_{em} what can be seen in both instances is a slight bathochromic shift associated with the successive heating method, attributed to the additional heating step. The additional time which **InP/ZnS (2)** QDs have under higher

temperatures result in the slight movement of emission maxima (less than 10

nm) to that of a higher wavelength (figure 2.14).
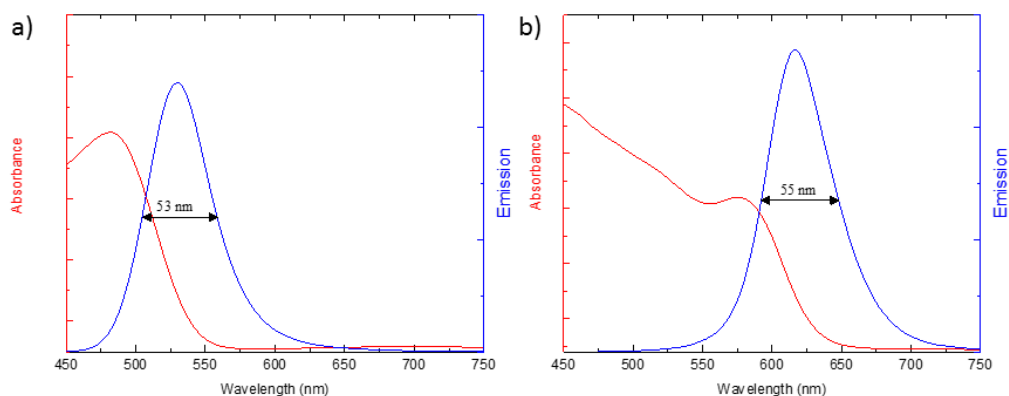
Figure 2.13. Absorption and emission spectra showing the first excitonic peaks
and emission maxima of InP/ZnS (2) as well as displaying the FWHM on the
emission spectra. a - InP/ZnS (2) formed using InI_3 b - InP/ZnS (2) formed using
$InCl_3$

Interestingly, after the second addition of ZnS precursor only a very small

increase in FWHM was able to be observed. An increase of 2 and 3 nm within

the FWHM was observed for **InP/ZnS (2)** when synthesised with InI_3 and $InCl_3$

respectively, compared to QDs synthesised using a traditional synthesis
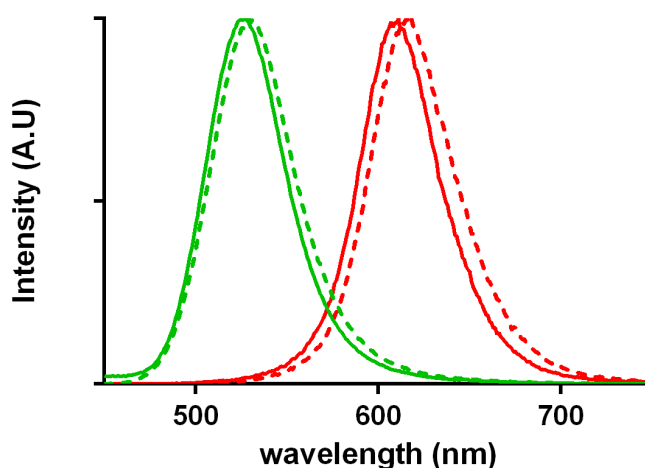
method.

Figure 2.14. Fluorescent emission spectra for InP/ZnS (1)/(2) showing a small bathochromic shift in emission maxima with synthesis change from traditional (solid line) to successive (hashed line) methods, this can be seen for InP/ZnS QDs synthesised with both $InCl_3$ and InI_3.

The small increase in FWHM witnessed when comparing the traditional and successive heating method would indicate that any increase in polydispersity between the two synthetic methods would be able to be described as negligible. The use of 3D excitation/emission plots (figure 2.15) for **InP/ZnS (2)** synthesised with both In(III) halides, have again been used to show the broad λ_{ex} as well as the narrow λ_{em} range. Furthermore, within the 3D plots the characteristic Stokes shift which was identified earlier as ca 200 nm remain present within QDs synthesised using the successive heating method.
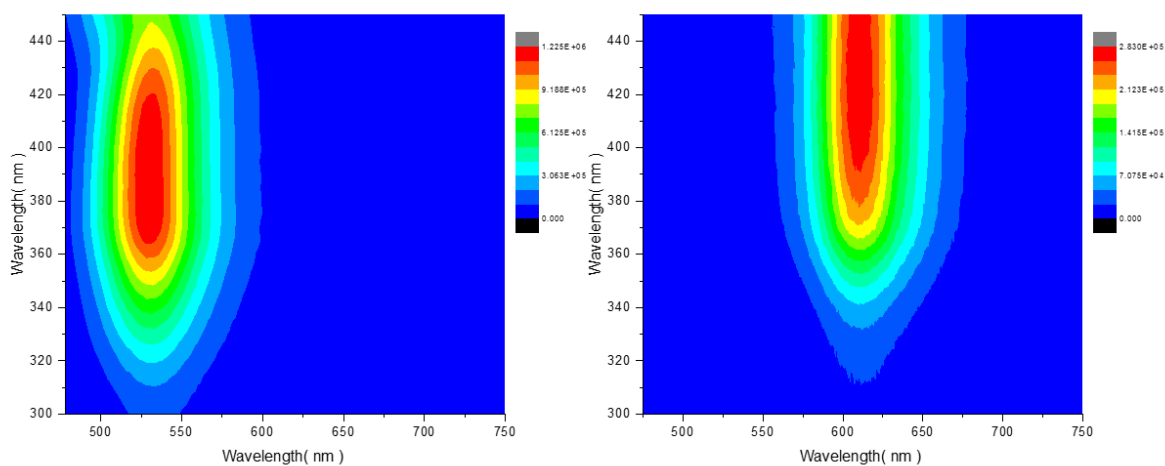
Figure 2.15. 3D excitation/emission spectra for InP/ZnS (2) (InI$_3$ – left, InCl$_3$ – right)

On the inclusion of a temperature controlled cooling step within the synthesis of **InP/ZnS (2)** QDs, an increase in the overall PLQY is seen within organic solvent of 1.7 times. PLQYs of up to 85.3% in organic solvent (measurements taking in hexane) can be achieved using the **InP/ZnS (2)** core/shell QDs, with accurate values for the all synthesised QDs displayed in table 2.5. The PLQY value of 85.3% is the highest recorded PLQY for InP based QDs to date. Previously, Hines and co-workers achieved a PLQY of up to 60% with the same precursor and Deng *et al.* achieved 76.1% when synthesising blue emitting InP QDs.[115,189]

QD	Zn:In ratio[a] / atomic %	Diameter[b] (nm)	λ_{em} (nm)	PLQY Φ	Lifetime (ns)	Γ_{rad} (ns^{-1})	$\Gamma_{non\ rad}$ (ns^{-1})
InP	25:75 (± 0.4)	1.91 ± 0.27	-	-	-	-	-
InP	37:63 (± 1.27)	2.42 ± 0.45	-	-	-	-	-
InP/ZnS (1)	76:24 (± 0.45)	2.28 ± 0.37	534	39.0%	21.65	0.0166	0.0296
InP/ZnS (1)	57:33 (± 1.36)	2.67 ± 0.48	613	49.0%	19.70	0.0249	0.0259
InP/ZnS (2)	85:15 (± 0.13)	2.76 ± 0.37	535	49.0%	20.20	0.0174	0.0251
InP/ZnS (2)	73:21 (± 0.28)	2.75 ± 0.45	623	85.3%	20.50	0.0416	0.0072
InP/ZnS (DC)	89:11 (± 0.11)	2.88 ± 0.49	611	47.0%	22.08	0.0213	0.0240

Table 2.5. Full table with displaying all QD lifetime data and PLQY as well as emission properties

The increase within PLQY of **InP/ZnS (2)** QDs when compared to **InP/ZnS (1)** can be seen as indicator of the successive heating method creating a greater surface coverage of ZnS on the surface of InP cores. This leads to the reduction in non-radiative decay pathways which are available for the first exciton to decay in **InP/ZnS (2)** as compared to **InP/ZnS (1)**. To evaluate this further, equation 2.2 is again used in combination with the fluorescent lifetime measurements (table 2.5) to show an increase in radiative decay channels against non-radiative decay channels. This is illustrated using InP cores which have been synthesised using InCl$_3$. The relationship between **InP/ZnS (1)/(2)** and their fluorescent lifetimes are shown in table 2.5. The Γ_{RAD} for **InP/ZnS (1)** is given as 0.0249 ns^{-1} whilst having a PLQY of 49.0%. However, for **InP/ZnS (2)** we see a PLQY of 85.3% and a Γ_{RAD} = 0.0416 ns^{-1} whilst a notable fall in $\Gamma_{NON-RAD}$ value from 0.0259 to 0.0072 ns^{-1} is observed. This equates to an increase in the radiative decay channels within **InP/ZnS (2)** QDs as well as a fall in the number of non-radiative decay pathways. However, these numbers alone cannot be seen as conclusive evidence that the use of a cooling step within the successive heating method will result in an increased PLQY when compared to

InP/ZnS core/shell QDs which have been synthesised using a traditional synthetic method. Further investigative methods were needed to identify the reason for the large increases in PLQY with the addition of a 30-minute temperature controlled cooling phase, these methods include the use of DFT calculations with the results being discussed in detail in section 2.4.4.

2.4.4 Thermal diffusion of ZnS shell in InP/ZnS (2) QDs

As discussed previously, the shape of the synthesised InP/ZnS core/shell QDs is reliant on the synthetic method used, with the traditional method yielding ZnS island formation on the surface of InP cores as the successive heating method results in the synthesis of quasi-spherical QDs. In conjunction with the change in shape which is observed, a dramatic change in PLQY can also be seen when altering the synthesis method, further investigation was needed to gain a deeper understanding as to ascertain if both the change in shape and increase in PLQY are related. To do this, computational modelling in the form of density functional theory (DFT) calculations was used to identify the factors which govern the evolutions of the InP/ZnS QD shapes following their synthesis. First, we looked at comparing the shapes of **InP/ZnS (1)** and **(2)** to determine if/how the shape of the synthesised QDs were playing a role in the changeable PLQY observed. Second, the thickness of the ZnS shell which was deposited on the surface of the InP cores was determined (section 2.4.4).

With regard to the epitaxial growth of a ZnS shell onto the surface of InP cores using a traditional synthetic methodology, we first must assume that the

initial growth stage of the ZnS shell takes place following a kinetic regime. This means that the required activation barriers for the surface diffusion of ZnS cannot be overcome, resulting in a thermodynamic equilibrium not being reached. DFT calculations have been used to evaluate how the failure to reach thermodynamic equilibrium can affect the shape of the **InP/ZnS (1)** QDs when compared to QDs synthesised using a successive heating method. Calculations based on QDs synthesised in a traditional methodology suggest a strong preference of binding of Zn atoms to already formed ZnS on the surface of InP cores (the adsorption energy is 2.7 eV on surface), this is compared to the energy needed to bind to InP (1.9 eV). The preference of Zn atoms to nucleate on ZnS, if it is present, will result in the formation of islands being formed on the surface of InP rather than a covering of ZnS shell on the InP core due to the lower adsorption energy which is required. This expectation is consistent with the observation of irregularly shaped, asymmetric QDs with bare InP patches and small islands of ZnS located sporadically on the surface (figure 2.7). The sporadic nature produced by the formation of ZnS islands creates many bare patches to be present on the surface of the InP cores, resulting in poor overall passivation of non-radiative decay pathways. This will result in a lower PLQY in those QDs made using the traditional synthetic method, which is what is observed within this work.

The irregularity in QDs shape observed when synthesised via a traditional synthetic method (**InP/ZnS (1)**) is not seen following the use of a successive heating method (**InP/ZnS (2)**). Experimentally the shape of the QDs prepared using the successive heating method tendered towards a quasi-

spherical nature. The quasi-spherical nature observed is attributed to a

relaxation of the 3D ZnS islands formed on the InP core towards the equilibrium

shape. Given sufficient time, the ZnS islands which have initially formed before

the thermally controlled cooling step will relax towards its equilibrium state. In

the case of ZnS, this shape is bounded entirely by (110) facets.[190] The time scale

for the relaxation process is determined by the energy barriers for the surface

diffusion of Zn and S atoms of the ZnS shelling material. With these barriers

being well defined by the well-defined (110) facets. DFT nudged-elastic band

calculations were carried out to determine the energy barriers required to start

the relaxation process of ZnS around the InP core. The values obtained were

0.69 eV and 0.75 eV for Zn and S respectively. This can be seen in figure 2.16.
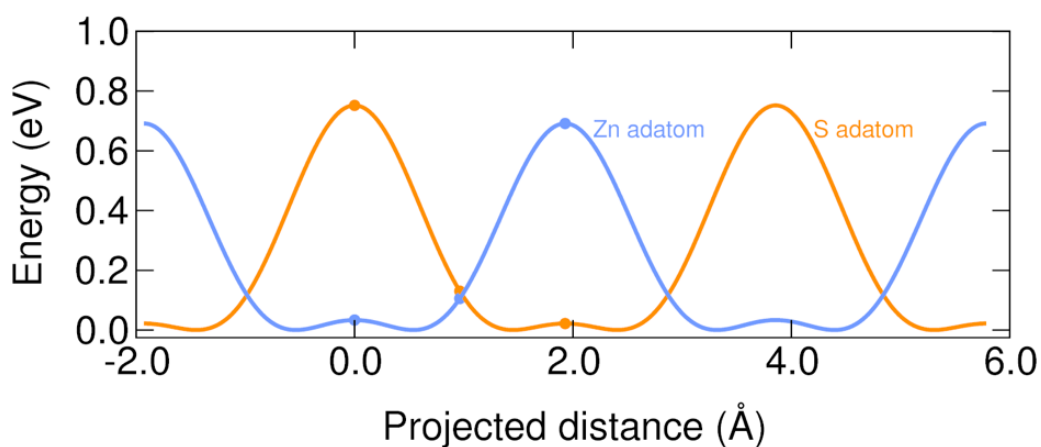
Figure 2.16. DFT nudged-elastic band calculations for Zn and S atoms for the
redistribution around the InP core.

Such modest barriers are easily surmounted by the time and

temperatures that are used (180°C, 30 minutes) within the thermally controlled

cooling step used within the successive heating method. Therefore, the

equilibrium quasi-spherical shape can be reached. The resulting physical

picture, then, is that when growth is restarted, the small ZnS islands

redistribute themselves over the surface, leading to a conformal quasi-spherical

core/shell QDs. The redistribution leads to an increase in the overall surface

area of the InP cores which are covered by the ZnS, this results in the higher

PLQY when the successive heating methodology is used. Therefore, the cooling

phase prior to the second addition of Zn and S precursors, plays a major role in

increasing ZnS coverage of the InP core. Decreasing non-radiative decay

pathways leading to an increase in both **InP/ZnS (2)** QDs when in organic

solvent (hexane).

2.4.5 Quantification of shell thickness.

The Quantification of the ZnS shelling material in terms of shell thickness

which has been deposited on onto the surface of InP core only QDs has been

performed by expressing the thickness in terms of monolayers of ZnS.[176] A

monolayer refers to the smallest subunit of ZnS shelling material, consisting of a

single cation (Zn) and anion (S). Expressing the amount of shelling material on

the surface of the InP cores in this way gives a numerical value which can be

associated with each methodology, thus allowing them to be compared. TEM

measurements have shown an increase in particle size for both synthetic

methods (traditional/successive), which can be assumed to be the addition of a

ZnS shell on the surface of InP. The addition can be calculated and the number

of monolayers determined due to the average increase in diameter. Using the

assumption that the as-synthesised InP core QDs are spherical in nature with a

radius (r in nm), the volume of the ZnS shell (V in nm^3) can be derived by the difference in the volume of the InP/ZnS (V_{cs}) and the volume of InP core (V_c). These values can be linked together using equations 2.2 and 2.3 below, where x is the number of ZnS monolayers and d is the thickness of one monolayer.

$$V_s = V_{CS} - V_c \tag{2.2}$$

$$V_s = \frac{4}{3}\pi(r + xd)^3 - \frac{4}{3}\pi r^3 \tag{2.3}$$

The thickness of one complete monolayer of ZnS is reported at 0.32 nm.[191] On the addition of ZnS to the surface of InP, the increase in size within the NPs formed using a traditional synthesis method of 1.91 ± 0.27 nm to 2.28 ± 0.37 nm and 2.48 ± 0.45 nm to 2.67 ± 0.48 nm for InI$_3$ and InCl$_3$ respectively. This addition in size equates to 0.578 and 0.391 ZnS monolayers added to the surface of InP cores. The combination of ZnS island formation on the surface of InP cores and the inability to deposit a complete monolayer of ZnS onto the surface of InP contribute to the lower than previously reported PLQY for InP/ZnS core/shell QDs.

Investigations show that when using the successive heating method, a further increase in size of nanoparticles is observed. This is again attributed to the addition of ZnS on the surface. The addition of ZnS is added to the redistributed ZnS already present on the InP core, this can be seen pictorially in figure 2.17.
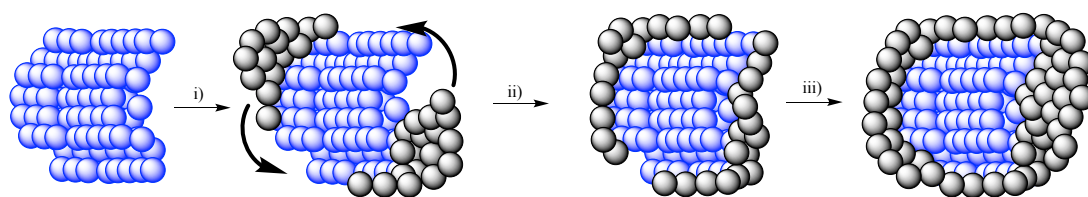
Figure 2.17. Schematic diagram of ZnS growth and redistribution around the InP core. i) initial shell growth, ii) thermal equilibrium of ZnS across core, iii) further growth of shell.

Increases in size of nanoparticles of 1.91 ± 0.27nm to 2.76 ± 0.37nm and 2.48 ± 0.45 nm to 2.75 ± 0.45 nm are seen when comparing **InP/ZnS (1)** and **InP/ZnS (2)**. Increase results in 1.32 and 0.481 monolayers of ZnS are added for the InI_3 and the $InCl_3$ respectively. Increase in ZnS monolayers added to the surface plus the relaxation of the ZnS to the thermodynamic equilibrium around the InP which is seen during the temperature controlled cooling phase (thermal diffusion), results in InP/ZnS core/shell QDs synthesised using a successive heating method to have a greater surface coverage of InP with the ZnS shelling material despite the low number of monolayers which are deposited onto the surface. Both of the aforementioned factors determine that an increase in PLQY is able to be seen when comparing **InP/ZnS (1)** to QDs synthesised using a successive heating method (**InP/ZnS (2)**).[192]

In order to validate the success of novel synthetic approach outlined within the successive heating method, leading to the enhancement within PLQY of InP based QDs systems. A control reaction was carried out using a traditional single heating method with double the concentration of Zn and S precursors

added to the InP cores forming **InP/ZnS (3)** (Figure 2.18) using InCl$_3$ based

synthesis. Allowing for comparisons to be drawn between all 3 synthetic

methods.
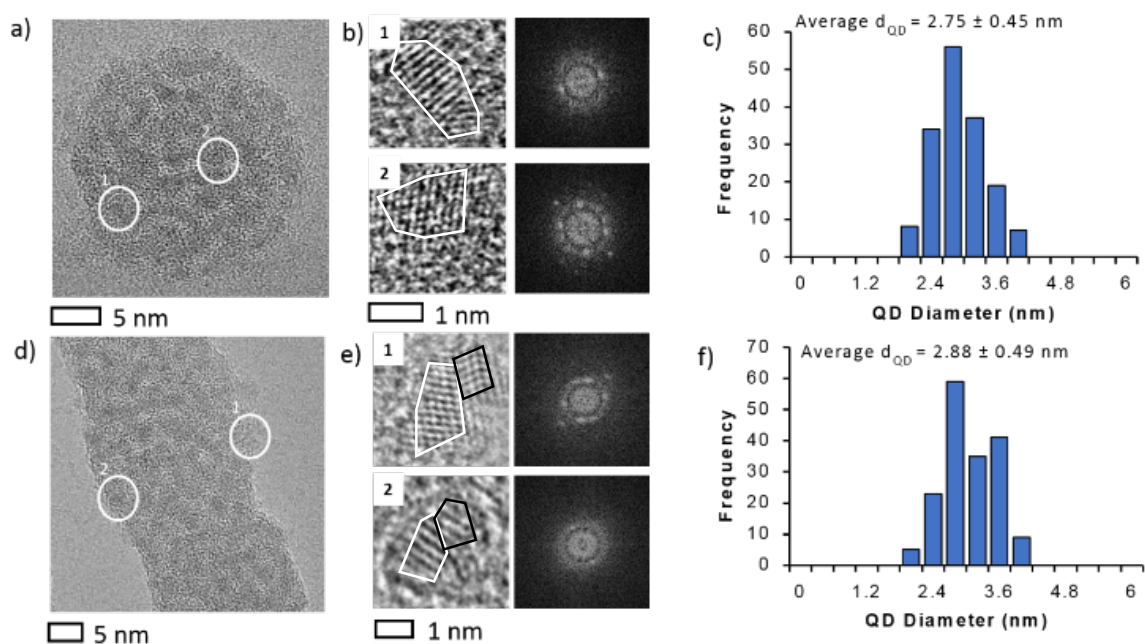
Figure 2.18. Physical properties of the InP/ZnS (2) QDs. (a-d) TEM images
showing the InP/ZnS (2) (top) QDs and InP/ZnS (3) (bottom), highlighting the
crystalline nature of QDs, and (b-e), showing magnified images of two individual
QDs (left) and the corresponding FFTs (right). (c-f) Size distribution of InP/ZnS
(2) (top) and InP/ZnS (3) (bottom).

The synthesises of **InP/ZnS (3)** was expected to produce QDs with a

thickness and quantity of Zn(II) metal which is comparable to that observed

within the **InP/ZnS (2)** QDs, showing that simply increasing in the

concentration of Zn and S precursors alone does not improve the PLQY. Thus,

the cooling phase which is added within the successive heating method plays a

pivotal role within the increase observed in PLQY. **InP/ZnS (3)** showed a Zn:In

ratio of 89:11 with a diameter of 2.88 ± 0.49 nm and using equations 2.3 and 2.4, 0.715 monolayers of ZnS can be shown to be on the surface of InP cores. The size of the **InP/ZnS (3)** was shown to be slightly larger than synthesised using the successive heating methodology, however the Zn(II) content was seen to be greater. Therefore, the Zn(II) metal content can be assumed to not be the cause of the PLQY enhancement as **InP/ZnS (3)** shows a PLQY of 47%, which can be seen to be more comparable to the traditionally synthesised QDs (cf. (**InP/ZnS (1)** = 49%). Lifetime measurements for all the QDs in hexane from all three methods show a single exponential decay corresponding to an excited lifetime in a similar range of 20 ns (Table 2.5). However, **InP/ZnS (2)** shows a suppression of non-radiative decay pathways, suggesting greater passivation of the core using the successive method (Table 2.5). The observed increase in the PLQY for **InP/ZnS (2)** is not therefore attributed to the higher zinc content, but rather to the thermally activated diffusion of the first ZnS layer to an equilibrium state which coats a larger amount of the surface of the core (Figure 2.17). This increased coverage provides greater passivation of the core against non-radiative decay pathways from holes and solvent quenching effects. If allowed to continually grow in a one step process (which is observed for QDs synthesised in both **InP/ZnS (1)/(3)**), the ZnS shell will not cover as much of the core as it promotes ZnS island formation rather than an even monolayer formation on the surface of InP cores. The high concentration of Zn(II) and S metal is therefor found to have less of an overall effect on the PLQY of the synthesised core/shell QDs.

2.5 Phase transfer of InP/ZnS

2.5.1 Aqueous phase transfer of InP/ZnS QDs.

The PLQY of **InP/ZnS (2)** has been shown to be enhanced to a value in excess of 80% when in organic solvents (hexane) when synthesised using a successive heating method. However, for **InP/ZnS (2)** to be used in biological imaging applications (such as biomedical imaging) then conservation of PLQY into aqueous phase is of great importance. Following the procedure outlined by Tamang *et al.*, a ligand exchange reaction can be used replacing hydrophobic ligands present on the surface of **InP/ZnS (2)** with a hydrophilic thiolic acid (figure 2.19).[181] A purified sample of **InP/ZnS (2)** QDs in chloroform underwent phase transfer into aqueous solution using 0.2 M thioglycolic acid (TGA) as the transfer ligand. The reaction is undertaken at an elevated pH (10.5) as to ensure the deprotonation of the thiolate within the TGA ligand as well as to drive the formation of **InP/ZnS (2) - TGA**. A pH of 10.5 is used due to the pK_a of the thiolate within the TGA ligand being 9.30 ± 0.1, therefore the elevated pH produces $-S^-$. The reaction is also carried out in the presence of Tris(2-carboxyethyl) phosphine (TCEP). TCEP is used to aid in the selective reduction of dithiol bonds. Phase transfer reactions were able to be carried out at room temperature in a time of 2 hours under vigorous stirring.

∿∿S = Thioglycolic acid (TGA)
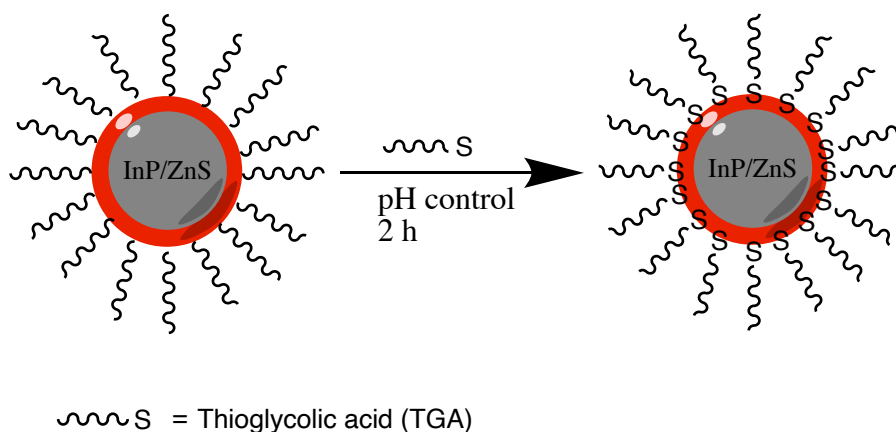
Figure 2.19 Cartoon image depicting phase transfer reaction, showing the addition of a thiol based capping ligand (TGA) to the surface of InP/ZnS QD.

Purification of **InP/ZnS (2) – TGA** QDs following phase transfer is complete *via* spin filtration techniques, this method allows for the removal of any unreacted reactants as well as the pH to be lowered to within a physiological range (7.4 – 7.8). **InP/ZnS (2)** QDs which have been synthesised using both In(III) halide precursors were able to undergo phase transfer reactions with both their physical and fluorescent properties being evaluated.

2.5.2 Physical properties of InP/ZnS - TGA QDs

Following the phase transfer of InP/ZnS QDs into aqueous solvent using 0.2 M TGA as a surface ligand, HRTEM techniques were used to analyse any changes to the size and shape of **InP/ZnS (2) – TGA** which were synthesised using both In(III) halides. A reduction in size of core/shell QD from the initial **InP/ZnS (2)** can be seen in both cased following the ligand exchange reaction. The **InP/ZnS (2)** size changes from 2.76 ± 0.37 nm to 2.52 ± 0.46 nm and 2.75 ±

0.45 to 2.63 ± 0.41 nm for **InP/ZnS (2)** synthesised with InI_3 and $InCl_3$

respectively (figure 2.20)
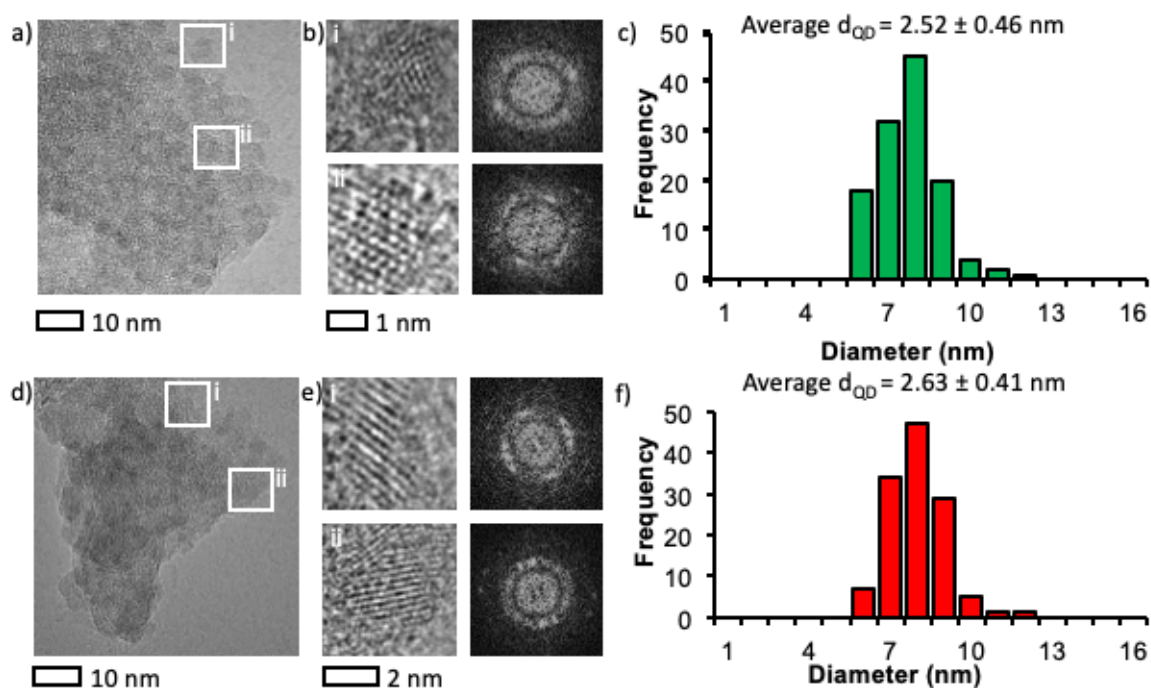
Figure 2.20. Physical properties of the InP/ZnS (2) - TGA QDs. (a-d) TEM images showing the InP/ZnS (2) – TGA (InI_3 and $InCl_3$ – top and bottom respectively) and (b-e), showing magnified images of two individual QDs (left) and the corresponding FFTs (right). (c-f) Size distribution of InP/ZnS (2) – TGA (InI_3 and $InCl_3$ – top and bottom respectively).

HRTEM images of **InP/ZnS (2) – TGA** (figure 2.20) also show a quasi-spherical

shape is maintained following the ligand exchange process on the surface of the

ZnS. However, the reduction in size observed is attributed to the removal of the

ZnS from the surface during the vigorous stirring procedure needed to form

InP/ZnS (2) – TGA QDs. Dynamic light scattering (DLS) is able to be used to

determine the hydrodynamic diameter (D_h) of **InP/ZnS – TGA** for both the

traditional and successive heating methods (table 2.6). What can be observed is an increase in size of D_h when moving from the traditional to the successive heating method once they have undergone a phase transfer reaction, with this increase being seen regardless of In(III) halide being used. D_h values can be seen in table 2.6 below.

	D_h (nm)	
QD	InI$_3$	InCl$_3$
InP/ZnS (1) – TGA	3.67	4.80
InP/ZnS (2) – TGA	4.73	5.81

Table 2.6. comparison of hydrodynamic diameter (D_h) values obtained for InP/ZnS – TGA capped QDs synthesised using both a traditional (1) and successive heating (2) synthetic method.

Following evaluation of both size and shape of **InP/ZnS (1)/(2)** - TGA capped QDs, it can be assumed that a loss of the ZnS secondary shelling material takes place during the phase transfer procedure due to the decrease in overall size of nanoparticles. To investigate this further, In:Zn ratios for **InP/ZnS (2)** QDs were compared to those of **InP/ZnS (2) – TGA** shown below in table 2.7 as well as the EDX spectroscopy being carried. EDX spectroscopy showed a drop in Zn(II) metal was present on the surface of the **InP/ZnS (2) – TGA** QDs following the ligand exchange reaction on the surface. A change within the In:Zn ratio can be seen in table 2.7 below.

QD	Indium halide	In:Zn Ratio	
		In(III)	Zn(II)
InP/ZnS (2)	InI$_3$	15.00 ± 0.13	85.00 ± 0.13
	InCl$_3$	26.51 ± 0.28	73.49 ±0.28
InP/ZnS (2) - TGA	InI$_3$	23.00 ± 0.06	77.00 ± 0.06
	InCl$_3$	40.00 ± 0.02	60.00 ± 0.02

Table 2.7. In:Zn ratio following the ligand exchange reaction on the surface of InP/ZnS (2) QDs.

The reduction in Zn(II) metal which can be seen on the surface following phase transfer reaction can be visualised using STEM imaging. STEM imaging allows for the surface of **InP/ZnS (2) - TGA** to be imaged and the metals which are present to be defined, this can then be compared with previous images of **InP/ZnS (2)** QDs in organic solvent. STEM images shown in figure 2.21 show a comparison between QDs synthesised using InI$_3$ precursors before and after phase transitions.
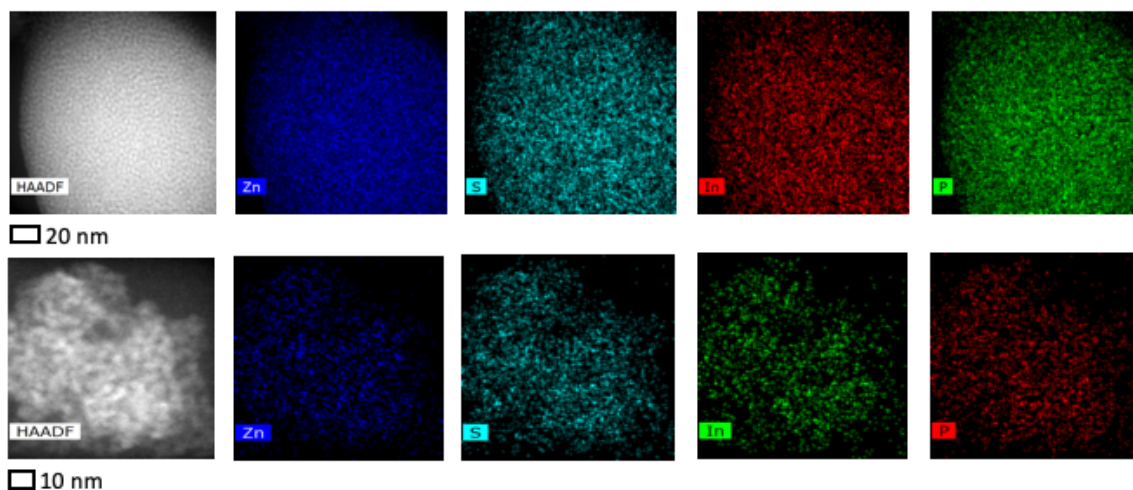
Figure 2.21. STEM images of InP/ZnS (2) QDs in hexane (top) compared to InP/ZnS (2) – TGA (bottom). InI$_3$ was used to illustrate the changes seen in metal composition.

As can be seen in figure 2.21, a reduction in the level of Zn(II) metal is present on the surface. This confirms what is observed in the In:Zn ratio obtained using EDX spectroscopy and shows when InP/ZnS QDs undergo a surface ligand exchange reaction with TGA a loss of Zn metal is observed from the surface of ZnS.

On the addition of a hydrophilic surface ligand (TGA) to the surface of the **InP/ZnS (1)/(2)** a negative surface charge is observed, indicated by the surface zeta potential. Zeta potential was recorded at a physiological pH (7.4 – 7.8) and the values observed can be seen below in table 2.8.

	Zeta (mV)	
QD	InI$_3$	InCl$_3$
InP/ZnS (1) - TGA	-23.96	-16.10
InP/ZnS (2) - TGA	-20.26	-25.30

Table 2.8 Zeta potentials observed for InP/ZnS (1)/(2) – TGA

The negative zeta potential observed in both methods are due to the de-protonation of the carboxylic acid proton at physiological pH (7.4 – 7.8). The pK$_a$ of the carboxylic proton is 3.83 , therefore a resultant negative charge is seen when **InP/ZnS –TGA** are capped QDs are in aqueous solution at physiological pH.[193] The high negative surface charge as well as the high binding affinity of the thiol to the surface of the InP/ZnS QDs results in a high colloidal stability in aqueous media.[181]

2.5.3 Fluorescent properties of InP/ZnS – TGA Capped Quantum Dots

As can be shown in earlier publications such as the one by Tamang *et al.*, phase transfer by way of surface ligand exchange reaction is commonly accompanied by a dramatic decrease in PLQY.[181] A major drawback if the intended use is to be within the biomedical imaging field is the lack of fluorescence intensity available following phase transfer into aqueous phase. Therefore, conservation of PLQY is of paramount importance following the surface ligand exchange reaction. As detailed in section 2.4.3, PLQYs of up to 85.3% were able to be achieved in organic solvents and thus must be conserved whilst being transferred into aqueous phase to allow InP based QDs which have

been synthesised to be a viable option within the field of biological imaging.

Following phase transfer of **InP/ZnS (2)**, PLQY of up to 57% were able to be

achieved in aqueous phase, with exact values being shown in table 2.9.

	PLQY	
QD	**InI_3**	**$InCl_3$**
InP/ZnS (1) - TGA	2.9%	20.0%
InP/ZnS (2) - TGA	19.2%	57.1%

Table 2.9. Exact values for PLQY after phase transfer reaction.

Phase transfer reactions were carried out using 0.2 M TGA as a capping ligand

for aqueous phase transfer, a large proportion of the PLQY is able to be

maintained within **InP/ZnS (2)** QDs for both samples regardless of indium

halide used. As can be seen in table 2.9 PLQY values of up to 57.1% in water are

able to be achieved, this is the highest PLQY value achieved to date following

phase transfer of QDs synthesised using InP. Following the surface ligand

exchange the excitation and emission properties of the **InP/ZnS – TGA** QDs

were evaluated and compared to those obtained spectra for the **InP/ZnS**

(1)/(2) in hexane. Firstly, using 3D excitation/emission spectra, the broad

excitation ranges of **InP/ZnS – TGA** QDs is able to be shown following the phase

transfer into aqueous phase *(*figure 2.22*).*
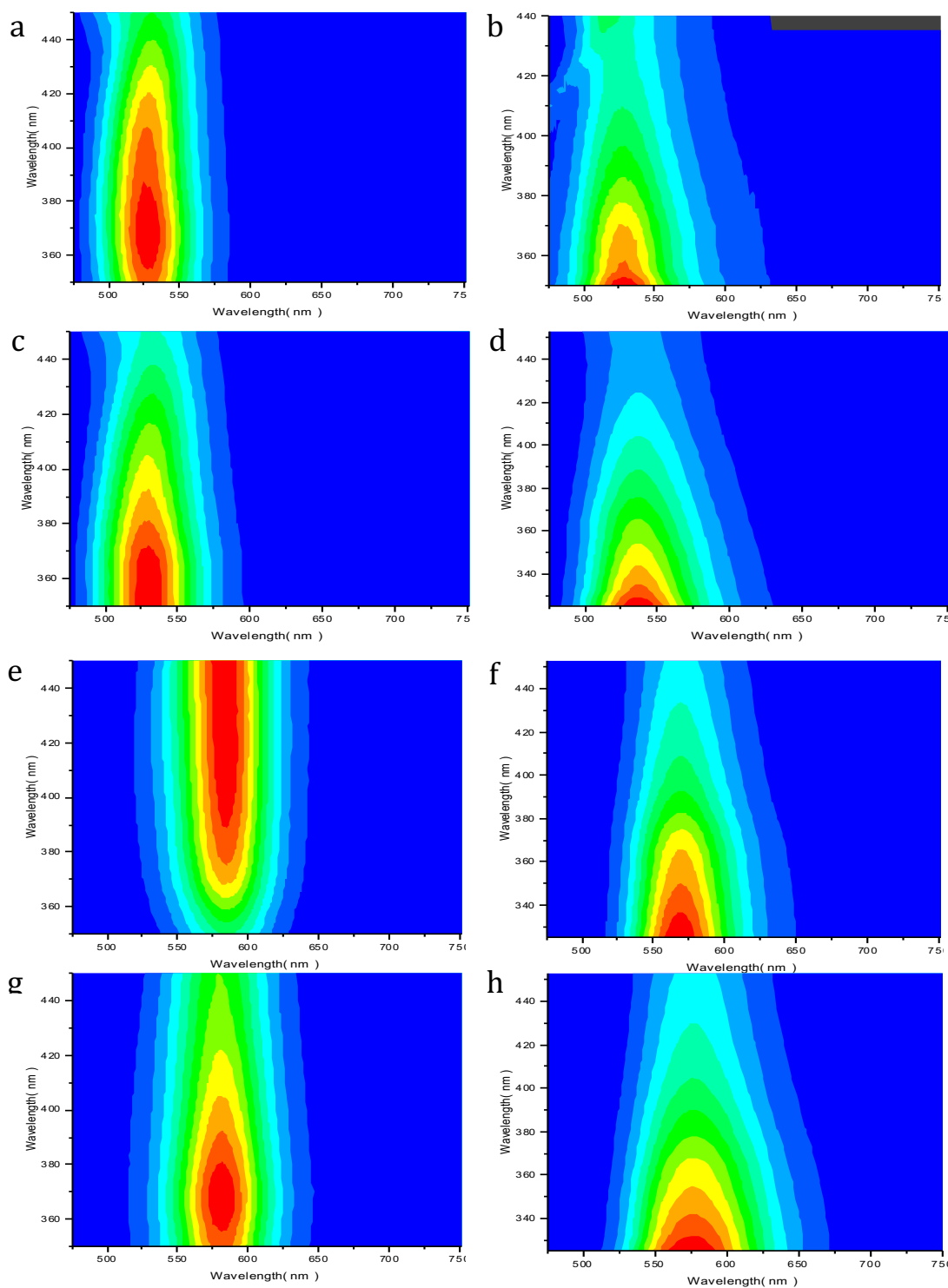
Figure 2.22. 3D excitation/emission spectra showing the comparison between InP/ZnS (1/2) QDs in both hexane (left column) and water (right column) following TGA capping. a-d QDs synthesised with InI_3, e-h QDs synthesised with

InCl$_3$. Images a b,e,f are of InP/ZnS (1) whereas images c,d,g,h are of InP/ZnS (2) QDs

One noticeable difference can be seen within the FWHM of the emission spectra following phase transition. A larger FWHM can be observed in **InP/ZnS – TGA** QDs than is observed for InP/ZnS in organic solvent, an increase of 7-10 nm is observed alluding to a greater dispersity in particle size following the phase transfer into aqueous phase. This is accompanied by a decrease in excitation wavelength which can be seen in all of the examples shown.

QD	PLQY	Lifetime (ns) Decay component	
		1	2
InP/ZnS (1) - TGA	20.0%	15.32 52.8%	1.413 47.2%
InP/ZnS (2) - TGA	57.1%	17.62 72.4%	0.708 27.6%

Table 2.10. PLQY and lifetime decay values for InP/ZnS (1/2) for QDs synthesised using InCl$_3$.

Following phase transfer, lifetime measurements showed the addition of a further decay component when compared to QDs with only one decay component when in organic solvents. The two component systems which are observed for QDs following phase transfer can be seen to have both fast and slow components (Table 2.10). This can be shown using InP/ZnS QDs synthesised using InCl$_3$ in both a traditional and successive heating methods before undergoing phase transfer. The lifetimes of both **InP/ZnS (1/2)** are shown to be ca 15-17 ns, however there is a stark charge in the percentage of

decay observed through the fast and slow components. This difference in decay

channels between the fast and slow ultimately results to a larger PLQY being

maintained for QDs synthesised using a successive heating method as opposed

to a tradition synthetic method. The ability to maintain the PLQY (values of

57%) opens doors for InP based QDs to be used in the form as a fluorescent

scaffold in the development of a dual modal imaging probe with uses in

biomedical imaging.

Chapter 3: Design and synthesis of a multimodal OI/MRI contrast agent

3.1 Introduction

Dual-modal diagnostics within the clinical field have evolved over the last 20 years since the first reported use of a PET/CT instrument following its developed by Townsend and coworkers.[105] In theory, the combination of two or more imaging modalities should see the offsetting of the inherent limitations which are observed when using a single imaging technique as a stand-alone method. The resulting higher quality image has ultimately led to improved patient care. The use of optical imaging (OI) has recently become more prevalent within the clinical setting, mainly used for the localisation of tumours and metastases as well as the monitoring of disease progression or regression. However, within research its ability to be able to offer real time information of interactions between light and tissue results in OI being used in a wide range of *in vitro* and *in vivo* applications.[113] One of these being the increased use within image guided surgical applications.[194] Furthermore, the use of OI probes including but not limited to quantum dots, organic dyes and fluorescent proteins allows for the overcoming of intrinsic drawbacks observed within other imaging modalities whilst improving detection sensitivity and accuracy which OI probes lack on combination with other commonly used modalities.[119,121,128,143,158,195,196]

The combining of OI alongside MRI offsetting both modalities limitations, produces a technique which has the ability to produce an image capable of providing anatomical information for use within diagnostics (pre-treatment scans/imaging of disease states). As well as being able to provide real-time information for techniques such as image guided surgery applications, which MRI alone is unable to provide. The complimentary pairing of MRI and OI is detailed below in section 3.1.1.

3.1.1 OI/MRI Multi-modal Imaging

Kinetically inert gadolinium(III) complexes based on Gd-DOTA are used throughout the clinical environment (due to their lack of activity and thus stability within the body); However, as already discussed (section 1.3), the inherent problems with relatively low sensitivity associated with MR imaging has resulted in the use of OI combined with MR to form a range of dual modal imaging probes. Gau *et al.* used this principle of attaching a Gd(III) chelate in the form of Gd-DTPA to an organic fluorophore to form a relatively simple OI/MR probe.[197] This work resulted in the formation of near infrared-Gd(III) dual modal probe (LS-479-Gd(III)) (figure 3.1) which was designed to allow the use of MRI specific properties whilst also using the targeting properties of LS479 to specifically target Human Serum Albium (HSA). LS479 was shown to have a relaxativity of 15 mM^{-1}s^{-1}, which was shown to be an improvement from Magnevist™ (3.9 mM^{-1}s^{-1}). This is attributed to the increasing of inner sphere hydration state (q=2) and large complex size of LS479.
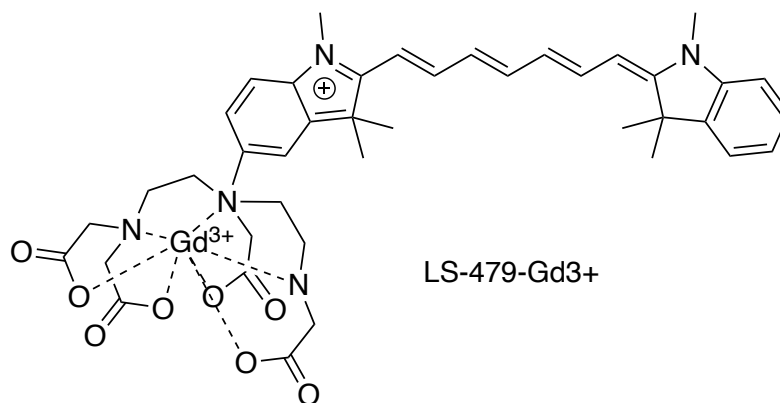
LS-479-Gd3+

Figure 3.1 Image of LS-479-Gd(III) shown with both Gd(III)-DTPA and targeting group LS-479 which have been combined to form a dual modal MR/OF imaging probe.

Yamana *et al.* also looked to combine a Gd(III)-DOTA derivative with an OI reporting group in a 1:1 ratio.[198] The work presented by Yamana and team used highly hydrophobic OI reporting groups (BDP, CY-7) in order to allow the complexes to migrate into the cell, thus achieving a multi-modal probe capable of achieving non-specific cell labelling. However, a major problem with the dual modal probes presented in the work by both Gau and Yamana was the use of the 1:1 ratio of MRI chelates to OI reporter results in a large offset in sensitivity between the two imaging modalities being used. This is due to the low concentration of Gd(III) chelate present within the designed dual modal probes when used in a 1:1 ratio with an OI reporter.

3.1.2 Design of multimeric OI/MRI agents

To alleviate the problems associated with the offset in sensitivity observed when combining OI/MRI in a 1:1 ratio, the design and use of multimeric contrast agents have been on the increase. Harrison *et al.* was able to increase the ratio of Gd(III) chelate to near-infrared (NIF) reporters to 3:1, with relaxivity values of up to 17.5 mM^{-1}s^{-1} (52.5 mM^{-1}s^{-1} molecular, 60 MHz) being achieved.[103] As previously discussed, the addition of a specific organic dye (IR-783) orchestrated the cell uptake through organic-anion transporting polypeptides (OATPs), however, only the fluorescent properties can be seen following cellular uptake. This showed that a greater ratio that 3:1 in favour of Gd(III) is needed when designing an OI/MR dual modal probe. As a more significant amount of Gd(III) derivative is required in order to observe a MR signal, a shift from small molecules can be seen when looking at the development of other OI/MR probes. Hu *et al.* were able to increase the longitudinal relaxation time (T_1) and relaxivity (r_1) by a factor of 1.6 times to a value of 7.1 mM^{-1}s^{-1} when compared to conventional Gd-DOTA derivatives.[96] The increase in r_1 value was observed due to the use of large molecule (ca 8 nm) which was able to be formed following a self-assembly system, allowing for a star like polymer. The star-like shape was formed with a porphyrin core, Gd(III) chelates seen at the outer extremities, with the addition of a 42-unit PEG chain to aid in the solubilisation when in water (figure 3.2).
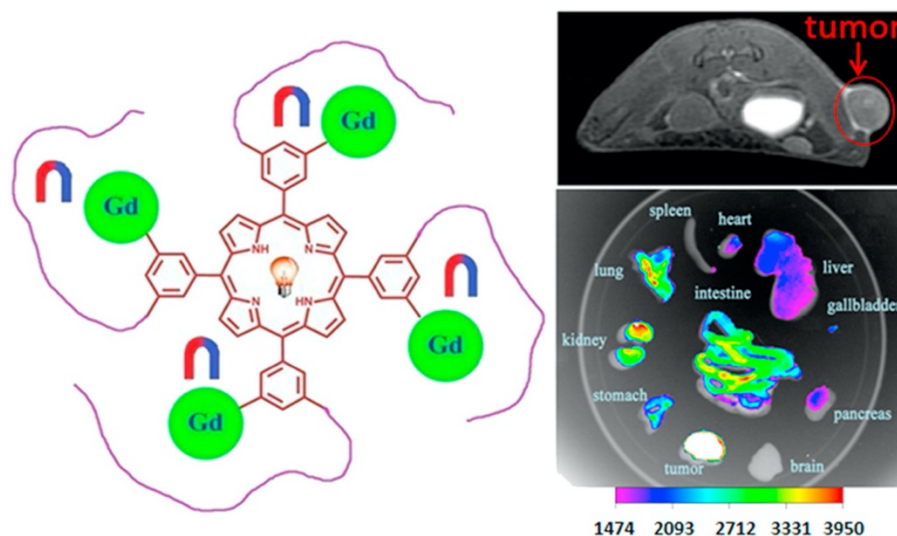
Figure 3.2. Hu star like polymer design (left), MR imaging capability (top right) 60-minute post inject as well as the NIR imaging signal intensity from organs following sacrifice of animals used (bottom right).[96]

The dual modal probe developed by Hu showed both MR and NIR imaging capabilities following *in vivo* studies on nude mice, both modalities within the probe were able to be used to detect the tumour boundary 60 minutes post injection (figure 3.2). The success of large molecule systems with a greater ratio of MR to OI probes gave the green light for further development of increased ratio imaging agents.

3.1.3 Nanoparticle modification in the design of OI/MR dual modal probes

The use of large molecules to increase signal to noise ratio has seen the rise of the use of nanoparticles in the development of OI/MR when looking to develop new dual-modal contrast agents. The ability to use a large nanoparticle which has the potential to be loaded with a large amount of Gd(III) contrast

agent see the possibility to increase relaxation value ratios. Zhu *et al.* made

great use of mesoporous silica nanoparticles (MSNs) as a scaffold to build a

NIR/MR probe which was capable of very good biocompatibility as well as

excellent retention times within the cells.[199] The high biocompatibility of the

Gd/NIR-MSNs opened the door for their use within the bio-imaging field, this

combined with an improved r_1 value of 14.54 mM^{-1}s^{-1} led to the *in vivo* testing of

the probe. The *in vivo* testing was carried out on a U87-MG glioblastoma tumour

rodent model and showed that after 4 hours post injection both a MR and NIR

contrast image was able to be taken; However, the NIR signal continued to grow

exponentially until the last image was taken at 48 hours post injection which

suggests poor clearance out of the animal model (figure 3.3).
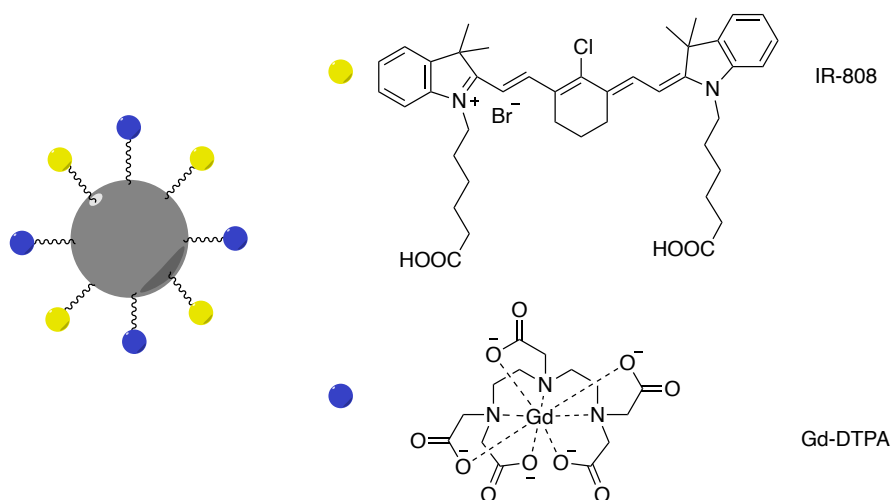
Figure 3.3. Mesoporous silica nanoparticles capped with both IR-808 (yellow) and
Gd(DTPA) (blue) to form a high biocompatible NIR/MR probe.

The modification of nanomaterials such as iron oxide nanoparticles has also

been widely investigated as a method for developing a OI/MR imaging probe.

The use of super paramagnetic iron oxide nanoparticles (SPIONs) can be seen to

be used in the literature when forming a T_2 weighted chelating agent.[200] The

surface modification of SPOINs has been used by Chen *et al.* and utilise the

surface modification of SPOINs with a tumour targeting peptide (RDG) as well

as a fluorescent modality (ICG) to form SPIO-Liposome-ICG-RGD.[201]

Remarkably, SPIO-Liposome-ICG-RGD was able to demonstrate its uses in pre-

operative diagnosis and intraoperative resection guidance when used in a

mouse model.[201] The T_2 weighted MR modality as well as the long clearance rate

of the compound allowed for the fluorescent imaging to take place, this resulted

in Chen's team being able to preoperatively diagnose and image tumours of

sizes smaller than 1 mm in a mouse model at a time point of 72 h post injection.

Core/shell nanoparticles such as those used by Stasiuk *et al.* in 2011

showed a different method for the design of a OI/MR contrast agent.[156] Within

this work the team utilise the use of non-toxic InP based QDs as a scaffold for

functionalisation as well as their optical properties. The functionalisation of InP

QDs with a Gd(III) contrast agent allows for a MR/OF imaging agent which has a

OF signal whilst also carrying a large payload of Gd(III) chelate (figure 3.4)
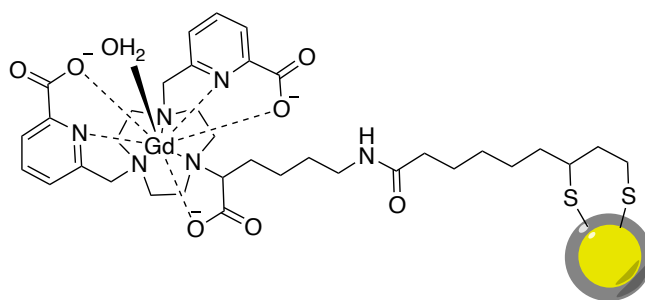
figure 3.4. Image showing InP/ZnS quantum dots loaded with a gadolinium

chelating NOTA derivative with a hydration number of q = 1.

The resultant MR/OI probe which is produced following functionalisation of InP with Gd(III) chelates shows a high relaxivity per nanoparticle (900 mM^{-1}s^{-1}), this large relaxivity value per nanoparticle is enabled by the high volume of up to 80 chelates per InP QD, each with a relaxivity value of ca 13 mM^{-1}s^{-1} per Gd(III) ion. This work presented by Stasiuk is built upon within this results chapter to allow for an OI/MR dual-modal imaging probe to be developed by the functionalisation of a non-toxic InP/ZnS core/shell QD (synthesis and characterisation in chapter 2 above) with a derivative of a Gd(III) MR chelating agent, thus, forming a multimeric OI/MR dual-modal imaging agent (figure 3.5).
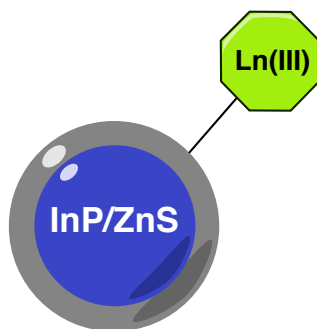
Figure 3.5 A cartoon image of the aim multimodal OI/MRI imaging agent design, derived from the surface functionalisation of InP/ZnS core/shell QDs with small molecule Gd(III) MR chelating agents.

3.2 Design and synthesis of gadolinium(III) chelate thiol derivatives

Scheme 3.1 Formation of small molecule MR chelating agent.

3.2.1 Formation of ethyl 6-benzamido-2-bromohexanoate side arm (2)

The synthesis of ethyl 6-benzamido-2-bromohexanoate **(2)** was

completed *via* a two-step process as opposed to the traditional three step

process which was previously reported by Stasiuk *et al.*[156] Within the work

previously reported, **(2)** is formed first by the protection of the terminal amine

group with a benzyl protection group as shown in scheme 3.1. However, when

using the method previously reported by Stasiuk, the bromination of the α-

carbon to the carboxylic acid group has to be complete before the protection of

the carboxylic acid group can take place, resulting in a 3-step process. The

methods presented within this work use a two-step method, with the α-carbon

bromination occurring alongside the protection of the carboxylic acid in a one-

step methodology.
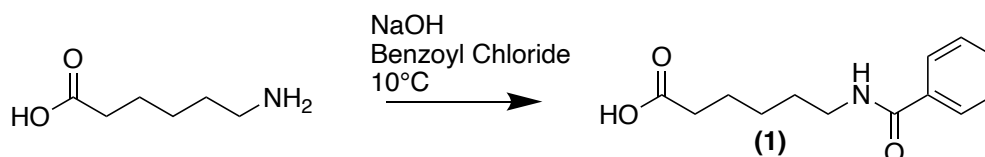
Scheme 3.2. Protection of the terminal amine group with benzoyl chloride
forming product **(1)**.

First, **(1)** was prepared by the protection of the terminal amine group on

6-aminobenzanoic acid with benzoyl chloride in the presence of sodium

hydroxide (NaOH). **(1)** was precipitated out of the reaction solution by the

gradual addition of 2 M HCl. On acidification, **(1)** protonates at a pH (ca.3.5) at

the carboxylic acid region due to the carboxylic acid proton having a *pKa* of

4.43, driving the reaction to a greater production yield. **(1)** was able to be

formed at a 63% yield which is in line with literature previously reported

(68%).[156] The ESMS+ showed a peak at *m/z* 236.2 [M+H]+ giving a good

indication for the formation of the product. ^{1}H-NMR spectroscopy confirmed

the addition of the benzyl protecting group with the appearance of peaks in the

aromatic region of the spectrum integrating to a value of 5 H.

The bromination of **(1)** at the α-carbon to the carboxylic acid is required

for the formation of **(2)** followed by the protection of the carboxylic acid with

an ethyl protecting group. Scheme 3.3 below shows the reaction for the two-

step process which was followed in order to form **(2)**.
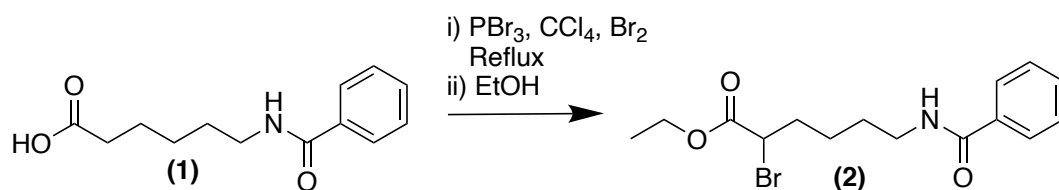
Scheme 3.3 Bromination at the α-carbon position of **(2)** complete in a one-step
process.

(2) was successfully synthesised as a brown oil with a yield of 25%, following

the successive bromination and ethyl protection of carboxylic acid within **(1)**.

The ESMS+ showed the presence of **(2)** with a m/z peak at 344.2 [M+H]+ with

the characteristic 1:1 bromine isotope pattern following its addition at the α-

position. The ^{1}H-NMR spectrum confirmed the formation of **(2)** with the

addition of peaks at 4.13 - 4.08 m (1H) showing the presence of a single

hydrogen at the α-position after the addition of the bromine. ^{1}H-NMR

spectroscopic data also shows peaks for C**H**2-CH3 of the ethyl protecting group

with a chemical shift of 4.26 – 4.16 (m, 2H) confirming the protection of the

carboxylic acid functional group. The Hell-Volhard-Zelinsky reaction is used to

convert carboxylic acids into an α-halo carboxylic acid using a phosphorous

catalyst and nucleophile when in the presence of a halogen (Scheme 3.4), an

acyl bromide is formed using catalytic amounts of PBr3, thus allowing for the

formation of the enol form of **(1)**.
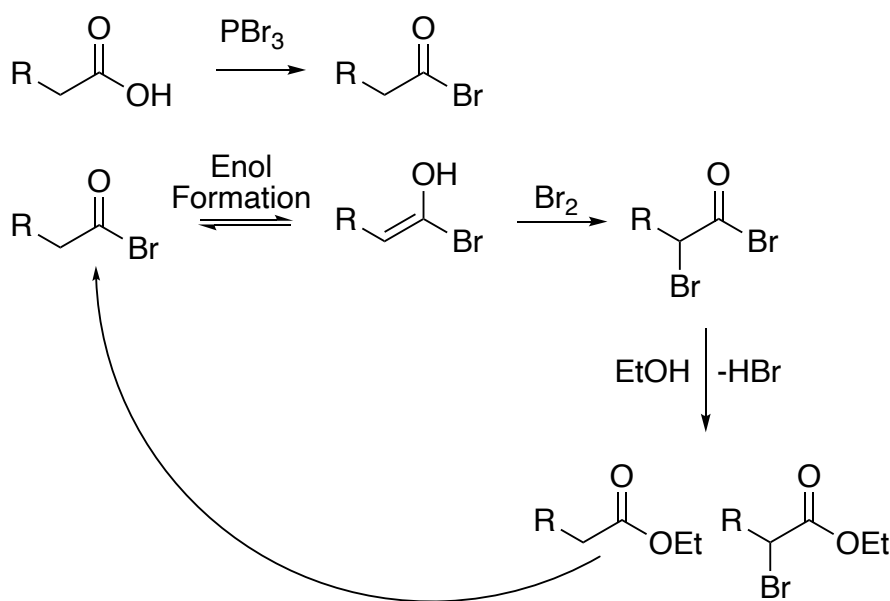
Scheme 3.4. Hell-Volhard-Zelinsky reaction depicting the bromination of the α-
carbon position

Bromination at the α-position is then possible. Once bromination at the α-

hydrogen is complete a nucleophilic addition reaction is utilised to protect the

carboxylic acid group. In the traditional synthesis used by Stasiuk *et al.*, water

was added as the nucleophile to protonate the carboxylic acid group, however,

here ethanol is used as the nucleophile and as a result can drive the protection

of the carboxylate group with an ethyl protecting group. Following the

protection of the carboxylic acid, the removal of HBr results in the formation of

the ethyl protected α-halo carboxylic acid **(2)**.

3.2.2 Formation of tri-tert-butyl 2,2',2''-(10-(6-benzamido-1-ethoxy-1-oxohexan-2-yl)-1,4,7,10-tetraazacyclododecane-1,4,7-triyl)triacetate (3)

The formation of pro-ligand **(3)** (Scheme 3.5) was formed successfully

by the addition of **(2)** to a previously synthesised precursor of TbutylDO3A.HBr

salt, this precursor is formed following work previously published by Jagadish

et al.[202]
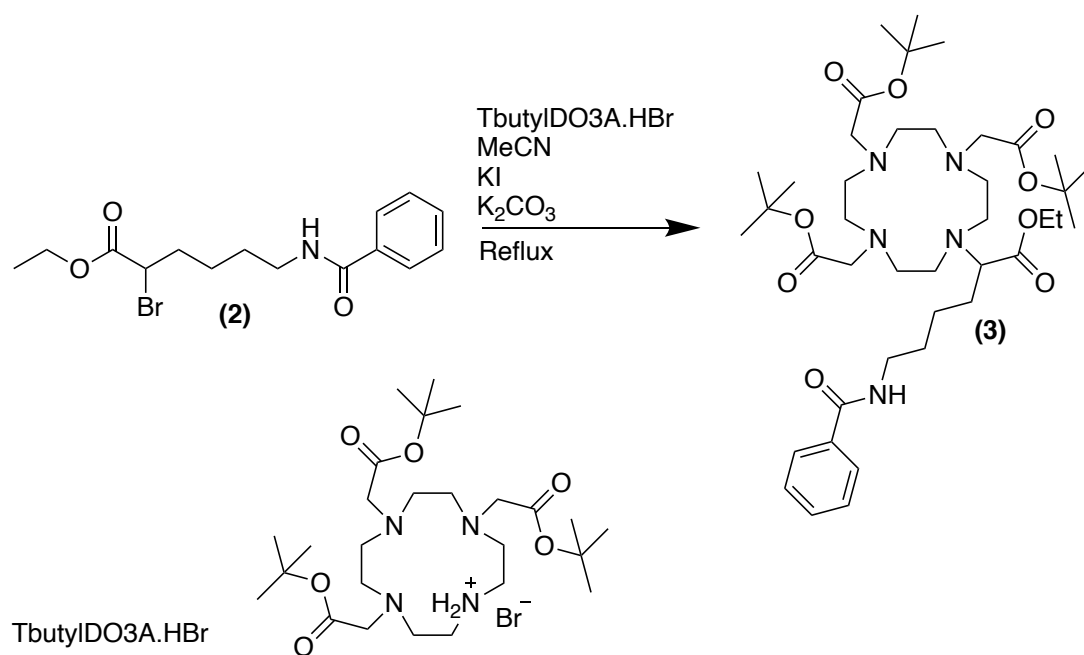
Scheme 3.5 Synthesis of pro-ligand **(3)**.

Initially, **(2)** was stirred in acetonitrile (MeCN) for 1 hour with KI,

resulting in the halogen exchange of Br with I, instilling a better leaving group

within **(2)** for the addition of **(2)** with TbutylDO3A.HBr. Following this **(2)** was

added to a solution of TbutylDO3A.HBr and K_2CO_3 in MeCN and the reaction
was heated at reflux for 18 hours. Within the reaction, **(2)** and TbutylDO3A.HBr
salt were reacted in a 1:1.1 ratio as to try to increase overall reaction yield. On
the completion of the reaction ESMS$^+$ showed peaks present for both **(3)** at
776.2 m/z as well as unreacted TbutylDO3A.HBr at *m/z* of 515.5. ^{1}H-NMR
spectroscopy of crude **(3)** also confirmed the presence of a large amount of
unreacted TbutylDO3A.HBr salt present due to the Tbutyl singlet peak at
chemical shift 1.45 not integrating correctly to 27 H when integrated against the
aromatic peaks from the benzyl ring. Purification of **(3)** was complete *via* a two-
step process. Initially, the majority of unreacted TbutylDO3A.HBr salt present in
crude **(3)** was removed using silica column chromatography with gradient
elution DCM:MeOH (100 : 0 – 95 : 5). Following this, semi purified **(3)** was
dissolved in minimal amounts of MeCN followed by excess diethyl ether, this
allowed for the precipitation of any remaining unreacted TbutylDO3A.HBr
whilst **(3)** remained in solution. Pure **(3)** was attained in a yield of 9.9% and
confirmed following observation of a large Tbutyl singlet peak at 1.45 (s, 27H)
with no excess Tbutyl-DO3A present. High resolution mass spectroscopy
(HRMS) showed a peak at *m/z* 776.5168 [M+H]$^+$ for **(3)** (calculated m/z value =
775.5095) with no peak present for TbutylDO3A.HBr confirming the synthesis
of pure **(3)**.

3.2.3 Formation of amine chelate ligand derivative (4)
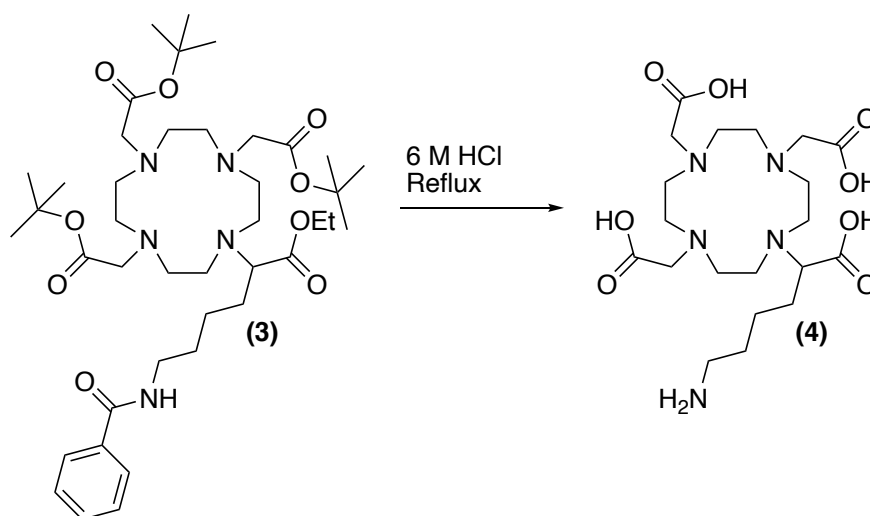
Scheme 3.6 Deprotection of all protection groups using 6 M HCl prior to form **(4)**.

The amine chelate derivative **(4)** was synthesised by the acid hydrolysis of **(3)** using 6 M HCl. This method of deprotection was used as there is no need for the selective de-protection with the functional groups present. Instead a one-step deprotection is able to be used. The synthesis of **(4)** was confirmed using both mass spectrometric and NMR spectroscopic methods. Within the HRMS+ a m/z peak of 476.2715 [M+H]+ (calculated m/z value = 475.2642) is observed indicating the deprotonation of protected pro-ligand forming **(4)**. Confirmation of **(4)** *via* 1H NMR spectroscopy was evident via absence of the singlet hydrogen peak observed at chemical shift 1.45 indicating all Tbutyl peaks have been removed, furthermore, absence of the aromatic peaks with the removal of the benzyl protective group following deprotection is seen within the 1H NMR spectrum. Purification of **(4)** was complete with diethyl ether washing resulting in a 93% yield of pure product **(4)**.

3.2.4 Lanthanide amine chelate preparation (Ln.5)

All lanthanide complexes were synthesised using the same synthetic

method to form **Ln.5**, with respect to the lanthanide used within the synthetic

reaction. The three lanthanides chosen to be used to form chelates with the

synthesised pro-ligand **(4)** were gadolinium, terbium and europium, as this

allows for the full physical evaluation (T_1 and luminescence) of the newly

formed chelates **(Ln.5)**. **(Ln.5)** was synthesised by stirring **(4)** overnight with

$LnCl_3.6H_2O$ in water with the pH of the solution adjusted between the range 5.5

– 6. To ensure the complexation of Ln(III) metal into the co-ordination sites

present within ligand **(4)** it is essential that the reaction is carried out in this pH

range . This is to drive both the complexation of the lanthanide into the ligand

(to be complete at a pH of above 4) whilst also avoiding the formation of any

lanthanide hydroxides within the reaction which are liable to form at pH >

6.5.[156]
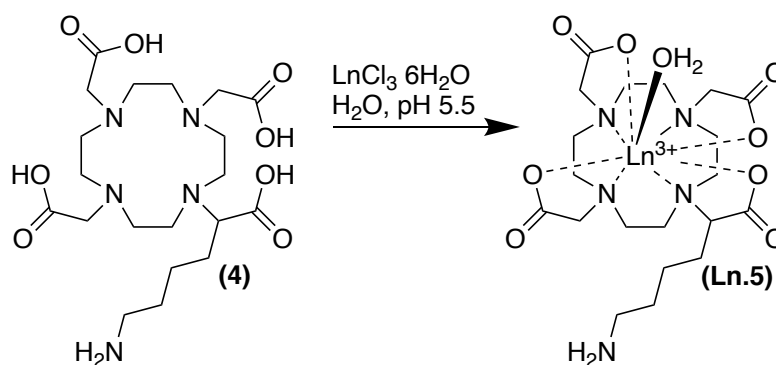
Scheme 3.7 Lanthanide complexation of pro-ligand **(4)** with $LnCl_3.6H_2O$ to form

(**Ln.5**) where Ln^{3+} = Gd, Tb, Eu

Following the completion of the complexation reaction, removal of unreacted lanthanide metal was undertaken by raising the pH to a value in excess of 7.5. The elevated basic pH is used to drive the formation of lanthanide hydroxide salts within the reaction solution, allowing for the removal of any uncoordinated lanthanide from the reaction. Following the formation of hydroxides, the reaction solution was centrifuged at 10000 rpm forming a pellet with Ln.5 remaining in the supernatant. Ln.5 solutions were then filtered and brought back to a neutral pH of ca 6.5 before undergoing a test for any free metal. Xylenol orange at pH 5.5 in sodium acetate buffer in a 1:1 ratio followed by dilution in excess water was used to detect the presence of any un-complexed lanthanide metal within the solution. If the solution remained yellow/orange then no free lanthanide remained in solution. Before moving forward to characterisation, a solution with no free metal was required.

3.3 Lanthanide chelate characterisation.

On the formation of **Ln.5**, the lanthanide metal is expected to adopt an 8-coordinate geometry within the chelated complex.[81] This is expected due to the 4 nitrogen atoms within the backbone of the cyclen ring as well as the 4 oxygen donor atoms available within deprotonated carboxylic acid groups which are available at a complexation pH of 5.5 (3 within the DO3A structure and 1 from the pendant arm carboxylate group). In aqueous solution, lanthanides will adopt a Ln(III) configuration, with both 8 and 9 CN being observed across the period (due to lanthanide contraction). In the cases of Gd(III), Eu(III) and Tb(III), all will be expected to form 9-coordinate complexes when in aqueous solution.[151] This therefore, will result in lanthanide complexes being formed which have one coordination site available for water binding to the metal centre. This in theory will give hydration states (q) of lanthanide chelates equal to 1, with the terminal amine within the pendant arm not playing a role in the metal binding into the binding pocket of the cyclen backbone.[81] On binding of the Ln(III) metal centre to form a metal complex, an overall negative charge (-1) is observed, as a result of the 4 negatively charged carboxylate arms present in the ligand.

3.3.1 Characterisation of Eu.5

Eu.5 was readily synthesised from **(4)** and $EuCl_3.6H_2O$ giving a white solid in a 70% yield. Eu.5 amine chelate derivative is shown to have formed using HRMS, with an m/z peak of 626.1772 [M+2H]$^+$ (calculated m/z value =

624.1525), whilst having a characteristic europium splitting pattern. Within the HRMS an m/z peak corresponding to a compound, two mass units heavier was observed due to the overall charge on the chelate (-1). Therefore, two protons are needed to give an overall positive (+1) charge resulting in the addition of two mass units. In order to determine an experimental value for q, fluorescent lifetimes were measured in conjunction with the photoluminescent properties of **Eu.5**, in both water and deuterium oxide.
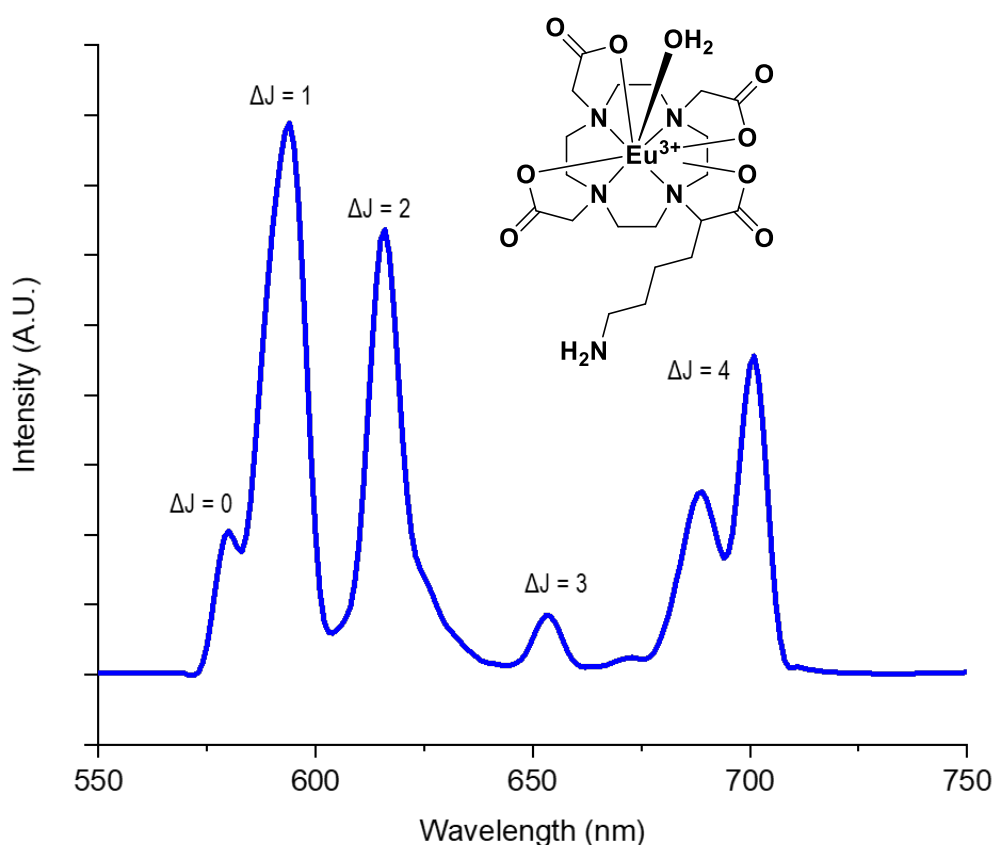
Figure 3.6 Emission spectrum of Eu.5 (λ_{ex} = 395 nm, 298 k, pH 7, H_2O)

The emission spectrum shown in figure 3.6 was obtained at a λ_{ex} = 395 nm to correlate with the pseudo direct excitation of the Eu(III) metal centre. The emission spectrum clearly shows that the **Eu.5** chelate complex is present, this

can be seen by the visibility of the $^5D_0 - {}^7F_J$ transitions (labelled in figure),

characteristic of a q = 1 complex. The pseudo direct excitation of **Eu.5** at a

wavelength of λ_{ex} = 395 nm was the only wavelength able to be used for

excitation, this is due to **Eu.5** not having any available antenna present within

the Ln.5 complex (figure 3.6 inset). The lifetime studies which were carried out

on **Eu.5** record the intensity of the ΔJ = 1 transition at λ_{em} = 595 nm with an λ_{ex} =

395 nm to determine the rate constants (k) in D_2O and H_2O.

Figure 3.7 Excited state life time studies for Eu.5 at 298 K, λ_{ex} = 395 nm, λ_{em} = 595 nm, pH 7. Blue = H_2O, Black = D_2O.

The data shown in figure 3.7 can be used to determine rate constants for **Eu.5**,

thus determine a value for q. The rate constant for decay rate of H_2O is seen to

be faster than that of D_2O (table 3.1), this is due to the O-H oscillators quenching

the Eu(III) ion more efficiently than O-D oscillators.[154] **Eu.5** is shown to have a q

= 1.1, this therefore correlates to a complex which has an 8 co-ordinate

geometry due to only one water molecule being able to bind to the metal centre.

Complex	λ_{ex} / nm	λ_{em} / nm	k_{H2O} / ms^{-1}	k_{D2O} / ms^{-1}	q (± 0.2)
Eu.5	395	595	1.612	0.482	1.1
Tb.5	377	545	0.506	0.297	0.7

Table 3.1 Depicting constants, k, for depopulation of the excited states as well as q, hydration state of Eu.5 and Tb.5

3.3.2 Characterisation of Tb.5

Tb.5 was prepared using **(4)** and $TbCl_3.6H_2O$ to give a white solid (77%

yield). HRMS showed an m/z peak for Tb.5 at 632.1734 [M+2H]+ (calculated

m/z value = 630.1566) , m/z value is again 2 mass units above were **Tb.5** was

expected to be seen due to the charges associated with the binding of the

negative carboxylate groups. As for **Eu.5**, the coordination geometry for **Tb.5**

was expected to be 8 thus giving q = 1. The luminescent properties and

hydration state (q) were evaluated for the **Tb.5** complex using lifetime and

photoluminescent measurements.
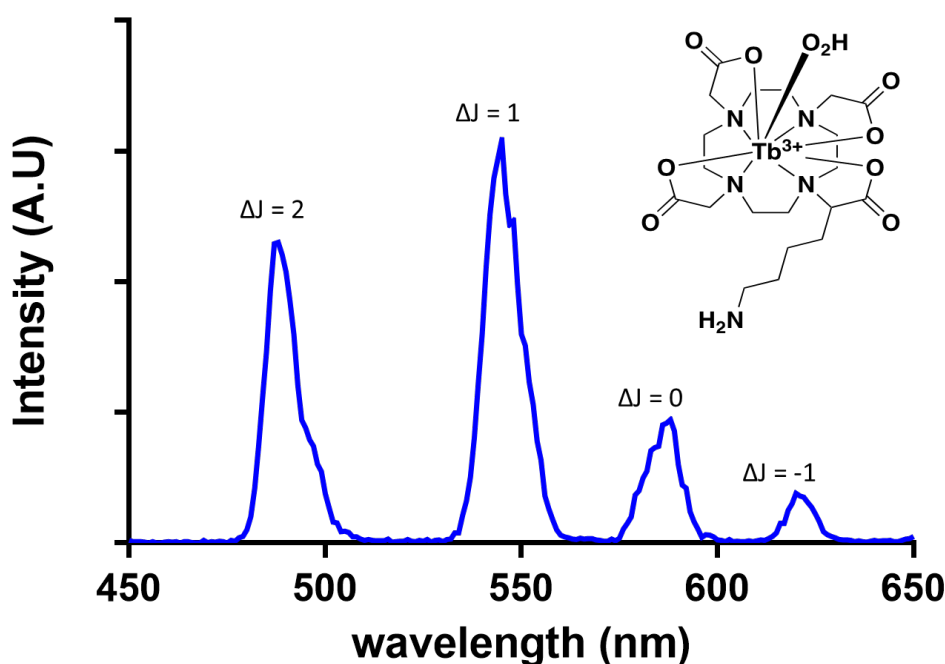
Figure 3.8 Emission spectrum of Tb.5 (λ_{ex} = 377 nm, 298 k, pH 7, H_2O)

The emission spectrum shown in figure 3.8 was obtained at a λ_{ex} = 377 nm with the spectrum shown that of an expected of a complex which contains Tb(III) metal. This is due to the $^5D_4 - {}^7F_J$ transitions which are clearly able to be seen within the spectra (labelled in figure 3.8). The excitation spectrum recorded for Tb.5 record the intensity of the ΔJ = 1 ($^5D_4 - {}^7F_5$) transition at an λ_{em} = 545 nm. The excitation spectrum shows one strong peak at λ_{ex} = 377 nm indicative of the pseudo direct excitation of the Tb(III) metal centre. Photoluminescent lifetime studies follow the ΔJ = 1 transition at λ_{em} = 545 nm with the use of an λ_{ex} = 377 nm. The decay curves for **Tb.5** in both H_2O and D_2O can be seen below in figure 3.9, with the rate constants being displayed in table 3.1.
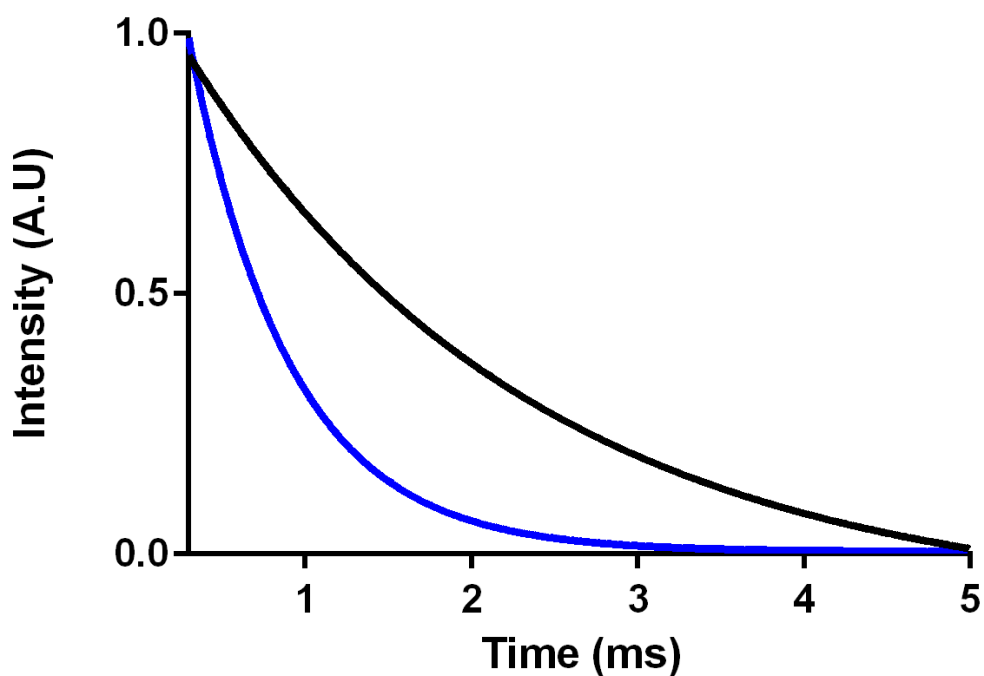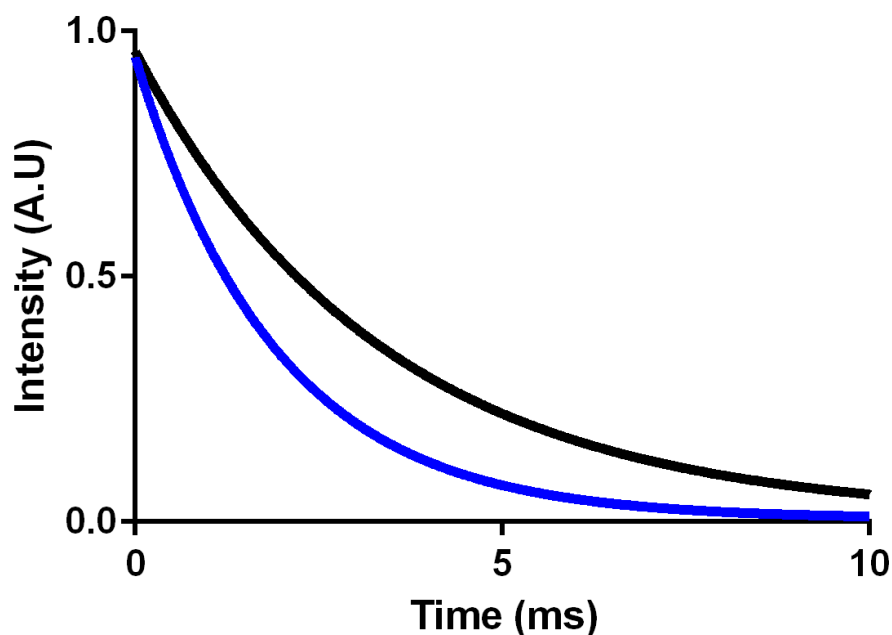
Figure 3.9 Excited state lifetime decay curves for Tb.5 at 298 K, λ_{ex} = 377 nm, λ_{em} = 545 nm, pH 7. Blue = H_2O, Black = D_2O.

A point of interest within the decay constants of **Tb.5** when compared to the Eu analogue is that the rate constants for **Tb.5** are considerably larger in time than that of **Eu.5** (values shown in table 3.1). This is attributed to the less efficient quenching of O-H oscillators in the **Tb.5** complex due to overlap of the less populated v = 5 vibrational levels of water within the $^5D_4$ excited state of Tb(III). This however, is not observed within the **Eu.5** complex. The use of determined rate constants for **Tb.5** show a q = 0.7. Due to **Tb.5** and **Eu.5** analogues both having q = 1, a high level of confidence is able to be used when determining that the **Gd.5** complex will also have 1 water molecule bound directly to the metal centre. This determination of Gd.5 having 1 water molecule bound directly to

the metal centre therefore allows comparisons to be drawn with other chelates in the field where $q = 1$.

3.3.3 Characterisation of Gd.5 amine.

^{1}H-NMR spectroscopy of **Gd.5** in H_2O in a capillary tube surrounded by D_2O is able to show that water is bound directly to the metal centre as expected ($q = 1$), as two peaks are visible within the ^{1}H-NMR spectroscopy (figure 3.10). The two peaks which are visible within the spectrum represent both bound (H_2O) and residual water molecules (present within D_2O) within the vicinity of the Gd(III) metal centre, with the separation between them being proportional to the concentration of Gd(III) chelate within solution. The Evans method was used for T_1 relaxation studies due to the low volumes of solution being used.[203] As can be seen in figure 3.10 when using the Evans method for calculating T_1 relaxation of Gd(III) contrast agents, a clear separation of bound to unbound water was able to be obtained when using a 2 mmol **Gd.5** amine solution.
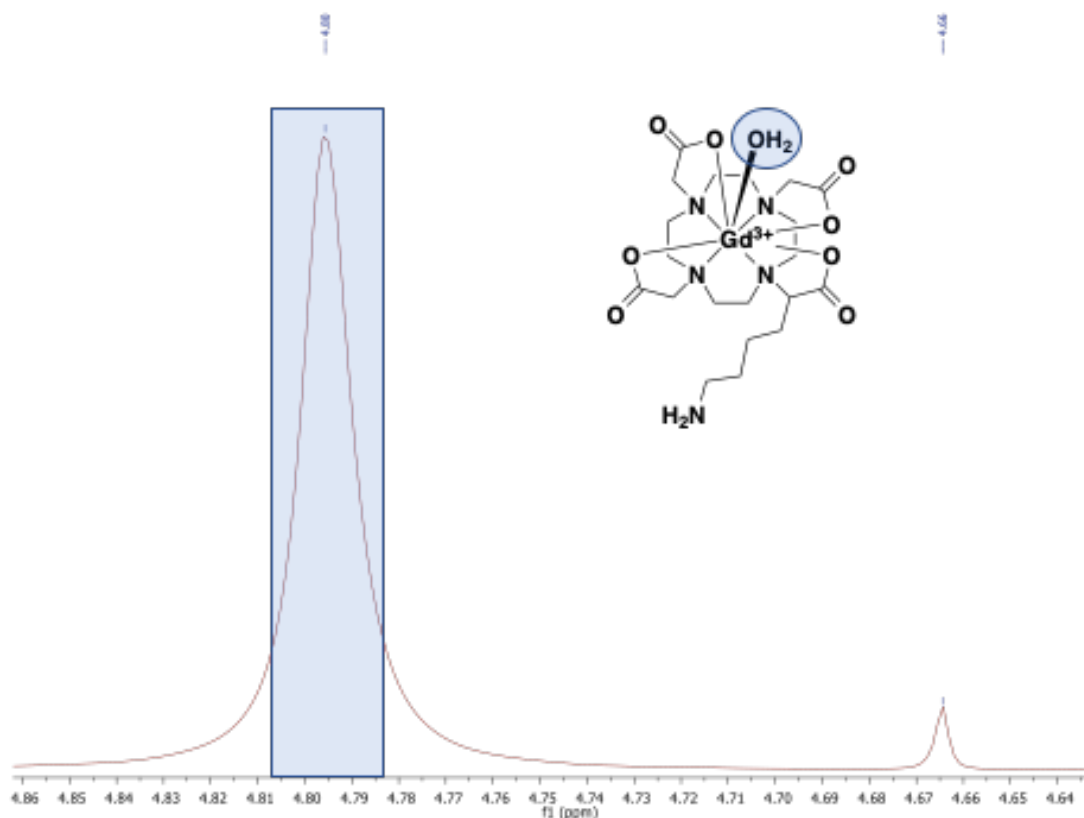
Figure 3.10 ^{1}H-NMR spectrum showing the separation of bound (highlighted in blue) and unbound water to the gadolinium metal centre in a 2 mmol Gd.5 amine chelate sample (insert).

A T_1 value for **Gd.5** was determined using a series of delay increments (Tau) ranging between 10 ms and 6 s, all with a relaxation delay of 24 s in between each pulse sequence. A T_1 value of 0.0867 seconds was recorded when a concentration of ca 2 mmol **Gd.5** solution is used. This results in a longitudinal relaxation (r_1) value of 4.93 mM^{-1}s^{-1} recorded on a 400 MHz spectrometer. r_1 value for **Gd.5** is comparable to that of other cyclic DOTA-based gadolinium contrast agents (r_1 values typically range from 3.5 – 5.5 mM^{-1}s^{-1} when recorded on a 400 MHz spectrometer).[204] When comparing **Gd.5** to similar T_1 relaxation systems such as the one developed by Stasiuk, an increase in relaxivity can be

seen. Stasiuk and team used a cyclic NOTA structure with the same side arm resulting in a $q = 1$ contrast agent with an r_1 value of 4.19 mM^{-1}s^{-1} (200 MHz).[156] The increased size of DOTA like **Gd.5** system results in an improved r_1 value on previously reported compounds.

3.4 Lanthanide Chelate/linker preparation

The functionalisation of the terminal amine group present seen within the **Ln.5** complexes with a thiolic acid derivative was undertaken for both chelate design and functionalisation purposes. This can be seen to have a dual effect within the chelate design. First, the addition of a thiolic acid at the terminal amine (therefore increasing chain length) such as α-lipoic acid, 3-mercaptopropanoic acid and 4-mercaptobenzoic acid can be used to increase observed r_1 values due to the increase in size following the formation of a peptide bond. Second, the addition of a terminal thiolic group leads to the possibility of Ln.5-DOTA complex being used in the surface functionalisation reaction with InP/ZnS, Thus, aiding in the design of a in the development of a dual-modal multimeric OI/MRI probe.

Peptide bonding of readily prepared **Ln.5** to the three short thiolic acids, lipoic acid, 3-mercaptopropanoic acid and 4-mercaptobenzoic acid (labelled as a, b and c respectively through this work), results in a small catalogue of lanthanide complexes with differing terminal sulphur (**Ln.5(a/b/c)** respectively) containing groups capable of functionalisation to the surface of InP/ZnS core/shell QDs. Differences the thiolic acids being added allows for

additional comparisons to be undertaken later in the synthetic pathway

(Scheme 3.8), Thus allowing for comparisons to be drawn when investigating

their potential as dual modal contrast agents following surface modification of

InP/ZnS core/shell QDs. As well as offering differences in the number of

terminal thiols available, the use of α-lipoic acid, 3-mercaptopropanoic acid and

4-mercaptobenzoic acid also gives the opportunity to investigate the effect in

which the likers backbone structure has on overall r_1 value of contrast agents,

with differences in rigidity and length observed.
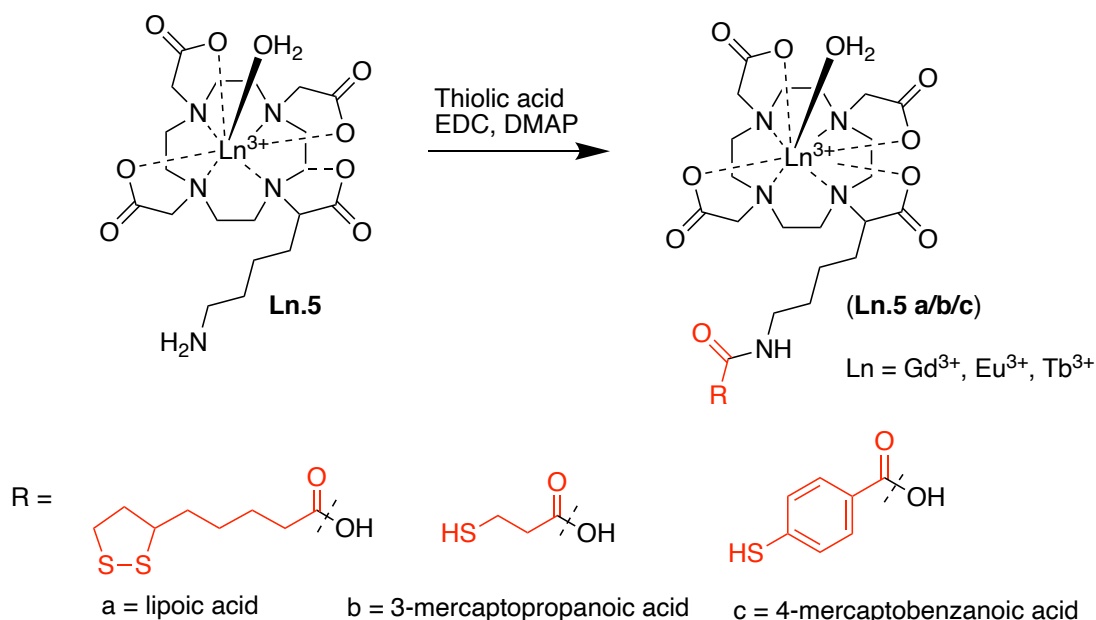
Scheme 3.8 Structure of **Ln.5 a/b/c** following the formation of an amide bond being formed using a thiolic acid derivative (a= lipoic acid, b= 3-mercaptopropanoic acid and c = 4-mercaptobenzanoic acid).

Scheme 3.8 shows the general synthetic method used to form the small

catalogue of terminal thiolic acid lanthanide chelate (**Ln.5 (a/b/c)**). The

reaction depicted in scheme 3.8 is an amide bond formation reaction between

the carboxylic acid of the thiolic acid and the terminal amine of **Ln.5**. In all

cases, the reaction is carried out in a 1:1 H_2O:DMF solution. Within the reaction,

both dimethylaminopyridine (DMAP) as well as 1-Ethyl-3-(3-

dimethylaminopropyl)carbodiimide (EDC) in a 1:2:2 ration with respect to Ln.5

can be seen to be used, DMAP used as the base within the reaction due to its

easily soluble nature in the solvent system whilst EDC is used as the coupling

agent within the reaction. EDC is the coupling agent used due to the pH range

which this reaction is carried out at. The working pH range within the reaction

is 5 - 5.5 which falls in the working pH range of the EDC coupling agent (pH 4 –

6). One important aspect to note however about this reaction is the formation of

DMAP salts, these have to be removed during the workup of the reaction by the

resuspension of the crude product in a 10% solution of methanol:DCM before

filtration. Following the successful preparation of **Ln.5 a/b/c** a total of 9

complexes were evaluated for their physical and fluorescent properties, as well

as looking at the effects in which the greater size had on the relaxation rates.

3.4.1 Characterisation of Eu.5 thiolic acid derivatives

Eu.5 (a/b/c) thiolic acid chelate derivatives were synthesised *via* the

method outlined in scheme 3.8. **Eu.5** was stirred with a thiolic acid derivative in

a 1:2 molar ratio in the presence of EDC and DMAP, resulting in an off-white

solid being formed with yields of 78%, 83% and 77% respectively. Following

the formation of **Eu.5 (a/b/c)**, no change is expected to be observed within the

expected chelate geometry, with the Eu(III) metal centre still displaying an 8-

coordinate geometry. This assumption is investigated further below using

phosphorescent lifetime of **Eu.5 (a/b/c)** in both H_2O and D_2O. To determine as

to whether the newly formed amide bond effects the hydration following the

formation of **Eu.5 (a/b/c)**, the luminescent properties were fully investigated

for amide functionalised **Eu.5 (a/b/c)** chelates. Changes in emission spectra,

specifically in the ratio between $\Delta J = 1$ and $\Delta J = 2$ allow for indication into

geometric changes within the structure. Furthermore, changes in hydration

state would further indicate the newly formed amide bond would be having an

effect on the water binding to the metal centre.

The luminescent properties for **Eu.5 (a/b/c)** were determined by pseudo direct

excitation of Eu metal centre at an $\lambda_{ex} = 395$ nm, showed the presence of Eu(III)

metal within the all functionalised complex, this can be seen in figure (3.11)

showing the transitions between the $^5D_0 - {}^7F_J$ transitions expected. The

phosphorescence emission spectra for **Eu.5 (a/b/c)** are shown in figure 3.11

above were obtained using an $\lambda_{ex} = 395$ nm as well as following the $\Delta J = 1$

emission peak at $\lambda_{em} = 595$. The emission profiles depicts the $^5D_0 - {}^7F_J$

transitions. These observed transitions are characteristic of an Eu(III) metal

complex which have a hydration state $q = 1$, determined due to the ratio of $\Delta J =$

1 when compared to $\Delta J = 2$. The larger $\Delta J = 1$ peak is indicative of a $q = 1$ system.

The emission maxima for **Eu.5** shown above were obtained using an $\lambda_{ex} =$

395 nm as well as following the $\Delta J = 1$ emission peak at $\lambda_{em} = (595$ nm). The

emission profile depicts the $^5D_0 - {}^7F_J$ transitions (labelled in figure). These

transitions which are observed are characteristic of an Eu metal complex which

have a hydration state $q = 1$, determined due to the ratio of $\Delta J = 1$ when

compared to $\Delta J = 2$. The larger $\Delta J = 1$ peak is indicative of a $q = 1$ system. To

confirm a *q* = 1, lifetime experiments were carried out using **Eu.5 (a/b/c)** in both H_2O and D_2O solutions. These excited state lifetime decay curves shown in figure 3.12 have been used to determine the rate constants which are in table 3.2.
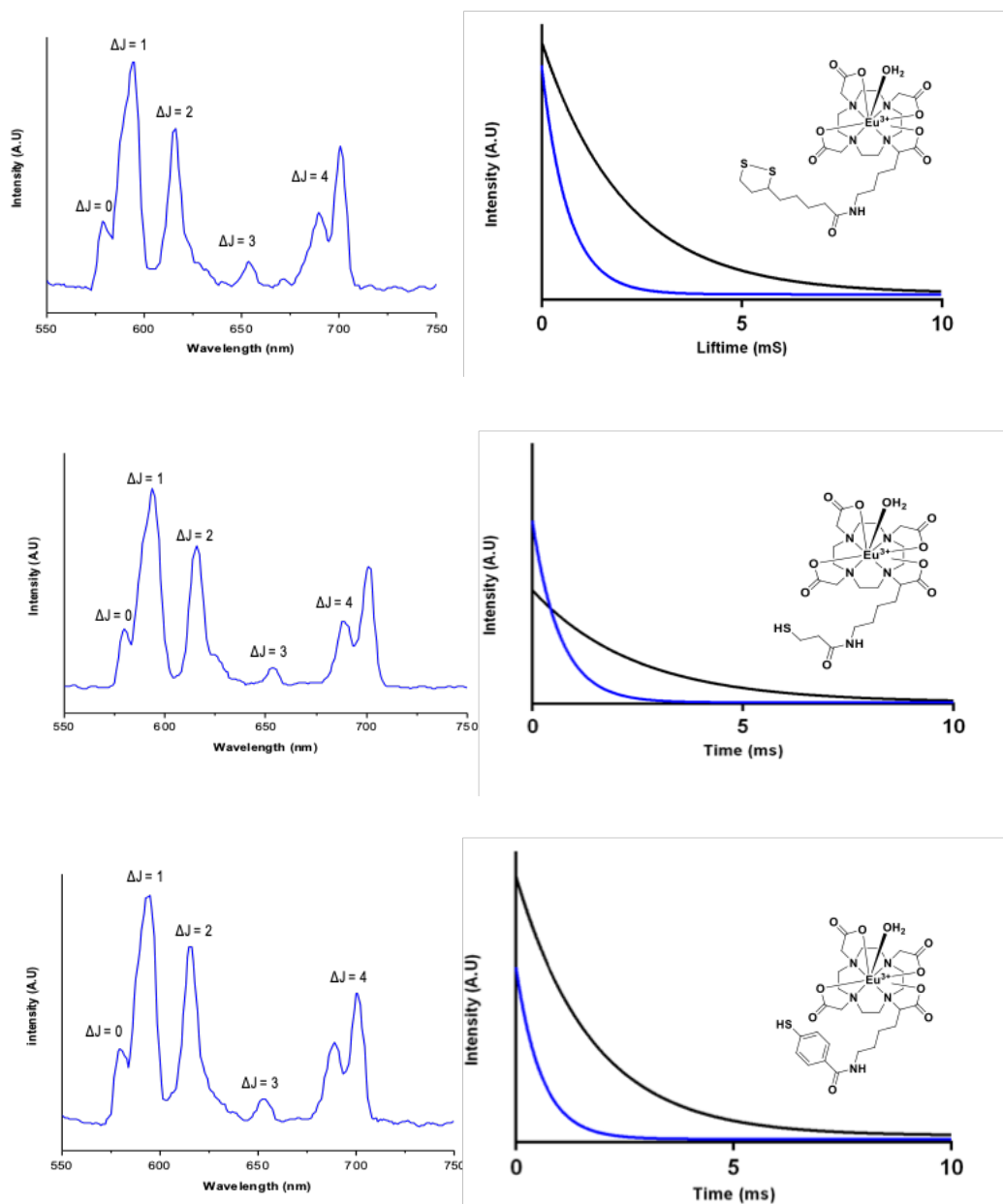
Figure 3.12 Excited state decay curves (right) and phosphorescent emission spectra (left) studies for Eu.5a (top), Eu.5b (middle), Eu.5c (bottom)- recorded at 298 K, λ_{ex} = 395 nm, λ_{em} = 595 nm, pH 7. Blue = H_2O, Black = D_2O.

The use of excited state lifetime decay allowed for the determination of

hydration states for all Eu(III) thiol derivative chelates (**Eu.5 (a/b/c)**); with all

complexes having a q = 1. On the addition of a small range of thiolic acid linkers

to the terminal amine forming an amide bond within **Eu.5 (a/b/c)**, it can be

shown using hydration state calculations that the addition of an amide bond

within the complex seems to have no overall effect on the hydration state of the

Eu.5 (a/b/c) complexes. This is able to be investigated further by determining

the hydration state of **Tb.5 (a/b/c)** complexes, which is complete below.

The hydration state of 1 confirms that the functionalisation of the amine with a

range of thiolic acids does not have an effect on the q of the metal centre. Values

for rate constants which were determined can be seen in the table below.

Complex	λ_{ex} / nm	λ_{em} / nm	k_{H2O} / ms^{-1}	k_{D2O} / ms^{-1}	q (± 0.2)
Eu.5	395	595	1.61	0.48	1.1
Tb.5	377	545	0.51	0.30	0.7
Eu.5 a	395	595	1.52	0.48	1.0
Eu.5 b	395	595	1.52	0.41	1.0
Eu.5 c	395	595	1.70	0.57	1.1
Tb.5 a	377	545	1.23	1.02	0.8
Tb.5 b	377	545	0.53	0.31	0.8
Tb.5 c	377	545	0.62	0.42	0.7

Table 3.2 depicting rate constants, k, for depopulation of the excited states as

well as hydration state (q) for Eu.5/Eu.5(a/b/c) and Tb.5/Tb.5(a/b/c).

On the addition of a thiolic acid linker to the terminal amine within Eu.5/Tb.5 to

form **Eu.5 (a/b/c)** and **Tb.5 (a/b/c),** determination of changes to hydration

state and rate constants following amide formation was complete. Hydration

state and rate constant values show negligible change on the addition of an

amide bond (table 3.2), with the determination that addition of an amide bond

within the inner-sphere has no effect on the water binding to the metal centre.

However, the use of the **Tb.5** with lipoic acid (**Tb.5a**) sees a rise in both rate

constants (k_{H2O} =1.23ms^{-1}, k_{D2O} = 1.02 ms^{-1}) when compared to **Tb.5** (k_{H2O} = 0.51

ms^{-1}, k_{D2O} = 0.30ms^{-1}). Increased residency time of inner-sphere water is a

possibility following the addition of lipoic acid due to the long-saturated carbon

chain, *via* either restricting access to the metal centre, driving of the TSAP/SAP

ratio or disrupting second sphere water. Thus increasing the observed

residency time on the metal centre.

3.4.2 Characterisation of Tb.5 thiolic acid derivatives

Tb.5 (a/b/c) thiolic acid derivatives were synthesised again using the

method outlined in scheme 3.4. **Tb.5** was stirred with a thiolic acid derivative in

a 1:2 molar ratio in the presence of EDC and DMAP, resulting in an off-white

solid being formed with yields of 69%, 89% and 72% respectively. As with **Eu.5**

(a/b/c) analogue, one molecule of water is expected to be bound to the metal

centre following the addition of thiolic acid to the terminal amine functional

group within the **Tb.5 (a/b/c)** thiolic acid complexes. To investigate this

further, both the photoluminescent properties and excited state lifetime of **Tb.5**

complexes are studied.

Pseudo direct excitation of Tb(III) metal centre at a λ_{ex} = 377 nm allows for the determination of the luminescent properties of **Tb.5 (a/b/c)**. As seen in figure 3.13, following the direct excitation of the metal centre characteristic emission spectra are observed for all Tb.5 thiolic acid chelates. The emission spectra shown in figure 3.13 obtained at a λ_{ex} = 377 nm, these are typical of complese of Tb(III). The $^5D_4 - {}^7F_J$ transitions are able to be seen within the spectra (labelled in figure 3.13). The excitation spectra recorded for **Tb.5 a/b/c** follows the ΔJ = 1 ($^5D_4 - {}^7F_5$) transition at an λ_{em} = 545 nm. The excitation spectra show one strong peak at λ_{ex} = 377 nm indicative of pseudo direct excitation of the Tb(III) metal centre. In order to determine the hydration state for all Tb.5 thiolic acid chelates the ΔJ = 1 transition at λ_{em} = 545 nm is followed with the use of an λ_{ex} = 377 nm. The decay curves for all **Tb.5 (a/b/c)** thiolic acid complexes in both H_2O and D_2O can be seen below in figure 3.13, with the rate constants being displayed in table 3.2 above.
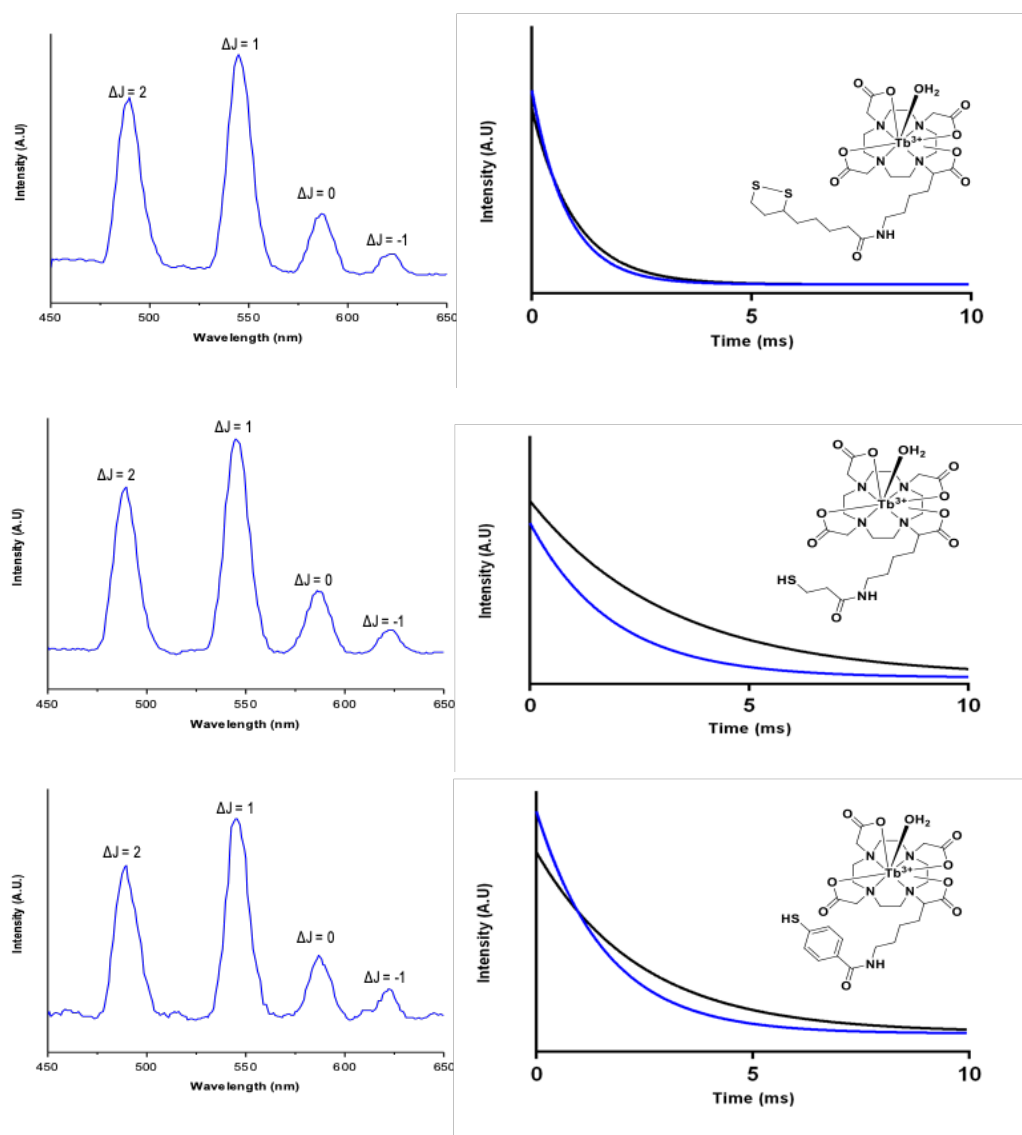
Figure 3.13 Phosphorescent emission spectra (left) and excited state life time studies (right) for Tb.5a (top), Tb.5b (middle), Tb.5c (bottom) thiolic acid complexes following direct excitation at 298 K, λ_{ex} = 377 nm, λ_{em} = 545 nm, pH 7. Blue = H_2O, Black = D_2O

Following the excited state lifetime decay studies showing in figure 3.13, the rate constants shown in table 3.2 result in q = 1 for all Tb.5 thiolic acid complexes as expected.

3.4.3 Characterisation of Gd.5 thiolic acid derivatives

Gd.5 (a/b/c) thiolic acid amide derivatives were synthesised in a reaction using **Gd.5** amine chelate previously synthesised, which was stirred overnight with a thiolic acid in a molar ratio of 1:2 (the excess molar ratio of thiolic acid being used to drive the reaction to completion). This reaction was carried out at pH 9 to drive amide bond formation, as well as being completed in EDC coupling agent and DMAP base. This resulted in off white oils being formed for **Gd.5 (a/b/c)** in yield of (84%, 89%, 98%) for **Gd.5 a/b/c** respectively. As in section 3.4.1/2, it is expected that the use of lanthanide incorporation in the centre of the macrocyclic compound being used will yield **Gd.5** thiolic derivatives will have a q = 1 with one inner-sphere water bound to the Ln(III) metal within the complex. In section 3.3.3, an r_1 value of 4.932 mM^{-1}s^{-1} was determined for the **Gd.5** amine chelate derivative (400 MHz). An increase to the observed r_1 of **Gd.5** amine chelate can be achieved by altering the chelate design in ways such as inner-sphere water exchange rate (k_{ex}), the hydration number (q) and the rotational correlation time (τ_R).[205] As q is to be fixed at 1 inner-sphere water molecule, both τ_R and k_{ex} can be manipulated to increase the observed r_1 value for **Gd.5** thiolic acid derivatives. This addition of the thiolic acid has the possibility to increase r_1 values, the addition of the small molecule gadolinium chelates results in a longer τ_R and therefore an increase to the water exchange rate. This increase in size can be seen to have a large effect within the r_1 values which can be obtained cf. **Gd.5** with the exact values showing in table 3.3 below

Functionalised amine chelates	Thiolic acid	T_1 / ms	r_1 / mM^{-1}s^{-1}
Gd.5a	Lipoic acid	0.143	7.39
Gd.5b	3-mercaptopropanoic acid	0.131	6.85
Gd.5c	4-mercaptobenzanoic acid	0.135	7.13

Table 3.3 Gd.5 thiolic acid T_1 and r_1 measurements recorded on at 400 MHz

r_1 values where determined for functionalised amine chelates **Gd.5 (a/b/c)** using the pulse sequence and tau intervals which were used previous in the determination of r_1 of the Gd amine chelate in section 3.3. Following the addition of thiolic acid to form **Gd.5 a/b/c,** observed r_1 values of 7.39, 6.85 and 7.13 mM^{-1}S^{-1} are seen for the Gd amide chelate respectively. Increased r_1 value when compared against Gd amine chelate is observed, with this increase attributed to the slower rotational correlation time due to the additional peptide bond which has been created on addition of the thiolic acid. The increase in obtained r_1 values for Gd amine chelate derivatives allows for the assumption that the creation of a peptide bond following the addition of thiolic acid does not have a detrimental role on inner-sphere water-exchange rate.
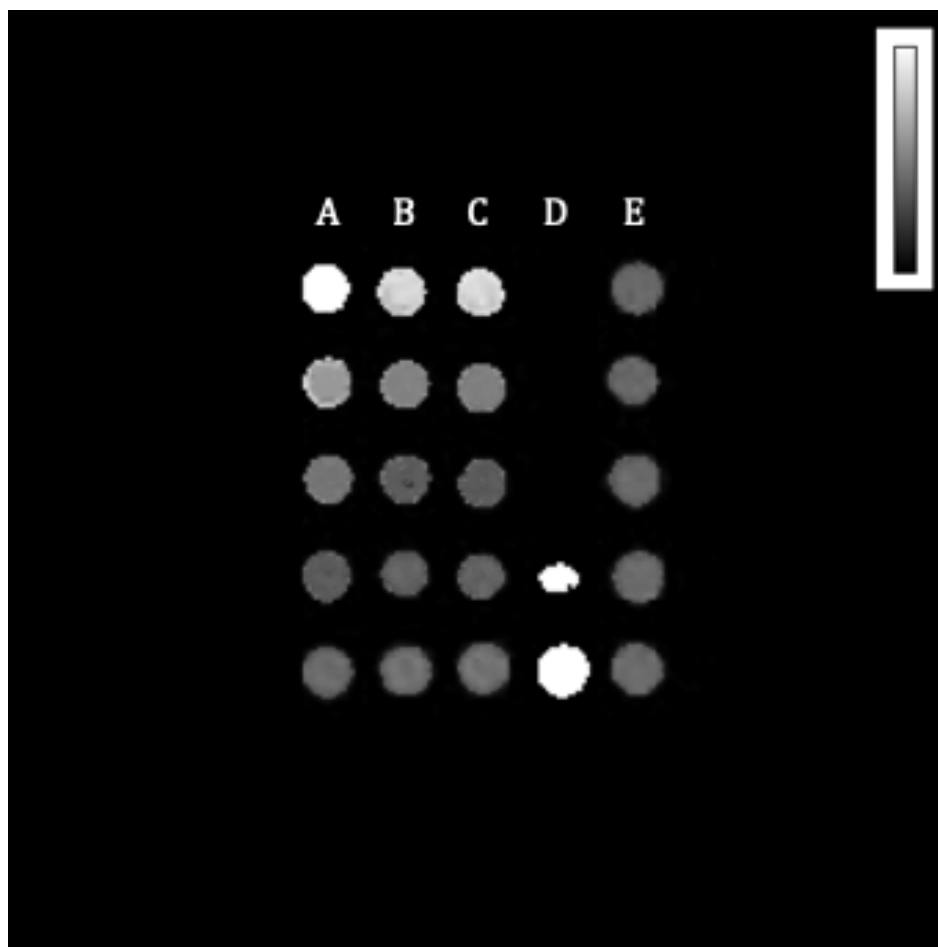
Figure 3.14 MRI phantom image showing Gd.5a (A), Gd.5b (B) and Gd.5c (C) at a range of concentrations from 2-0.125 mmol (top to bottom), against Gd(III)DOTA (D) at the same concentration with H_2O (E) for comparison)

The use of phantom images allows for the effect of the additions have had on the contrast, the images were taken in a 20 MHz field using samples from 2.0 mM to 0.125 mM. These can be seen in figure 3.14.

The addition of a thiolic acid to **Gd.5** to form **Gd.5 (a/b/c)** gives a small catalogue of chelating agents all with increased relaxivity due to increase size when compared to its amine chelate derivative. Along with this, **Gd.5 (a/b/c)** have at least a single terminal thiol for functionalisation to a QD. This small

catalogue of chelating agents is therefore able to be developed further into a

multi-modal/multimeric (fluorescent-MRI) contrast agent. This is able to be

complete *via* the surface functionalisation of **InP/ZnS (2) – TGA** (chapter 2)

with previously synthesised small molecule Gd(III) chelators (**Gd.5 a/b/c**) from

this body of work. It is thought however, that due to both the increase size (nm

from the QD) as well as increased payload size from surface functionalisation,

multimodal multimeric OI/MR imaging agents synthesised later in the chapter

are expected to increase longitudinal relaxation rates, due to the slower

tumbling rates exhibited.

3.5 Functionalisation and analysis of an OI/MRI chelating agent

3.5.1 Synthesis of functionalised InP/ZnS – thiol chelating OI/MR imaging agent

The development of a dual-modal multimeric OI/MR imaging agent has

been able to be developed using two constituent parts outlined in previous

sections within this thesis. The combination of both non-toxic InP/ZnS QDs

described in chapter 2, with the **Gd.5 a/b/c** thiolic acid derivatives synthesised

within this chapter allow for the development of an OFI/MR probe with the

potential to have improved imaging capabilities. The functionalisation of the

surface of InP/ZnS QDs with **Gd.5 a/b/c** can be achieved following the addition

of at least one terminal thiol after the formation of an amide bond between **Gd.5**

and simple thiolic acids. The reaction shown in scheme 3.9 sees the

replacement of surface ligand TGA on the surface of **InP/ZnS – TGA** with the

Gd.5 a/b/c.
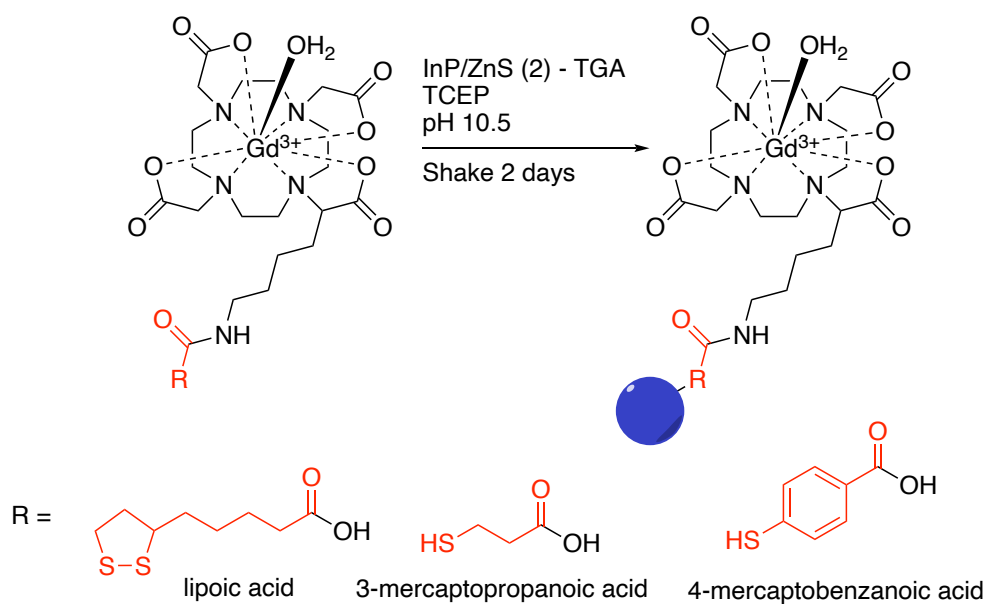
Scheme 3.9 Surface ligand replacement of TGA with Gd.5 a/b/c (a = lipoic acid, b = 3-mercaptopropanoic acid, c = 4-mercaptobenzanoic acid) on the surface of InP/ZnS (2) – TGA forming an OFI/MR imaging agent.

Due to the small size of the InP/ZnS QDs being used (ca 2-3 mm in diameter), a 1:1000 ratio of Gd(III) chelating agent was used in order to give the highest possibility of optimum payload on the surface following the completion of the reaction. In a similar reaction, where Stasiuk *et al.* loaded InP based QDs with Gd(III) chelating agents they found that a maximum payload of 80 chelates could be attached to the surface.[156] TCEP is used within the reaction in a ratio of 1:3000 to reduce dithiol bonds following their formation therefore driving the surface functionalisation of InP/ZnS QDs. The reaction solution was raised to a pH to 10.5 using TMAOH as the base within the reaction before being stirred/vortexed vigorously for 2 days. During this time the centrifuge tube was wrapped in foil to protect the QDs from photo-degradation. On completion, the product formed was able to be purified *via* centrifuge filtration removing all unreacted chelates before re-diluting the product in fresh mΩ water. Once

InP/ZnS – Gd.5 a/b/c are re-diluted in water both the physical and

photophysical properties can be investigated.

3.5.2 Evaluation of physical properties of synthesised OI/MR imaging agent

Following the synthesis steps previously outlined and in further detail in

the experimental section 6.14, the successful synthesis of an OI/MR multi-

modal multimeric imaging probe was achieved. The ligand substitution reaction

in which **InP/ZnS – TGA** QDs undergo to produce **InP/ZnS – Gd.5 a/b/c** is

expected to yield both a size (hydrodynamic diameter) and surface charge (zeta

potential) change following ligand substitution on the surface. Initially, the

hydrodynamic diameter for both **InP/ZnS (2) – TGA** QDs is 4.73 nm and 5.81

nm for **InP/ZnS (2)** synthesised with InI_3 and $InCl_3$ respectively. However, on

substitution of **Gd.5 a/b/c,** the size increases with all values being able to be

see in table 3.4 below. From the data in table 3.4 a trend within the

hydrodynamic sizing of the thiolic acid gadolinium chelate linkers following

their functionalisation onto the surface of the **InP/ZnS (2) – TGA** can be seen.

The trend points to that of lipoic acid, the thiolic linker with the longest and

most flexible backbone having the largest hydrodynamic diameter when

functionalised onto the surface of **InP/ZnS (2) – TGA**.

Functionalised QD	DLS / nm	
	InI_3	$InCl_3$
InP/ZnS (2) - TGA	4.73	5.81
InP/ZnS (2) - Gd.5a	11.09	9.56
InP/ZnS (2) - Gd.5b	7.82	7.21
InP/ZnS (2) - Gd.5c	10.05	8.82

Table 3.4 DLS hydrodynamic diameters following the functionalisation of InP/ZnS (2) – Gd.5 a/b/c (labelled) for both green and red emitting QDs against InP/ZnS (2) – TGA

What can also be alluded from the obtained DLS numbers is that when 3-mercaptopropanoic acid is used as the linker to form **InP/ZnS (2) – Gd.5b**, a smaller overall size of particle is formed. This is attributed to the small chain length, however, good rotation around the thiol linker allows for good loading of many **Gd.5b** chelates on the QD surface. Hydrodynamic diameter is able to be increased in size from 4.73 and 5.81 nm (InI_3 and $InCl_3$ respectively), the size increase however is dependent on the DOTA-ligand used for surface functionalisation. Small increases in size can be forced *via* the addition of **Gd.5b** (DOTA-3-mercaptopropanoic acid) 7.82 and 7.21 nm respectively. Whilst large increases in hydrodynamic diameter can be forced following the surface functionalisation of **InP/ZnS (2) – TGA** with **Gd.5a** (DOTA.lipoic acid), with D_h of 11.09 and 9.56 nm respectively. The use of Gd.DOTA-4-mercaptobenzoic acid produces functionalised **InP/ZnS (2) – Gd.5c** QDs with hydrodynamic diameters of 10.05 and 8.82 nm for InI_3 and $InCl_3$, thus allowing for a tunability within the functionalisation of InP/ZnS (2) QDs (ligands for increased size (Gd.5b < Gd.5c < Gd.5a).

The change in zeta potential on the surface was also investigated. Due to the addition of a negatively charged macrocyclic complex, which is expected to force a move to a more overall negatively charged surface. Table 3.5 shows the comparison of the zeta potentials which were recorded for both the original **InP/ZnS (2) – TGA** and the functionalised **InP/ZnS (2) – Gd.5 a/b/c**.

	Zeta / mV	
Functionalised QD	**InI$_3$**	**InCl$_3$**
InP/ZnS (2) - TGA	-20.26	-25.30
InP/ZnS (2) - Lipoic acid	-28.30	-27.63
InP/ZnS (2) - 3-mercaptopropanoic acid	-27.00	-31.13
InP/ZnS (2) - 4-mercaptobenzanoic acid	-32.70	-28.73

Table 3.5 Zeta potential results following the formation of InP/ZnS (2) - Gd.5 a/b/c DOTA derivatives.

As can be seen in table 3.5, **InP/ZnS (2) – TGA** QDs have an initial zeta potential of -19-(-)23 mV. Following the functionalisation, there is a distinct move to a more negative zeta potential within the range of -27 – (-) 32 mV. This change to a more negative zeta potential is able to show that the surface of InP/ZnS QDs have been functionalised with **Gd.5 a/b/c**.

As previously discussed, r_1 values for **InP/ZnS (2) – Gd.5 a/b/c** are expected to exceed that of the r_1 value recorded for **Gd.5 a/b/c** due to the increase in rotational correlation time following the surface functionalisation of **InP/ZnS (2) – TGA** QDs. Table 3.6 below shows a comparison between all gadolinium chelates, including **Gd.5**, **Gd.5 a/b/c** and **InP/ZnS (2) - TGA** QDs functionalised with **Gd.5 a/b/c**.

Gadolinium Chelate	Thiolic acid	Concentration / mM	T_1 / ms	r_1 (per Gd chelate) / $mM^{-1}s^{-1}$
Gd.5	N/A	10.5	0.0204	4.58
Gd.5a	Lipoic acid	0.891	0.143	7.39
Gd.5b	3-mercaptopropanoic acid	1.05	0.131	6.85
Gd.5c	4-mercaptobenzanoic acid	0.982	0.135	7.13
QDs synthesised with InI$_3$				
InP/ZnS (2) - Gd.5a	Lipoic acid	0.318	0.292	9.49
InP/ZnS (2) - Gd.5b	3-mercaptopropanoic acid	0.354	0.305	8.11
InP/ZnS (2) - Gd.5c	4-mercaptobenzanoic acid	0.282	0.318	9.73
QDs synthesised with InCl$_3$				
InP/ZnS (2) - Gd.5a	Lipoic acid	0.30	0.299	9.80
InP/ZnS (2) - Gd.5b	3-mercaptopropanoic acid	0.273	0.44	6.86
InP/ZnS (2) - Gd.5c	4-mercaptobenzanoic acid	0.163	0.575	8.17

Table 3.6 r_1 and T_1 values for all gadolinium chelates including functionalised InP/ZnS (2) QDs (both InI$_3$ and InCl$_3$ QDs used).

On completion of functionalisation, an increase of obtained r_1 values is seen within all **InP/ZnS (2) – Gd.5 a/b/c** when compared to non-functionalised **Gd.5 a/b/c**. r_1 with values of up to 9.49 mM^{-1}s^{-1} (**InP/ZnS (2) – Gd.5** lipoic acid, QDs synthesised with InI$_3$) being obtained (400 MHz). As previously mentioned, Stasiuk *et al.* reported an OI/MR dual modal multimeric imaging probe using gadolinium surface functionalised InP/ZnS QDs. Within their work, they reported each gadolinium chelate on the surface of the InP based QDs had an r_1 value of 13 mM^{-1}s^{-1}, however, this value was recorded at the much lower field strength of 30 MHz.[156] The value obtained by Stasiuk is shown to decrease however when subjected to a 200 MHz field to 4.19 mM^{-1}S^{-1}, a two-fold

decrease when compared to OI/MR imaging agents prepared in this body of

work. Furthermore, the group were able to attach a maximum of 80 chelates

per InP QD when looking to develop a multimeric OI/MR imaging probe.

Resulting in a r_1 value of (900 mM^{-1}s^{-1}, 13 mM^{-1}s^{-1} per Gd chelate at 35 MHz) per

InP/ZnS QD. In order to determine the surface loading of **Gd.5 a/b/c** on

InP/ZnS (2) – TGA following functionalisation, both ^{1}H-NMR spectroscopy

(**Gd.5 a/b/c** surface concentration) and UV-Vis spectroscopy (QD solution

concentration) were used. Using these quantification methods, surface loading

of up to 190 chelates per QD was found to be possible following the

functionalisation of **InP/ZnS (2) – TGA** (table 3.7).

QDs synthesised with InI$_3$	Conc of QD / μM	Conc.surface chelate / mM	loading per QD	r_1 per QD / mM^{-1}s^{-1}
InP/ZnS (2) - Gd.5 a	0.976	0.1638	168	1610
InP/ZnS (2) - Gd.5 b	0.814	0.1547	190	1557
InP/ZnS (2) - Gd.5 c	0.895	0.1274	142	1399
QDs synthesised with InCl$_3$	**Conc of QD / μM**	**Conc.surface chelate / mM**	**loading per QD**	**r_1 per QD /mM^{-1}s^{-1}**
InP/ZnS (2) - Gd.5 a	0.939	0.1456	155	1536
InP/ZnS (2) - Gd.5 b	0.939	0.1547	165	1140
InP/ZnS (2) - Gd.5 c	1.08	0.1274	118	974

Table 3.7 Values determined for the surface loading of InP/ZnS based QDs with Gd.5 a/b/c thiolic chelates to form a multimeric OI/MR imaging agent.

The values seen in table 3.7 show a familiar loading pattern of **Gd.5 a/b/c**

chelates on the surface of InP based QDs. The trend in loading is consistent

across both synthesised QDs, with 3-mercaptopropanoic acid having the

greatest loading on the surface. Followed by lipoic acid, with 4-

mercaptobenzoic acid having the fewest chelates loaded onto the surface. The

combination of high loading of lipoic acid chelates on the surface along with the

high r_1 values obtained result in an effective T_1 value per QD of up to 1600 mM^{-1}s^{-1} (with exact values shown in table 3.7). Phantom image in figure 3.15 is able

to show the differing levels of surface loading between **InP/ZnS (2) –**

Gd.5a/b/c below.
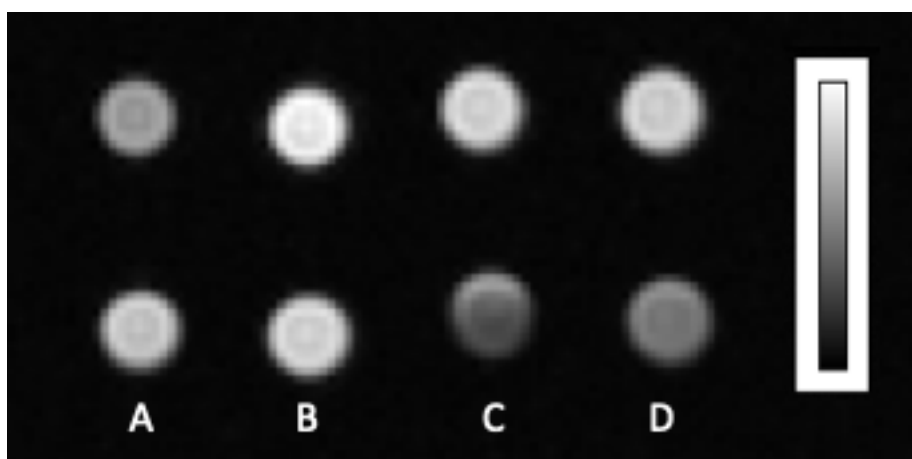
Figure 3.15 Phantom image depicting loading of InP/ZnS (2) – Gd.a (B), InP/ZnS (2) – Gd.b (C) and InP/ZnS (2) – Gd.c (D). InP/ZnS (2) synthesised with InCl$_3$ (top) and InI$_3$ (bottom). Gd.5 amine (A) used as reference. Samples all at 0.1 mM with respect to Gd(III) chelate on the surface of InP/ZnS (2) QDs.

3.5.3 Evaluation of luminescent properties of OI/MR imaging agents.

To investigate further the dual-modal properties of the as-synthesised

OI-MR imaging probes, the luminescent properties including PLQY were

evaluated. First, comparisons were drawn between emission profiles of

unfunctionalised **InP/ZnS (2) – TGA** QDs when compared to emission profiles

of functionalised **InP/ZnS (2) – Gd.5** DOTA chelates (figure 3.15)
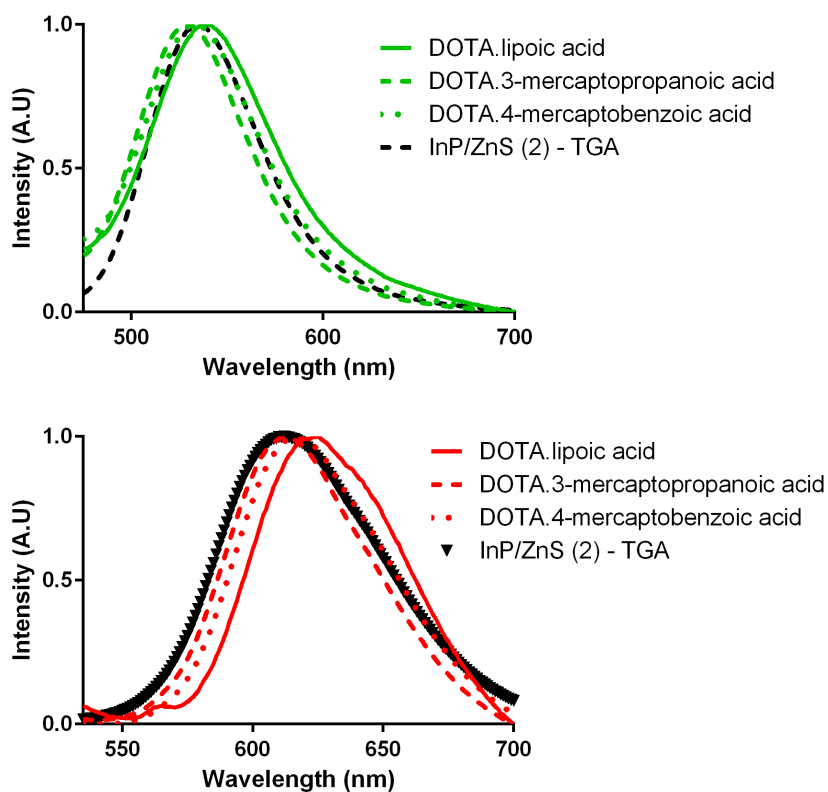
Figure 3.16 Comparison between unfunctionalised InP/ZnS (2) – TGA QDs and InP/ZnS QDs functionalized with all previously functionalized gadolinium containing DOTA chelates.

As seen in figure 3.16 no large shifts in emission wavelengths are observed following surface functionalisation of **InP/ZnS (2) – TGA**. This is echoed in the excitation spectra, demonstrated in figure 3.17 which showed 3D excitation and emission profiles of functionalised **InP/ZnS (2) – Gd.5** DOTA chelates. Following this, an investigation into any observable change within PLQY once functionalisation has taken place was undertaken. This investigated both the overall PLQY of the OI/MR imaging probe which had been developed, but also to determine as to whether there was a distinct difference in PLQY when different thiolic acid chelates where added to the surface of QDs. To do

this, initially the **InP/ZnS (2) – TGA** values outlined in 2.5.3 were used as a

baseline reading before again determining the PLQY once undergoing the

surface functionalisation to form **InP/ZnS (2) – Gd.5 a/b/c**. On completion of

functionalisation, PLQY values were re-determined and values recorded in table

3.8.
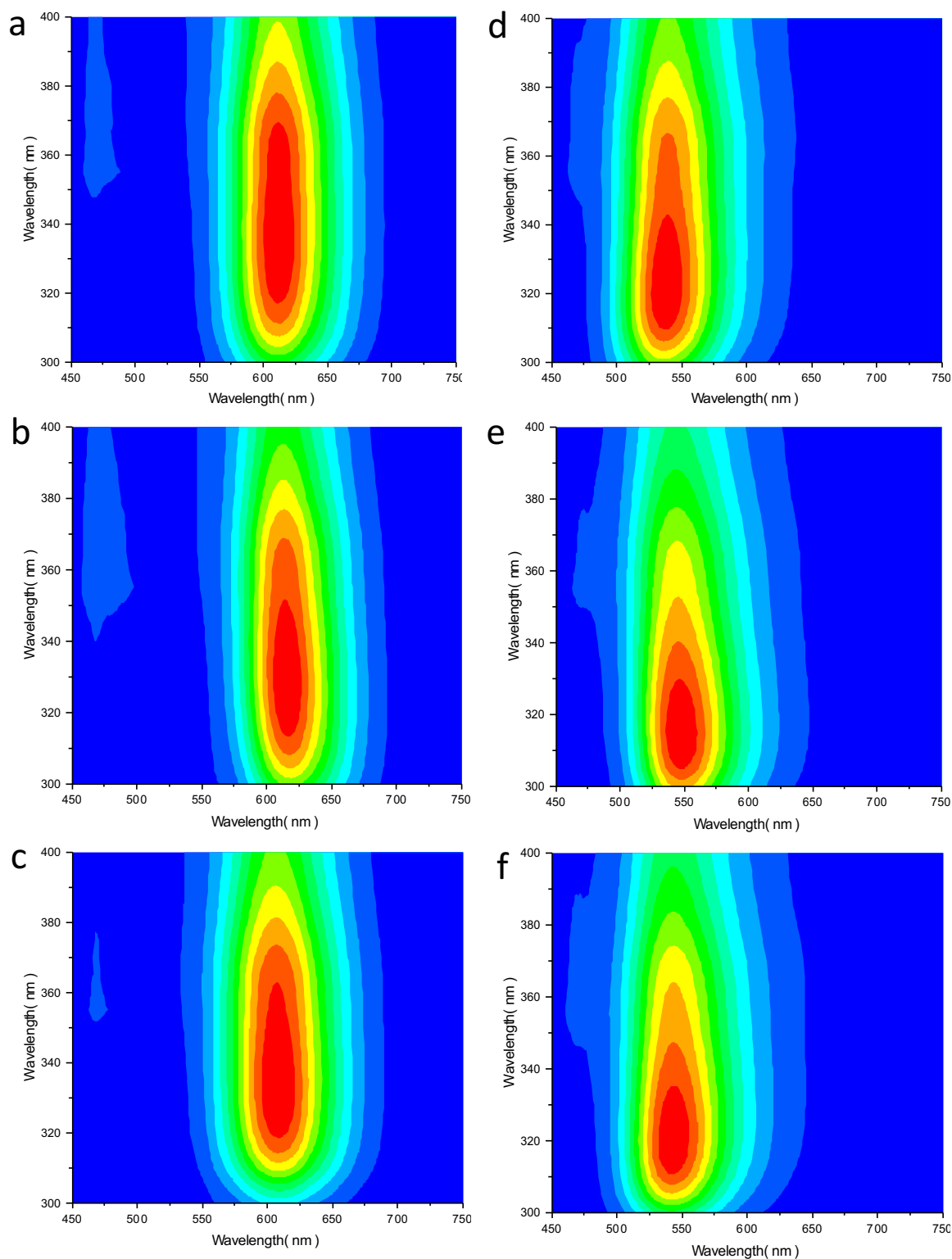
Figure 3.17 3D excitation/emission spectra of InP/ZnS (2) – Gd.5 a/b/c. a-c synthesised with InI$_3$ and d-f synthesised with InCl$_3$. (a,d – lipoic acid), (b,e – 3-mercaptopropanoic acid), (c,f – 4-mercaptobenzoic acid).

Values of 19.2% and 57.1% were determined for **InP/ZnS (2) – TGA** when

synthesised with InI_3 and $InCl_3$ respectively. These values are expected to drop

on functionalisation due to the harsh nature of the reaction in which they

undergo. On completion of the reactions, PLQY values were able to be achieved

of up to 19% and 20% when complete with QDs made with InI_3 and $InCl_3$

respectively. Interestingly, both of these high PLQY values were obtained using

InP/ZnS (2) – Gd.5 b (3-mercaptoprpanoic acid). This due to the larger

percentage of slow component in its two-component lifetime measurement

(59% and 45% respectively) (Table 3.9). Thus, resulting in a decrease in non-

radiative decay (section 2.4.2) events ultimately leading to an increase in PLQY

following functionalisation.

QD	PLQY	
	InI_3	$InCl_3$
InP/ZnS (1) – TGA	2.9%	20.0%
InP/ZnS (2) – TGA	19.2%	57.1%
InP/ZnS (2) – Gd.5 a	6.9%	5.0%
InP/ZnS (2) – Gd.5 b	18.9%	19.9%
InP/ZnS (2) – Gd.5 c	8.4%	6.6%

Table 3.8 Determined PLQY values obtained for both InP/ZnS (2) – TGA and

InP/ZnS (2) – Gd.5 a/b/c.

| QD | Lifetime decay component (ns) | | | |
| | InI_3 | | $InCl_3$ | |
	Fast	Slow	Fast	Slow
InP/ZnS (2) - Gd.5 a	0.972	10.763	1.522	12.239
	68.75%	31.25%	58.20%	41.80%
InP/ZnS (2) - Gd.5 b	0.781	15.986	1.435	13.668
	40.76%	59.24%	55.31%	44.69%
InP/ZnS (2) - Gd.5 c	0.917	10.187	1.420	11.926
	51.43%	48.57%	55.61%	44.39%

Table 3.9 showing lifetime decay components values (ns) for functionalised InP/ZnS (2) – TGA., where a = lipoic acid, b = 3-mercaptopropanoic acid and c = 4-mercaptobenzanoic acid.

Therefore, the PLQY of **InP/ZnS (2) – Gd.5** has the ability to be maintained, dependent on the Gd.5 DOTA chelate which undergoes surface functionalisation of **InP/ZnS (2) – TGA**.

The synthesis of non-targeted OI/MR dual-modal imaging agents are described within the work outlined in this chapter, outlining the surface functionalisation of **InP/ZnS (2) – TGA** with Gd(III) DOTA derivatives (**Gd.5 a/b/c**). Prior to surface functionalisation, as synthesised Ln(III) DOTA derivatives (Ln(III) – Gd(III), Eu(III) and Tb(III)) exhibit a q=1, determined experimentally using excited state lifetime measurements for Eu(III) and Tb(III) analogues of Ln(III) DOTA derivatives. r_1 values of up to 7.39 mM^{-1}s^{-1} (Gd.5a) were obtained before undergoing surface functionalisation to **InP/ZnS (2) – TGA** QDs with Gd(III) DOTA derivatives was undertaken.

OI/MR dual-modal imaging agents are successfully synthesised within

the work following the addition of Gd(III) DOTA derivatives to the surface, with increases in size (D_h), surface zeta potential and r_1 values all recorded. Increases to r_1 values of up to 9.80 mM^{-1}s^{-1} (**InP/ZnS - Gd.5a**, InCl$_3$) were able to be recorded with maximum loadings of up to 190 chelates per **InP/ZnS (2) QD**. Thus, resulting in effective r_1 value of up to 1600 mM^{-1}s^{-1} being reported (**InP/ZnS - Gd.5a**, InCI$_3$).

Following functionalisation, PLQY is able to be maintained with values of up to 19.9%, with PLQY values being controlled *via* the Gd(III) DOTA derivative functionalised to the surface. However, despite the change in PLQY with change in Gd(III) DOTA derivative, no bathochromic shifts are observed in λ_{em} maxima.

The synthesised OI/MR imaging probes which have been developed have the ability to maintain PLQY (up to 19.9%) after undergoing surface functionalisation with Gd(III) DOTA derivative, whilst exhibiting a large r_1 *per QD* value due to high levels of surface loading of Gd(III) DOTA derivative onto **InP/ZnS (2)**. The addition of a targeting motif, such as Endo180 specific antibodies (A5.158/39.10) (chapter 4), results in the synthesis of a targeted dual-modal OI/MR imaging probe.

Chapter 4: Development of a multimodal imaging probe for prostate cancer detection

4.1 Introduction

Early and accurate detection of a patient's cancer is a vital step within any effective treatment plan. Non-invasive molecular imaging, specifically targeted multimodal imaging, has in recent years allowed for all steps of cancer treatment (diagnosis through therapeutic intervention) to be visually monitored. Meaning therefore, cancer detection, progression as well as the tracking of therapeutic intervention can now be more accurately followed, leading to the advent of precise/patient tailored care. This coupled with better understanding of molecular imaging biomarkers within cancer/cancer progression has produced an all-round better understanding of disease progression as well as greater certainty of patient prognosis.[206] The improvements made within imaging instruments, non-invasive imaging probes, assay methods and quantitative techniques has vastly improved the overall image capture used during this process.[207] With some probes having dual function, within diagnosis and treatment (targeted image guided surgery as in this thesis). Multimodal imaging, as discussed above in section 3.1, combines two or more molecular imaging modalities into one imaging system. Thereby producing a more precise clinical diagnostic tool than conventional single modality imaging by offsetting limitations when imaging with one modality alone. The binding of a targeting moiety (such as an antibody, peptide or small molecule) to a multimodal molecular imaging systems, offers the possibility of

increased diagnostic accuracy.[201,208–210] Therefore, increasing the level of specific binding to a target of interest greatly improving spacial resolution, soft tissue contrast and molecular level biological information.[206]

4.1.1 Targeted multimodal imaging for cancer diagnosis

Introduction of a targeting moiety, such as antibodies (mAb A5.158 and mAb 39.10 for Endo180 within PCa used within this thesis), peptides or small molecules allows for large increases in targeted specific binding of multimodal imaging probes. This was shown by Lee *et al.,* the group developed a PET-MRI probe centered around the surface modification of T_2-weighted iron oxide nanoparticles for the imaging of $\alpha_v\beta_3$ intergrin.[211] 5 nm polyaspartic acid (PASP) coated iron oxide nanoparticles with a hydrodynamic diameter of 45 nm ± 10 nm were synthesized in a one-step co-precipitation synthesis process. PASP-iron oxide nanoparticles exhibited an r_2 value of 105.5 mM^{-1}s^{-1} prior to the surface modification with cyclic arginine-glycine-aspartic (cRGD) used as a targeting moiety for $\alpha_v\beta_3$ integrin. The surface was also modified with DOTA and labelled with ^{64}Cu (PET modality). Following surface modification, the PET-MRI probe was tested using *in vitro* and in *vivo* methods.[211] Displacement binding assay showed the specific binding properties that RGD has for the $\alpha_v\beta_3$ integrin receptor when tested against $\alpha_v\beta_3$ – positive U87MG cells. Small animal *in vivo imaging* carried out on nude mice bearing U87MG tumours and T_2-weighted MRI was performed on a 3T clinical scanner. Following injection of 300 µg of functionalized nanoparticle, T_2 signal intensity dropped after 4 h post

injection. However, large accumulation in both the liver and spleen is seen within this study (Figure 4.1).
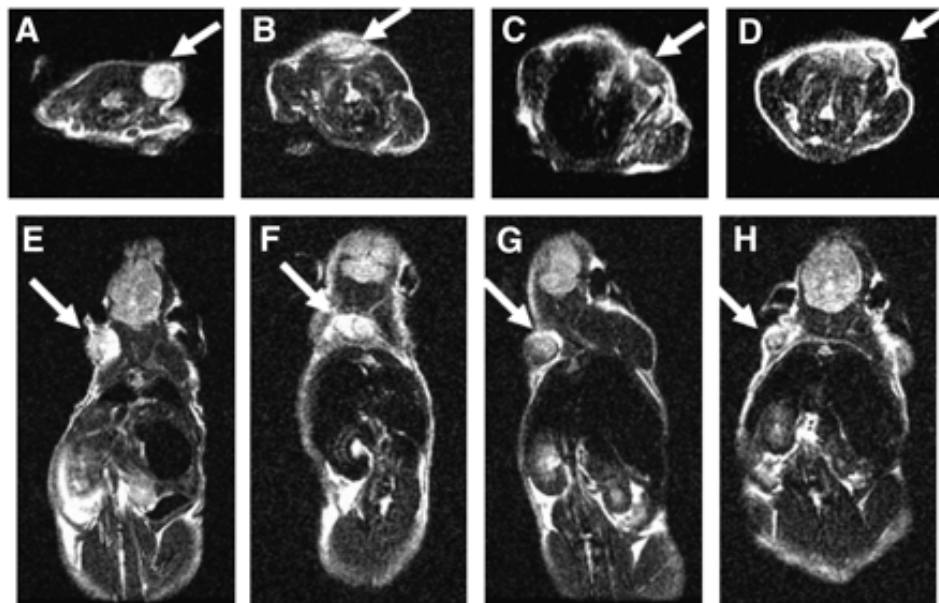
Figure 4.1. T_2 weighted MR image of nude mice bearing U87MG tumour before injection of iron oxide nanoparticles (A and E), 4 h post injection through the tail with DOTA-IO (B and F), DOTA-IO-RGD (C and E). blocking dose of c(RGDyk) also shown (D and H). White arrow in all images showing location of tumor at different time intervals.[211]

Li *et al.* used the same targeting agent (cRGD) to effectively create a multimodal (OI/MRI) imaging agent for use within brain tumour resection.[209] Outlined within the work, PAMAM-G5 dendrimer is labelled with, cRGD peptides (1:3 ratio, PAMAM-G5 : cRGD), MRI small molecule chelates containing Gd(III) as well as optical imaging agents (rhodamine-NHS and Cy5.5). Initially, cRGD present targets $\alpha_v\beta_3$ receptors within the vasculature, thus increasing the nanoprobes ability to infiltrate the blood brain barrier (BBB). Following that, the nanoprobes which have permeated the BBB will target the RGD receptors which are over expressed within the brain tumour endothelium cells, which are

visible due to the OI modality within the imaging agent. *In vivo* imaging studies carried out using U87MG glioblastoma xenografts placed into mice showed a heterogeneous MR signal 10 minutes post injection (PI). With the tumour being more prevalent 2 hours PI. *In vivo* fluorescent imaging studies showed that the nanoprobes had good targeting specificity for $\alpha_v\beta_3$ at 2 and 24 hour PI.[209] This is evidenced by the increased fluorescence at the tumour margins, as β_3 integrin resides at these margins.

The use of antibodies to directly target cancer cells is a method illustrated in the work of Boonstra *et al*.[212] The team used anti-urokinase plasminogen activator receptor (uPAR) antibodies to target carcinomas in colorectal cancer due to the important roles in which uPAR plays in tumour invasion, angiogenesis and metastasis.[212] SPECT with ^{111}In, was combined with near-infra red fluorescence imaging, producing a SPECT/NIR antibody targeted imaging agent (ATN-658) capable of non-invasive diagnosis as well as using fluorescence to aid with fluorescence guided surgery applications. This is shown *via* the use of *in vivo* bio-distribution assays, as well as non-invasive SPECT imaging techniques. A subcutaneous HT-29 colorectal cancer model in mice was used, with mice being injected with 150 μg ATN-658. The work showed that during a period of 24-72 hours post injection, the tumour is clearly visible both using SPECT and NIR modalities. Bio-distribution patterns observed showed decreasing signals in the urine, blood, heart and lungs with time with increased signal in the liver due to the metabolisation and clearance of the imaging agent.

4.1.2 Prostate cancer targeted multimodal imaging.

Rapid technological advances over recent years have permitted the mainstream use of prostate imaging for the management of PCa. Imaging modalities such as multiparamagnetic ultrasound (mpUS), nuclear imaging and multiparamagnetic MRI (mpMRI) are used within diagnosis, staging and active surveillance/disease progression.[213] However, nuclear imaging methods have long been used in the diagnosis of PCa, with several PET/CT tracers being investigated for staging of primary PCa. Oncologic radio tracers such as 2-deoxy-2-(^{18}F)fluoro-D-glucose ([^{18}F]FDG) have been investigated for their ability to diagnose primary PCa tumours with limited success. This is attributed to low glucose metabolism in PCa lesions.[214,215] Krause *et al.* reported chlorine derivatives of labelled with [^{11}C] and [^{18}F] for the detection of primary PCa.[216] Imaging however was found to be heavily reliant on configuration as well as the number of micro carcinomas present, resulting in the author being unable to recommend the use of the method for use for front line scanning of primary tumours. Prostate-specific membrane antigen (PSMA), known also as glutamate carboxypeptidase II, is weakly expressed in normal prostate tissue and overexpressed in PCa. With expression levels directly associated with PCa aggressiveness.[217,218] Currently, ^{68}Ga-PSMA-HBED-CC (known also as ^{68}Ga-PSMA, ^{68}Ga-PSMA-11) is the most widely used radiotracer (PET/CT) within clinical practice for the detection of primary PCa.[219] Commonly however, ^{68}Ga-PSMA is combined with MR imaging modality (PET/CT/mpMR imaging) as well as a targeting agent in order to increase targeting accuracy/specificity while increasing image quality.[220–222] However, intrinsic pitfalls arising from the use

of PSMA as a targeting motif for the imaging of PCa, such as excess levels of

^{68}Ga-citrate as well as non-specific uptake within bone regeneration.[217]

The use of PET/OI methods for the detection of PCa have been

developed and have shown to have interesting real-world applications for the

treatment PCa, such as image guided surgery. The goal of this application is to

be able to completely resect the primary tumour (*via* radical prostatectomy)

whilst retaining continence as well as potency. Weber *et al.* were able to

demonstrate this by developing a targeted OI/MRI probe for the potential use

within image guided surgery.[223] The work presented targeted gastrin-releasing

peptide (GRP) receptor (GRPr) due to overexpression levels in PCa when

compared to normal prostate and other prostate (BPH) conditions, making

GRPr and ideal targeting modality. Within the study, a ^{68}Ga and fluorescent

GRPr (^{68}Ga-HZ220 (figure 4.2)) was synthesised with its dual modal imaging
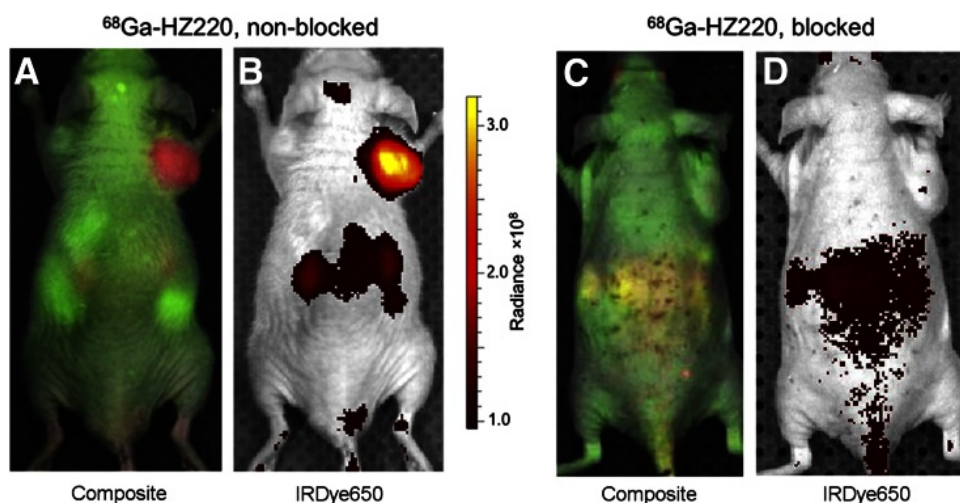
properties investigated.

Figure 4.2. *In vivo imaging of* ^{68}Ga-HZ220 GRPr targeted imaging probe of PC-3 xenografts in tumour bearing mice 1 h post injection (a and b), ^{68}Ga-HZ220 plus unlabelled ligand (c and d).[223]

Initially, animals with PC-3 xenographs were injected with ^{68}Ga-HZ220 and after 1 h post injection tumour are clearly visible using PET imaging. ^{68}Ga-HZ220 showed a good tumour uptake 4.63 ± 0.31%IA/mL. However, a large excess of unlabelled ligand (1.09 ± 0.09%IA/mL) was also up taken by the tumour. Indicating that the uptake was receptor-mediated.[223] NIRF imaging showed a large signal intensity for ^{68}Ga-HZ220 in PC-3 xenografts, confirming dual modal use of the probe. The work also detailed the increased level of fluorescence of ^{68}Ga-HZ220 in PC-3 xenografts when compared to a comparison blocking study carried out ([6.98 ± 0.61 vs. 1.73 ± 0.93 vs. 0.27 ± 0.01] · 108 p/s/cm^2/sr per μW/cm^2, P < 0.005).

4.1.3 Aims

The work within this chapter looks to build on previously published work by Sturge *et al.* wherein the relationship between the conformational state of Endo180 surface membrane and PCa diagnosis was investigated with the results of the study suggesting Endo180 could be used as a new potential diagnostic biomarker for PCa progression.[41,42] Within the work presented by Sturge and team, it was shown that the selective targeting of separate C-type lectin domains was possible via the use of specific mAb (CTLD-2/mAb A5.158, CTLD-4/mAb 39.10). Further to this, selectivity was shown to be determined *via* the conformational state in which Endo180 membrane protein was in within prostate tissue with a switch in conformation being aligned with PCa disease progression following the breakdown of the Endo180-CD147 complex (section 1.2.3.1).

The aim of the work presented is to describe a novel 'traffic light' PCa diagnostic system which has the potential to diagnose as well as monitor disease progression following the combination of previously described OI/MR tunable dual modal imaging probes (**InP/ZnS (2) – Gd.5.a**, chapter 3), with Endo180 conformational specific antibodies (mAb A5.158/39.10). Resulting in the synthesis of a targeted dual modal imaging probes which have the potential to selectively target and image both CTLD-2 and CTLD-4, therefore, opening the possibility to distinguish between indolent (mAb A5.158) and aggressive (mAb 39.10) PCa states in line with increase Endo180-CD147 binding complex breakdown.

4.2 Synthesis of OI/MR multimodal targeted imaging probe

4.2.1 Development of a targeted multimodal imaging probe *via* surface modification methods

The development of a targeted dual-modal OI/MR imaging probe requires modification of previously reported **InP/ZnS (2) – Gd.5(a)** with a conformational specific Endo180 antibody. As described in section 1.2.3, two specific mouse anti-human Endo180 mAbs - mAb 39.10 and mAb A5.158 - have application for respectively targeting CTLD-4 and CTLD-2 in the Endo180 protein backbone. With this in mind, two synthetic routes were devised with varying success and are described below. The first method looked at the direct surface modification of **InP/ZnS (2) – TGA** with endo180 conformational specific mAb's as well as Gd(III) DOTA derivative, in a one-step process. Whereas, the second method used a two-step synthesis process: First adding a PEG linker to the surface of **InP/ZnS (2) –TGA** in conjunction with Gd(III) chelate, before the addition of an Endo180-targeting mAb following purification in a secondary reaction. Both methods are outlined below, with physical and photophysical properties explained as well as any limitations experienced within the process.

4.2.1.1 Development *via* direct surface functionalisation method (one-step process)

Endo180 conformational specific antibodies (mAb 39.10 and mAb A5.158) were used for the surface modification of λ_{em} specific **InP/ZnS (2) – TGA** throughout this work, with mAb 39.10 used to modify the surface of QDs synthesised with $InCl_3$ (λ_{em} = ca 620 nm) and mAb A5.158 used to modify QDs synthesised with InI_3 (λ_{em} = ca 525 nm). This is complete in order to mimic a 'traffic light' detection system designed to detect both indolent and aggressive PCa with the use of mAb A5.158/39.10, green QDs (λ_{em} = ca 525 nm) being targeted to CTLD-2 and red QDs (λ_{em} = ca 620 nm) targeted to CTLD-4. This allows for the specific targeting of either the non-invasive (green) or invasive (red) phenotype of PCa following the disassociation of Endo180 and its binding partner CD147 (as explained in section 1.2.3). The surface modification of **InP/ZnS (2) – TGA** with the Endo180 mAb's was initially carried out in two separate one-step surface modification processes. One surface modification looked to add just Endo180 specific mAb to the surface, while the other, looked to add both Endo180 mAb and Gd(III) DOTA derivative (**Gd.5a**) at the same time. The first surface modification carried out as a control for use within biological assays (flow cytometry as well as imaging), with the later forming a targeted OI/MRI probe. These processes are depicted in scheme 4.1 below.
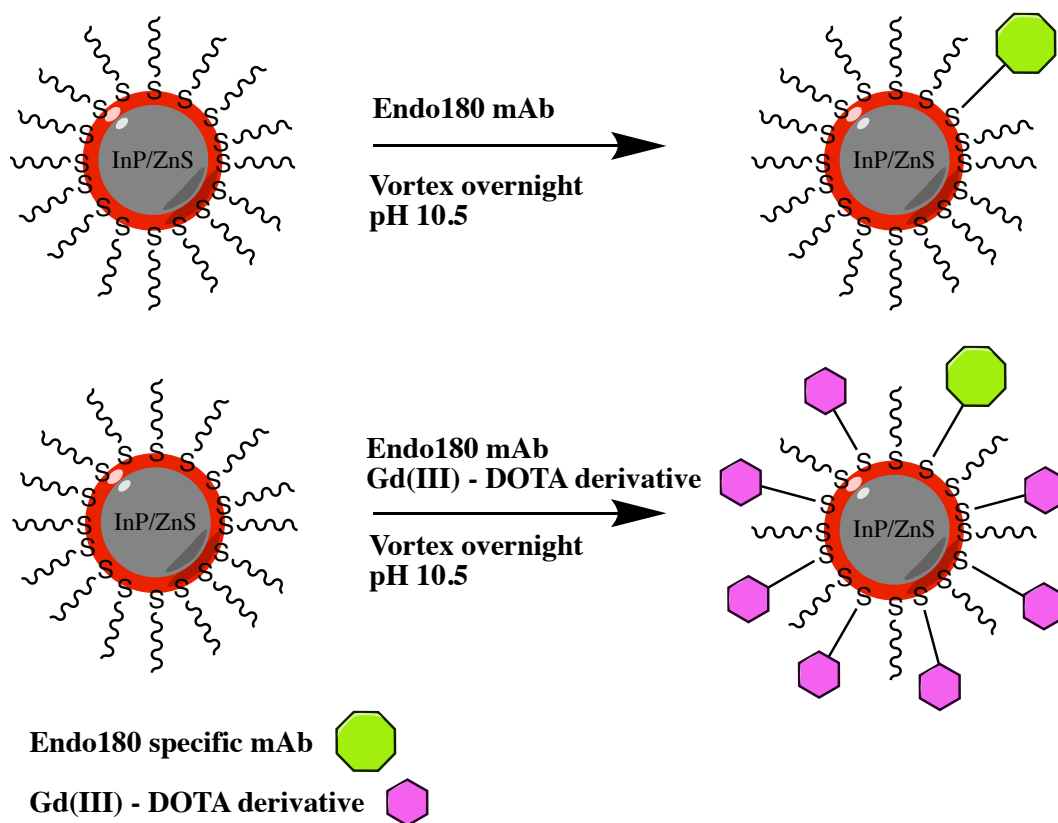
Scheme 4.1 showing two initial synthetic routes taken for the addition of Endo180 mAbs onto InP/ZnS (2) – TGA. (Top) shows the formation of InP/ZnS (2) – mAb, bottom route shows the formation of targeted OI/MRI probe.

Direct surface modification of **InP/ZnS (2) – TGA** with Endo180 conformational specific mAbs, was carried out in a 1:2 molar ratio, with respect to InP based QDs and is shown in more detain below in scheme 4.2.
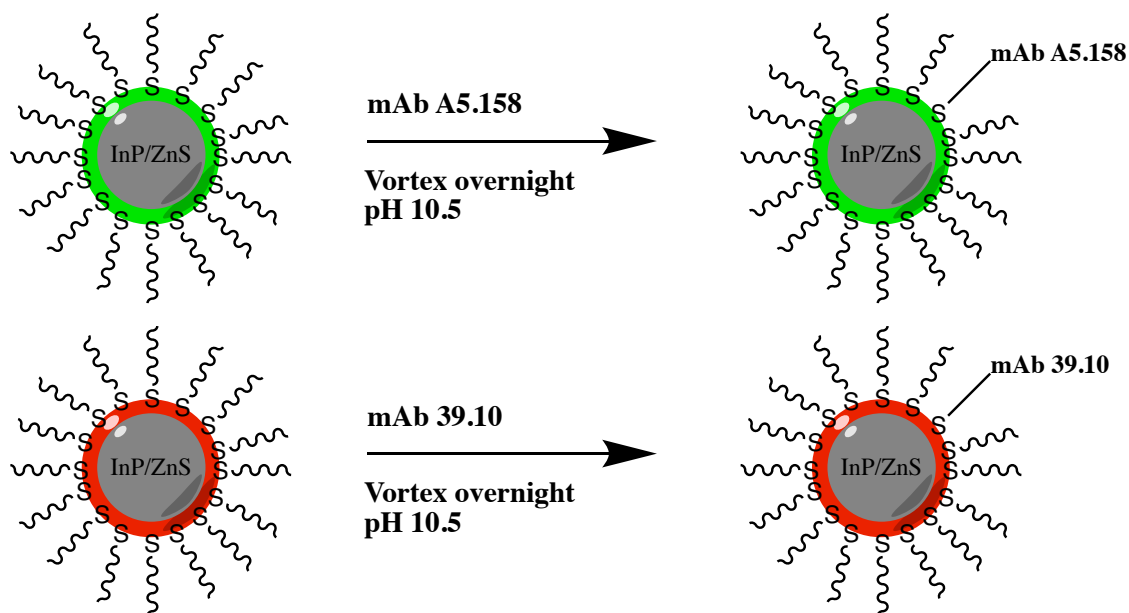
Scheme 4.2 InP/ZnS (2) – TGA underwent surface modification with Endo180 conformational specific mAb. (Top) InP/ZnS (2) $(\lambda_{em}$ = Ca. 525 nm) modified with mAb A5.158 targeting CTLD-2. (Bottom) InP/ZnS (2) (λ_{em} = Ca. 620 nm) modified with mAb 39.10 targeting CTLD-4.

The surface modification reactions depicted in scheme 4.2 are carried out at an elevated reaction pH of 10.5, TMAOH is used to increase the reaction pH ensure the deprotonation of any thiolates formed within the reaction, following the removal of TGA from the surface of **InP/ZnS (2)** QDs. A result of the aggressive nature of the reaction whilst using a vortex shaker. The reaction is also carried out in the presence of TCEP to drive the selective reduction of dithiol bond formation. Surface modifications are carried out using a vortex machine and are allowed to 'shake' violently overnight at room temperature. One limitation within the reaction, however, is the need to for the reaction to be carried out in a glass reaction vial as opposed to plastic. This due to product

from the reactions being unable to be removed from plastic eppendorf containers following vortex. The resultant products **InP/ZnS (2) – 39.10** and **InP/ZnS (2) – A5.158** are removed from glass reaction vials on completion and are able to be purified *via* spin filtration, washing with mΩ water. During the purification process, the pH of solution is brought back down to a physiological pH range of 7.4-8.0 due to the washing out of any base in the reaction solution. Resulting in purified **InP/ZnS (2) – 39.10** and **InP/ZnS (2) – A5.158** being formed.

The use of a direct surface modification method for the formation of OI/MR targeted imaging probes was outlined in scheme 4.1 (bottom) above. **InP/ZnS (2) – TGA** QDs were loaded into a glass vial (due to inherent problem with removal detailed above) with Gd(III) DOTA derivative (**Gd.5a**) and Endo180 specific antibody at a molar ratio of 1:1000:2. As with the surface modification of InP based QDs with endo180 specific mAb's, the pH was raised using TMAOH to 10.5 with TCEP added as in previous direct surface modification. Scheme 4.3 shows initial probe development using direct surface modification methodology.

Gd(III) - DOTA derivative
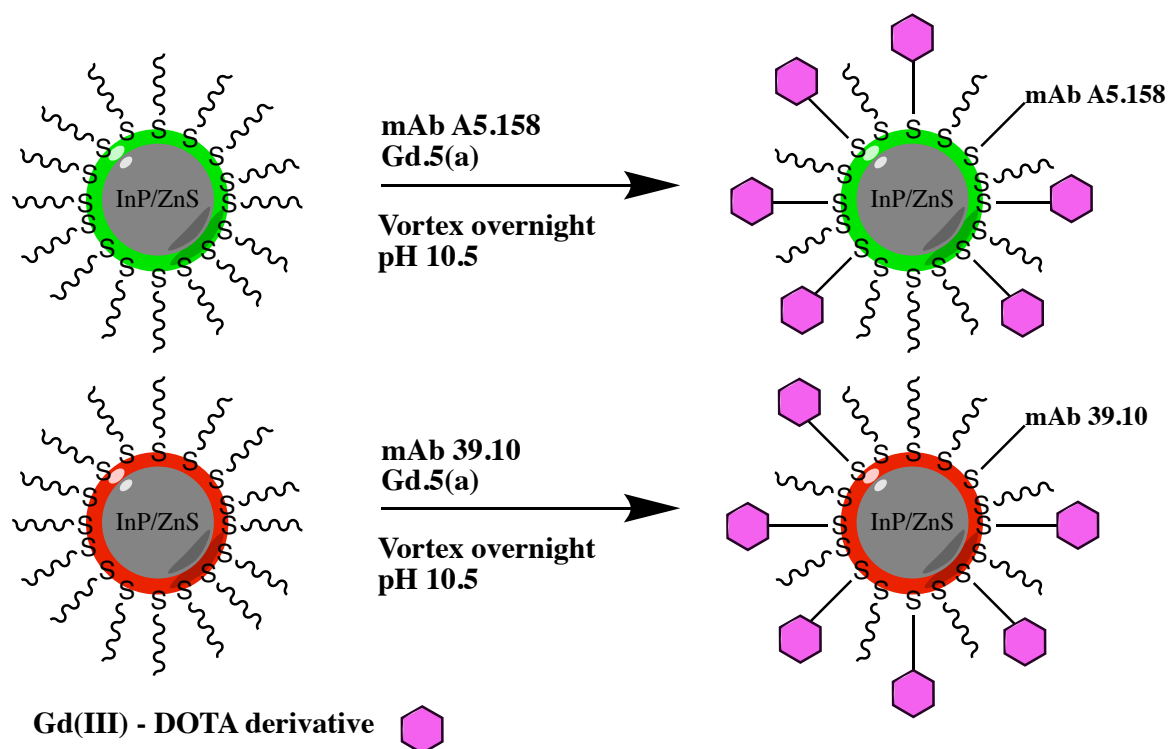
Scheme 4.3 (top) OI/MRI probe targeted probe for CTLD-2 due to the use of mAb A5.158. (bottom) OI/MRI probe targeted to CTLD-4 following the surface modification with mAb 39.10.

Following completion of the reaction after overnight vortex, purification of **InP/ZnS (2) – probe 39.10** and **InP/ZnS (2) – probe A5.158** follows the same purification method as above. Centrifuge filtration washing with mΩ water allows for any unreacted reactants to be discarded whilst product is kept due to increase in size following surface modification. Resuspension of OI/MR targeted probes using 100 μl of mΩ water following repeated washing results in **InP/ZnS (2) – probe 39.10** and **InP/ZnS (2) – probe A5.158** at a physiological pH (ca 7.4 – 8.0) which are able to be evaluated for their physical properties below.

4.2.1.2 Evaluation of probe development using a one-step modification methodology

On formation of **InP/ZnS (2) – mAb** (where mAb is either A5.158 or 39.10) an increase in hydrodynamic diameter (D_h) is expected, due to the addition of a large molecular weight (180 KDa) Endo180 conformational specific antibody. However, investigation into D_h showed a large amount of aggregation present following the direct addition of Endo180 mAb to the surface of **InP/ZnS (2) – TGA** when using a one-step surface modification method. Values of up to 223.0 nm were obtained (**InP/ZnS – mAb.39.10**), indicating a large amount of aggregation within the sample when compared to D_h of **InP/ZnS (2) – TGA** (4 – 6 nm). With all values obtained being shown in table 4.1 below.

QD	D_h (nm)	
	InI_3	$InCl_3$
InP/ZnS (2) - TGA	4.73	5.81
InP/ZnS (2) - mAb	152.0	223.0

Table 4.1 hydrodynamic diameter data for surface modified InP/ZnS (2) QDs with Endo180 specific mAb, showing aggregation present following the use of a one-step surface modification method.

Aggregation present following the addition of Endo180 conformational specific mAbs *via* direct surface modification) is attributed to the reaction conditions in which the surface modification is carried out. Reaction conditions include the use of elevated pH (10.5) for a period in excess of 12 h, as well as the use of

TCEP. These reaction conditions are considered to be too harsh for Endo180

specific mAbs to survive intact throughout the 12 h period for reaction to go to

completion. The use of high pH in conjunction with TCEP for the length of

reaction results in Endo180 mAbs becoming denatured and resulting in a large

amount of aggregation observed. Thus, resulting in larger than expected D_h

values of 152 nm and 223 nm (InI_3 and $InCl_3$ respectively) for **InP/ZnS (2) –**

mAb A5.158/39.10. Due to the aggregation observed, it was determined that

no further physical evaluation would be complete on **InP/ZnS (2) – mAb** which

had been synthesised using a direct surface modification methodology. Rather,

an alternative method for the synthesis of both **InP/ZnS (2) – mAb** and or

InP/ZnS (2) – probe was derived and outlined below in section 4.2.1.3, before

undergoing physical evaluation.

4.2.1.3 Development of OI/MRI targeted probe *via* two-step surface modification

A move to a two-step surface modification for the synthesis of **InP/ZnS**

(2) – mAb and targeted OI/MR imaging probe (**InP/ZnS (2) – probe**) was

devised following large amounts of aggregation which resulted from a one-step

synthesis methodology. The devised two-step process utilizes the addition of a

PEG NHS dithiol ester (figure 4.3) to the surface of **InP/ZnS (2) – TGA** as a

precursor to the addition of Endo180 specific antibody. Thus, allowing for a

reduction in the reaction pH required (7.4 – 8.4) as well as the elimination of

the need for TCEP, due to the Gd(III) DOTA derivative being added during step

one. The lower pH, no need for TCEP and lower reaction time of 2 h during

addition of mAb was hoped would all lead to a lower level of overall aggregation when compared to the one-step or direct surface modification method.
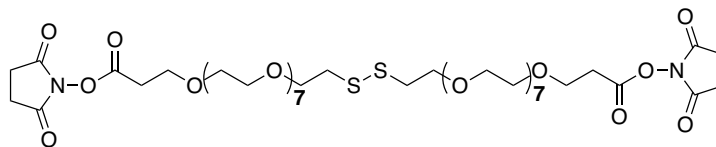

Figure 4.3 Dithiol NHS ester used to functionalise surface of InP/ZnS (2) – TGA during step one of two-step surface modification process.

Initially, as within the one-step process, **InP/ZnS (2) – TGA** QDs were loaded into a glass vial with TCEP and the pH adjusted to 10.5 using TMAOH. Reaction pH was again increased to 10.5 promote the selective reduction of dithiol bonds during the reaction. However, PEG NHS ester is added in a molar ratio of 1:1 with respect to QDs. Thus, allowing for Endo180 antibody to be added to the surface following the initial reaction step *via* the NHS ester, done at a lower pH in step-two. On completion of overnight (12 h) vortex, the purification and lowering of reaction pH was undertaken (7.4 – 8.0) using centrifuge filtration methods, before being suspended in 100μl of mΩ water. Resulting in **InP/ZnS (2) – NHSPEG**. The addition of Endo180 specific antibodies was complete *via* the reaction of purified **InP/ZnS (2) – NHSPEG** in a 1:1 molar ratio with selected antibody (mAb 39.10 modifying the surface of QDs synthesised with InCl$_3$ and mAb A5.158 used to modify the surface of QDs synthesised with InI$_3$) and vigorously stirring for 2 h at pH 7.4 – 8.0. This reaction can also be carried out without the use of TCEP as the control of dithiol bonds is no longer needed. The shorter reaction time of 2 h for the addition of Endo180 mAb is achieved

following surface activation of **InP/ZnS (2) –TGA** with NHSPEG, resulting in decreased reaction times.

The two-step surface modification method was then employed for the synthesis of targeted OI/MR imaging probes. However, in the case of **InP/ZnS (2) – NHS – probe**, the loading of Gd(III) DOTA derivative as well as dithiol PEGNHS ester was observed within the first step at elevated pH. This results in a dual modal probe following the addition of Endo180 conformational specific mAb after purification methods. Endo180 specific mAbs were able to be added successfully at a pH range of 7.4 – 8.0 over a period of 2 h (vortex) resulting in the formation of **InP/ZnS (2) – NHS – mAb** and **InP/ZnS (2) – NHS – probe** which are able to be assessed for their physical and photoluminescent properties.

4.2.1.4 Evaluation of physical and photophysical properties following use of two-step methodology

Initially, D_h of **InP/ZnS (2) – NHS –mAb** and **InP/ZnS (2) –NHS – probe** was explored and compared to values obtained when synthesised using a one-step direct synthesis method. Values are shown in table 4.2 below, values have also been shown for **InP/ZnS (2) – TGA** and **InP/ZnS (2) – NHS** for comparison.

QD	D_h (nm)	
	InI_3	$InCl_3$
InP/ZnS (2) – TGA	4.73	5.81
InP/ZnS (2) - NHS Ester	12.79	13.71
InP/ZnS (2) - NHS – mAb	16.20	16.58
InP/ZnS (2) - NHS – Probe	19.16	17.03

Table 4.2 comparison of D_h of InP/ZnS (2) – NHS – mAb and InP/ZnS (2) – NHS – probe with InP/ZnS (2) – TGA and InP/ZnS (2) – NHS ester derivatives. All values shown were recorded at 25°C and pH of 7.4-8.0

As can be seen from table 4.2, when using a two-step synthesis method for the direct surface modification of **InP/ZnS (2) – TGA**, D_h increased, with values being recorded in a range of 16 and 20 nm (with large D_h being observed for OI/MR targeted imaging probe of up to 19.16nm (InI_3)). Increase in D_h with surface modification follows a trend which is expected, with size being with increased following the addition of a large (180kDa) antibody. No aggregation was observed on completion of reaction within **InP/ZnS (2) – NHS – mAb** or **InP/ZnS (2) – NHS – probe**. This was attributed to the Endo180 specific antibody addition following the reaction pH being lowered to below 8.0 and the omission of TCEP during the reaction preventing denaturation of the antibody during the reaction process, as observed during the one-step process.

An insight into the charge exhibited on the surface of both **InP/ZnS (2) – NHS – mAb** (mAb = 39.10 or A5.158) and **InP/ZnS (2) – NHS – probe** can be given using surface zeta potential. The surface zeta potential was recorded at a pH of 7.4 – 8.0 and is shown in table 4.3 below

QD	Zeta (mV)	
	InI_3	$InCl_3$
InP/ZnS (2) – TGA	-20.3	-25.3
InP/ZnS (2) - NHS - mAb	-27.9	-31.2
InP/ZnS (2) - NHS - Probe	-24.4	-14.7

Table 4.3 showing surface zeta potentials (mV) for InP/ZnS (2) – NHS – mAb and InP/ZnS (2) – NHS – Probe. Recorded at 25°C and pH of 7.4-8.0

Table 4.3 suggests a move to a more negative surface charge upon addition of Endo180 specific antibody to the surface, this is consistent with both mAb 39.10 and mAb A5.158 with surface charges of -31.2 and -27.9 mV. However, in the case of **InP/ZnS (2) – NHS – Probe**, more positive values of up to -14.7 mV were observed. A value this positive is surprising due to the dual surface loading which is expected on **InP/ZnS (2)** with Gd(III) DOTA derivative (expected to carry a -1 charge) and Endo180 mAb. When compared to values obtained for **InP/ZnS (2) – Gd.5a** in section 3.5.2, a much more negative surface is observed with values of -28.30 and -27.63 mV when QDs were synthesised with InI_3 and $InCl_3$ respectively. Therefore, leading to the conclusion that surface loading of Gd(III) DOTA derivative within **InP/ZnS (2) – NHS – probe** is lower than that of **InP/ZnS (2) – Gd.5**.

In order for synthesised **InP/ZnS (2) – NHS – probe** to be considered as a viable dual modal imaging probe, both OI and MR viability has to be confirmed. First the luminescent properties (including PLQY) were investigated of **InP/ZnS (2) – NHS – probe**, allowing for comparisons to be drawn with

InP/ZnS (2) –TGA as well as dual modal probes synthesised earlier within this body of work.
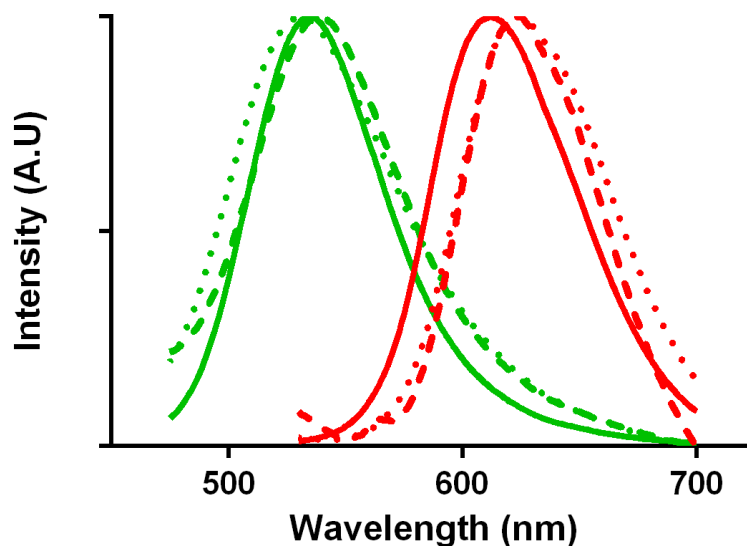

Figure 4.4 comparison of λ_{em} of InP/ZnS (2) – TGA (solid line), InP/ZnS (2) – Gd.5a (hash line) and InP/ZnS – NHS – probe (dotted line). Green) InP/ZnS QDs synthesised using InI$_3$, red) InP/ZnS QDs synthesised using InCl$_3$.

On surface modification of **InP/ZnS (2) – TGA** to form both a targeted (**InP/ZnS (2) – NHS – probe**) and non-targeted (**InP/ZnS (2) – Gd.5a)** dual modal OI/MR imaging probe, maximum λ_{em} can be seen to remain constant, with no large bathochromic shifts (figure 4.4) following surface modification. This is observed regardless of In(III) halide used during the synthesis of InP based QDs. λ_{em} maxima for synthesised **InP/ZnS (2) – NHS - probes** were found to be λ_{em} = 532 nm and λ_{em} = 625 nm (InI$_3$ and InCl$_3$ respectively) and as with all other QDs synthesised through this thesis, were found to have large λ_{ex} ranges.

These phenomena are shown in the 3D excitation/emission spectra below (figure 4.5).
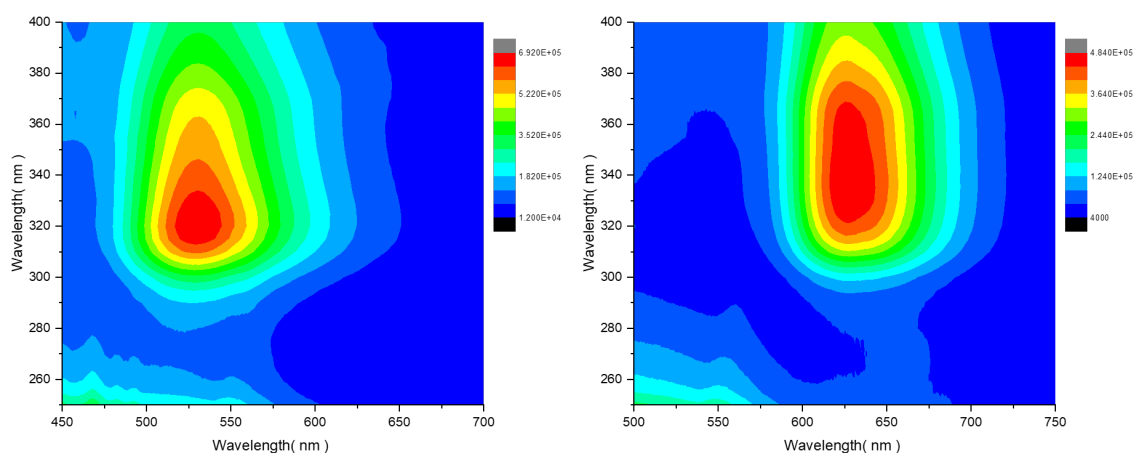

Figure 4.5 3D excitation vs emission spectra of InP/ZnS (2) – NHS – Probe. (left) λ_{em} = 532, InI$_3$. (right) λ_{em} = 625 nm, InCl$_3$.

Products produced from the two-step synthesis method presented above were investigated for PLQY properties following the formation of OI/MRI targeted dual modal probe. PLQY is reported at 6.64% and 3.43% (InI$_3$ and InCl$_3$ based QDs/probes respectively). Values reported are seen to be similar to previously synthesised **InP/ZnS (2) – Gd.5** (section 3.5.3) dual modal probes. Obtained values for non-targeted dual modal probes ranged from 5.0% to 19.9% (Table 3.8). Therefore, following the addition of a targeting Endo180 mAb, PLQY is able to be maintained. The ability to maintain PLQY is attributed to the large percentage of slow component make up within the lifetime decay component shown in table 4.4 below. Therefore, resulting in increased radiative decay as appose to non-radiative decay pathways and loss of PLQY.

QD	Lifetime decay component / ns			
	InI_3		$InCl_3$	
	Fast	Slow	Fast	Slow
InP/ZnS (2) – NHS - Probe	1.77	11.64	1.27	11.75
	46%	54%	54%	46%

Table 4.4 Comparison in non-radiative decay lifetime (ps) between InP/ZnS (2) – NHS – Probe (InI_3 – mAb = A5.158, $InCl_3$ – mAb = 39.10).

The increase in slow decay component percentage within InI_3 when compared to $InCl_3$ within **InP/ZnS (2) – NHS – Probe** results in the increase PLQY observed (6.6% to 3.4% respectively) when comparing between the two synthesised OI/MR targeted imaging probes.

4.3 Biological evaluation of targeting OI/MR imaging probe

4.3.1 Cell lines used within *in vitro* cellular validation

In order to biologically evaluate the OI/MR probes and their constituent components used in their synthesis, three PCa cell lines previously confirmed to express different levels of Endo180, and Endo180-negative and positive breast cancer cell line controls, were chosen for *in vitro* validation studies. RWPE-1 prostate epithelial cells were used to represent the epithelium in the peripheral zone of the normal prostate without oncogenic mutation. RWPE1 cells express Endo180,[42] allowing for the study of Endo180 under non-oncogenic conditions. RWPE-2 cells were used due to their ability to act as cancer-like cells and represent an 'intermediate' step between RWPE-1 cells (non-cancerous) and PC-3 cells (metastatic). RWPE-2 cells were derived by the transformation of RWPE-1 cells with the oncogene Ki-ras, giving them cancer-like properties.[42] PC-3 cells were derived from a stage IV PCa adenocarcinoma following metastasis to a secondary bone cancer site. By using all three cell lines (RWPE-1, RWPE-2 and PC-3) the Endo180-targeted probes can be assessed in different stages of PCa progression. Likewise, MCF7 cells derived from breast cancer adenocarcinoma were included as a negative control due to their negligible/low levels of Endo180 expression.[42,43,58] MCF7-E cells were used as a positive control that overexpress Endo180 following transfection of parental MCF7 cells[42,43,206]. Endo180 expression levels in RWPE-1, RWPE-2, PC-3, MCF7 and MCF7-E cells were confirmed by western blot analysis, data for which is not shown within this thesis due to images being lost with no time to generate new date. Initially, protein lysates were formed following the procedure outlined in

6.16.1 before a Pierce™ BCA protein assay was complete, allowing for 50μg/ml

to be added for each cell line. Endo180 expression levels within normal prostate

and PCa cell line models were determined to be in the following order: PC-3 >

RWPE-2 > RWPE-1. MCF7 cells were confirmed to be Endo180-negative and

MCF7-E cells were confirmed to express a high level of Endo180.

4.3.2 In-vitro cellular studies of OI/MR targeted imaging probes.

4.3.2.1 Toxicity of InP/ZnS (2) quantum dots in cells

Despite possessing many benefits within the design of dual modal

imaging probes such as their broad λ_{ex}, narrow $\lambda_{em,}$ and ability to be used as a

'scaffold' for loading of multimeric surface payloads (such as Gd(III) chelates).

QDs as discussed in section 1.5.3.2 have previously seen reports toxic effects

when used within the biological setting usually in the form of heavy metal

leaching, due to lack of stability when used in a biomedical application resulting

in cytotoxic effects. **InP/ZnS (2) – TGA** QDs used within this work therefore,

have been evaluated for cytotoxic effects within all cells lines (RWPE-1, RWPE-

2, PC-3, MCF7 and MCF7-E) at concentration ranges used for imaging with

OI/MR targeted imaging probes (**InP/ZnS (2) – NHS – probe**).

InP/ZnS (2) – TGA QDs (synthesised with both InI_3 and $InCl_3$) at

concentrations ranges of 0.03 to 10.0 mM were used to treat all cell types

overnight (>12 h duration). The cell counting kit-8 (CCK-8) reagent was added

to determine the percentage of living cells following addition of QDs (detailed in

section 6.18). The bio-reduction of WST-8 present in CCK-8 to a water-soluble

formazan dye (figure 4.6) is directly proportional to the number of viable cells. With the number of viable cells being able to be determined by absorbance, due to WST-8 formazan having a large absorbance maxima at 460nm.

WST-8   WST-8 Formazan
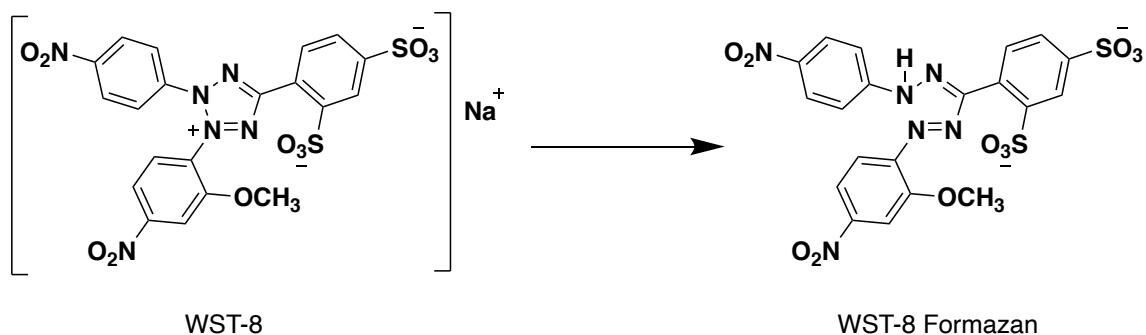
Figure 4.6 bio reduction reaction of WST-8 to water soluble WST-8 formazan used within viability assay of cell counting kit-8 (CCK-8).

Initially, all cell lines underwent incubation with **InP/ZnS (2) – TGA** which had been synthesised with InI_3 (λ_{em} = 525 nm). On completion of incubation, 10 µl of CCK-8 testing solution was added to all wells and a further 2 h incubation time was allowed. Following this, absorption was read on a plate reader using λ_{ex} = 450 nm. The viability of cells following incubation with **InP/ZnS (2) – TGA** (λ_{em} = 525 nm) are shown below in figure 4.7.
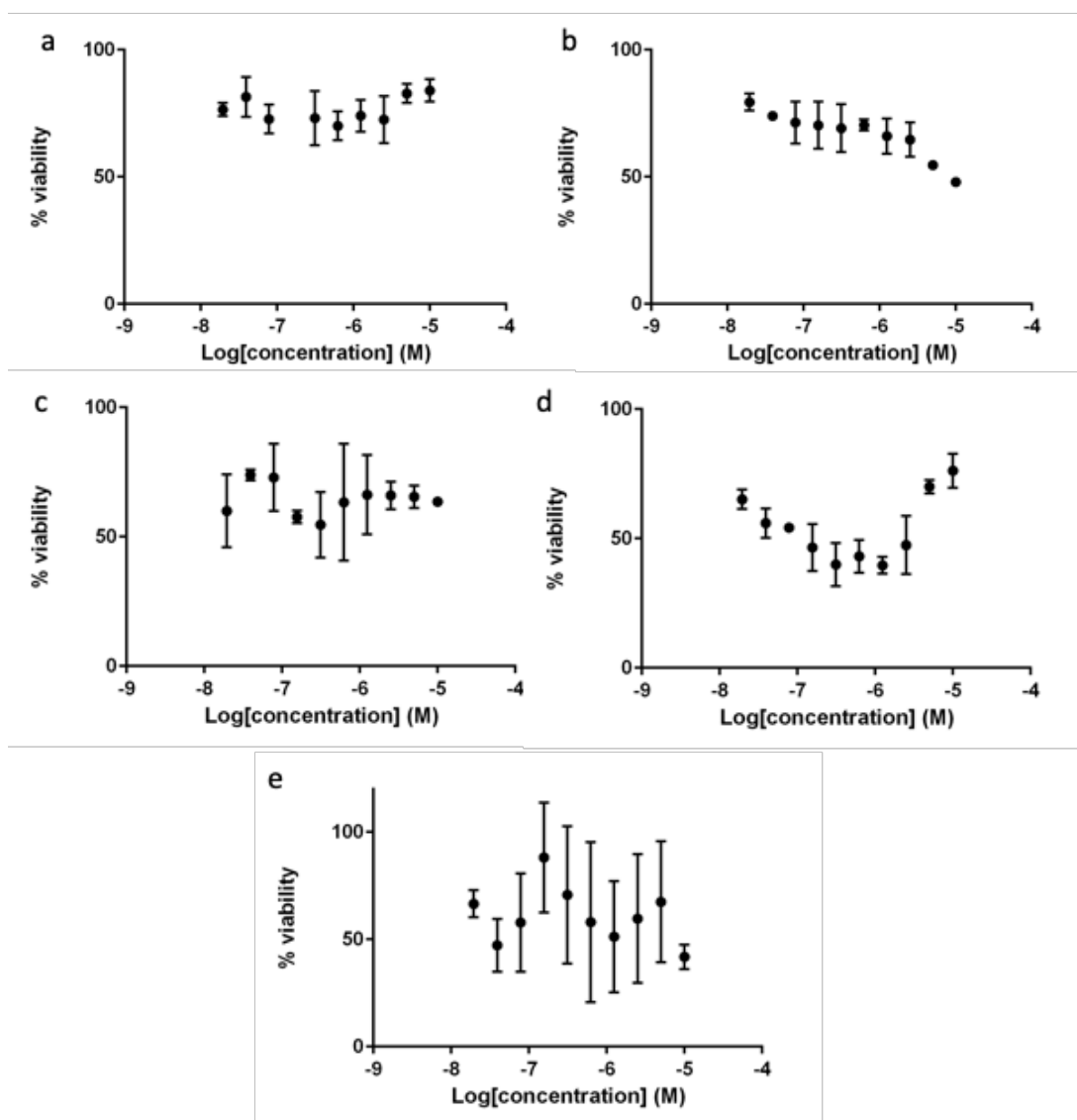
Figure 4.7 CCK-8 assays following overnight incubation of InP/ZnS (2) – TGA (λ_{ex} = 525 nm) with RWPE-1 (a), RWPE-2 (b), PC-3 (c), MCF7 (d) and MCF7-E (e) cells. Data shown is the combination of 3x technical repeats with error bars.

Cells lines also underwent overnight incubation with **InP/ZnS (2) – TGA** synthesised with $InCl_3$ (λ_{em} = 620 nm), allowing CCK-8 assay to be complete. Evaluation of cell viability is shown in figure 4.8.
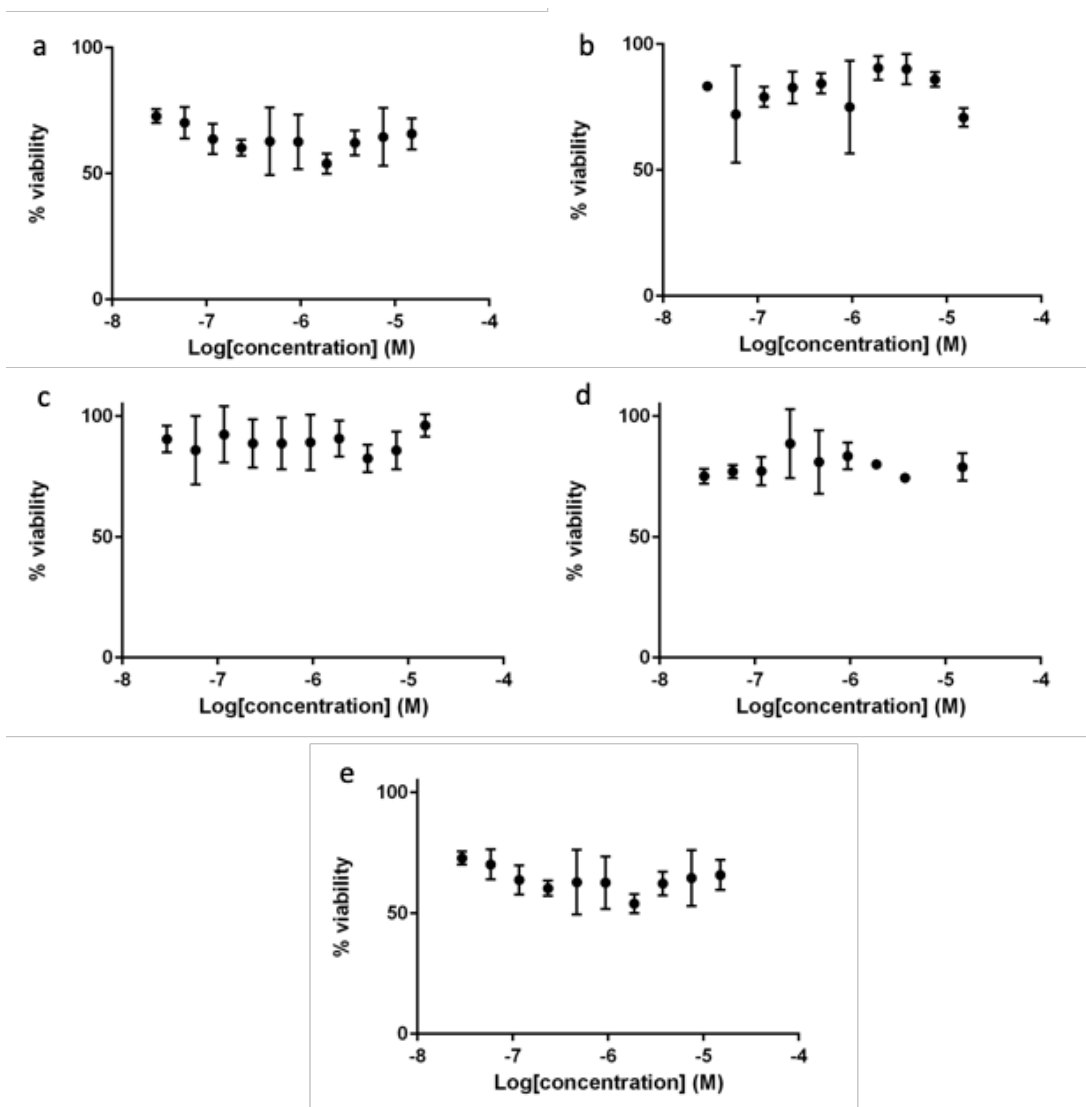
Figure 4.8 CCK-8 assays following overnight incubation of InP/ZnS (2) – TGA (λ_{ex} = 620 nm) with RWPE-1 (a), RWPE-2 (b), PC-3 (c), MCF7 (d) and MCF7-E (e) cells. Data shown is the combination of 3x technical repeats with error bars

At concentrations used to synthesise **InP/ZnS (2) – mAb – probe** (0.1 µM), cell viability appears to be retained (above 50% viability) when compared to non-treated cells following overnight incubation with **InP/ZnS (2) – TGA** (InI$_3$ and InCl$_3$). However, one point of note is the viability of cells prior to the addition of **InP/ZnS (2) – TGA**. In all CCK-8 assays shown, all of the cells show less than 100% viability including cells used as the 100% comparator indicating losses in

the cell lines prior to incubation with **InP/ZnS (2) – TGA**, with these losses attributed to cell death during the culturing of the cell lines as oppose to cell death when treated with **InP/ZnS (2) – TGA**. Initial confirmation of the non-toxic effects of **InP/ZnS (2) – TGA** at concentrations used for imaging was able to be shown using a small sample size within this work (using technical repeats, with some cell death in cells prior to work being complete), however, for quantitative confirmation of the non-toxic effects of **InP/ZnS (2) – TGA** further repeats with fresh cells of increased viability would have to be undertaken.

4.3.2.2 Specific binding affinity of synthesised OI/MR imaging probe

A hurdle within the cellular validation of synthesised OI/MR targeted imaging probe **InP/ZnS (2) – NHS – probe** (mAb = 39.10/A5.158), is the determination of cell surface specific binding to cell lines following the addition of Endo180 conformational specific mAbs to previously synthesised non-targeted OI/MR imaging probes (chapter 3). Flow cytometry, specifically fluorescence-activated cell sorting (FACS), was used within this work to determine the percentage surface binding of OI/MR targeted imaging probes to Endo180 protein. InP/ZnS QDs integrated within targeted OI/MR probes are used as a detection system within FACS analysis carried out, as opposed to a traditional fluorescent secondary antibody (such as Alexa Fluor-488). Thus, allowing for the specific surface binding of OI/MR targeted imaging probes to be determined experimentally, with **InP/ZnS (2) – TGA** QDs exhibiting a maximum λ_{em} of 532nm and 620 nm (for QDs synthesised with InI_3 and $InCl_3$ respectively), these wavelengths overlap with two commonly used biological

fluorescent dyes (FITC-A and Q-DOT 605). Therefore, **InP/ZnS –TGA (2)**

emission properties are exploited within the FACS analysis completed

throughout this work allowing for the evaluation of specific binding of

synthesised OI/MR targeted imaging probes to Endo180 surface membrane

protein present within a range of cells to be determine. As well as using FACS

analysis for the specific binding of **InP/ZnS (2) – NHS – probes**, the use of

controls to investigate non-specific surface binding of constituent parts of the

targeted imaging probe to the cell surface was also completed. Controls include,

InP/ZnS (2) – TGA QDs, **InP/ZnS (2) – NHS – mAb** (mAb A5.158/39.19) and

cell only analysis being complete before the addition of the fully synthesised

probe was investigated to a range of prostate cell lines .

RWPE-1, RWPE-2, MCF7 and MCF7-E cell lines (PC-3 cell line was not

included in FACS evaluation due to issues with cell growth) were prepared as

outlined in section 6.18, followed by incubation with 0.1 μM OI/MR targeted

imaging agent (controls were also incubated with cell lines at a concentration of

0.1 μM). On completion of incubation (20 minutes), washing with PBS was

undertaken to remove any unbound OI/MR targeted imaging probe, before

being redispersed in PBS solution (1 ml). In order to quantitatively calculate

both specific and non-specific surface binding of synthesised OI/MR dual modal

targeted imaging probes as well as controls used, specific binding was

determined *via* the use of percentage frequency of specific binding with respect

to cell only control with results being shown in table 4.5.

Imaging agent	Cell line			
	RWPE-1	RWPE-2	MCF7	MCF7-E
Cell only	0.5%	7.9%	19.2%	7.21%
InP/ZnS (2) – TGA	29.3%	52.5%	37.6%	66%
InP/ZnS (2) - NHS – mAb	20.9%	29.3%	54.1%	78.9%
InP/ZnS (2) - NHS - Probe	35.8%	49.9%	37.7%	78.8%
Imaging agent	Cell line			
	RWPE-1	RWPE-2	MCF7	MCF7-E
Cell only	5.8%	4.8%	4.3%	10.3%
InP/ZnS (2) – TGA	19.2%	63.2%	72.9%	69.5%
InP/ZnS (2) - NHS – mAb	96.7%	76.6%	68.1%	76.2%
InP/ZnS (2) - NHS - Probe	22.6%	25.5%	20.7%	78.8%

Table 4.5 Values for percentage specific binding of on InP/ZnS (2) – NHS – Probe (mAb A5.158) (top) and InP/ZnS (2) – NHS – probe (mAb 39.10) (bottom) for all cell lines tested following FACS analysis, included within the table are the values for percentage specific binding of controls undertaken (cell only, QD only and probe without Gd(III) on the surface of InP/ZnS (2) (InP/ZnS (2) – NHS – mAb))

On the completion of FACS analysis, **InP/ZnS (2) – TGA** QDs can be seen to exhibit a large amount of non-specific surface binding in all cell lines which have undergone testing. However, previously discussed by Tamang and shown in further investigations (section 4.3.4, figure 4.12) InP based QDs which have been used within this work have the possibility of a large cellular uptake, due to their small size and high negative charge (phase transfer being complete with TGA).[181] This is evident with percentage specific binding values of up to 68.6% (MCF7, InCl$_3$) being recorded, highlighting the potential of non-specific binding/cellular uptake of **InP/ZnS (2) – TGA** when TGA is used as a surface capping ligand. In the work presented by Tamang, the author suggests an increase in PLQY when using TGA as a capping ligand for phase transfer results

218

in having a detrimental effect with regard cellular uptake due to the size and charge of the resultant InP/ZnS QDs produced.[181] Issues with cellular uptake are exhibited within this work when using **InP/ZnS (2) – TGA**, The very small (<10 nm), highly negative (-30mV) QDs produced following phase transfer using TGA show large amounts of non-specific surface binding as described by Tamang in all cell lines used evident in the results in table 4.5. However, as discussed in section 4.3.4, non-specific binding observed can also be attributed to the internalization of **InP/ZnS (2) – TGA** during primary incubation period**.** This is observed despite the incubation procedure being carried out at a reduced temperature (4°C), used in an attempt to reduce cellular internalization.

Figure 4.9 depicts the FACS analysis results of synthesised OI/MR targeted imaging probes and derivatives following incubation with RWPE-1 cell line, changes in percentage specific binding are able to be seen with exact values given in table 4.5.
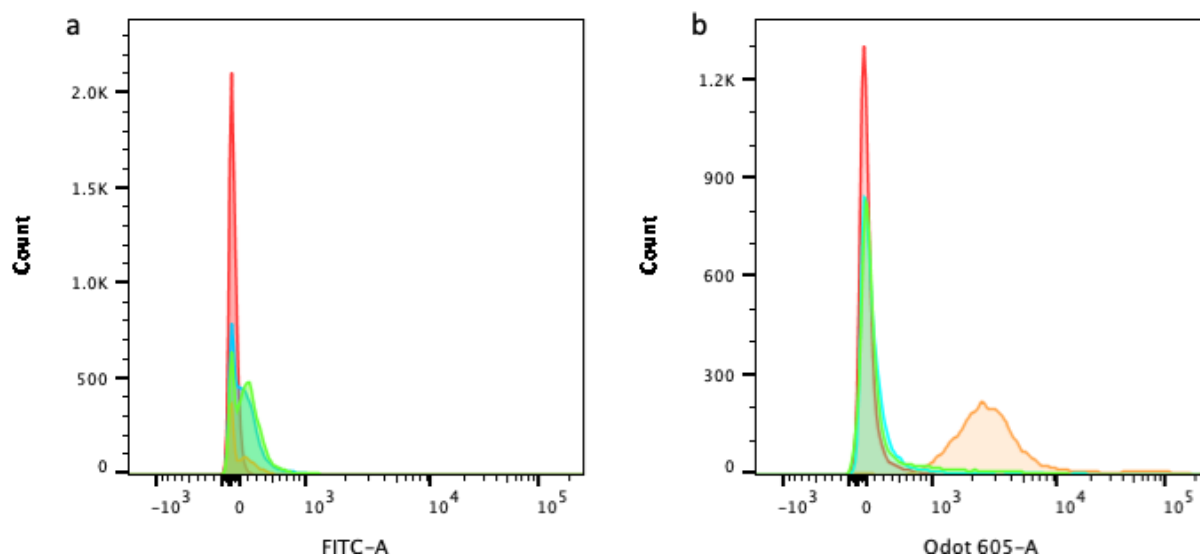
Figure 4.9 FACS analysis of RWPE-1 cell line using InP/ZnS (2) – TGA synthesised using InI_3 – mAb A5.158 (a) and $InCl_3$ – mAb 39.10 (b). containing RWPE-1 cells (red) as control, InP/ZnS (2) – TGA (blue), InP/ZnS (2) – NHS - mAb (orange) and InP/ZnS (2) – NHS – probe (Green). FITC-A used for probes λ_{em} = 535 nm, Qdot 605-A used for probes λ_{em} = 620 nm

Following incubation, percentage specific binding values for synthesised OI/MR targeted imaging probes and constituent parts are seen to rise, with a maximum value of 90.9% achieved for **InP/ZnS (2) – NHS – 39.10** (figure 4.9.b orange). As discussed previously, incubation with **InP/ZnS (2) – TGA** results in the increase of percentage surface specific binding due to issues with non-specific binding/cellular uptake. With this able to be seen with values recorded 29.3% and 19.2% (A5.158 and 39.10 respectively). On the completion of FACS analysis with **InP/ZnS (2) – NHS – mAb** with RWPE-1 cells, increases of 20.9% and 96.7% are observed (A5.158 and 39.10 respectively). Despite the increase in percentage specific surface binding recorded for **InP/ZnS (2) – NHS – A5.158** (figure 4.9.a.orange) a minimal shift is seen with this attributed to the high background cell count when compared to recorded cells. Therefore, resulting in

a smaller than expected shift for **InP/ZnS – NHS – mAb A5.158** following the targeting of CTLD-2 within the Endo180 backbone. A large increase in percentage specific binding following incubation with **InP/ZnS (2) – NHS – mAb 39.10** with a value of over 90% is attributed to the possible targeting of Endo180 specific mAb 39.10 to CTLD-4 present on the surface of RWPE-1 cells. However, the large increase in percentage surface binding is not seen when targeting the available CTLD-2 domain with **InP/ZnS (2) – NHS – mAb A5.158** (figure 4.9.a. orange), therefore, the increase in specificity is more likely due to a combination of both the direct targeting of CTLD-4 as well as a large amount of non-specific binding following improper washing during the preparation of cells. Analysis of **InP/ZnS (2) – NHS – Probe** resulted in percentage specific binging values of 35.8% and 22.6% respectively. When tested against the RWPE-1 cell line, OI/MR targeted imaging probes exhibit similar specific binding values to that of **InP/ZnS (2) – TGA**, suggesting no specific binding to the surface of the RWPE-1 cell line.

The percentage specific binding against RWPE-2 cell line is show in figure 4.10, with analysis reported in table 4.5 and the differences within specific binding following incubation with OI/MR targeted imaging probes and derivatives. **InP/ZnS (2) – NHS – mAb** and **InP/ZnS (2) – NHS – Probe**.
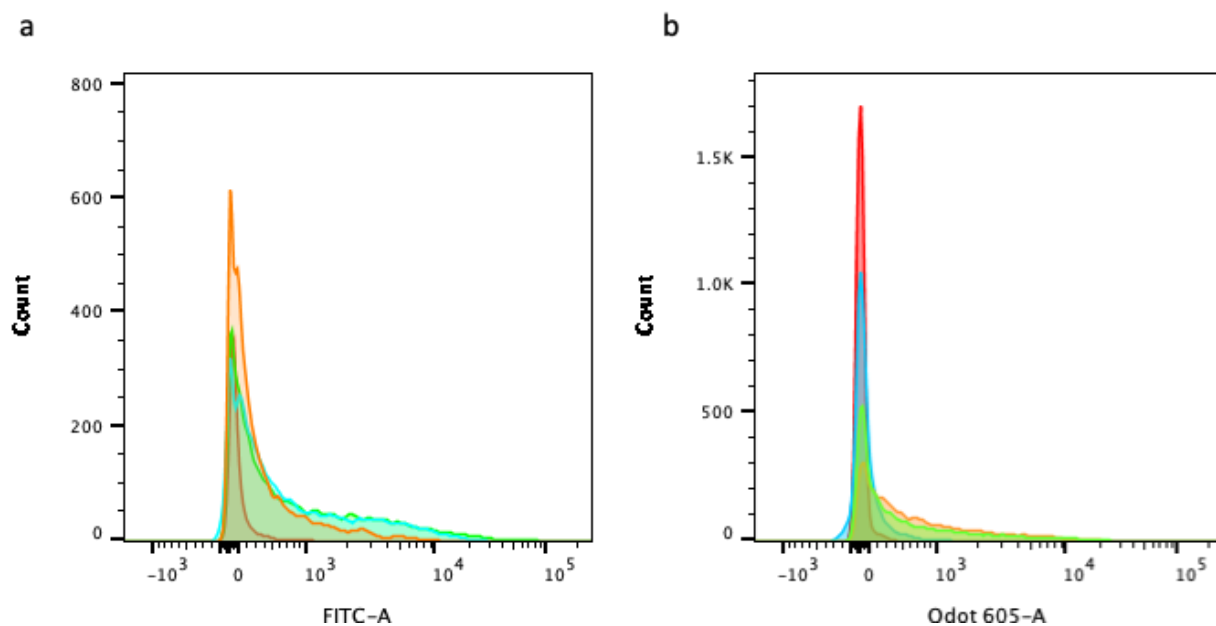
Figure 4.10 FACS analysis of RWPE-2 cell line using InP/ZnS (2) – TGA synthesised using InI_3 – mAb A5.158 (a) and $InCl_3$ –mAb 39.10 (b). containing RWPE-2 cells (red) as control, InP/ZnS (2) – TGA (blue), InP/ZnS (2) – NHS – mAb (orange) and InP/ZnS (2) – NHS – probe (Green). FITC-A used for probes $\lambda_{em} =$ 535 nm, Qdot 605-A used for probes $\lambda_{em} = 620$ nm

RWPE-2 cells, due to their ability to 'act' as a PCa-like cell are expected to show specific binding when using both Endo180 specific antibodies with both CTLD-2/4 binding sites available. Initially, percentage specific binding of **InP/ZnS (2) – TGA** QDs were evaluated with values of 52.5% and 63.5% obtained respectively. The increase when compared to the RWPE-1 cell line is attributed to both an increase of cell internalization (small size and high negative charge) of **InP/ZnS (2) –TGA** as well as poor sample preparation (improper washing) prior to the analysis being complete, resulting in large amounts of **InP/ZnS (2) - TGA** being present through non-specific surface binding. Figure 4.10 depicts the shifts in FACS analysis showing the percentage surface binding between of

InP/ZnS (2) – NHS – mAb and **InP/ZnS (2) – NHS – Probe**. A two-fold increase

in specific binding (29.3% to 49.9%) was observed (figure 4.10.a) following the

use of OI/MR targeted probe (mAb – A5.158) when compared to **InP/ZnS (2) –**

NHS – mAb (mAb = A5.158). In comparison, difference in binding shown in

figure 4.10.b rises to 71.84% **InP/ZnS (2) – NHS – mAb** (mAb - 39.10) whereas

the binding of **InP/ZnS (2) – NHS – Probe** (mAb 39.10) falls to 20.74%. The

large rise in binding specificity when using **InP/ZnS (2) – NHS – mAb** (mAb –

39.10) is possibly due to the direct targeting of CTLD-4 within RWPE-2 cells.

However, it is more likely due to the non-specific binding which was previously

observed within the RWPE-1 cell line. **InP/ZnS (2) – NHS – probe** (mAb 39.10)

in both RWPE-1/2 decreases in surface specific binding when compared to

InP/ZnS (2) – NHS – mAb. A possible reason for the drop observed in

specificity of OI/MR targeted imaging probes when compared to **InP/ZnS (2) –**

NHS – mAb could be the interaction between Gd(III) chelate and Endo180

antibody. However, during the synthesis of the OI/MR targeted imaging probe,

the possible denaturing of the binding site of the Endo180 mAbs may result in

the lower than expected percentage surface specific binding values recorded.

        MCF7-E was used as a positive control cell line within FACS, with the

analysis being shown in figure 4.11. An increase in percentage surface specific

binding is expected when tested against the positive control cell line MCF7-E
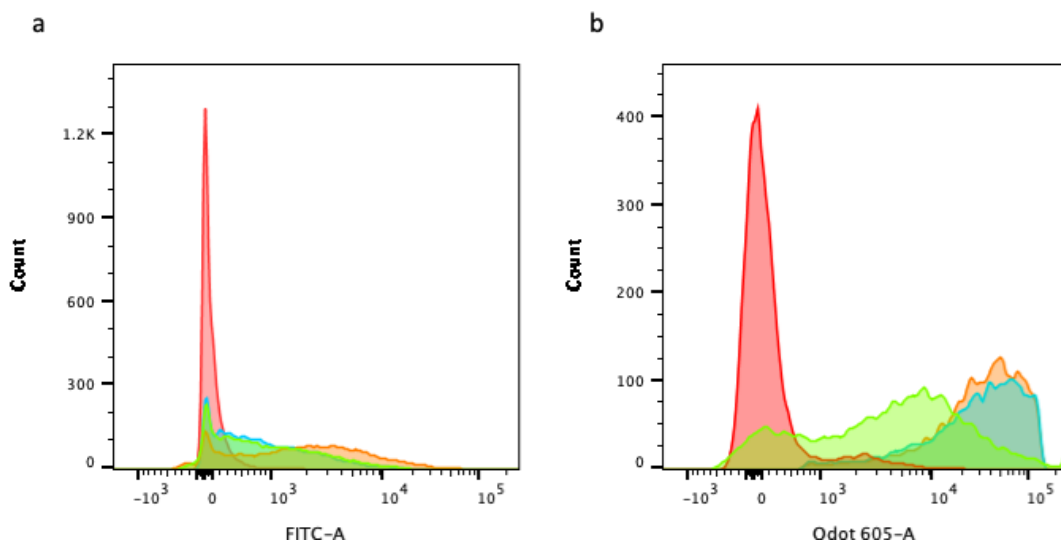
following incubation.

Figure 4.11 shows FACS analysis of MCF7-E cell line using InP/ZnS (2) – TGA synthesised using InI$_3$ (a) and InCl$_3$ (b). containing MCF7-E cells (red) as control, InP/ZnS (2) – TGA (blue), InP/ZnS (2) – NHS – mAb (orange) and InP/ZnS (2) – NHS – probe (Green). FITC-A used for probes λ_{em} = 535 nm, Qdot 605-A used for probes λ_{em} = 620 nm

As with previous cell lines, **InP/ZnS (2) – TGA** exhibits large amounts of non-specific binding (66% and 69.5% - InI$_3$ and InCl$_3$) for reasons explained previous. However, increases in specific binding are observed when using **InP/ZnS (2) - NHS – mAb** (71.69% - mAb A5.158 and 65.90% - mAb 39.10) and **InP/ZnS (2) – NHS – probe** (71.68% - mAb A5.158 and 68.50% - mAb 39.10). The increase observed suggests the direct targeting of both CTLD-2 and CTLD-4 with both available following transfection of Endo180 specific vector into the MCF7 cell line. The transfection of Endo180 specific vector into the MCF7 cell line results in the over expression of Endo180 on the surface of the MCF7-E cell line, however, may also lead to the pseudo increase of percentage specific surface binding *via* an increase in cell internalization with increased Endo180.

Thus, leading to the greater values observed for all percentage specific surface binding being recorded within the MCF7-E cell line.

4.3.4 Ex-vivo imaging

The use of immunofluorescent staining has been used to validate the non-specific binding/cellular uptake of **InP/ZnS (2) – TGA** QDs, as well as being used as to determine the surface localization of **InP/ZnS (2) – NHS – Probe**. This work was carried out in collaboration with the Coffey lab (Newcastle university). Initially, incubation of 0.1 µM **InP/ZnS (2) – TGA** QDs (with λ_{em} = 532 and 620 nm) was added to sections of prostate tissue which contained a PCa tumour over a period of 12 h. PCa tumour was graded using the Gleason grading system, resulting in a tumour with Gleason score 6 being imaged. Following incubation, permeableisation and fixing of cells was undertaken. Additional staining using DAPI nuclear stain to enable visualization of cell nucleus was also used, with confocal imaging of **InP/ZnS (2) – TGA** and nuclear DAPI stain being undertaken at an λ_{ex} = 405 nm shown in figure 4.12 below. Resulting images show a large amount of non-specific binding and cellular uptake of **InP/ZnS (2) – TGA**, following a 12 h incubation period. The elevated level of non-specific surface binding and cellular uptake observed within confocal imaging (figure 4.12), was comparative to results found during FACS analysis. This again attributed to the use of TGA as a surface capping ligand, as

the small size and very high negative charge results in non-specific surface

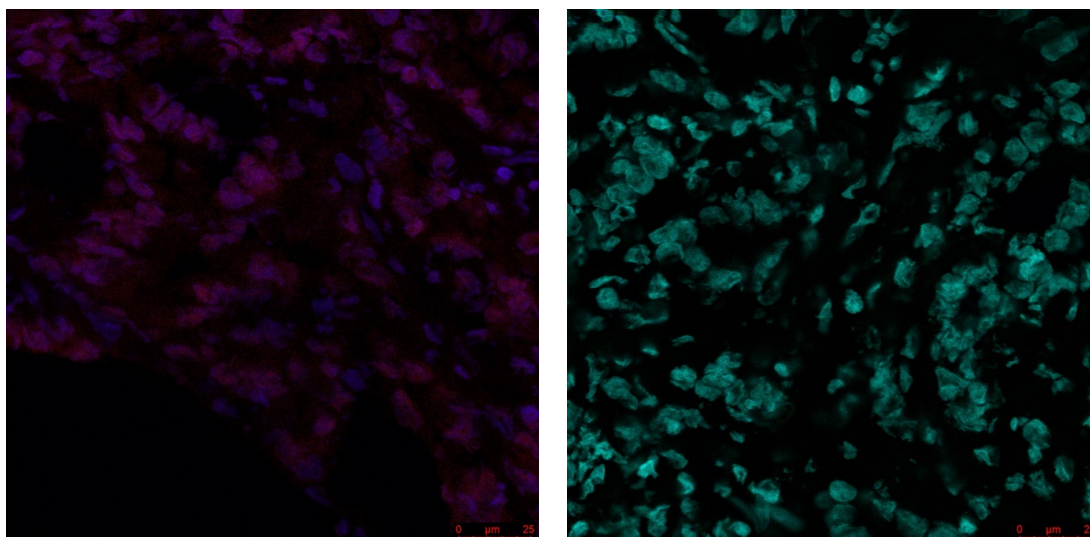binding and cellular uptake being observed.

Figure 4.12 Confocal imaging of InP/ZnS (2) – TGA on prostate tissue with PCa
tumour present (Gleason score = 6). (left) InP/ZnS (2) – TGA (InCl$_3$), imaged
using QDOT-605 filter (red). (right) InP/ZnS (2) – TGA (InI$_3$), Imaged using FITC
confocal filter (green). Both images are overlaid onto corresponding DAPI nuclear
stain image (blue) λ_{ex} = 405 nm

Following visualization of large amounts of non-specific surface binding and

cellular uptake of **InP/ZnS (2) – TGA**, confocal imaging of cancerous prostate

tissue was complete using synthesised **InP/ZnS (2) – NHS – mAb** as well as

synthesised OI/MR targeted imaging probe (**InP/ZnS (2) – NHS – Probe)**.

Initially, investigations into the cell surface binding of **InP/ZnS (2) – NHS –

A5.158/39.10** were complete and are shown in figure 4.13. Imaging showed

small amounts of surface binding were observed when imaging with **InP/ZnS

(2) – NHS – A5.158** (figure 4.13 (left)), due to conformation of endo180 within

the Gleason grade 6 tissue being imaged (**InP/ZnS (2) – NHS – A5.158** being

depicted as red in figure 4.13 (left)). The surface binding of **InP/ZnS (2) – NHS**

– A5.158 is explained due to the availability of target CTLD-2 within PCa

tumours with Gleason grade 6, with mAb 39.10 target CTLD-4 being

inaccessible in Gleason 6 PCa tissue as endo180 is bound to binding partner

CD147 *via* CTLD-4 in low grade PCa.[42,155] Hence, no surface binding of **InP/ZnS**

(2) – NHS – 39.10 (figure 4.13 right) is observed, when imaging a low Gleason
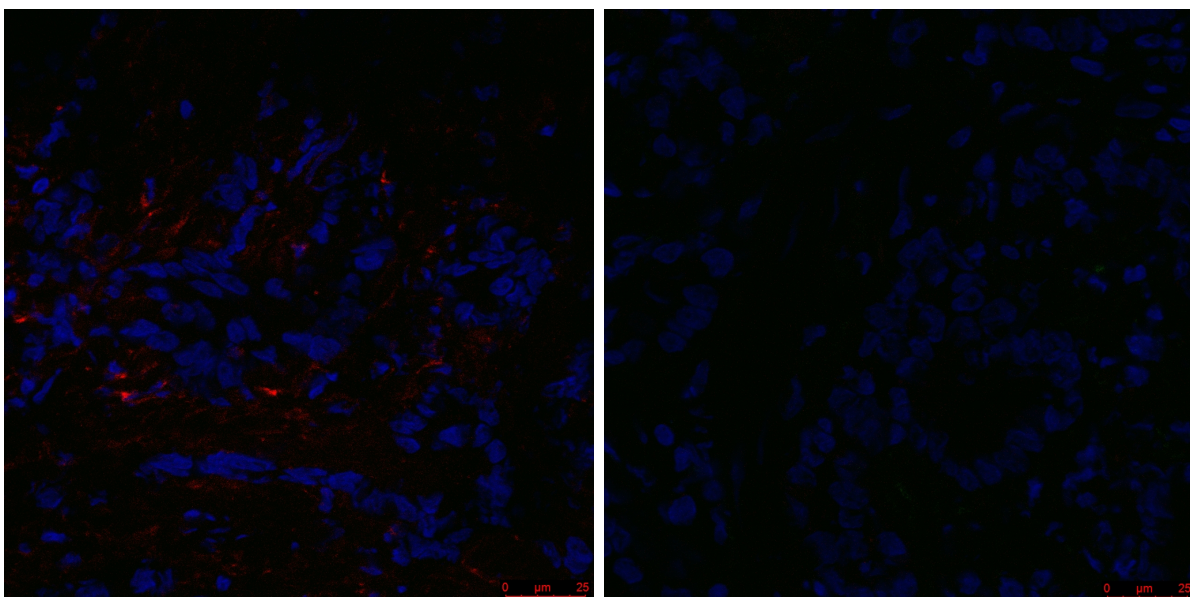
score PCa in prostate tissue

Figure 4.13 Confocal imaging of (left) InP/ZnS (2) – NHS – A5.158 (red) and
(right) InP/ZnS (2) – NHS – 39.10 with no binding observed. DAPI nuclear
staining (blue) used in both images. λ_{ex} = 405

Finally, synthesised OI/MR targeted imaging probe (**InP/ZnS (2) – NHS – probe**) underwent confocal imaging as to evaluate cell surface binding. Figure 4.14 (left) shows **InP/ZnS (2) – NHS – Probe** (mAb A5.158) (overlaid image of cell only stained with DAPI and bound **InP/ZnS (2) – NHS – probe (A5.158)**) on the surface of cells). As with **InP/ZnS (2) – NHS – mAb** (**A5.158**) in figure 4.13, surface binding using mAb A5.158 is possible only when targeting CTLD-2 whereas the targeting of inaccessible CTLD-4 with mAb 39.10 in Gleason grade 6 tissue results in negligible binding to the surface (figure 4.14 (right)). This, due to the nature of the PCa tumour being labelled with synthesised OI/MR targeted probe (Gleason score 6) and the availability of target binding site CTLD-4 being bound to binding partner CD-147.
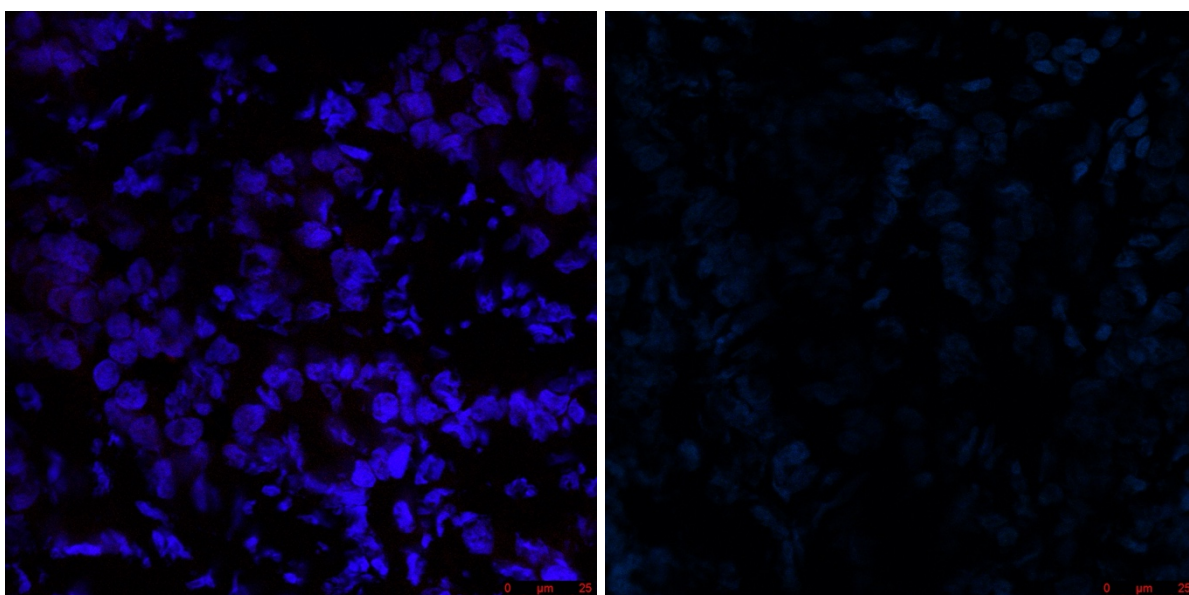

Figure 4.14 Confocal images of InP/ZnS (2) – NHS – A5.158 (red) (left) and InP/ZnS (2) – NHS – 39.10 (red) (right). DAPI nuclear staining (blue) used in both images. $\lambda_{ex} = 405$ nm

Ex vivo imaging results shown within this chapter align with the FACS analysis reported previously in section 4.3.2.2. The data showed the use of TGA as a capping ligand encourages increased non-specific binding due to the small size and high negative charge present on the surface of **InP/ZnS (2) – TGA**, which has also been shown following incubation of **InP/ZnS (2) – TGA** with prostate tissue figure 4.12. However, on the addition of endo180 specific antibodies (A5.158/39.10) to InP based QDs resulting in a targeted imaging probe, an apparent reduction in non-specificity is observed. Furthermore, due to the conformation of PCa within the Gleason grade 6 tumour present, a degree of specific binding of **InP/ZnS (2) – NHS – A5.158** is seen (figure 4.13 (left)). This attributed to the availability of imaging target CTLD-2 within the endo180 backbone, however, no such specificity is observed for **InP/ZnS (2) – NHS – 39.10** as imaging target CTLD-4 is unavailable in Gleason grade 6 PCa tumour with CTLD-4 bound to binding partner CD147. Further imaging of **InP/ZnS (2) – NHS – probe** showed a similar tread in binding, with only OI/MR dual modal probes synthesised with **A5.158** mAb showing any specific binding to the surface of prostate tissue within confocal imaging (figure 4.14 (left)). The work presented within this chapter has been able to show early evidence of specific binding of synthesised OI/MR dual modal targeted imaging probes (figure 4.13/4) to endo180 specific target domains (CTLD-2/CTLD-4), with this able to be complete in both *in vitro* and *ex vivo* biological settings.

Chapter 5: Conclusions and future work

5.1 Synthesis and development of InP based QDs and further work

5.1.1 Conclusion of chapter

The work outlined within chapter 2 details the development of a novel synthesis method for the formation of non-toxic InP/ZnS core/shell QDs. **InP/ZnS (2)** core/shell QDs are successfully synthesised using schlenk line techniques as opposed to traditional glove box methods, due to the use of phosphorus precursor P(DMA)$_3$ (non-air sensitive) resulting in the development of a tuneable fluorescence system with an emission range of λ_{em} = 535 - 623 nm with λ_{em} maxima dependent on core size. **InP/ZnS (2)** QDs formed *via* a successive heating methodology resulted in an increased overall size (2.28 ± 0.37 nm to 2.76 ± 0.37 nm and 2.67 ± 0.48 nm to 2.75 ± 0.45 nm), increased surface Zn:In ratio, a change in shape (non-spherical to quasi-spherical) as well as a large increase in photoluminescent quantum yield when compared to **InP/ZnS (1)** QDs synthesised using a tradition methodology. PLQY was also seen to increase up to 2-fold using a successive heating method when compared to a traditional heating method, with a maximum PLQY of 85.30% (**InP/ZnS (2)** InCl$_3$ - hexane) being achieved. The changes in physical properties as well as increased PLQY observed within **InP/ZnS (2)** QDs when compared to **InP/ZnS (1)**, are attributed to increased ZnS surface coverage following the use of a cooling step within the successive heating methodology. The cooling step used in the successive heating method allows for redistribution of ZnS (*via* thermal diffusion around InP core) which we have shown results in an increase

in radiative decay pathways.[192] DFT calculations were used to illustrate the preferential binding affinity of Zn(II) atoms to ZnS already present on the surface of InP core NPs, as opposed to binding directly to InP. The preferential binding is attributed to the higher adsorption energy required for direct binding to InP core surface. Therefore, the use of a thermal diffusion (temperature controlled) step allows for increased surface coverage of InP with ZnS as the energy barriers required for redistribution of ZnS over the surface of InP (0.69 eV and 0.75 eV for Zn and S respectively results) are more than overcome. This redistribution on the surface of InP when using a successive heating method is able to be shown *via* the calculation of monolayer coverage of both **InP/ZnS (1)** and **InP/ZnS (2)**, with an increase in ZnS monolayers observed following redistribution of ZnS within the formation of **InP/ZnS (2)**. Following phase transfer of **InP/ZnS (2)** into aqueous solution using surface ligand exchange thioglycolic acid (TGA), a high PLQY was able to be maintained (up to 57% $InCl_3$). Along with the high PLQY, a large negative charge was also observed in **InP/ZnS (2) – TGA** regardless of In(III) halide used of up to -24 mV.

5.1.2 Future Work

If time allowed, further investigation into the relationship between the increase in PLQY with the use of the successive heating methodology would be undertaken. With this work looking into the increase in PLQY of InP/ZnS core/shell QDs with increased number of thermal diffusion steps (n = 3 or 4). Thus, allowing to determine the optimum number of thermal diffusion steps (as

used in the synthesis of **InP/ZnS (2)**) for optimum PLQY. In addition to this

further experimentation with alternate surface ligands for use during phase

transfer would also be undertaken, allowing for investigation into the role in

which the surface ligand plays during phase transfer in both physical and photo

physical properties of InP/ZnS core/shell QDs.

5.2 Development of a dual-modal OFI/MR imaging probe and further work

5.2.1 Conclusions to chapter

Detailed within chapter 3 is the design and synthesis of a dual-modal

multimeric OI/MR imaging probe, followed by the evaluation of its physical and

luminescent properties. Initially, protected side arm **(2)** was successfully

synthesised *via* the bromination of the alpha-carbon of the carboxylic acid of

(1) using the Hell-Volhard-Zelinsky reaction mechanism. The novel two-step

reaction process used, lead to the bromination at the alpha-carbon position

followed by the selective nucleophilic protection of the carboxylic acid with an

ethyl protecting group. **(2)** was successfully added to TbutylDO3A.HBr salt

before complete deprotection using 6M HCl resulting in proligand **(4)**. The

addition of $LnCl_3.6H_2O$ (where Ln(III) = Gd(III), Eu(III) and Tb(III)) to **(4)**

resulted in the formation of **Ln.5**. Relaxation measurements using **Gd.5** amine

chelate resulted in a value of 4.93 $mM^{-1}s^{-1}$ when recorded on a 400 MHz

instrument. A hydration state (q) equal to 1 was determined following the

evaluation of lifetime rate of decay in both H_2O and D_2O in **Eu.5/Tb.5**. Increased

relaxation rates were able to be achieved following the formation of an amide

bond with addition of thiolic acid derivative to terminal amine, resulting in the

formation of **Ln.5a/b/c** (where a – lipoic acid, b – 3-mercaptopropanoic acid, c -

4 -mercaptobenzanoic acid). Investigation into obtained r_1 values of **Gd.5a/b/c**

were found to be 7.39, 6.85 and 7.13 mM^{-1}s^{-1} respectively, with q of complexes

containing Ln(III) (Eu(III) and Tb(III)) remaining at 1.

 Surface functionalisation of **InP/ZnS (2) – TGA** with **Gd.5a/b/c** resulted

in the synthesis of a small catalogue of multimeric dual-modal OI/MR imaging

probes being formed, with their physical properties being evaluated.

Hydrodynamic diameter of OI/MR dual-modal probe was able to be controlled

via the selective addition **Gd.5a/b/c** onto the surface of **InP/ZnS (2)** QDs

(decreasing size – lipoic acid > 4-mercaptobenzoic acid > 3-mercaptopropanoic

acid). In addition to this, the surface zeta potential following surface

functionalisation with **Gd.5a/b/c** is seen to become more negative with values

ranging from -27-(-)30 mV. This was attributed to the addition of surface

chelates which carry a negative (-1) charge. On surface functionalisation of

InP/ZnS (2) – TGA (where InP/ZnS QDs are synthesised using InI$_3$ and InCl$_3$)

obtained r_1 values increase with a maximum r_1 of 9.80 mM^{-1}s^{-1} (**InP/ZnS (2) –**

Gd.5a, InI$_3$ used as halide). High loading of Gd(III) chelate onto the InP/ZnS

surface was able to be tuned dependent on **Gd.5a/b/c** used for surface

functionalisation, with r_1 values per nanoparticle of up to 1610 mM^{-1}s^{-1} being

obtained. Evaluation of the luminescent properties of **InP/ZnS (2) – Gd.5a/b/c**

showed the ability of all OI/MR dual-modal imaging probes synthesised to

retain good levels of PLQY post surface functionalisation (minimum value

5.01% (**InP/ZnS (2) – Gd.5a** synthesised initially with InCl3, maximum value

19.90% (**InP/ZnS (2) - Gd.5b** synthesised initially with InCl3). Therefore,

OI/MR dual-modal imaging system presented within chapter 3 offers a wide

range of tunability, both in λ_{em} (520 nm – 620 nm) as well as PLQY dependent

on **Gd.5** DOTA derivative which is surface functionalised onto **InP/ZnS (2) –**

TGA surface.

5.2.2 Future work

The work in chapter 3 presents the successful synthesis of a range of

OI/MR dual modal imaging probes, which show the ability to maintain PLQY

whilst also exhibiting a large r_1 values per QD due to high loading of Gd(III)

chelates. However, given more time on this project, further investigation would

be undertaken, completing the following work. First, the isolation of **Ln.5** DOTA

derivative chelates *via* the use of HPLC techniques would be complete. Thus,

allowing for determination of SAP/TSAP ratio present within complexes. This

would be complete with the use of Eu(III) ^{1}H-NMR specrtoscopy, with the

isolation of **Ln.5** DOTA derivatives also being used to obtain accurate mass of all

Ln.5 DOTA derivative complexes. Second, the functionalisation of **Eu.5** and **Tb.5**

DOTA derivatives onto the surface of InP based QDs (λ_{em} = 525nm and 620 nm)

would be complete to allow for two studies to be carried out. Initially, the

determining of q for both Eu(III) and Tb(III) DOTA derivatives following

functionalisation to **InP/ZnS (2) – TGA** would be undertaken. The

determination of q would allow for the investigation to be complete to

determine if there is any change from a q=1 observed prior to functionalisation.

Following this, investigation into possible energy transfer pathways between **InP/ZnS (2) -TGA** and lanthanide metal centre present on the surface would be explored.

5.3 Development of a multi-modal imaging probe for prostate cancer detection

5.3.1 Conclusions to chapter

Chapter 4 outlines the synthesis of OI/MR dual modal targeted imaging probes, following the surface modification of **InP/ZnS (2) – TGA** with endo180 specific membrane antibodies (mAbs) A5.158 and 39.10. Surface modification was undertaken in a two-step process to alleviate aggregation (>200 nm D_h) which was observed following the use of a one-step surface modification process. Initially, Gd(III) chelates (Gd.5a) were added to the surface of **InP/ZnS (2) – TGA** with PEGNHS dithiol ester in an overnight reaction in the presence of TCEP at elevated pH, before purification and subsequent addition of endo180 mAb's in a short 2 hr reaction. Resulting in the formation of **InP/ZnS (2) – NHS – probe**. The physical properties were evaluated followed by the biological validation in a range of biomedical applications as to assess the viability of synthesised **InP/ZnS (2) – NHS – probe** as an imaging probe. The hydrodynamic diameter (D_h) was shown to increase in size on formation of OI/MR targeted imaging probe, with D_h of 19.16 and 17.03 nm (InI$_3$ and InCl$_3$) being observed when compare to **InP/ZnS (2) – TGA** (4.73 nm and 5.81 nm). Surface zeta potential recorded was able to show that on formation of OI/MR

targeted imaging probe, the overall surface charge retains a high negative

charge (-24.4 mV and -14.7 mV – InI$_3$ and InCl$_3$). The evaluation of the

luminescent properties of **InP/ZnS (2) – NHS – probe** showed PLQYs of 6.6%

and 3.4% (InI$_3$ and InCl$_3$) following a two-step surface modification of **InP/ZnS**

(2) QDs., the values obtained (PLQY in excess of 3%) being able to be used for

biomedical imaging applications. OI/MR dual modal targeted imaging probes

synthesised were again designed with a wide range of tunability in λ_{em} (530 nm

– 635 nm) with little shift in λ_{em} maxima when compared to **InP/Zns (2) - TGA**,

with both having large λ_{ex} ranges (figure 4.5).

As synthesised **InP/ZnS (2) – NHS – probe** underwent cellular

validation studies on a range of PCa cell lines, in both *in vitro* and *ex vivo*

applications. Cell viability using cell counting kit-8 was shown to be unaffected

following overnight incubation with **InP/ZnS (2) – TGA** (both InI$_3$ and InCl$_3$

used) at concentrations ranging from 10- 0.03 mM (n = 3 with only technical

repeats undertaken). Investigations into percentage surface specific binding *via*

FACS analysis as well as cellular imaging (confocal imaging) was also

undertaken. Analysis methods showed that **InP/ZnS (2) - TGA** QDs suffer from

a large amount of non-specific binding/cell internalisation due to the high

negative surface charge and small size. This was evident initially within the

FACS analysis conducted as all cell lines tested exhibited a large percentage

specific binding (section 4.3.2.2), followed by the observation of cell

internalisation within *ex vivo* imaging on prostate tissue cells (section4.3.4).

However, in both FACS and *ex vivo* imaging, varying degrees of specific binding

is observed following the addition of Endo180 specific mAbs, with large

amounts of non-specific binding and cell internalisation suggested. When using

positive control cell line, MCF7-E, increase in percentage specific surface

binding was attributed to the possibility of both increased cell internalisation

(increased Endo180 expression) as well as the direct targeting of CTLD-2 and

CTLD-4 when compared to PCa cell lines. Surface specific binding to primary

target CTLD-2 is evident most *within ex* vivo imaging of PCa tumorous tissue

(Gleason grade = 6), the direct targeting of available CTLD-2 with **InP/ZnS (2) –**

NHS – A5.158 and **InP/ZnS (2) – NHS – probe** (where mAb used is A5.158) is

seen to be complete within figures 4.13,4.14 providing potential evidence of

probe viability going forward. However, due to the unavailability of CTLD-4 for

binding within Gleason grade 6 prostate tissue as CTLD-4-CD-147 complex

remains present within the tissue tested, resulting in no specific binding when

using imaging probes designed with mAb 39.10 (figure 4.14).

5.3.2 Future work

Chapter 4 outlines the development, synthesis and evaluation of targeted

OI/MR dual modal imaging probes for PCa detection, which are reported with

limited success. Given further time on this project, further work within both the

chemical and biological validation of synthesised PCa imaging probes would be

undertaken.

Initially, work would look to determine r_1 values of synthesised

InP/ZnS (2) – NHS – probes, as in the work presented within the chapter r_1

values are not able to be obtained. This is due to the low concentration of

sample following the completion of the surface modification, resulting in poor

resolution within ^{1}H-NMR spectroscopy. This limitation could be overcome in

future work by increasing concentrations of **InP/ZnS (2) – NHS – probe** by

running reactions in parallel, then completing the analytical method on the

combined products. On completion of determination of r_1 values for synthesised

OI/MR targeted imaging probes, Gd(III) chelates surface loading would then be

experimentally determined following the same method shown in chapter 3.

The use of TGA as a capping ligand in this thesis to drive phase transfer

of InP based QDs into aqueous phase whilst maintaining PLQY at high levels,

can be seen to limit the effectiveness of the biological evaluations carried out on

as synthesised OI/MR targeted imaging probes. Due to the large amount of non-

specific surface binding and cellular uptake observed following incubation with

InP/ZnS (2) – TGA QDs. Therefore, given further time, alternative capping

ligands such as D-Penicilamine or cysteine would be used for phase transfer of

InP based QD as to investigate if levels of non-specific binding and cell uptake

could be lowered. Following the synthesis of OI/MR targeted imaging probes

synthesised using InP based QDs capped in an alternative capping ligands.

The further biological validation of synthesised targeted imaging probes

would be explored in more detail given the time and resource, in an attempt to

understand in more detail, the effect that which the synthesised imaging probes

have on both cells and tissue alike. Within the work presented in chapter 4,

toxicity investigations were only complete on a technical repeat scale (n=3) to

allow initial conclusions to be drawn. However, this scale allows for error and

therefore, further repeats would be used to gain a fuller understanding of the *in vitro* effects the probes have on cells whilst also reducing the error associated within the study. Further to this, the *ex vivo* works presented in collaboration with Newcastle university was only able to be complete using one tissue sample at Gleason grade 6 due to resource and time restraints, again limiting conclusions being able to be drawn from the investigations with such a small sample size. If time and further resource allowed, a further collaboration with Newcastle university (Dr. Kelley Coffey's laboratory) would be explored in able to further the *ex vivo* work undertake to gain a deeper understanding, using tissue samples of different Gleason scores (6-9) to assess targeted specific binding of synthesised probes.

Chapter 6: Materials and methods

6.1.1 Reagents

Reagents. Reagents were received in the following purities and used without further purification: 99.999%—indium chloride (Alfa Aesar), indium iodide (Alfa Aesar) and zinc chloride (Sigma-Aldrich); 90%—sulphur powder (Sigma Aldrich) and D-penicillamine (Alfa Aesar); 97%—tris(diethylamino)phosphine, trioctyl- phosphine (Sigma-Aldrich) and tetramethylammonium hydroxide solution (Sigma-Aldrich); 90%—1 – octadecene technical grade (Sigma-Aldrich); 70%— oleylamine technical grade (Sigma-Aldrich); phosphate-buffered saline (PBS; 1×, pH 7.4) (Gibco); tris(2-carboxyethyl)phosphine hydrochloride solution (0.5 M pH) (Sigma-Aldrich); Endo180 specific antibodies mAb A5.158 (2mg/ml), mAb 39.10 (4mg/ml) in PBS obtained from Dr Kai Wang (Hull University, Sturge Group).

6.1.2 Instruments

TEM was undertaken on a FEI Titan (university of Leeds) Themis G2 operating at 300 kV fitted with 4 EDX silicon drift detectors and a Gatan One-View CCD. Bruker Esprit software (Version 1.9.4) was used for EDX spectra collection and analysis. High-angle annular dark field scanning TEM (STEM) and EDX mapping were conducted using a probe current of ~150 pA. Samples were prepared for TEM by placing a drop of suspended QDs on a graphene oxide-

coated holey carbon film supported on a copper TEM grid (EM Resolutions, UK).

QD sizing was performed by measuring the diameter of a statistically relevant

number of individual QDs (~150 QDs per sample) in the STEM images. NMR

spectra were obtained using an Oxford A4500 spectrometer operating at 400

MHz. Mass spectra were obtained using an Avion Expression CMS with a Hitachi

chromaster 5110 pump. Hydrodynamic diameter and Zeta potential was

recorded on a Malvern, Zetasizer Nano-z5 instrument.

6.1.3 Fluorescent measurements

All fluorescent measurements were completed using a Horiba

Fluoromax-4P spectrofluorometer in a 10 mm quartz cuvette. All spectra were

taken in either aqueous or hexane solutions dependent on whether QDs had

undergone phase transfer. All UV-Vis absorption spectra were recorded on a

thermoscientific Evolution 300. Fluorescence quantum yields were determined

by comparison of the integrated fluorescent intensity of QDs against the

integrated standard (blanks were used as integrated standards—hexane

(organic) milli-Ω water (aqueous)), using an integration sphere. All samples

(including blanks) were excited at 405 nm for spectra to be produced in QY

measurements (Supplementary Note 1). The lifetime was measured in a 10 mm

quartz cuvette. Excitation was at 405 nm and emission was collected at 526 nm

or 612 nm using a Becker and Hickl HPM-100 detector.

6.1.3.1 Photoluminescent Quantum yield calculations

Photoluminescent Quantum yield PLQY was calculated using the equation 6.1

below;

$$\emptyset = \frac{E_c - E_a}{(L_a - L_c)250} \qquad 6.1$$
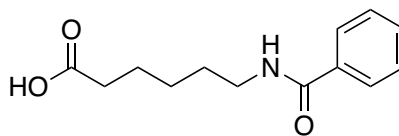
Where E_c – Emission of with sample

E_a – Emission of blank

L_a – absorbance of blank

L_c – absorbance of sample

With the bottom line being multiplied by 250 due to a 0.04% filter being used.

6.2 Synthesis of 6-benzomidohexanoic acid (1)

A solution of NaOH (16.8 g, 0.419 moles) in water (18 ml) was added to a solution of 6-aminohexanoic acid (25.0 g, 0.191 moles) in water (500 ml). The solution temperature was lowered to a temperature below 10°C before benzoyl chloride (29.5 g, 0.201 moles, 24.3 ml) was added drop wise over the course of 0.5 h. Once complete the solution was brought to a neutral pH using 2 M HCl solution to induce precipitation of product. Product was the collected and washed 3 times first with water then with petroleum ether. Product was then dried under vacuum overnight to yield a pure white solid **(1)**.[156] (Yield = 28.482 g, 63%). ^{1}H NMR (400 MHz,), CD_3CN: δ 7.75 – 7.73 (m, 2H), 7.50 – 7.46 (m, 1H), 7.43 – 7.39 (t, 2H), 3.31 (dd, J = 12.8, 5.7 Hz, 2H), 2.29 (t, J = 7.4 Hz, 2H), 1.61 – 1.50 (m, 4H), 1.40 – 1.30 (m, 2H). ^{13}C NMR (400 MHz, CD_3CN) δ **C**O-CH_2 174.4 (s), **C**ONH 167.1 (s), **C**-Aryl 135.1 (s), **C**-Aryl para 131.1 (s), **C**-Aryl ortho 128.3 (s) **C**-Aryl Meta 127.0 (s), **C**H_2NH 39.3 (s), **C**H_2CO 33.2 (s), **C**H_2CH_2NH 29.0 (s), **C**$H_2CH_2CH_2$CO 26.2 (s), **C**H_2CH_2CO 24.3 (s). ESMS = 236.2 [M +H]$^+$, 258.1 [M + H + Na]$^+$. CHN expected analysis: C 66.36%, H 7.28%, N 5.95%, analysis found: C 65.60%, H 7.30%, N 5.86%

## 6.3 Synthesis of ethyl 6-benzamido-2-bromohexanoate (2)
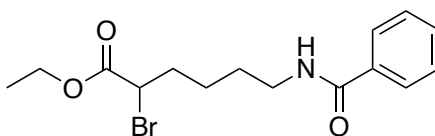
(1) (2.40 g, 0.010 moles) and PBr_3 (3.03 g, 0.010 moles, 1.06 ml) were dissolved under argon in CCl_4 (40 ml), in a 250 mL three neck round bottom flask, equipped with a reflux condenser bearing a calcium chloride drying tube and heated to 60°C before Br_2 (3.51 g, 0.022 moles, 1.133 ml), was added slowly over the period of 0.5 h at 0°C. After the addition, the reaction was heated at reflux for 18 h. When cool, $CHCl_3$ (20 ml) was added before the reaction mixture was added to EtOH (100 ml). The solvents were then removed under vacuum to give a crude product. Crude product was then dissolved in $CHCl_3$ (50 ml) and washed with successive acid/base washings. First, 2% w/v $NaHCO_3$ solution was used followed by 1 M HCl solution. Organic phase was dried with $MgSO_4$, filtered, and dried under vacuum yielding pure product **(2)** in the form of an oil. (Yield = 0.875 g, 26%).^{1}H NMR (400 MHz) $CDCl_3$: δ 7.75 (d, J = 5.5, 2H), 7.51 – 7.45 (m, 1H), 7.45 – 7.39 (m, 2H), 4.26 – 4.16 (m, 2H), 4.134 - 4.080 (m, 1H), 3.488 - 3.431(m, , 2H), 2.163 – 1.975 (m, 2H), 1.704 – 1.593 (m, 3H), 1.499 – 1.372 (m, 2H), 1.293 – 1.215 (m, 3H). ^{13}C NMR (400 MHz, CD_3CN) δ **C**O-CHBr 173.4 (s), **C**ONH 166.9 (s), **C**-Aryl 135.2 (s), **C**-Aryl para 131.1 (s), **C**-Aryl ortho 128.4 (s), **C**-Aryl Meta 127.0 (s), **C**H_2CH_3 59.9 (s), **C**HBrCH_2 39.3 (s), **C**H_2NH 33.8 (s), **C**H_2CHBr 29.0 (s), **C**H_2CH_2NH 26.2 (s), **C**H_2CH_2CHBr 24.5 (s), **C**H_3CH_2 13.7 (s). ESMS = 342.2 [M +H]$^+$.

## 6.4 Synthesis of 1,4,7-Tris(tert-butoxycarbonylmethyl)-1,4,7,10-tetraazacyclododecane hydrobromide
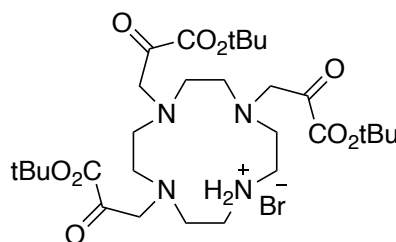
To a suspension of cyclen (15.00 g, 87.1 mmol) and sodium acetate (23.58 g, 287.4 mmol) in N,N-dimethylacetamide (DMA, 60 mL) at 20 C was added a solution of Tbutyl bromoacetate (56.1 g, 42.3 mL, 267 mmol) in DMA (40 ml) dropwise over a period of 0.5 h. The temperature was maintained at 20 C during the addition, after which the reaction mixture was allowed to come to room temperature. After 24 h of vigorous stirring, the reaction mixture was poured into water (300 mL) to give a clear solution. Solid $KHCO_3$ was added portion wise in order to form a white solid. The white precipitate was collected by filtration and dissolved in $CHCl_3$ (250 mL). The solution was washed with water (100 mL), dried (MgSO$_4$), filtered, and concentrated to about 50 ml and excess ether was added to induce precipitation of product as a white fluffy solid.[202] (Yield =27.1 g, 60%). ^{1}H NMR (400 MHz) CDCl$_3$. δ 1.44 (s, 9H), 1.45 (s, 18H), 2.86-2.95 (m, 12H), 3.09 (m 4H), 3.28 (s 2H), 3.36 (s 4H), 10.04 (br, s 1H). ESMS = 515.1 [M +H]$^+$. CHN expected analysis: C 52.43%, H 8.63%, N 9.41%, analysis found: C 52.18%, H 8.90%, N 9.35.

6.5 synthesis of tri-*tert*-butyl-2,2',2''-(10-(6-benzamido-1-ethoxy-1-oxohexan-2-yl)-1,4,7,10-tetraazacyclododecane-1,4,7-triyl)triacetate (3)


.
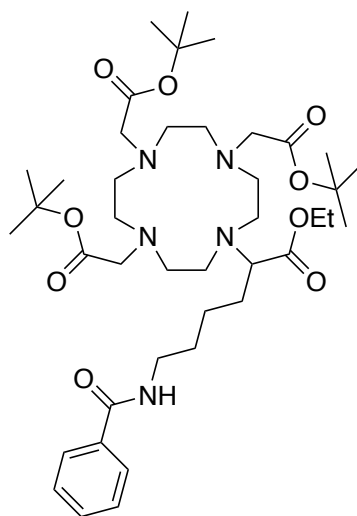
(2) (0.875 g, 2.55 mmol) and KI (0.424 g, 2.55 mmol) were stirred under argon in a 3-neck flask in dry MeCN (50 ml) for 1 h. When complete, a solution of DO3A.HBr (1.827 g, 3.06 mmol) and K_2CO_3 (0.428 g, 3.10 mmol) in dry MeCN (30 ml) was added and the solution refluxed overnight. When cool, the reaction mixture was filtered and excess solvent removed under vacuum to yield a crude product. Pure product is obtained by dissolving crude product in minimal MeCN and excess diethyl ether. Solution is then filtered and reduced under vacuum yielding pure **(3)** in the form of an oil. (yield = 196 mg, 10%). ^{1}H NMR (400 MHz), CD_3OD δ 7.77 (dd, J = 5.3, 3.3 Hz, 2H), 7.51 – 7.47 (m, 1H), 7.43 (dt, J = 9.5, 3.5 Hz, 2H), 4.12 – 4.04 (m, 2H), 3.12 (t, J = 5.6 Hz, 6H), 2.95 (t, J = 5.6 Hz, 6H), 2.77 (dd, J = 6.3, 4.0 Hz, 6H), 2.66 (dd, J = 6.3, 4.0 Hz, 6H), 1.68 – 1.57 (m, 5H), 1.45 (s, 27H), 1.23 (t, 3H), ^{13}C NMR (400 MHz, CD_3OD). δ 173.4, 173.2, 168.6, 134.4, 131.3, 128.3, 126.9, 81.6, 61.1, 60.8, 55.5, 52.5, 39.1, 29.2, 27.0, 23.9, 13.4 HRMS = found 776.5168 [M +H]$^+$; calculated value for $C_{41}H_{69}N_5O_9$ = 776.0290, 798.4987 [M + H + Na]$^+$.

6.6 Synthesis of 2,2',2''-(10-(5-amino-1-carboxypentyl)-1,4,7,10-tetraazacyclododecane-1,4,7-triyl)triacetic acid (4)
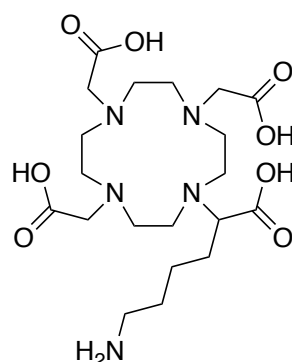
(3) (0.196 g, 0.252 mmol) was dissolved in 6 M HCl (20 ml) and heated at reflux for a period of 24 h. Following this, solvents were removed under vacuum and the residue dissolved in water (50 ml). The solution was washed with diethyl ether (3 x 30 ml) before solvent was removed under vacuum. Yielding product (4) as a clear brown oil (Yield = 112 mg, 93%). ^{1}H NMR (400 MHz,), D$_2$O: δ 1.42 (s 2H), 1.49-1.62 (m 4H), 2.85-3.93 (m 28H). HRMS = found 476.2715 [M + H]$^+$; calculated value for C$_{20}$H$_{37}$N$_5$O$_8$ = 475.2642, 498.2534 [M + H + Na]$^+$.

6.7 Synthesis of lanthanide amine complex. (Ln.5)
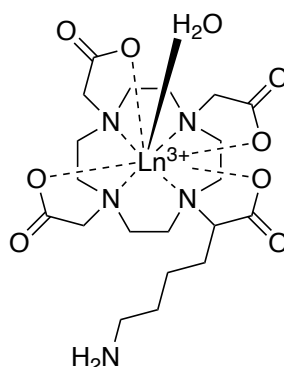
General scheme

A solution of Ln(III).6H$_2$O in H$_2$O (5 ml) was added to a solution of **(4)** in H$_2$O (5 ml) with the pH being adjusted to 5.5 using 1 M NaOH. The solution was stirred at room temperature overnight and on completion the pH of the reaction was take to 8.5 and allowed to stir at room temperature for 1 h to remove any free lanthanide. following this, the solution was centrifuged at 10000 rpm for 5 minutes before being filtered using cotton wool in a glass pipette. The crude Lanthanide amine complex was then reduced under vacuum to produce pure **Ln.5.**

Gadolinium complexation Gd.5

(4) (500 mg, 1.052 mmol), GdCl$_3$.6H$_2$O (508 mg, 1.367 mmol). Yield = 506 mg, 77%, HRMS = found 631.1621 [M + 2H] $^+$, calculated value for C$_{20}$H$_{33}$GdN$_5$O$_8^{3+}$ = 629.1554 , r_1 = 5.77 mM^{-1}s^{-1}

Europium complexation Eu.5

(4) (250 mg, 0.5260 mmol), EuCl$_3$.6H$_2$O (251 mg, 0.6838 mmol). Yield = 230 mg, 70%, HRMS = found 627.1772 [M + 2H]$^+$, calculated value for C$_{20}$H$_{33}$EuN$_5$O$_8^{3+}$ = 624.1525, 649.1591 [M + H + Na]$^+$

Terbium complexation Tb.5

(4) (250 mg, 0.5260 mmol), TbCl$_3$.6H$_2$O (255 mg, 0.6838 mmol). Yield = 256

mg, 77% HRMS = found 632.1734 [M + 2H]$^+$, calculated value for

C$_{20}$H$_{33}$TbN$_5$O$_8$$^{3+}$ = 623.1566, 654.1553 [M + H + Na]$^+$

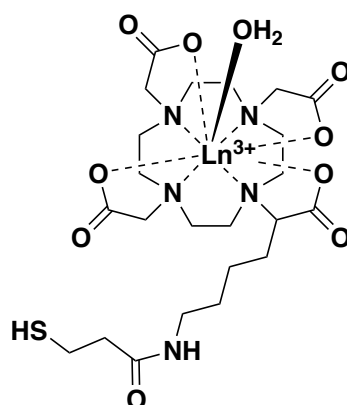## 6.8 Synthesis of Ln.5 lipoic acid chelate (Ln.5a)
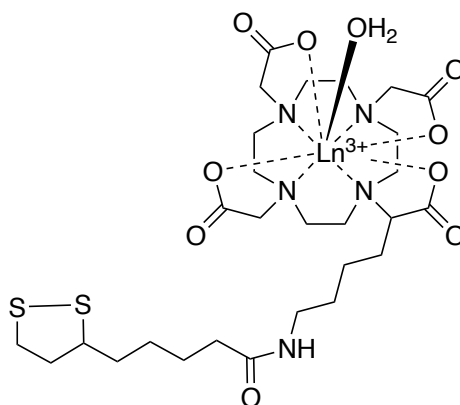
General scheme

Ln.5, lipoic acid, EDC and DMAP were all added to a 25 ml round bottom flask

(ratio 1:2:2:2) and dissolved in 10 ml of H$_2$O: DMF (1:1) solution. The solution

was then allowed to stir for 24 h at room temperature. On completion, the

solvent was removed under vacuo before solid was suspended in 10%

MeOH:DCM solution to precipitate DMAP salts formed in the reaction. Solution

was then centrifuged at 10000 RPM for 3 minutes and solution filtered through

cotton wool before being reduced to dryness under vacuo to yield pure product

(**Ln.5a**).

Gadolinium complexation Gd.5

(**Gd.5**, 50 mg, 0.0975 mmol), Lipoic acid (32 mg, 0.1589 mmol). Yield = 54 mg,

84%, r_1 = 7.39 mM^{-1}s^{-1}

6.9 Synthesis of Ln.5 3-Mercaptopropanoic acid chelate (Ln.5b)
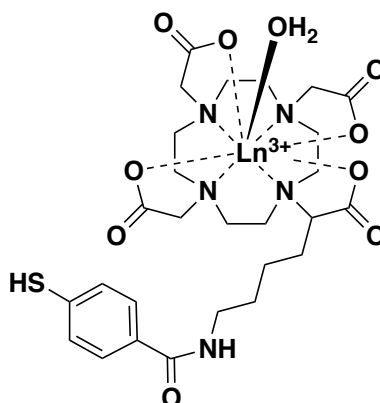

General scheme

Ln.5, 3-Mercaptopropanoic acid, EDC and DMAP were all added to a 25ml round bottom flask (ratio 1:2:2:2) and dissolved in 10 ml of H_2O: DMF (1:1) solution. The solution was then allowed to stir for 24 h at room temperature. On completion, the solvent was removed under vacuo before solid was suspended in 10% MeOH:DCM solution to precipitate DMAP salts formed in the reaction. Solution was then centrifuged at 10000 RPM for 3 minutes and solution filtered through cotton wool before being reduced to dryness under vacuo to yield pure product (**Ln.5b**).

Gadolinium complexation Gd.5

(**Gd.5**, 50 mg, 0.0795 mmol), 3-Mercaptopropanoic acid (17 mg, 0.1589 mmol).

Yield = 50 mg, 89%, r_1 = 6.85 mM^{-1}s^{-1}

6.10 Synthesis of Ln.5 4-Mercaptobenzoic acid complex (Ln.5c)

General scheme

Ln.5, 4-Mercaptobenzoic acid, EDC and DMAP were all added to a 25 ml round bottom flask (ratio 1:2:2:2) and dissolved in 10 ml of H_2O: DMF (1:1) solution. The solution was then allowed to stir for 24 h at room temperature. On completion, the solvent was removed under vacuo before solid was suspended in 10% MeOH:DCM solution to precipitate DMAP salts formed in the reaction. Solution was then centrifuged at 10000 RPM for 3 minutes and solution filtered through cotton wool before being reduced to dryness under vacuo to yield pure product (**Ln.5c**).

Gadolinium complexation Gd.5

(Gd.5 50 mg, 0.0795 mmol), 4-mercaptobenzoic acid (25 mg, 0.1589 mmol).

Yield = 59 mg, 99%, r_1 = 7.13 mM^{-1}s^{-1}

6.11 Synthesis of InP core only quantum dots.

General synthesis of InP cores designed to synthesise cores with average diameter of 2.48 nm ± 0.45 nm when synthesised using $InCl_3$ and InI_3 respectively.

6.11.1 General synthesis method

In(III) halide (halide = Cl) (0.45 mmol) and Zn(II) chloride (300 mg, 2.2 mmol) were added to oleylamine (5.0 mL,15 mmol) in a 100 ml three-neck flask before the reaction mixture was stirred and degassed for a minimum of 30 minutes at 120 °C. Following this the reaction mixture was backfilled with Ar and heated to 180 °C (the temperature allowed to stabilise before progressing with the reaction). After 10 minutes at 180°C, tris(diethylamino) phosphine (0.45 mL, 1.6 mmol) was rapidly injected, on injection of the phosphine precursor the reaction occurred rapidly with core only InP QDs formed within 30 minutes. On completion, the reaction was cooled to room temperature and core only InP QDs were precipitated in ethanol (50 mL) before being re-suspended in organic solvent (hexane).[115] For synthesis of InP cores of average diameter 1.91 ± 0.27 nm InI_3 (0.224 mg, 0.45 mmol) is used in place of the In(III) halide.

6.12 Synthesis of InP/ZnS (1) core/shell quantum dots.

InP core only QDs were formed following procedure outlined in section 6.11.1, however, at a time point of approximately 20 minutes into the reaction saturated TOP-S solution (1 mL of a 2.2 M solution) at a temperature of 120°C was injected slowly into the InP cores reaction solution at 180°C and allowed to continue stirring. After 60 minutes, the temperature of reaction was increased to 200°C and stirred for a further 60 minutes before a degassed solution of Zn(stearate)$_2$ (1g) in 1-octadecene (ODE) (4 mL) was injected slowly followed by an increase in temperature from 200 to 220 °C. After 150 minutes, degassed TOP-S (0.7 mL of a 2.2 M solution) was injected slowly alongside a temperature increase from 220 to 240 °C. After 180 minutes, degassed solution of Zn(stearate)$_2$ (0.5 g) in ODE (2 mL) was injected slowly, with a temperature increase from 240 to 260 °C. After 210 minutes the reaction was complete and the solution was brought down to room temperature via quenching of reaction in chloroform (10 ml), followed by the precipitiation of **InP/ZnS (1)** QDs in ethanol (50 mL) before being washed and re-suspended in organic solvent (hexane).[192]

- Both Saturated TOP-S and Zn-Stearate solutions are to be degassed to avoid any oxygen being added to the system on injection.

6.13 Synthesis of InP/ZnS (2) core/shell quantum dots.

On completion of reaction for **InP/ZnS (1)**, the reaction mixture

containing **InP/ZnS (1)** QDs was cooled to 180 °C and temperature allowed to

stabilize for 30 minutes instead of undergoing quenching as in section 6.12.1.

Following stabilisation of temperature, degassed saturated TOP-S ((1 mL of a

2.2 M) solution was injected slowly and after 30 minutes of stirring the

temperature was increased from 180 to 200 °C. After 90 minutes a degassed

solution of Zn(stearate)$_2$ (1g) in ODE (4 mL) was injected slowly and the

temperature was then increased from 200 to 220 °C. After 120 minutes,

degassed TOP-S (0.7 mL of a 2.2 M solution) was injection slowly and the

temperature was then increased from 220 to 240 °C. At a time point of 150

minutes, solution of Zn(stearate)$_2$ (0.5 g) in ODE (2 mL) was further injected

and the temperature was raised further to 260 °C. After 180 minutes the

reaction was complete and the solution quenched with chloroform (10 ml)

before **InP/ZnS (2)** QDs were precipitated in ethanol (50 ml). Purification of

InP/ZnS (2) QDs was complete *via* centrifuge at 10000 rpm for 3 minutes with

InP/ZnS (2) pellet re-suspended in organic solvent (hexane) as required.[192]

6.14 Phase transfer of InP/ZnS core/shell quantum dots to aqueous solution

Phase transfer was completed following a procedure previously reported by

Tamang *et al*, where **InP/ZnS (2)** QDs first undergo a thorough purification to

remove any hydrophobic ligands before undergoing a surface ligand substitution reaction.[181] A 5 mL solution containing **InP/Zns (2)** QDs in organic solvent was mixed with anhydrous ethanol (1:3) and centrifuged at 10000 rpm for 6 minutes. The pellet was then re-suspended in a chloroform:ethanol (1:3) solution before being centrifuged again at 10000 rpm for 6 minutes. On completion, the pellet was then suspended in minimum amounts of chloroform. For a typical phase transfer of **InP/ZnS (2)** QDs from organic to aqueous solution, a 0.2 M solution of hydrophilic surface ligand (D-Penicilamine or thioglycolic acid) was prepared in degassed Milli-Q water (1 mL, 8 MΩ), and the pH was adjusted *via* the dropwise addition of 0.5 M tetramethylammonium hydroxide. This solution is mixed with a ~5 µM dispersion of the QDs in chloroform (1.5 mL). The biphasic mixture is stirred vigorously at 14000 rpm for up to 2 h. On completion, the biphasic mixture can result in a clear separation of two distinct layers or in an emulsion. If the latter is the case, the mixture is centrifuged at low speed (1000 rpm) for 1 minute to obtain a separation of two phases. Following centrifugation, **InP/ZnS (2)** QDs in the aqueous phase will be in the upper phase. QDs in aqueous phase were purified via centrifuged through Millipore centrifuge filters (VWR) (30 KD) at 6000 rpm for 2 minutes. Then washed with 200 µl of 1 x PBS buffer (pH 7.4) or milli-Q water, with milli-Q water used to re-disperse the pellet before the sample is stored in the dark at 4°C.

6.15 Functionalisation of InP/ZnS (2) – TGA with Gd(III) chelates to form a Dual modal OI/MR imaging probe.

6.15.1 General Scheme

100 μl of **InP/ZnS (2) – TGA** solution (typically of concentration 1×10^{-6}) was loaded into a 2 ml centrifuge tube followed by 100 μl of Gd(III) gadolinium chelate (ca.1mmol) in a ratio of 1:1000, as well as TCEP in a molar ratio of 1:3000. The reaction was stirred vigorously using a vortex plate overnight before being purified under centrifuge (3000 rpm) through a Millipore centrifuge filter (VWR) (30 KD). Pellet obtained was washed with degassed Milli-Q water (1 ml) before being suspended and stored in the dark at 4°C.

6.16 Cell culture methods

Primary cell lines RWPE-1, RWPE-2, PC-3 and MCF7 cells were obtained from ATCC where they were verified before use. MCF7-E cells were obtained from Dr Daniel Diaz (post-doctoral research associate of Dr Justin Sturge). RWPE-1 and RWPE-2 cells were grown in Keratinocyte Serum Free Medium (K-SFM) with the addition of 0.05 mg/ml BPE and 5 ng/ml EGF. PC-3 and MCF7 cells were grown in standard DMEM culture medium with the addition of 10% FBS and 5 ml pen/strep solution. MCF7-E cells were cultured in the same media as MCF7 cells above, however due to the Endo180 vector addition, further additions

of 5 ml of G418 solution and 500µl of 10 µg/ml insulin were added to complete a

stable selection of only MCF7-E transfected cells.

6.17 Western blot analysis

6.17.1 preparation of lysates

6.17.1.1 Materials

RIPA buffer (Thermo Fisher Scientific, 89900; contains 25mM Tris.HCl

pH 7.6, 150mM NaCl, 1% NP-40, 1% sodium deoxycholate, 0.1% SDS). 1% (v/v)

protease and phosphatase inhibitor cocktail (Thermo Fisher Scientific, 78440)

were added to the precooled RIPA buffer immediately before use. Pierce BCA

Protein Assay Kit (Thermo Fisher Scientific, 23227).

6.17.1.1 Methods

Using a 6-well plate, 200000 cells were added per well in cell culture

media before being incubated in a humidified incubator (37°C, 5% CO_2)

overnight. The following morning the media within each well within the 6-well

plate was changed and the process of overnight incubation repeated until 80%

confluence was achieved. Upon confluency, cell media was removed before

200µl of trypLE™ Express (an enzyme replacement protein) was added and

incubated for a period of 5 minutes. Following this , 800µl of PBS was used to

wash/collect detached cells before complete solution, including cells was

transferred to a 1.5ml epindorph tube. In a pre-cooled centrifuge (4°C),

epindorph tubes containing cells were centrifuged at 7000 rpm for 1 minute

before discarding the supernatant solution. Cell pellet was then washed a

further 3 times with 500μl PBS solution to ensure removal of trypLE™ Express,

centrifuging cell suspension after each wash before re-suspension in fresh PBS

(1ml). Following washing of cells, 100μl of RIPA buffer/PPI solution (1 ml

RIPA/10μl PPI) was added and left on ice for 30 minutes before undergoing

intermittent sonication (30 seconds on 30 seconds off) for 5 minutes. Following

this, cell suspension was centrifuged for 1 minute at 7000 rpm before

supernatant was removed and cell pellet was re-suspended into 1ml PBS and

separated into fresh epindorph tubes before being stored for short periods at

4°C or freeze at -18°C for long periods.

6.17.2 BCA assay for protein quantification

BCA assay was used for the quantification of protein which was loaded

onto pre-cast gels for western blot analysis. The testing kit was bought from

Pierce™ and followed the microplate procedure for the determination of

protein within lysates prepared following procedure in section 6.16.1. This was

completed in order to quantitatively load 50μg/ml of each protein onto the gel

for western blot.

6.17.3 Western blot procedure

6.17.3.1 Materials

The SDS-PAGE Buffer System Stock Solutions, Transfer Buffer (pH 8.3, 25mM Tris, 192mM glycine, with 20% Methanol), Blocking Buffer (Tris-buffered saline (TBS) with 0.05% Tween-20 and 5% of non-fat dry milk), Washing Buffer (TBS with 0.05% Tween-20). Other materials include: Protein ladder – Precision Plus Protein™ WesternC™ Standards (Bio-Rad, 161-0376) or PageRuler™ Prestained Protein Ladder (Thermo Fisher Scientific, 26616). Primary antibody – mouse anti-Endo180 monoclonal antibody A5/158, mouse anti β-actin monoclonal antibody (Thermo Fisher Scientific, AM4302). Secondary antibody – HRP-conjugated anti-mouse immunoglobulins (Sigma-Aldrich, A9044). Substrates –Enhanced chemiluminescence substrate (Thermo Fisher Scientific, 32209). Immobilon-P Polyvinylidene Fluoride (PVDF) Membrane (Merck Millipore, IPVH00010). Mini-PROTEAN Tetra System and power pack (Bio-Rad).

6.17.3.2 Methods

Western blot procedure followed has been adapted for purpose from BIO-RAD© laboratories general protocol for western blotting.

Appropriate volume of protein-containing cell lysate (equal to 50 µg total protein) of each sample was mixed with 1/5 volume of sample buffer. Samples were then heated to 65℃ for 5 minutes before being cooled to room

temperature and loaded on to 7.5% (w/v) discontinuous polyacrylamide gel

(BIO-RAD© laboratories). Protein loaded gels then underwent electrophoresis

in running buffer using the Mini-PROTEAN Cell System and the power pack set

at 95V for 1.5 hours until the bromophenol blue band was about to reach the

bottom of the gel. Gels, membrane, filter paper as well as fibre pads were

equilibrated and soaked in transfer buffer for 15 minutes prior to transfer,

PVDF membranes were activated in methanol before being soaked in transfer

buffer. Gel sandwich was assembled according to manufacturer's manual. The

blot was run in transfer buffer at 100V, 4 ℃ for 1 hour. After the transfer

finished, protein-containing membranes were blocked using blocking buffer for

1 hour at room temperature. Afterwards, each membrane was incubated with 5

mL primary antibody solution (final concentrations: A5/158 – 4 µg/mL) in a 50

mL centrifuge tube, which was placed on a universal turning device with

continuous rotation at 4℃ overnight. After overnight incubation with the

primary antibody, membranes were washed 3 × 10 minutes with washing

buffer and incubated with secondary antibody for one hour at room

temperature using the same method as the primary antibody incubation. After 3

× 10 minute washes, membranes were incubated with ECL substrate for 3

minutes before undergoing membrane exposure, image acquisition, and

subsequent band analyses on ChemiDoc™ XRS+ System with associated

ImageLab software (Bio-Rad).

6.18 CCK-8 cytotoxicity assay

Initially, a 100μl cell suspension containing 5000 cells were dispensed per well in a 96 well plate and incubated for a period of 24 h in a humidified incubator (37°C, 5% CO_2) allowing cells to become confluent. Following this, 10μl of InP/ZnS (2) – TGA in varying concentrations were added to each well and allowed to incubate overnight. On completion of incubation with InP based QDs, 10μl of CCK-8 testing solution was added to each well incubation period, taking care not to add any bubbles to the wells (as bubbles will interfere with the absorbance reading). Note that 30 minutes prior to the use of the CCK-8 testing solution thawing on the bench top is required. The plate was then allowed to incubate for a period of 2h before absorbance reading were taken determining cell viability (λ_{ab} = 450 nm).

6.19 Flow Cytometry

6.19.1 Materials

Primary antibody: mouse anti-Endo180 monoclonal antibody A5/158 or 39.10. Secondary antibody: Alexa Fluor 488 Rabbit Anti-Mouse IgG (H+L) (Invitrogen, A-11059). Blocking buffer: 5% BSA (Sigma-Aldrich, A2153). Fixation buffer: 4% PFA (Insight Biotechnology, sc-281692).

6.19.2 Methods

Using a 6-well plate, 200000 cells in cell culture media were added to each well and incubated in a humidified incubator (37°C, 5% CO2) allowing the cells to become confluent (at least 80% before use). Following this, 200μl of trypLE™ Express was used to detach cells from the surface of the plate before 800μl of PBS was added to each well before cells were then collected and split by adding 333 μl to three epindorph tubes. In a cooled centrifuge (4°C), the cells were centrifuged at 7000 rpm for 1 minute to allow the formation of a pellet before the discarding of excess supernatant. The re-suspension of cells in 200μl 1% BSA blocking solution was then complete for a period of 20 minutes over ice to discourage . On completion, 800μl of PBS was used to wash and cells underwent re-centrifuge at 7000 rpm for 1 minute (washing process with 800μl of PBS completed x2). Following the washing process, re-suspend cells in 100μl of primary antibody (A5.158/39.10, concentrations used in section 6.1.1) in a ratio of 1:2500 and leave on ice for 20 minutes. On completion, 800μl of PBS solution was again added and centrifuged at 7000 rpm for 1 minute (x2). Re-suspend cells in 200μl of secondary antibody (ratio of 1:1000) and washed/centrifuged in PBS as earlier outlined. Cells are then re-suspended in 500μl of PBS and FACS analysis complete.

Flow cytometry analysis was carried out using FACS Calibur™flow cytometer with associated BD CellQuest™ Pro data collection and analysis software (BD Biosciences).

6.20 Immunofluorescence Protocol for Tissue samples

6.20.1 Preparation of prostate cancer patient tissue samples

protocol for immunostaining of PCa tissue samples derived and obtained in collaboration with Dr. Kelly Coffey's laboratory at Newcastle university.

Following ethical approval, human prostate tissue was obtained from PC patients undergoing robotic radical prostatectomy or channel transurethral resection of the prostate, with written, informed consent. Immediately following surgery, biopsies were taken of both benign and tumour tissue, where possible. Patient samples were then transported to the laboratory. Arrival samples were immediately fixed in 4% (v/v) paraformaldehyde in PBS for 24 hours at room temperature. Samples to be used as patient-derived explants were culturedex vivo, as described by Centenera and colleagues, before being fixed. Samples were then embedded in paraffin blocks and sectioned using a microtome, to a thickness of approximately 5 μm, before being mounted on SuperFrost-plus slides. Slides were stored at room temperature.[224]

6.20.2 Immunofluorescence imagine

Slides were de-paraffinised in xylene before being hydrated by sequentially dipping in 100%, 95%, 70%, and 50% (v/v) ethanol solutions. Antigen was retrieved by incubating in citrate buffer and heating to 125^{0}C in a 2100-Retriever decloaking chamber (Aptum Biologicals). Slides were then rinsed in running tap-water for 5 minutes and placed into T-TBS. Non-specific binding was blocked by incubating slides with 4% (w/v) BSA solution for 1

hour at room temperature. Following this, slides were incubated with primary

antibody, incubated with fluorophore-conjugated secondary antibody,

mounted, and imaged on a Leica DM6 fluorescence microscope and analysed

using LAS-X (Leica) and ImageJ (Fiji).

Chapter 7: References

(1)   Standring, S. *Gray's Anatomy: The Atomical Basis of Clinical Practice*;

        Elsevier Ltd, 2008.

(2)   Thibodeau, Gary A. Patton, K. T. *Anatomy and Physiology*; Elsevier Inc.,

        1999.

(3)   Mcneal, J. The Zonal Anatomy of the Prostate. *Prostate* **1981**, *2*, 35–49.

(4)   Gronau, J. H. The Role of Endo180 in Prostate Cancer Cell Migration and

        Metastasis : PhD Thesis, Imperial College London, 2012.

(5)   Miller, K. D.; Siegel, R. L.; Lin, C. C.; Mariotto, A. B.; Kramer, J. L.; Rowland,

        J. H.; Stein, K. D.; Alteri, R.; Jemal, A. Cancer Treatment and Survivorship

        Statistics, 2016. *CA. Cancer J. Clin.* **2016**, *66* (4), 271–289.

(6)   Siegel, R. L.; Miller, K. D. Cancer Statistics. **2019**, *69* (1), 7–34.

(7)   Pu, F.; Qiao, J.; Xue, S.; Yang, H.; Patel, A.; Wei, L.; Hekmatyar, K.; Salarian,

        M.; Grossniklaus, H. E.; Liu, Z.-R.; Yang, J. J. GRPR-Targeted Protein

        Contrast Agents for Molecular Imaging of Receptor Expression in Cancers

        by MRI. *Sci. Rep.* **2015**, *5*, 1–14.

(8)   Litwin, M. S.; Tan, H.-J. The Diagnosis and Treatment of Prostate Cancer.

        JAMA. **2017**, *317* (24), 2532–2542.

(9)   Gandhi, J.; Afridi, A.; Vatsia, S.; Joshi, G.; Joshi, G.; Kaplan, S. A.; Smith, N. L.;

        Khan, S. A. The Molecular Biology of Prostate Cancer: Current

        Understanding and Clinical Implications. *Prostate Cancer Prostatic Dis.*

        2018, *21* (1), 22–36.

(10)   Parker, C.; Gillessen, S.; Heidenreich, A.; Horwich, A.; Committee, G.

Cancer of the Prostate : ESMO Clinical Practice Guidelines for Diagnosis, Treatment and Follow-Up. *Ann. Oncol.* **2015**, *26*.

(11)   Gleason, D. Classification of Prostatic Carcinomas. *Cancer Chemother.* **1966**, *50* (3), 125–128.

(12)   Gleason, D. F. Histologic Grading of Prostate Cancer: A Perspective. *Hum. Pathol.* **1992**, *23* (3), 273–279.

(13)   Osunkoya, A. O. Update on Prostate Pathology. *Pathology* **2012**, *44* (5), 391–406.

(14)   Epstein, J. I.; Egevad, L.; Amin, M. B.; Delahunt, B.; Srigley, J. R.; Humphrey, P. A.; Committee, G. The 2014 International Society of Urological Pathology (ISUP) Consensus Conference on Gleason Grading of Prostatic Carcinoma. *Am. J. Surg. Pathol.* **2016**, *40* (2), 244–252.

(15)   Humphrey, P. A. Gleason Grading and Prognostic Factors in Carcinoma of the Prostate. *Mod. Pathol.* **2004**, *17* (3), 292–306.

(16)   Bjurlin, M. A.; Carter, H. B.; Schellhammer, P.; Cookson, M. S.; Gomella, L. G.; Troyer, D.; Wheeler, T. M.; Schlossberg, S.; David, F. Optimization of Initial Prostate Biopsy in Clinical Practice: Sampling, Labeling, and Specimen Processing. *J. Urol.* **2014**, *189* (6), 2039–2046.

(17)   Rubin, M. A.; Demichelis, F. The Genomics of Prostate Cancer: Emerging Understanding with Technologic Advances. *Mod. Pathol.* **2018**, *31*, 1–11.

(18)   Huggins, C.; Hodges, C. V. Studies on Prostatic Cancer i. the Effect of Castration, of Estrogen and of Androgen Injection on Serum Phosphatases in Metastatic Carcinoma of the Prostate. *Cancer Res.* **1941**, *1* (4), 293–297.

(19)   Whitaker, H.; Tam, J. O.; Connor, M. J.; Grey, A. Prostate Cancer Biology &

Genomics. *Transl. Androl. Urol.* **2020**, *9* (3), 1481–1491.

(20) Feng, Q.; He, B. Androgen Receptor Signaling in the Development of

Castration-Resistant Prostate Cancer. *Front. Oncol.* **2019**, *9* (September),

1–10.

(21) Tan, M. E.; Li, J.; Xu, H. E.; Melcher, K.; Yong, E. L. Androgen Receptor:

Structure, Role in Prostate Cancer and Drug Discovery. *Acta Pharmacol.*

Sin. **2015**, *36* (1), 3–23.

(22) Buchanan, G.; Irvine, R. A.; Coetzee, G. A.; Tilley, W. D. Contribution of the

Androgen Receptor to Prostate Cancer Predisposition and Progression.

Cancer Metastasis Rev. **2001**, *20* (3–4), 207–223.

(23) Steinkamp, M. P.; O'Mahony, O. A.; Brogley, M.; Rehman, H.; Lapensee, E.

W.; Dhanasekaran, S.; Hofer, M. D.; Kuefer, R.; Chinnaiyan, A.; Rubin, M. A.;

Pienta, K. J.; Robins, D. M. Treatment-Dependent Androgen Receptor

Mutations in Prostate Cancer Exploit Multiple Mechanisms to Evade

Therapy. *Cancer Res.* **2009**, *69* (10), 4434–4442.

(24) Locke, J. A.; Guns, E. S.; Lubik, A. A.; Adomat, H. H.; Hendy, S. C.; Wood, C.

A.; Ettinger, S. L.; Gleave, M. E.; Nelson, C. C. Androgen Levels Increase by

Intratumoral de Novo Steroidogenesis during Progression of Castration-

Resistant Prostate Cancer. *Cancer Res.* **2008**, *68* (15), 6407–6415.

(25) Heemers, H. V; Tindall, D. J. Androgen Receptor (AR) Coregulators: A

Diversity of Functions Converging on and Regulating the AR

Transcriptional Complex. *Endocr. Rev.* **2007**, *28* (7), 778–808.

(26) Zhu, M.-L.; Kyprianou, N. Androgen Receptor and Growth Factor Signaling

Cross-Talk in Prostate Cancer Cells. *Endocr. Relat. Cancer* **2008**, *15* (4),

841–849.

(27)   Venkitaraman, R.; Thomas, K.; Huddart, R. A.; Horwich, A.; Dearnaley, D.
        P.; Parker, C. C. Efficacy of Low-Dose Dexamethasone in Castration-
        Refractory Prostate Cancer. *BJU Int.* **2008**, *101* (4), 440–443.

(28)   American Cancer Society. Hormone Therapy for Prostate Cancer
        https://www.cancer.org/cancer/prostate-cancer/treating/hormone-
        therapy.html (accessed Sep 11, 2020).

(29)   Manesh R. Patel, M.D., Kenneth W. Mahaffey, M.D., Jyotsna Garg, M.S., et
        al. Radiotherapy and Short-Term Androgen Deprivation for Localized
        Prostate Cancer. *N. Engl. J. Med.* **2011**, *365* (10), 883–891.

(30)   Denham, J. W.; Steigler, A.; Lamb, D. S.; Joseph, D.; Turner, S.; Matthews, J.;
        Atkinson, C.; North, J.; Christie, D.; Spry, N. A.; Tai, K. H.; Wynne, C.; D'Este,
        C. Short-Term Neoadjuvant Androgen Deprivation and Radiotherapy for
        Locally Advanced Prostate Cancer: 10-Year Data from the TROG 96.01
        Randomised Trial. *Lancet Oncol.* **2011**, *12* (5), 451–459.

(31)   D'Amico, A. V. Androgen Suprression and Radiation Vs Radiation Alone
        for Prostate Cancer. *JAMA.* **2008**, *299* (3), 289–295.

(32)   Botrel, T. E. A.; Clark, O.; Dos Reis, R. B.; Pompeo, A. C. L.; Ferreira, U.; Sadi,
        M. V.; Bretas, F. F. H. Intermittent versus Continuous Androgen
        Deprivation for Locally Advanced, Recurrent or Metastatic Prostate
        Cancer: A Systematic Review and Meta-Analysis. *BMC Urol.* **2014**, *14* (1),
        1–14.

(33)   Sweeney, C. J.; Chen, Y.-H.; Carducci, M.; Liu, G.; Jarrard, D. F.; Eisenberger,
        M.; Wong, Y.-N.; Hahn, N.; Kohli, M.; Cooney, M. M.; Dreicer, R.; Vogelzang,
        N. J.; Picus, J.; Shevrin, D.; Hussain, M.; Garcia, J. A.; DiPaola, R. S.
        Chemohormonal Therapy in Metastatic Hormone-Sensitive Prostate

Cancer. *N. Engl. J. Med.* **2015**, *373* (8), 737–746.

(34)   Welch, H. G.; Albertsen, P. C. Prostate Cancer Diagnosis and Treatment

after the Introduction of Prostate-Specific Antigen Screening: 1986-2005.

J. Natl. Cancer Inst. **2009**, *101* (19), 1325–1329.

(35)   Catalona, W. J.; Partin, A. W.; Slawin, K. M.; Brawer, M. K.; Flanigan, R. C.;

Patel, A.; Richie, J. P.; DeKernion, J. B.; Walsh, P. C.; Scardino, P. T.; Lange,

P. H.; Subong, E. N. P.; Parson, R. E.; Gasior, G. H.; Loveland, K. G.;

Southwick, P. C. Use of the Percentage of Free Prostate-Specific Antigen to

Enhance Differentiation of Prostate Cancer From Benign Prostatic

Disease. *JAMA.* **1998**, *279* (19), 1542.

(36)   Sutcliffe, S.; Pakpahan, R.; Sokoll, L. J.; Elliott, D. J.; Nevin, R. L.; Cersovsky,

S. B.; Walsh, P. C.; Platz, E. A. Prostate-Specific Antigen Concentration in

Young Men: New Estimates and Review of the Literature. *BJU Int.* **2012**,

110 (11), 1627–1635.

(37)   Klein, E. A.; Cooperberg, M. R.; Magi-Galluzzi, C.; Simko, J. P.; Falzarano, S.

M.; Maddala, T.; Chan, J. M.; Li, J.; Cowan, J. E.; Tsiatis, A. C.; Cherbavaz, D.

B.; Pelham, R. J.; Tenggara-Hunter, I.; Baehner, F. L.; Knezevic, D.; Febbo,

P. G.; Shak, S.; Kattan, M. W.; Lee, M.; Carroll, P. R. A 17-Gene Assay to

Predict Prostate Cancer Aggressiveness in the Context of Gleason Grade

Heterogeneity, Tumor Multifocality, and Biopsy Undersampling. *Eur. Urol.*

2014, *66* (3), 550–560.

(38)   Knudsen, B. S.; Kim, H. L.; Erho, N.; Shin, H.; Alshalalfa, M.; Lam, L. L. C.;

Tenggara, I.; Chadwich, K.; Van Der Kwast, T.; Fleshner, N.; Davicioni, E.;

Carroll, P. R.; Cooperberg, M. R.; Chan, J. M.; Simko, J. P. Application of a

Clinical Whole-Transcriptome Assay for Staging and Prognosis of

Prostate Cancer Diagnosed in Needle Core Biopsy Specimens. *J. Mol. Diagnostics* **2016**, *18* (3), 395–406.

(39) Sommariva, S.; Tarricone, R.; Lazzeri, M.; Ricciardi, W.; Montorsi, F. Prognostic Value of the Cell Cycle Progression Score in Patients with Prostate Cancer: A Systematic Review and Meta-Analysis. *Eur. Urol.* **2016**, *69* (1), 107–115.

(40) Siegel, R.; Miller, K.; Jemal, A. Cancer Statistics , 2015 . *CA Cancer J Clin* **2015**, *65* (1), 29.

(41) Rodriguez-Teja, M.; Gronau, J. H.; Breit, C.; Zhang, Y. Z.; Minamidate, A.; Caley, M. P.; McCarthy, A.; Cox, T. R.; Erler, J. T.; Gaughan, L.; Darby, S.; Robson, C.; Mauri, F.; Waxman, J.; Sturge, J. AGE-Modified Basement Membrane Cooperates with Endo180 to Promote Epithelial Cell Invasiveness and Decrease Prostate Cancer Survival. *J. Pathol.* **2015**, *235* (4), 581–592.

(42) Rodriguez-Teja, M.; Gronau, J. H.; Minamidate, A.; Darby, S.; Gaughan, L.; Robson, C.; Mauri, F.; Waxman, J.; Sturge, J. Survival Outcome and EMT Suppression Mediated by a Lectin Domain Interaction of Endo180 and CD147. *Mol. Cancer Res.* **2015**, *13* (3), 538–547.

(43) Isacke, C. M.; van der Geer, P.; Hunter, T.; Trowbridge, I. S. P180, a Novel Recycling Transmembrane Glycoprotein With Restricted Cell Type Expression. *Mol. Cell. Biol.* **1990**, *10* (6), 2606–2618.

(44) Wu, K.; Yuan, J.; Lasky, L. A. Characterization of a Novel Member of the Macrophage Mannose Receptor Type C Lectin Family. *J. Biol. Chem.* **1996**, *271* (35), 21323–21330.

(45) East, L.; Isacke, C. M. The Mannose Receptor Family. *Biochim. Biophys.*

Acta **2002**, *1572*, 364–386.

(46)   Behrendt, N.; Jensen, O. N.; Engelholm, L. H.; Mørtz, E.; Mann, M.; Danø, K.
A Urokinase Receptor-Associated Protein with Specific Collagen Binding
Properties. *J. Biol. Chem.* **2000**, *275* (3), 1993–2002.

(47)   Melander, M.; Jï¿½rgensen, H.; Madsen, D.; Engelholm, L.; Behrendt, N.
The Collagen Receptor UPARAP/Endo180 in Tissue Degradation and
Cancer (Review). *Int. J. Oncol.* **2015**, 1177–1188.

(48)   Behrendt, N. The Urokinase Receptor (UPAR) and the UPAR-Associated
Protein (UPARAP/Endo180): Membrane Proteins Engaged in Matrix
Turnover during Tissue Remodeling. *Biol. Chem.* **2004**, *385* (2), 103–136.

(49)   Wang, K. Investigating the Biological and Clinical Implications of Endo180
in Breast Cancer, 2017.

(50)   Rivera-calzada, A.; Robertson, D.; Macfadyen, J. R.; Boskovic, J.; Isacke, C.
M. Three-Dimentional Interplay Amoung the Ligand-Binding Domains of
the Urokinase-Plasminogen-Activator-Receptor-Associated Protein,
Endo180. *Eur. Mol. Biol. Organ.* **2003**, *4*, 807–812.

(51)   Kogianni, G.; Walker, M. M.; Waxman, J.; Sturge, J. Endo180 Expression
with Cofunctional Partners MT1-MMP and UPAR-UPA Is Correlated with
Prostate Cancer Progression. *Eur. J. Cancer* **2009**, *45* (4), 685–693.

(52)   Engelholm, L. H.; Melander, M. C.; Hald, A.; Persson, M.; Madsen, D. H.;
Henrik, J.; Johansson, K.; Nielsen, C.; Nørregaard, K. S.; Ingvarsen, S. Z.;
Kjær, A.; Trovik, C. S.; Lærum, O. D.; Bugge, T. H.; Eide, J.; Behrendt, N.
Targeting a Novel Bone Degradation Pathway in Primary Bone Cancer by
Inactivation of the Collagen Receptor UPARAP / Endo180. *J. Pathol.* **2016**,
238, 120–133.

(53)   Sturge, J. Endo180 at the Cutting Edge of Bone Cancer Treatment and Beyond. *Pathology* **2016**, *238*, 485–488.

(54)   Lund, I. K.; Rasch, M. G.; Ingvarsen, S.; Pass, J.; Madsen, D. H.; Engelholm, L. H.; Behrendt, N.; Høyer-hansen, G. Inhibitory Monoclonal Antibodies against Mouse Proteases Raised in Gene-Deficient Mice Block Proteolytic Functions in Vivo. *Front. Pharmacolgy* **2012**, *3*, 1–6.

(55)   Sturge, J.; Wienke, D.; East, L.; Jones, G. E.; Isacke, C. M. GPI-Anchored UPAR Requires Endo180 for Rapid Directional Sensing during Chemotaxis. *J. Cell Biol.* **2003**, *162* (5), 789–794.

(56)   Sturge, J.; Wienke, D.; Isacke, C. M. Endosomes Generate Localized Rho-ROCK-MLC2-Based Contractile Signals via Endo 180 to Promote Adhesion Disassembly. *J. Cell Biol.* **2006**, *175* (2), 337–347.

(57)   Thiery, J. P.; Acloque, H.; Huang, R. Y. J.; Nieto, M. A. Epithelial-Mesenchymal Transitions in Development and Disease. *Cell* **2009**, *139* (5), 871–890.

(58)   Wienke, D.; Davies, G. C.; Johnson, D. A.; Sturge, J.; Lambros, M. B. K.; Savage, K.; Elsheikh, S. E.; Green, A. R.; Ellis, I. O.; Robertson, D.; Reis-filho, J. S.; Isacke, C. M. The Collagen Receptor Endo180 (CD280) Is Expressed on Basal-like Breast Tumor Cells and Promotes Tumor Growth In Vivo. *Cancer Res.* **2007**, *180* (21), 10230–10241.

(59)   D.E.Kim. *Primer on Cerebrovascular Diseases (Second Edition)*; 2017.

(60)   van der Meel, R.; Gallagher, W. M.; Oliveira, S.; O'Connor, A. E.; Schiffelers, R. M.; Byrne, A. T. Recent Advances in Molecular Imaging Biomarkers in Cancer: Application of Bench to Bedside Technologies. *Drug Discov. Today* **2010**, *15* (3–4), 102–114.

(61)   Edelman, R. R. The History of MR Imaging as Seen through the Pages of
       Radiology. *Radiology* **2014**, *273* (2), S181–S200.

(62)   Mansfield, P. Imaging Techniques Snapshot Magnetic Resonance Imaging.
       Angew. Chem. Int. Ed. **2004**, *43*, 5456–5464.

(63)   Lauterbur, P. C. All Science Is Interdisciplinary-from Magnetic Moments
       to Molecules to Men. *Biosci. Rep.* **2005**, *24* (3), 165–178.

(64)   Mark A. Brown, PhD. Richard C. Semelka, M. D. *MRI Basic Principles and
       Applications*, Third Edit.; Wiley, 2003.

(65)   Catherine Westbrook; Carolyn Kaut. *MRI in Practice*; Wiley, 1998; Vol. 37.

(66)   Tian, J. *Molecular Imaging : Advanced Topics and Applications*; Springer,
       2013.

(67)   Jones, D. B. D. M. and D. J. www.radiopaedia.org.

(68)   Keeler, J. *Understanding NMR Spectroscopy*; Wiley, 2010.

(69)   Chen, X. *Molecular Imaging Probes for Cancer Research*; World Scientific,
       2012.

(70)   Long, N. *The Chemistry of Molecular Imaging*; Wiley, 2015.

(71)   Chavhan, G. B.; Babyn, P. S.; Thomas, B.; Shroff, M. M.; Haacke, E. M.
       Principles, Techniques, and Applications of T2*-Based MR Imaging and Its
       Special Applications. *Radiographics* **2009**, *29*, 1433–1449.

(72)   Dong, H.; Du, S. R.; Zheng, X. Y.; Lyu, G. M.; Sun, L. D.; Li, L. D.; Zhang, P. Z.;
       Zhang, C.; Yan, C. H. Lanthanide Nanoparticles: From Design toward
       Bioimaging and Therapy. *Chem. Rev.* **2015**, *115* (19), 10725–10815.

(73)   Haimerl, M.; Wachtler, M.; Zeman, F.; Verloh, N.; Platzek, I.; Schreyer, A. G.;
       Stroszczynski, C.; Wiggermann, P. Quantitative Evaluation of
       Enhancement Patterns in Focal Solid Liver Lesions with Gd-EOB-DTPA-

Enhanced MRI. *PLoS One* **2014**, *9* (6), 2–7.

(74) Padhani, A. R.; Gapinski, C. J.; Macvicar, D. A.; Parker, G. J.; Suckling, J.;

Revell, P. B.; Leach, M. O.; Dearnaley, D. P.; Husband, J. E. Dynamic

Contrast Enhanced MRI of Prostate Cancer: Correlation with Morphology

and Tumour Stage, Histological Grade and PSA. *Clin. Radiol.* **2000**, *55* (2),

99–109.

(75) Jhaveri, K.; Cleary, S.; Audet, P.; Balaa, F.; Bhayana, D.; Burak, K.; Chang, S.;

Dixon, E.; Haider, M.; Molinari, M.; Reinhold, C.; Sherman, M. Consensus

Statements from a Multidisciplinary Expert Panel on the Utilization and

Application of a Liver-Specific MRI Contrast Agent (Gadoxetic Acid). *Am. J.*

Roentgenol. **2015**, *204* (3), 498–509.

(76) Laurent, S.; Henoumont, C.; Vander Elst, L.; Muller, R. N. Synthesis and

Physicochemical Characterisation of Gd-DTPA Derivatives as Contrast

Agents for MRI. *Eur. J. Inorg. Chem.* **2012**, No. 12, 1889–1915.

(77) Liao, Z.; Li, C.; Yang, Z.; Liao, Z.; Li, C.; Yang, Z. Synthesis and Evaluation of

Neutral Gd (III), Mn (II) Complexes From DTPA-Bisamide Derivative as

Potential MRI Contrast Agents. *Inorg. nano-metal Chem.* **2016**, *46*, 653–

658.

(78) Gao, Z.; Ma, T.; Zhao, E.; Docter, D.; Yang, W.; Stauber, R. H.; Gao, M. Small

Is Smarter: Nano MRI Contrast Agents - Advantages and Recent

Achievements. *Small* **2016**, *12* (5), 556–576.

(79) Lauffer, R. B. Paramagnetic Metal Complexes as Water Proton Relaxation

Agents for NMR Imaging : Theory and Design. *Am. Chem. Soc.* **1987**, 901–

927.

(80) Caravan, P.; Ellison, J. J.; McMurry, T. J.; Lauffer, R. B. Gadolinium(III)

Chelates as MRI Contrast Agents: Structure, Dynamics, and Applications. *Chem. Rev.* **1999**, *99* (9), 2293–2352.

(81)   Stasiuk, G. J.; Long, N. J. The Ubiquitous DOTA and Its Derivatives: The Impact of 1,4,7,10-Tetraazacyclododecane-1,4,7,10-Tetraacetic Acid on Biomedical Imaging. *Chem. Commun. (Camb).* **2013**, *49* (27), 2732–2746.

(82)   Shannon, R. D. Revised Effective Ionic Radii and Systematic Studies of Interatomic Distances in Halides and Chalcogenides. *Acta Crystallogr. Sect. A* **1976**, *32* (5), 751–767.

(83)   Shannon, R. D.; Prewitt, C. T. Effective Ionic Radii in Oxides and Fluorides. *Acta Crystallogr. Sect. B* **1969**, *25* (5), 925–946.

(84)   Lowe, M. P. MRI Contrast Agents: The Next Generation. *Aust. J. Chem.* **2002**, *55*, 551–556.

(85)   Datta, A.; Raymond, K. N. Gd-Hydroxypyridinone (HOPO)-Based High-Relaxivity Magnetic Resonance Imaging (MRI) Contrast Agents. *Acc. Chem. Res.* **2009**, *42* (7), 938–947.

(86)   Ur, H.; Antonio, M.; Martines, U.; Jorge, J.; Martin, P.; Moraes, D.; Naveed, M.; Khan, K.; Ur, H. Cyclen Based Gd(III) Complexes as MRI Contrast Agents : Relaxivity Enhancement and Ligand Design. *Bioorg. Med. Chem.* **2016**, *24* (22), 5663–5684.

(87)   Caravan, P. Strategies for Increasing the Sensitivity of Gadolinium Based MRI Contrast Agents. *Chem. Soc. Rev.* **2006**, *35*, 512–523.

(88)   Vincent, J.; Stephane, D.; Wei-Chuan, S.; Jeffrey s, T.; Matthew t, G.; Peter, C. High Relaxivity MRI Contrast Agents Part 2: Optimization of Inner- and Second-Sphere Relaxivity. *Natl. Inst. Heal.* **2011**, *45* (10), 613–624.

(89)   Siriwardena-mahanama, B. N.; Allen, M. J. Strategies for Optimizing

Water-Exchange Rates of Lanthanide-Based Contrast Agents for Magnetic Resonance Imaging. *Molecules* **2013**, *18*, 9352–9381.

(90) Woods, M.; Botta, M.; Avedano, S.; Wang, J.; Sherry, A. D. Towards the Rational Design of MRI Contrast Agents: A Practical Approach to the Synthesis of Gadolinium Complexes That Exhibit Optimal Water Exchange. *Dalton Trans.* **2005**, No. 24, 3829–3837.

(91) Laus, S.; Ruloff, R.; Toth, E.; Merbach, A. E. Gd III Complexes with Fast Water Exchange and High Thermodynamic Stability : Potential Building Blocks for High-Relaxivity MRI Contrast Agents. *Chem. - A Eur. J.* **2003**, *9*, 3555–3566.

(92) Clough, T. J.; Jiang, L.; Wong, K.; Long, N. J. Ligand Design Strategies to Increase Stability of Gadolinium-Based Magnetic Resonance Imaging Contrast Agents. *Nat. Commun.* **2019**, *10* (1420), 1–14.

(93) Opina, A. C. L.; Strickland, M.; Lee, Y.-S.; Tjandra, N.; Byrd, R. A.; Swenson, R. E.; Vasalatiy, O. Analysis of the Isomer Ratios of Polymethylated-DOTA Complexes and the Implications on Protein Structural Studies. *Dalton Trans.* **2016**, *45* (11), 4673–4687.

(94) Frullano, L.; Rohovec, J.; Peters, J. A.; Geraldes, C. F. G. C. Structures of MRI Contrast Agents in Solution. In *Contrast Agents I: Magnetic Resonance Imaging*; Krause, W., Ed.; Springer Berlin Heidelberg: Berlin, Heidelberg, 2002; pp 25–60.

(95) Woods, M.; Aime, S.; Botta, M.; Howard, J. A. K.; Moloney, J. M.; Navet, M.; Parker, D.; Port, M.; Rousseaux, O. Correlation of Water Exchange Rate with Isomeric Composition in Diastereoisomeric Gadolinium Complexes of Tetra(Carboxyethyl)Dota and Related Macrocyclic Ligands. *J. Am. Chem.*

Soc. **2000**, *122*, 9781–9792.

(96)   Hu, H.; Sheng, Y.; Ye, M.; Qian, Y.; Tang, J.; Shen, Y. A Porphyrin-Based

Magnetic and Fluorescent Dual-Modal Nanoprobe for Tumor Imaging.

Polymer (Guildf). **2016**, *88*, 94–101.

(97)   Ye, Z.; Wu, X.; Tan, M.; Jesberger, J.; Grisworld, M.; Lu, Z. Synthesis and

Evaluation of a Polydisulfide with Gd – DOTA Monoamide Side Chains as a

Biodegradable Macromolecular Contrast Agent for MR Blood Pool

Imaging. *Contrast Media Mol. Imaging* **2013**, *8*, 220–228.

(98)   Casali, C.; Janier, M.; Canet, E.; Obadia, J. F.; Benderbous, S.; Corot, C.;

Revel, D. Evaluation of Gd-DOTA-Labeled Dextran Polymer as an

Intravascular MR Contrast Agent for Myocardial Perfusion. *Acad. Radiol.*

1998, *5*, 214–218.

(99)   Aime, S.; Frullano, L. Compartmentalization of a Gadolinium Complex in

the Apoferritin Cavity : A Route To Obtain High Relaxivity Contrast

Agents for Magnetic Resonance Imaging. *Angew. Chem. Int. Ed.* **2002**, *521*

(6), 2001–2003.

(100) Schmieder, A. H.; Winter, P. M.; Caruthers, S. D.; Harris, T. D.; Williams, T.

A.; Allen, J. S.; Lacy, E. K.; Zhang, H.; Scott, M. J.; Hu, G.; Robertson, J. D.;

Wickline, S. A.; Lanza, G. M. Molecular MR Imaging of Melanoma

Angiogenesis with α Nβ3-Targeted Paramagnetic Nanoparticles. *Magn.*

Reson. Med. **2005**, *53* (3), 621–627.

(101) Woods, Mark. Zhang, Shanrong. Sherry, D. Toward the Design of MR

Agents for Imaging β -Cell Function. *Curr Med Chem Immunol. Endocr.*

Metab Agents **2004**, *4* (4), 349–369.

(102) Yaghini, E.; Turner, H. D.; Le Marois, A. M.; Suhling, K.; Naasani, I.;

MacRobert, A. J. In Vivo Biodistribution Studies and Ex Vivo Lymph Node
Imaging Using Heavy Metal-Free Quantum Dots. *Biomaterials* **2016**, *104*,
182–191.

(103) Harrison, V. S. R.; Carney, C. E.; MacRenaris, K. W.; Waters, E. A.; Meade, T.
J. Multimeric Near IR-MR Contrast Agent for Multimodal in Vivo Imaging.
J. Am. Chem. Soc. **2015**, *137* (28), 9108–9116.

(104) Stasiuk, G. J.; Tamang, S.; Imbert, D.; Gateau, C.; Reiss, P.; Fries, P.;
Mazzanti, M. Optimizing the Relaxivity of Gd(III) Complexes Appended to
InP/ZnS Quantum Dots by Linker Tuning. *Dalton Trans.* **2013**, *42* (23),
8197.

(105) Louie, A. Multimodality Imaging Probes: Design and Challenges. *Chem.
Rev.* **2010**, *110* (5), 3146–3195.

(106) Li, M.; Wang, Y.; Liu, M.; Lan, X. Multimodality Reporter Gene Imaging :
Construction Strategies and Application. *Theranostics* **2018**, *8* (11),
2954–2973.

(107) Banerjee, S. R.; Ngen, E. J.; Rotz, M. W.; Kakkad, S.; Lisok, A.; Pracitto, R.;
Pullambhatla, M.; Chen, Z.; Shah, T.; Artemov, D.; Meade, T. J.; Bhujwalla, Z.
M.; Pomper, M. G. Synthesis and Evaluation of Gd III -Based Magnetic
Resonance Contrast Agents for Molecular Imaging of Prostate-Specific
Membrane Antigen. *Angew. Chem. Int. Ed.* **2015**, *54*, 10778–10782.

(108) Townsend, T. R.; Moyle-heyrman, G.; Sukerkar, P. A.; Macrenaris, K. W.;
Burdette, J. E.; Meade, T. J. Progesterone-Targeted Magnetic Resonance
Imaging Probes. *Bioconjug. Chem.* **2014**, *25*, 1428–1437.

(109) Livramento, J. B., Tóth, E., Sour, A., Borel, A., Merbach, A. E., Ruloff, R. High
Relaxivity Confined to a Small Molecular Space: A Metallostar-Based,

Potential MRI Contrast Agent. *Angew. Chem. Int. Ed.* **2005**, *44*, 1480–1484.

(110) Holbrook, R. J.; Rammohan, N.; Rotz, M. W.; MacRenaris, K. W.; Preslar, A. T.; Meade, T. J. Gd(III)-Dithiolane Gold Nanoparticles for T1 -Weighted Magnetic Resonance Imaging of the Pancreas. *Nano Lett.* **2016**, *16*, 3202–3209.

(111) Sung, S.; Holmes, H.; Wainwright, L.; Toscani, A.; Stasiuk, G. J.; White, A. J. P.; Bell, J. D.; Wilton-ely, J. D. E. T. Multimetallic Complexes and Functionalized Gold Nanoparticles Based on a Combination of D- and f - Elements. *Inorg. Chem.* **2014**, *53*, 1989–2005.

(112) Chabloz, N. G.; Wenzel, M. N.; Perry, H. L.; Yoon, I.; Molisso, S.; Stasiuk, G. J.; Elson, D. S.; Cass, A. E. G.; Wilton-ely, J. D. E. T. Polyfunctionalised Nanoparticles Bearing Robust Gadolinium Surface Units for High Relaxivity Performance in MRI. *Chem. - A Eur. J.* **2019**, *25*, 10895–10906.

(113) Etrych, T.; Lucas, H.; Janoušková, O.; Chytil, P.; Mueller, T.; Mäder, K. Fluorescence Optical Imaging in Anticancer Drug Delivery. *J. Control. Release* **2016**, *226*, 168–181.

(114) Gibson, A.; Hebden, J.; Arridge, S. Recent Advances in Diffuse Optical Imaging. *Phys. Med. Biol.* **2005**, *50*, 1–42.

(115) Tessier, M. D.; Dupont, D.; De Nolf, K.; De Roo, J.; Hens, Z. Economic and Size-Tunable Synthesis of InP/ZnE (E = S,Se) Colloidal Quantum Dots. *Chem. Mater.* **2015**, *27*, 4893–4898.

(116) Cros-gagneux, A.; Delpech, F.; Cornejo, A.; Coppel, Y.; Chaudret, B. Surface Chemistry of InP Quantum Dots : A Comprehensive Study. *J. Am. Chem. Soc.* **2010**, *132* (7), 18147–18157.

(117) Zhang, Y.; Wang, T. H. Quantum Dot Enabled Molecular Sensing and

Diagnostics. *Theranostics* **2012**, *2* (7), 631–654.

(118) Freidel, C.; Kaloyanova, S.; Peneva, K. Chemical Tags for Site-Specific

Fluorescent Labeling of Biomolecules. *Amino Acids* **2016**, *48* (6), 1–16.

(119) Xu, G.; Zeng, S.; Zhang, B.; Swihart, M. T.; Yong, K. T.; Prasad, P. N. New

Generation Cadmium-Free Quantum Dots for Biophotonics and

Nanomedicine. *Chem. Rev.* **2016**, *116* (19), 12234–12327.

(120) Gioux, S.; Choi, H. S.; Frangioni, J. V. Image-Guided Surgery Using Invisible

near-Infrared Light: Fundamentals of Clinical Translation. *Mol. Imaging*

2010, *9* (5), 237–255.

(121) Zhao, J.; Chen, J.; Ma, S.; Liu, Q.; Huang, L.; Chen, X.; Lou, K.; Wang, W.

Recent Developments in Multimodality Fluorescence Imaging Probes.

Acta Pharm. Sin. B **2018**, *8* (3), 320–338.

(122) Ekimov, A. I.; Efros, A. L.; Onushchenko, A. A. Quantum Size Effect in

Semiconductor Microcrystals. *Solid State Commun.* **1985**, *56* (11), 921–

924.

(123) Brus, L. E. Electron–Electron and Electron-Hole Interactions in Small

Semiconductor Crystallites: The Size Dependence of the Lowest Excited

Electronic State. *J. Chem. Phys.* **1984**, *80* (9), 4403.

(124) Henglein, A. Small-Particle Research: Physicochemical Properties of

Extremely Small Colloidal Metal and Semiconductor Particles. *Chem. Rev.*

1989, *89* (8), 1861–1873.

(125) Rossetti, R.; Brus, L. Electron-Hole Recombination Emission as a Probe of

Surface Chemistry in Aqueous Cadmium Sulfide Colloids. *J. Phys. Chem.*

1982, *86* (23), 4470–4472.

(126) Bawendi, M. G.; Steigerwald, M. L.; Brus, L. E. The Quantum Mechanics Of

Larger Semiconductor Clusters. *Annu. Rev. Phys. Chem.* **1990**, *41* (4), 477–496.

(127) Li, L.; Reiss, P. One-Pot Synthesis of Highly Luminescent InP/ZnS Nanocrystals without Precursor Injection. *J. Am. Chem. Soc.* **2008**, *130* (35), 11588–11589.

(128) Bonilla, J. C.; Bozkurt, F.; Ansari, S.; Sozer, N.; Kokini, J. L. Applications of Quantum Dots in Food Science and Biology. *Trends Food Sci. Technol.* **2016**, *53*, 75–89.

(129) Dai, X.; Deng, Y.; Peng, X.; Jin, Y. Quantum-Dot Light-Emitting Diodes for Large-Area Displays : Towards the Dawn of Commercialization. *Adv. Mater.* **2017**, *29* (1607022), 1–22.

(130) Petta, J. R.; Johnson, A. C.; Taylor, J. M.; Laird, E. A.; Yacoby, A.; Lukin, M. D.; Marcus, C. M.; Hanson, M. P.; Gossard, A. C. Coherent Manipulation of Coupled Electron Spins in Semiconductor Quantum Dots. *Science (80-.).* **2005**, *309* (5744), 2180–2184.

(131) Baskoutas, S.; Terzis, A. F. Size-Dependent Band Gap of Colloidal Quantum Dots. *J. Appl. Phys.* **2006**, *99* (013708–1), 1–3.

(132) Tamang, S.; Lincheneau, C.; Hermans, Y.; Jeong, S.; Reiss, P. Chemistry of InP Nanocrystal Syntheses. *Chem. Mater.* **2016**, *28*, 2491–2506.

(133) Chan, W. C. W.; Maxwell, D. J.; Gao, X.; Bailey, R. E.; Han, M.; Nie, S. Luminescent Quantum Dots for Multiplexed Biological Detection and Imaging. *Curr. Opin. Biotechnol.* **2002**, *13* (1), 40–46.

(134) Pisanic, T. R.; Zhang, Y.; Wang, T. H. Quantum Dots in Diagnostics and Detection: Principles and Paradigms. *Analyst* **2014**, *139* (12), 2968–2981.

(135) Yang, S. J.; Oh, J. H.; Kim, S.; Yang, H.; Do, Y. R. Realization of InP/ZnS

Quantum Dots for Green, Amber and Red down-Converted LED and Their Color-Tunable, Four-Package White LEDs. *J. Mater. Chem. C* **2015**, *3*, 3582–3591.

(136) Byun, H.-J.; Song, W.-S.; Yang, H. Facile Consecutive Solvothermal Growth of Highly Fluorescent InP/ZnS Core/Shell Quantum Dots Using a Safer Phosphorus Source. *Nanotechnology* **2011**, *22* (23), 235605.

(137) Kim, S.; Fisher, B.; Eisler, H. J.; Bawendi, M. Type-II Quantum Dots: CdTe/CdSe(Core/Shell) and CdSe/ZnTe(Core/Shell) Heterostructures. *J. Am. Chem. Soc.* **2003**, *125* (38), 11466–11467.

(138) Weng, J.; Song, X.; Li, L.; Qian, H.; Chen, K.; Xu, X.; Cao, C.; Ren, J. Highly Luminescent CdTe Quantum Dots Prepared in Aqueous Phase as an Alternative Fluorescent Probe for Cell Imaging. *Talanta* **2006**, *70* (2), 397–402.

(139) Murray, C. B.; Norris, D.; Bawendi, M. G. Synthesis and Characterization of Nearly Monodisperse CdE (E= S, Se, Te) Semiconductor Nanocrystallites. *J. Am. Chem. Soc.* **1993**, *115* (4), 8706–8715.

(140) Zhang, J.; Zhang, X.; Zhang, J. Y. Dependence of Microstructure and Luminescence on Shell Layers in Colloidal CdSe/CdS Core/Shell Nanocrystals. *J. Phys. Chem. C* **2010**, *114* (9), 3904–3908.

(141) Xie, Renguo. Chen, Kai. Chen, Xiaoyuan. and Peng, X. InAs/InP/ZnSe Core/Shell/Shell Quantum Dots as Near-Infrared Emitters: Bright, Narrow-Band, Non-Cadmium Containing, and Biocompatible Renguo. *Natl. Inst. Heal.* **2011**, *4* (164), 457–464.

(142) Gerion, D.; Pinaud, F.; Williams, S. C.; PArak, W. J.; Zanchet, D.; Weiss, S.; Alivisatos, P. A. Synthesis and Properties of Biocompartible Water-

Soluble Silica-Coated CdSe/ZnS Semiconductor Quantum Dots. *J. Phys. Chem. B* **2001**, *105*, 8861–8871.

(143) Jaiswal, J. K.; Mattoussi, H.; Mauro, J. M.; Simon, S. M. Long-Term Multiple Color Imaging of Live Cells Using Quantum Dot Bioconjugates. *Nat. Biotechnol.* **2003**, *21* (1), 47–51.

(144) Hoshino, A.; Hanaki, K. I.; Suzuki, K.; Yamamoto, K. Applications of T-Lymphoma Labeled with Fluorescent Quantum Dots to Cell Tracing Markers in Mouse Body. *Biochem. Biophys. Res. Commun.* **2004**, *314* (1), 46–53.

(145) Ballou, B.; Lagerholm, B. C.; Ernst, L. A.; Bruchez, M. P.; Waggoner, A. S. Noninvasive Imaging of Quantum Dots in Mice. *Bioconjug. Chem.* **2004**, *15* (1), 79–86.

(146) Lewinski, N.; Colvin, V.; Drezek, R. Cytotoxicity of Nanopartides. *Small* **2008**, *4* (1), 26–49.

(147) Xu, S.; Kumar, S.; Nann, T. Rapid Synthesis of High-Quality InP Nanocrystals. *J. Am. Chem. Soc.* **2006**, *128* (4), 1054–1055.

(148) Lin, G.; Ouyang, Q.; Hu, R.; Ding, Z.; Tian, J.; Yin, F.; Xu, G.; Chen, Q.; Wang, X.; Yong, K. T. In Vivo Toxicity Assessment of Non-Cadmium Quantum Dots in BALB/c Mice. *Nanomedicine Nanotechnology, Biol. Med.* **2015**, *11* (2), 341–350.

(149) Choi, H. S.; Liu, W.; Misra, P.; Tanaka, E.; Zimmer, J. P.; Itty Ipe, B.; Bawendi, M. G.; Frangioni, J. V. Renal Clearance of Nanoparticles. *Nat. Biotechnol.* **2007**, *25* (10), 1165–1170.

(150) Su, Y.; Peng, F.; Jiang, Z.; Zhong, Y.; Lu, Y.; Jiang, X.; Huang, Q.; Fan, C.; Lee, S. T.; He, Y. In Vivo Distribution, Pharmacokinetics, and Toxicity of

Aqueous Synthesized Cadmium-Containing Quantum Dots. *Biomaterials* **2011**, *32* (25), 5855–5862.

(151) Cotton, S. *Lanthanide and Actinide Chemistry*; Wiley, 2006.

(152) Brunet, E.; Juanes, O.; Rodriguez-ubis, J. C. Supramolecularly Organized Lanthanide Complexes for Efficient Metal Excitation and Luminescence as Sensors in Organic and Biological Applications. *Curr. Chem. Biol.* **2007**, *1*, 11–39.

(153) Graeme; Stasiuk. Design and Synthesis of Novel Lanthanide Chelates for Use in Magnetic Resonance Imaging (MRI) : PhD Thesis, The universisy of Leicester, 2010.

(154) Beeby, A.; Clarkson, I. M.; Dickins, R. S.; Faulkner, S.; Parker, D.; Royle, L.; Sousa, A. S. De; Williams, J. A. G.; Woods, M. Non-Radiative Deactivation of the Excited States of Europium , Terbium and Ytterbium Complexes by Proximate Energy-Matched OH , NH and CH Oscillators : An Improved Luminescence Method for Establishing Solution Hydration States. *J. Chem. Soc.* **1999**, *2* (5), 493–503.

(155) Rodriguez-Teja, M.; Gronau, J. H.; Breit, C.; Zhang, Y. Z.; Minamidate, A.; Caley, M. P.; McCarthy, A.; Cox, T. R.; Erler, J. T.; Gaughan, L.; Darby, S.; Robson, C.; Mauri, F.; Waxman, J.; Sturge, J. AGE-Modified Basement Membrane Cooperates with Endo180 to Promote Epithelial Cell Invasiveness and Decrease Prostate Cancer Survival. *J. Pathol.* **2015**, *235* (4), 581–592.

(156) Stasiuk, G. J.; Tamang, S.; Imbert, D.; Poillot, C.; Giardiello, M.; Tisseyre, C.; Barbier, E. L.; Fries, P. H.; De Waard, M.; Reiss, P.; Mazzanti, M. Cell-Permeable Ln(III) Chelate-Functionalized InP Quantum Dots as

Multimodal Imaging Agents. *ACS Nano* **2011**, *5* (10), 8193–8201.

(157) Nann, T.; Skinner, W. M. Quantum Dots for Electro-Optic Devices. *ACS Nano* **2011**, *5* (7), 5291–5295.

(158) Jin, S.; Hu, Y.; Gu, Z.; Liu, L.; Wu, H.-C. Application of Quantum Dots in Biological Imaging. *J. Nanomater.* **2011**, *2011*, 1–13.

(159) Wells, R. L.; Pitt, C. G.; Mcphail, A. T.; Purdy, A. P.; Shafieezad, S.; Hallock, R. B. Use of Tris(Trimethylsilyl)Arsine to Prepare Gallium Arsenide and Indium Arsenide. *Chem. Mater.* **1989**, *1* (1), 4–6.

(160) Alivisatos, A. P. Semiconductor Clusters, Nanocrystals, and Quantum Dots. *Science (80-.).* **1996**, *271* (5251), 933–937.

(161) Lee, S.-H.; Lee, K.-H.; Jo, J.-H.; Park, B.; Kwon, Y.; Jang, H. S.; Yang, H. Remote-Type, High-Color Gamut White Light-Emitting Diode Based on InP Quantum Dot Color Converters. *Opt. Mater. Express* **2014**, *4* (7), 1297–1302.

(162) Fernando, K. A. S.; Sahu, S.; Liu, Y.; Lewis, W. K.; Guliants, E. A.; Jafariyan, A.; Wang, P.; Bunker, C. E.; Sun, Y. P. Carbon Quantum Dots and Applications in Photocatalytic Energy Conversion. *ACS Appl. Mater. Interfaces* **2015**, *7* (16), 8363–8376.

(163) Ma, G. Background-Free in Vivo Time Domain Optical Molecular Imaging Using Colloidal Quantum Dots. *ACS Appl. Mater. Interfaces* **2013**, *5* (8), 2835–2844.

(164) Lucey, D. W.; Macrae, D. J.; Furis, M.; Sahoo, Y.; Cartwright, A. N.; Prasad, P. N. Monodispersed InP Quantum Dots Prepared by Colloidal Chemistry in a Noncoordinating Solvent. *Chem. Mater.* **2005**, *17* (12), 3754–3762.

(165) Wells, R. L.; Aubuchon, S. R.; Kher, S. S.; Lube, M. S.; White, P. S. Synthesis

of Nanocrystalline Indium Arsenide and Indium Phosphide from Indium(III) Halides and Tris (Trimethylsilyl)Pnicogens. Synthesis, Characterization, and Decomposition Behavior of I3In.P(SiMe3)3. *Chem. Mater.* **1995**, *7* (4), 793–800.

(166) Healy, M. D.; Laibinis, P. E.; Stupik, P. D.; Barron, A. R. The Reaction of Indium(III) Chloride with Tris(Trimethylsilyl)Phosphine: A Novel Route to Indium Phosphide. *J. Chem. Soc. Chem. Commun.* **1989**, *6* (6), 359.

(167) Micic, O. I.; Curtis, C. J.; Jones, K. M.; Sprague, J. R.; Nozik, A. J. Synthesis and Characterization of InP Quantum Dots. *J. Phys. Chem.* **1994**, *98* (19), 4966–4969.

(168) Guzelian, A. A.; Katari, J. E. B.; Kadavanich, A. V.; Banin, U.; Hamad, K.; Juban, E.; Alivisatos, A. P.; Wolters, R. H.; Arnold, C. C.; Heath, J. R. Synthesis of Size-Selected, Surface-Passivated InP Nanocrystals. *J. Phys. Chem.* **1996**, *100* (17), 7212–7219.

(169) Battaglia, D.; Peng, X. Formation of High Quality InP and InAs Nanocrystals in a Noncoordinating Solvent. *Nano Lett.* **2002**, *2* (9), 1027–1030.

(170) Peter M. Allen, B. J. W. and M. G. B. Mechanistic Insights into the Formation of InP Quantum Dots. *Angew. Chem. Int. Ed.* **2010**, *49* (4), 760–762.

(171) Thuy, U. T. D.; Huyen, T. T. T.; Liem, N. Q.; Reiss, P. Low Temperature Synthesis of InP Nanocrystals. *Mater. Chem. Phys.* **2008**, *112* (3), 1120–1123.

(172) Jun, K. W.; Khanna, P. K.; Hong, K. B.; Baeg, J. O.; Suh, Y. D. Synthesis of InP Nanocrystals from Indium Chloride and Sodium Phosphide by Solution

Route. *Mater. Chem. Phys.* **2006**, *96* (2–3), 494–497.

(173) Liu, Z.; Kumbhar, A.; Xu, D.; Zhang, J.; Sun, Z.; Fang, J. Coreduction Colloidal

Synthesis of III-V Nanocrystals: The Case of InP. *Angew. Chem. Int. Ed.*

2008, *47* (19), 3540–3542.

(174) Li, L.; Protiere, M.; Reiss, P. Economic Synthesis of High Quality InP

Nanocrystals Using Calcium Phosphide as the Phosphorus Precursor.

Chem. Mater. **2008**, *20* (8), 2621–2623.

(175) Song, W. S.; Lee, H. S.; Lee, J. C.; Jang, D. S.; Choi, Y.; Choi, M.; Yang, H.

Amine-Derived Synthetic Approach to Color-Tunable InP/ZnS Quantum

Dots with High Fluorescent Qualities. *J. Nanoparticle Res.* **2013**, *15* (6), 1–

10.

(176) Li, L.; Reiss, P.; Protie, M. Core / Shell Semiconductor Nanocrystals. *Small*

2009, *5* (2), 154–168.

(177) Haubold, S.; Haase, M.; Kornowski, A. Strongly Luminescent InP / ZnS

Core/Shell Nanoparticles. *ChemPhysChem* **2001**, *2* (5), 331–334.

(178) Xie, R.; Battaglia, D.; Peng, X. Colloidal InP Nanocrystals as Efficient

Emitters Covering Blue to Near-Infrared. *J. Am. Chem. Soc.* **2007**, *129* (50),

15432–15433.

(179) Xu, S.; Ziegler, J.; Nann, T. Rapid Synthesis of Highly Luminescent InP and

InP/ZnS Nanocrystals. *J. Mater. Chem.* **2008**, *18* (23), 2653–2656.

(180) Wang, Y.; Hu, R.; Lin, G.; Roy, I.; Yong, K. T. Functionalized Quantum Dots

for Biosensing and Bioimaging and Concerns on Toxicity. *ACS Appl. Mater.*

Interfaces **2013**, *5* (8), 2786–2799.

(181) Tamang, S.; Beaune, G.; Texier, I.; Reiss, P. Aqueous Phase Transfer of

InP/ZnS Nanocrystals Conserving Fluorescence and High Colloidal

Stability. *ACS Nano* **2011**, *5* (12), 9392–9402.

(182) Dubertret, B.; Skourides, P.; Norris, D. J.; Noireaux, V.; Brivanlou, A. H.; Libchaber, A. In Vivo Imaging of Quantum Dots Encapsulated in Phospholipid Micelles. *Science (80-.).* **2002**, *298*, 1759–1763.

(183) Aldana, J.; Lavelle, N.; Wang, Y.; Peng, X. Size-Dependent Dissociation PH of Thiolate Ligands from Cadmium Chalcogenide Nanocrystals. *J. Am. Chem. Soc.* **2005**, *127* (8), 2496–2504.

(184) Moloney, M. P.; Govan, J.; Loudon, A.; Mukhina, M.; Gun'ko, Y. K. Preparation of Chiral Quantum Dots. *Nat. Protoc.* **2015**, *10* (4), 558–573.

(185) Xi, L.; Cho, D. Y.; Besmehn, A.; Duchamp, M.; Gr??tzmacher, D.; Lam, Y. M.; Kardyna??, B. E. Effect of Zinc Incorporation on the Performance of Red Light Emitting InP Core Nanocrystals. *Inorg. Chem.* **2016**, *55* (17), 8381–8386.

(186) Huang, K.; Demadrille, R.; Silly, M. G.; Sirotti, F.; Reiss, P.; Renault, O. Internal Structure of InP/ZnS Nanocrystals Unraveled by High-Resolution Soft X-Ray Photoelectron Spectroscopy Kai. *ACS Appl. Mater. Interfaces* **2010**, *4* (8), 4799–4805.

(187) Hines, M. A.; Guyot-Sionnest, P. Synthesis and Characterization of Strongly Luminescing ZnS-Capped CdSe Nanocrystals. *J. Phys. Chem.* **1996**, *100* (2), 468–471.

(188) Choi, E. Y.; Mazur, L.; Mager, L.; Gwon, M.; Pitrat, D.; Mulatier, J. C.; Monnereau, C.; Fort, A.; Attias, A. J.; Dorkenoo, K.; Kwon, J. E.; Xiao, Y.; Matczyszyn, K.; Samoc, M.; Kim, D. W.; Nakao, A.; Heinrich, B.; Hashizume, D.; Uchiyama, M.; Park, S. Y.; Mathevet, F.; Aoyama, T.; Andraud, C.; Wu, J. W.; Barsella, A.; Ribierre, J. C. Photophysical, Amplified Spontaneous

Emission and Charge Transport Properties of Oligofluorene Derivatives in Thin Films. *Phys. Chem. Chem. Phys.* **2014**, *16* (32), 16941–16956.

(189) Shen, W.; Tang, H.; Yang, X.; Cao, Z.; Cheng, T.; Wang, X.; Tan, Z.; You, J.; Deng, Z. Synthesis of Highly Fluorescent InP / ZnS. *J. Mater. Chem. C* **2017**, *5*, 8243–8249.

(190) Feigl, C.; Russo, S. P.; Barnard, A. S. Safe, Stable and Effective Nanotechnology: Phase Mapping of ZnS Nanoparticles. *J. Mater. Chem.* **2010**, *20* (24), 4971.

(191) Xie, R.; Kolb, U.; Li, J.; Basche, T.; Mews, A. Synthesis and Characterization of Highly Luminescent. *JACS* **2005**, *127* (25), 7480–7488.

(192) Clarke, M. T.; Viscomi, F. N.; Chamberlain, T. W.; Hondow, N.; Adawi, A. M.; Sturge, J.; Erwin, S. C.; Bouillard, J. G.; Tamang, S.; Stasiuk, G. J. Synthesis of Super Bright Indium Phosphide Colloidal Quantum Dots through Thermal Diffusion. *Commun. Chem.* **2019**, *2* (36), 1–7.

(193) Ripple, R. Mercaptoacetic Acid and Derivatives. *Wiley* **2012**, *22*, 555–557.

(194) Li, Y.; Li, Z.; Wang, X.; Liu, F.; Cheng, Y.; Zhang, B.; Shi, D. In Vivo Cancer Targeting and Imaging-Guided Surgery with Near Infrared-Emitting Quantum Dot Bioconjugates. *Theranostics* **2012**, *2*, 769–776.

(195) Bang, E.; Choi, Y.; Cho, J.; Suh, Y.-H.; Ban, H. W.; Son, J. S.; Park, J. Large-Scale Synthesis of Highly Luminescent InP/ZnS Quantum Dots Using Elemental Phosphorus Precursor. *Chem. Mater.* **2017**, *4* (29), 4236–4243.

(196) Resch-Genger, U.; Grabolle, M.; Cavaliere-Jaricot, S.; Nitschke, R.; Nann, T. Quantum Dots versus Organic Dyes as Fluorescent Labels. *Nat. Methods* **2008**, *5* (9), 763–775.

(197) Guo, K.; Berezin, M. Y.; Zheng, J.; Akers, W.; Lin, F.; Teng, B.; Vasalatiy, O.;

Gandjbakhche, A.; Griffiths, G. L.; Achilefu, S. Near Infrared-Fluorescent and Magnetic Resonance Imaging Molecular Probe with High T1relaxivity for in Vivo Multimodal Imaging. *Chem. Commun.* **2010**, *46* (21), 3705–3707.

(198) Yamane, T.; Hanaoka, K.; Muramatsu, Y.; Tamura, K.; Adachi, Y.; Miyashita, Y.; Hirata, Y.; Nagano, T. Method for Enhancing Cell Penetration of Gd3+-Based MRI Contrast Agents by Conjugation with Hydrophobic Fluorescent Dyes. *Bioconjug. Chem.* **2011**, *22* (11), 2227–2236.

(199) Fei-Peng, Z.; Guo-Tao, C.; Shou-Ju, W.; Ying, L.; Yu-Xia, T.; Ying, T.; Jian-Dong, W.; Chun-Yan, W.; Xin, W.; Jing, S.; Zhao-Gang, T.; Guang-Ming, L. Dual-Modality Imaging Probes with High Magnetic Relaxivity and near-Infrared Fluorescence Based Highly Aminated Mesoporous Silica Nanoparticles. *J. Nanomater.* **2016**, *2016*, 17–19.

(200) Stephen, Z. R.; Kievit, F. M.; Zhang, M. Magnetite Nanoparticles for Medical MR Imaging. *Natl. Inst. Heal.* **2012**, *14* (11), 330–338.

(201) Chen, Q.; Shang, W.; Zeng, C.; Wang, K.; Liang, X.; Chi, C.; Liang, X.; Yang, J.; Fang, C.; Tian, J. Theranostic Imaging of Liver Cancer Using Targeted Optical/MRI Dual-Modal Probes. *Oncotarget* **2017**, *8* (20), 32741–32751.

(202) Jagadish, B.; Brickert-Albrecht, G. L.; Nichol, G. S.; Mash, E. A.; Raghunand, N. On the Synthesis of 1,4,7-Tris(Tert-Butoxycarbonylmethyl)-1,4,7,10-Tetraazacyclododecane. *Tetrahedron Lett.* **2011**, *52* (17), 2058–2061.

(203) Evans, D. F. The Determination of the Paramagnetic Susceptibility of Substances in Solution by Nuclear Magnetic Resonance. *J. Chem. Soc.* **1959**, 2003–2005.

(204) Raymond, K. N.; Pierre, V. C. Next Generation, High Relaxivity Gadolinium

MRI Agents. *Bioconjug. Chem.* **2005**, *16* (1), 3–8.

(205) Lacerda, S.; Tóth, É. Lanthanide Complexes in Molecular Magnetic

Resonance Imaging and Theranostics. *ChemMedChem* **2017**, *12* (12),

883–894.

(206) Lee, S. Y.; Jeon, S. I.; Jung, S.; Chung, I. J.; Ahn, C. Targeted Multimodal

Imaging Modalities. *Adv. Drug Deliv. Rev.* **2014**, *76*, 60–78.

(207) Cheon, J.; Lee, J. Synergistically Integrated Nanoparticles as Multimodal

Probes for Nanobiotechnology. *Acc. Chem. Res.* **2008**, *41* (12), 1630–1640.

(208) Byrne, J. D.; Betancourt, T.; Brannon-peppas, L. Active Targeting Schemes

for Nanoparticle Systems in Cancer Therapeutics. *Adv. Drug Deliv. Rev.*

2008, *60* (15), 1615–1626.

(209) Yan, H.; Wang, L.; Wang, J.; Weng, X.; Lei, H.; Wang, X.; Jiang, L.; Zhu, J.

Two-Order Targeted Brain Tumor Imaging by Using an Optical /

Paramagnetic Nanoprobe across the Blood Brain Barrier. *ACS Nano* **2012**,

6 (1), 410–420.

(210) Wu, Y.-Z.; Sun, J.; Zhang, Y.; Pu, M.; Zhang, G.; He, N.; Zeng, X. Effective

Integration of Targeted Tumor Imaging and Therapy Using

Functionalized InP QDs with a VEGFR2 Monoclonal Antibody and a MiR-

92a Inhibitor. *ACS Appl. Mater. Interfaces* **2017**.

(211) Lee, H.; Li, Z.; Chen, K.; Hsu, A. R.; Xu, C.; Xie, J.; Sun, S.; Chen, X. PET / MRI

Dual-Modality Tumor Imaging Using Radiolabeled Iron Oxide

Nanoparticles. *J. Nucl. Med.* **2008**, *49* (8), 1371–1380.

(212) Boonstra, M. C.; Driel, P. B. A. A. Van; Willigen, D. M. Van; Stammes, A.;

Prevoo, H. A. J. M.; Tummers, Q. R. J. G.; Andrew, P. UPAR-Targeted

Multimodal Tracer for Pre- and Intraoperative Imaging in Cancer Surgery.

Oncotarget **2015**, *6* (16), 14260–14273.

(213) Sarkar, S.; Das, S. A Review of Imaging Methods for Prostate Cancer

Detection. *Biomed. Eng. Comput. Biol.* **2016**, *7*, 1–15.

(214) Shreve, P. D.; Grossman, H. B.; Gross, M. D.; Wahl, R. L. Metastatic Prostate

Cancer: Initial Findings of PET with 2-Deoxy-2-[F-18]Fluoro-D-Glucose.

Radiology **1996**, *199* (3), 751–756.

(215) Ghanem, N.; Uhl, M.; Brink, I.; Sch, O.; Kelly, T.; Moser, E.; Langer, M.

Diagnostic Value of MRI in Comparison to Scintigraphy , PET , MS-CT and

PET / CT for the Detection of Metastases of Bone. *Eur. J. Radiol.* **2005**, *55*,

41–55.

(216) Schwarzenböck, S.; Souvatzoglou, M.; Krause, B. J. Choline PET and

PET/CT in Primary Diagnosis and Staging of Prostate Cancer.

Theranostics **2012**, *2* (3), 319–330.

(217) Sheikhbahaei, S.; Werner, R. A.; Solnes, L. B.; Pienta, K. J.; Pomper, M. G.;

Gorin, M. A.; Rowe, S. P. Targeted PET Imaging of Prostate Cancer : An

Update on Important Pitfalls. *Semin. Nucl. Med.* **2019**, *49* (4), 255–270.

(218) Ribbat-idel, J.; Becker, F.; Joerg, V.; Duensing, S. Expression of Prostate-

Specific Membrane Antigen (PSMA) on Biopsies Is an Independent Risk

Stratifier of Prostate Cancer Patients at Time of Initial Diagnosis. *Front.*

Oncol. **2018**, *8*, 1–7.

(219) Afshar-Oromieh, A.; Malcher, A.; Eder, M.; Eisenhut, M.; Linhart, H. G.;

Hadaschik, B. A.; Holland-Letz, T.; Giesel, F. L.; Kratochwil, C.; Haufe, S.;

Haberkorn, U.; Zechmann, C. M. PET Imaging with a [68Ga]Gallium-

Labelled PSMA Ligand for the Diagnosis of Prostate Cancer:

Biodistribution in Humans and First Evaluation of Tumour Lesions. *Eur. J.*

Nucl. Med. Mol. Imaging **2013**, *40* (4), 486–495.

(220) Kesch, C.; Vinsensia, M.; Radtke, J. P.; Schlemmer, H. P.; Heller, M.; Ellert, E.; Holland-letz, T.; Duensing, S.; Grabe, N.; Afshar-oromieh, A.; Wieczorek, K.; Sch, M.; Neels, O. C.; Cardinale, J.; Kratochwil, C.; Hohenfellner, M.; Kopka, K.; Haberkorn, U.; Hadaschik, B. A.; Giesel, F. L.; Ct, P. E. T. Intraindividual Comparison of 18 F-PSMA-1007 PET/CT, Multiparametric MRI, and Radical Prostatectomy Specimens in Patients with Primary Prostate Cancer: A Retrospective, Proof-of-Concept Study. *J. Nucl. Med.* **2017**, *58*, 1805–1811.

(221) Zamboglou, C.; Drendel, V.; Jilg, C. A.; Rischke, H. C.; Beck, T. I.; Schultze-seemann, W.; Krauss, T.; Mix, M.; Schiller, F.; Wetterauer, U.; Langer, M.; Bock, M.; Meyer, P. T.; Grosu, A. L. Comparison of 68 Ga-HBED-CC PSMA-PET / CT and Multiparametric MRI for Gross Tumour Volume Detection in Patients with Primary Prostate Cancer Based on Slice by Slice Comparison with Histopathology. *Theranostics* **2017**, *7* (1).

(222) Eiber, M.; Weirich, G.; Holzapfel, K.; Souvatzoglou, M.; Haller, B.; Rauscher, I.; Beer, A. J.; Gschwend, J.; Schwaiger, M.; Maurer, T.; Novara, G.; Mri, G. H. P. E. T. Simultaneous 68 Ga-PSMA HBED-CC PET / MRI Improves the Localization of Primary Prostate Cancer. *Eur. Urol.* **2016**, *70*, 829–836.

(223) Zhang, H.; Desai, P.; Koike, Y.; Houghton, J.; Carlin, S.; Tandon, N.; Touijer, K.; Weber, W. A. Dual-Modality Imaging of Prostate Cancer with a Fluorescent and Radiogallium-Labeled Gastrin-Releasing Peptide Receptor Antagonist. *J. Nucl. Med.* **2017**, *51* (1), 29–35.

(224) Centenera, M. M.; Hickey, T. E.; Jindal, S.; Ryan, N. K.; Ravindranathan, P.; Mohammed, H.; Robinson, J. L.; Schiewer, M. J.; Ma, S.; Kapur, P.;

Sutherland, P. D.; Hoffmann, C. E.; Roehrborn, C. G.; Gomella, L. G.; Carroll,

J. S.; Birrell, S. N.; Knudsen, K. E.; Raj, G. V.; Butler, L. M.; Tilley, W. D. A

Patient-Derived Explant (PDE) Model of Hormone-Dependent Cancer.

Mol. Oncol. **2018**, *12* (9), 1608–1622.

Chapter 8: Appendix

8.1 DLS Data for synthesised InP/ZnS QDs
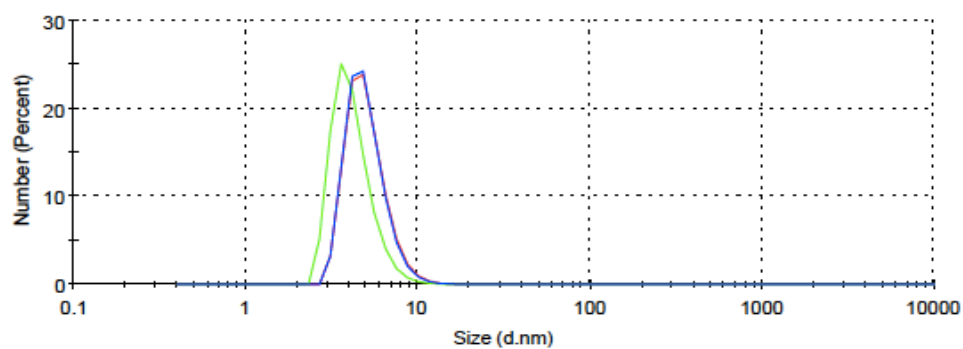
Figure 8.1 DLS image of InP/ZnS (1) –TGA synthesised with InCl$_3$. D$_h$ = 4.80 nm
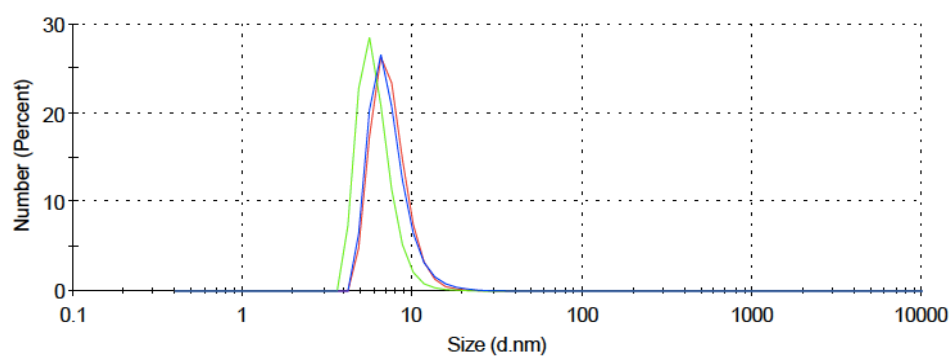
Figure 8.2 DLS image of InP/ZnS (2) – TGA synthesised with InCl$_3$, D$_h$ = 5.81 nm
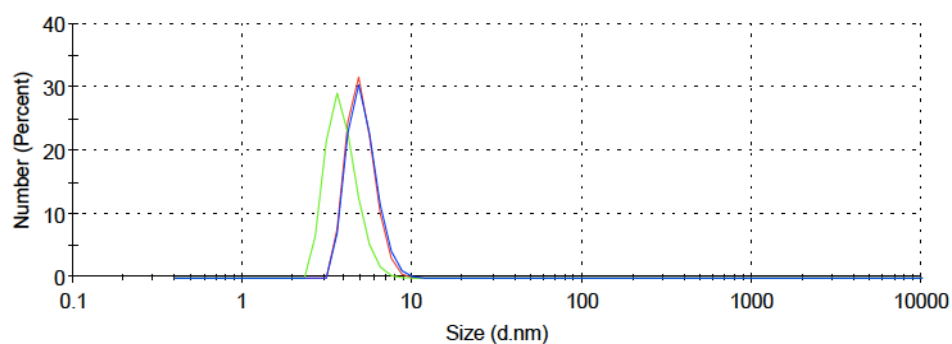
Figure 8.3 DLS image of InP/ZnS (1) – TGA synthesised with InI$_3$, D$_h$ = 3.67 nm
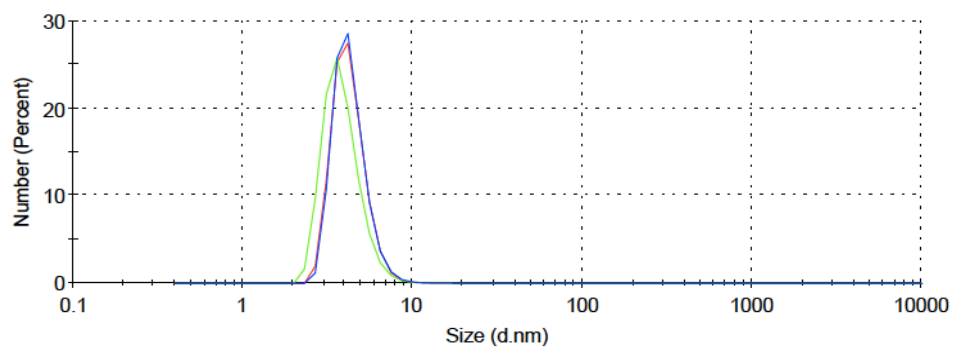
Figure 8.4 DLS image of InP/ZnS (2) – TGA synthesised with InI_3, D_h = 4.73 nm
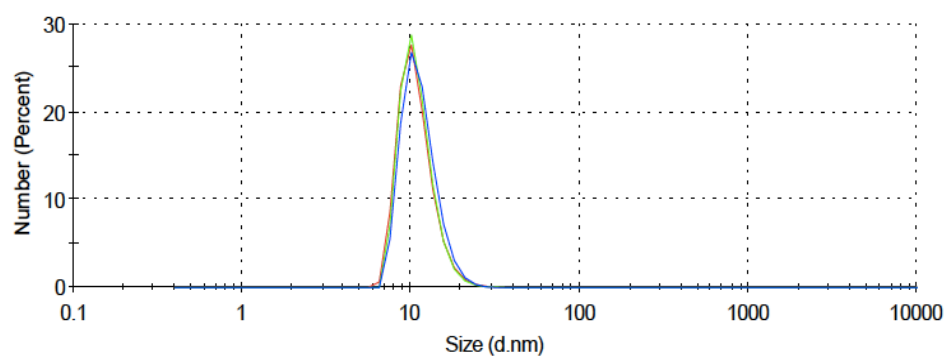
Figure 8.5 DLS image of InP/ZnS (2) – Gd.5a synthesised with InI_3, D_h = 11.09 nm
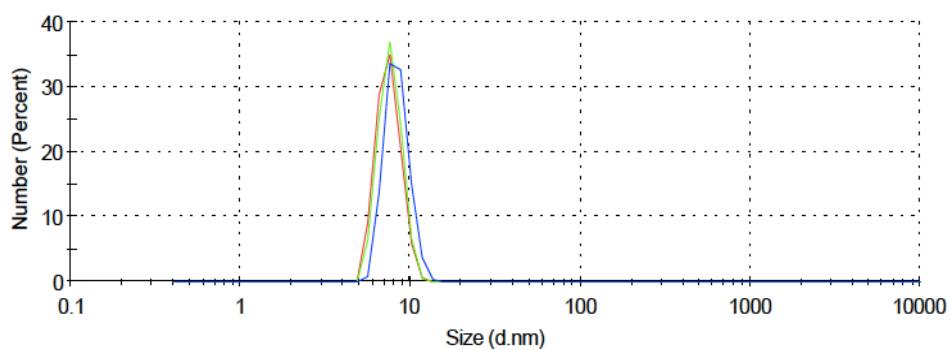
Figure 8.6 DLS image of InP/ZnS (2) – Gd.5b synthesised with InI_3, D_h = 7.82 nm
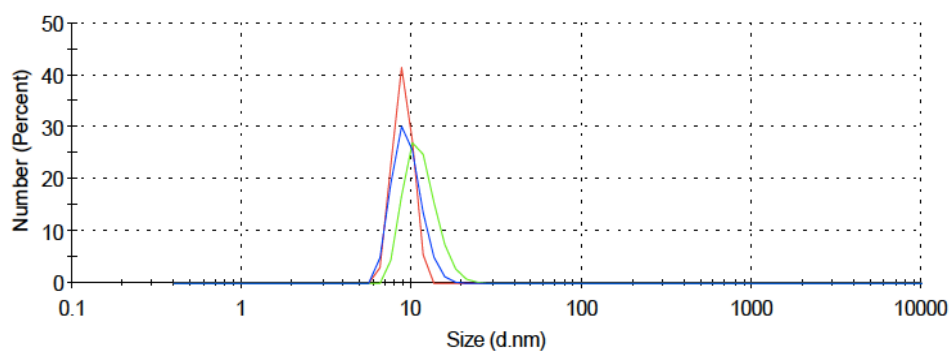
Figure 8.7 DLS image of InP/ZnS (2) – Gd.5c synthesised with InI_3, D_h = 11.05 nm
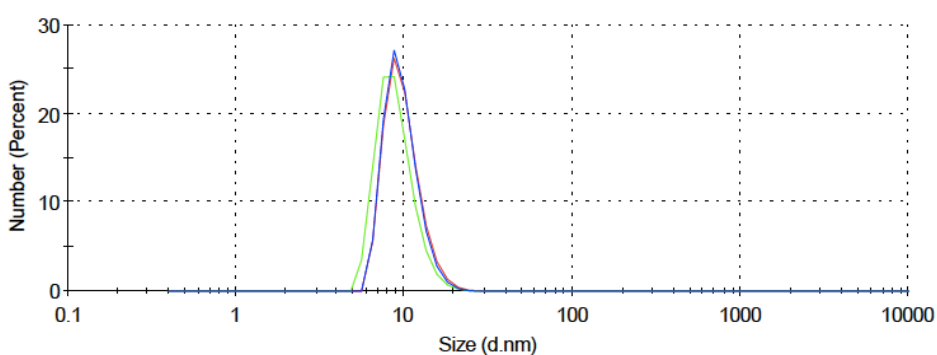
Figure 8.8 DLS image of InP/ZnS (2) – Gd.5a synthesised with $InCl_3$, D_h = 9.56 nm
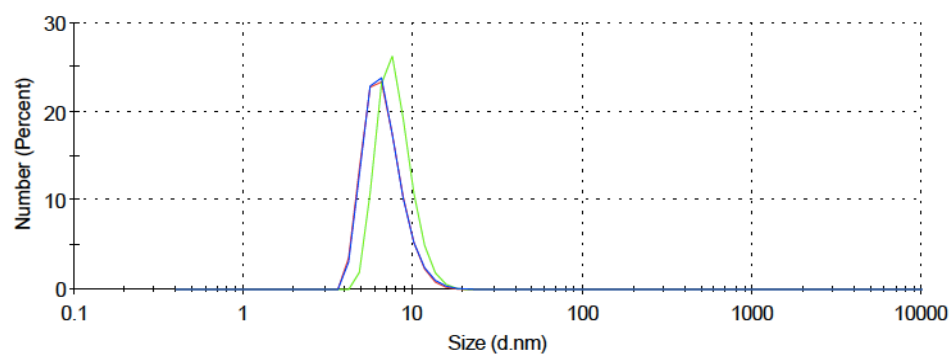
Figure 8.9 DLS image of InP/ZnS (2) – Gd.5b synthesised with $InCl_3$, D_h = 7.21 nm
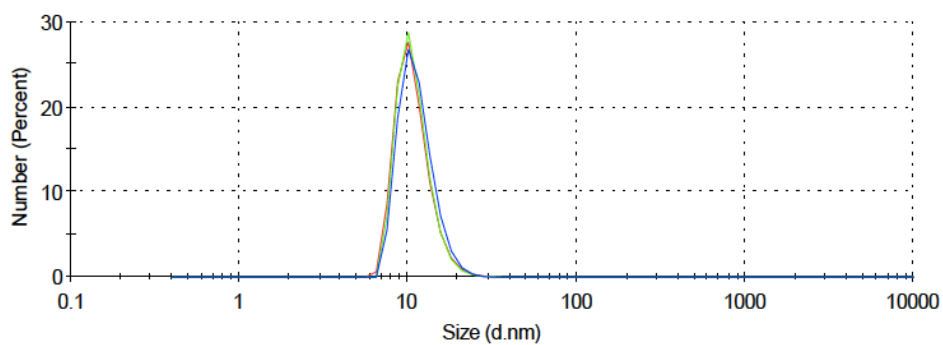
Figure 8.10 DLS image of InP/ZnS (2) – Gd.5c synthesised with $InCl_3$, D_h = 8.82 nm
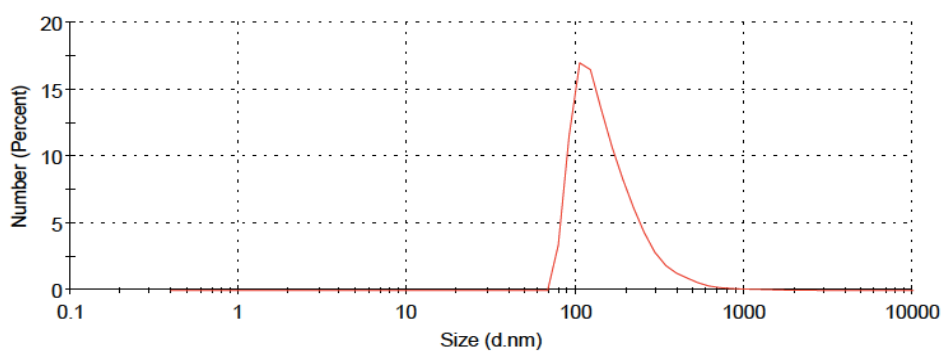
Figure 8.11 DLS image of InP/ZnS (2) – mAb (mAb – A5.158) synthesised using a one-step surface functionalisation method. InI_3, D_h = 152.0 nm
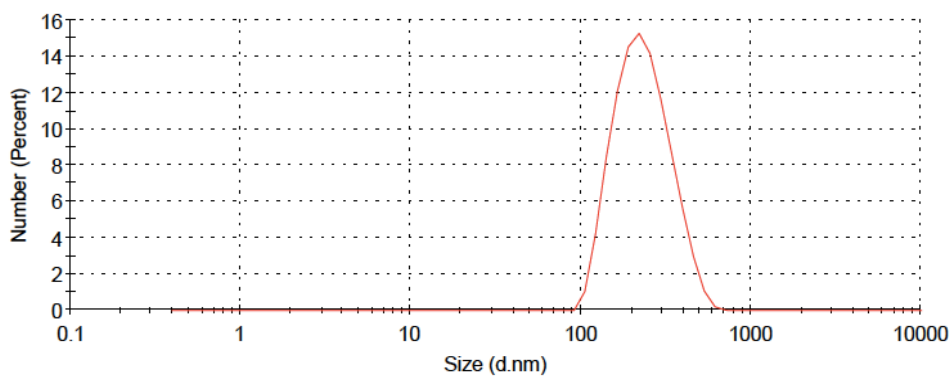
Figure 8.12 DLS image of InP/ZnS (2) – mAb (mAb – 39.10) synthesised using a one-step surface functionalisation method. $InCl_3$, D_h = 223.0 nm
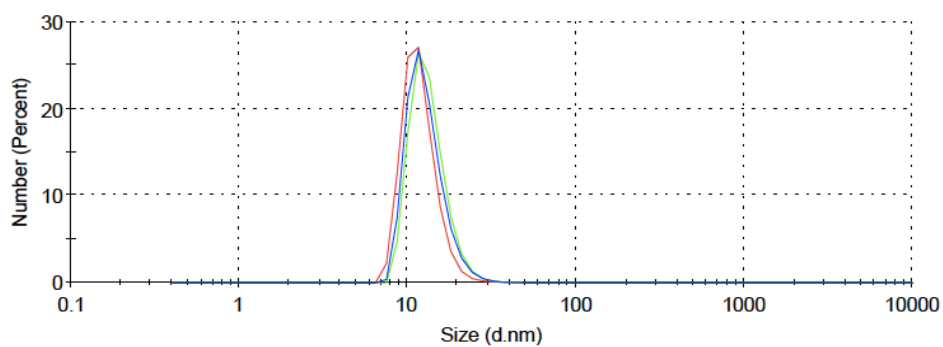
Figure 8.13 DLS image of InP/ZnS (2) – NHS, InI_3, D_h = 12.79nm
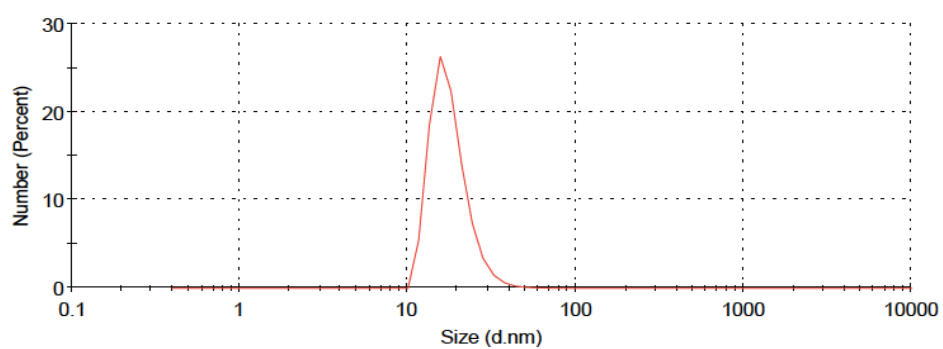
Figure 8.14 DLS image of InP/ZnS (2) – NHS - mAb (mAb – A5.158). InI_3, D_h = 16.20 nm
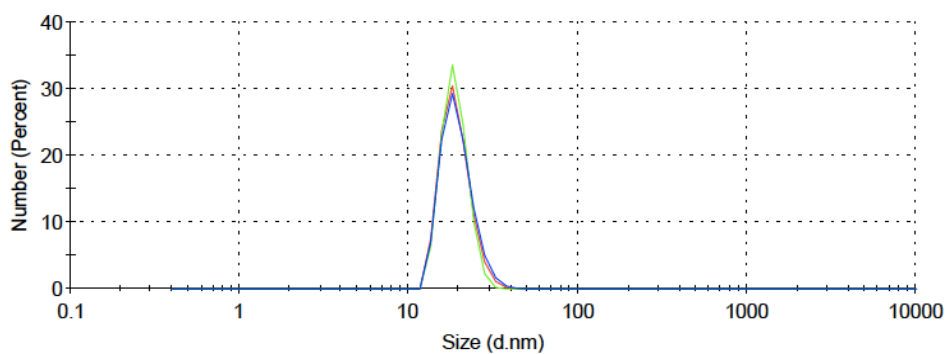
Figure 8.15 DLS image of InP/ZnS (2) – NHS - probe (mAb – A5.158). InI_3, D_h = 19.16 nm
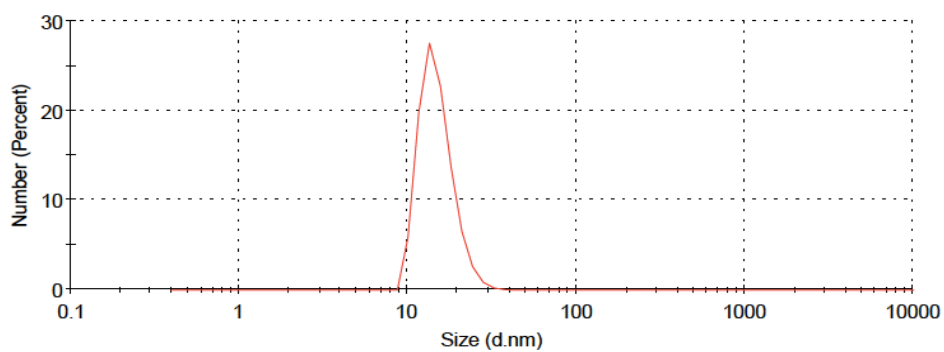
Figure 8.16 DLS image of InP/ZnS (2) – NHS, $InCl_3$, D_h = 13.71 nm
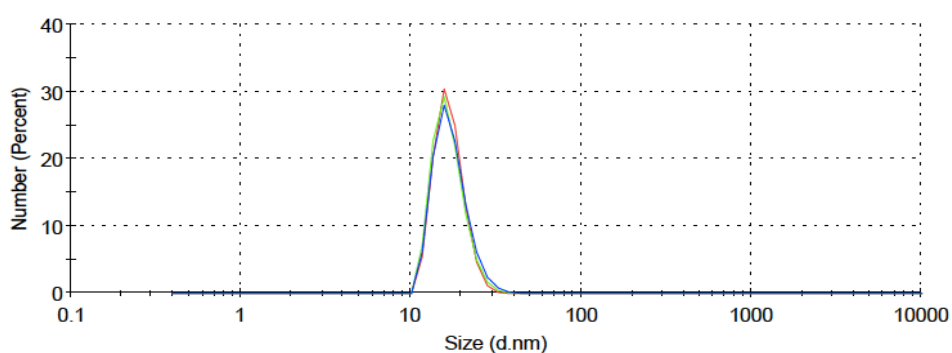
Figure 8.17 DLS image of InP/ZnS (2) – NHS - mAb (mAb – 39.10). $InCl_3$, D_h =
16.58 nm
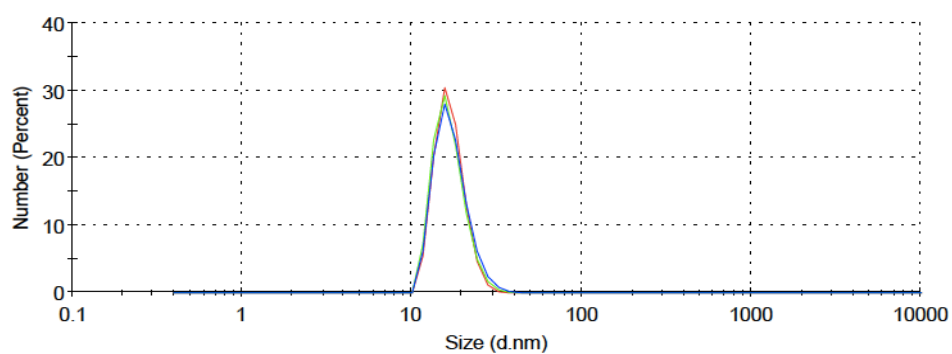
Figure 8.18 DLS image of InP/ZnS (2) – NHS - probe (mAb – 39.10). $InCl_3$, D_h =
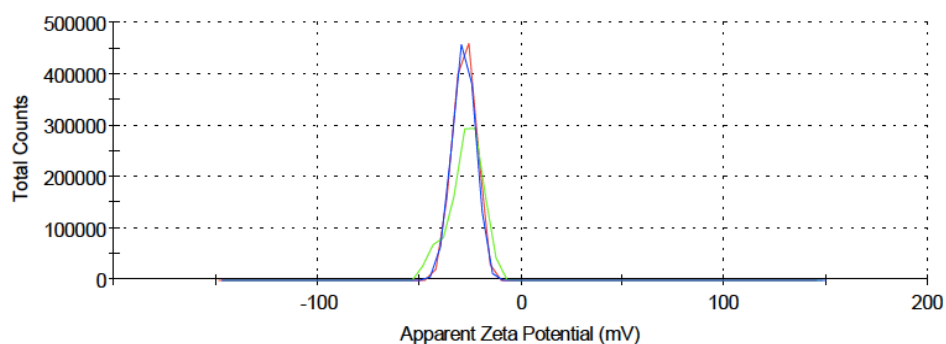17.03 nm

8.2 Surface Zeta Potential of InP/ZnS complexes.
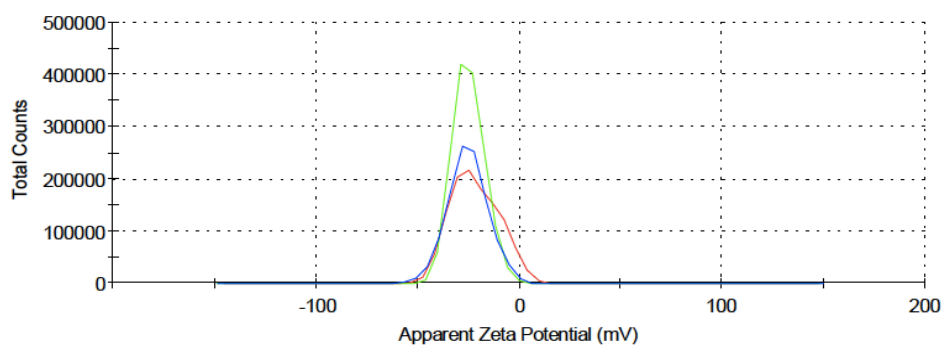
Figure 8.19 Surface zeta potential InP/ZnS (1) –TGA synthesised with InI3. Zeta potential = -23.96 mV
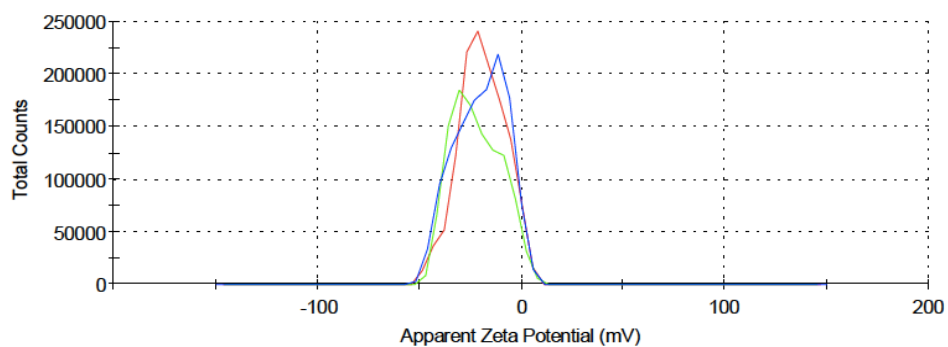
Figure 8.20 Surface zeta potential of InP/ZnS (2) –TGA synthesised with InI$_3$. Zeta potential = -20.26 mV
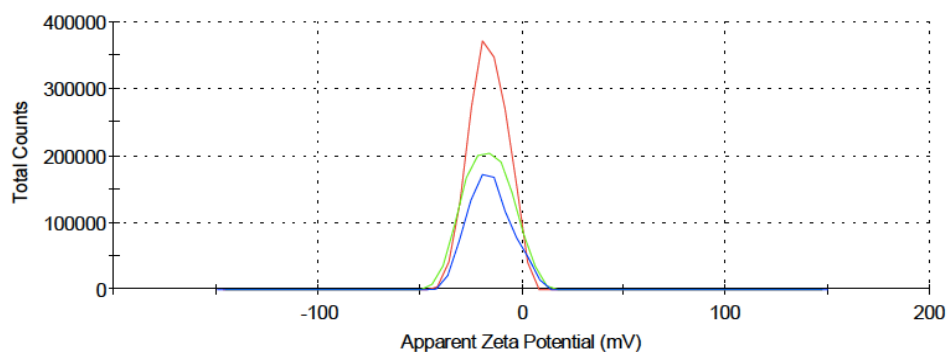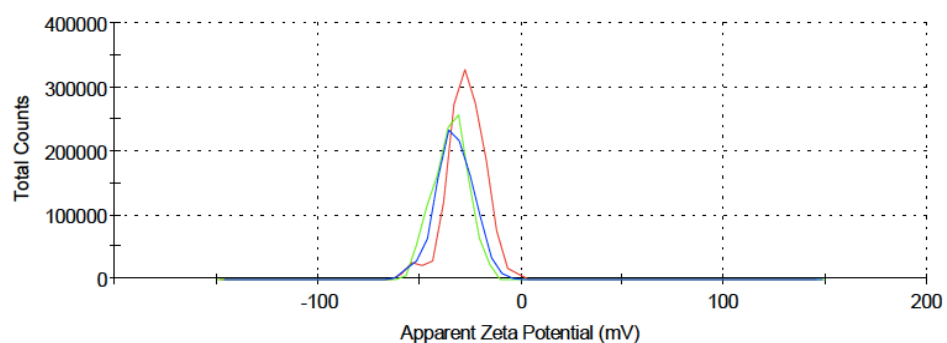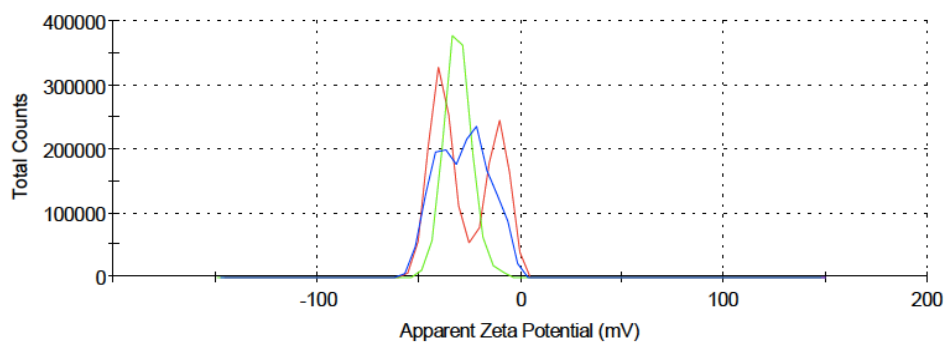

Figure 8.21 Surface zeta potential of InP/ZnS (1) –TGA synthesised with InCl$_3$. Zeta potential = -16.10 mV
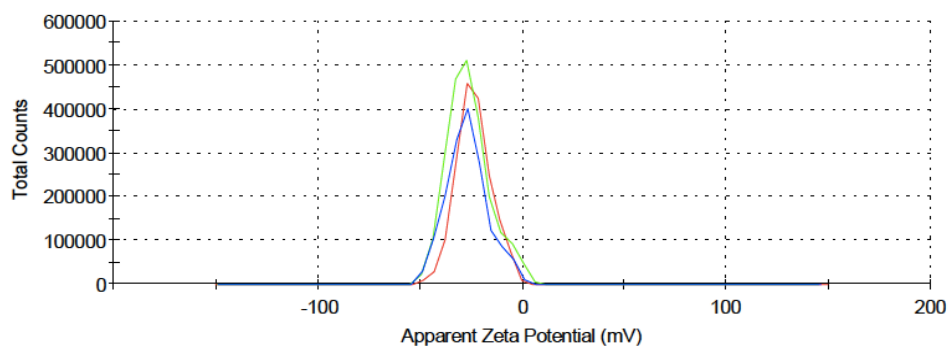
Figure 8.22 Surface zeta potential of InP/ZnS (2) –TGA synthesised with InCl3.

Zeta potential = -25.30 mV
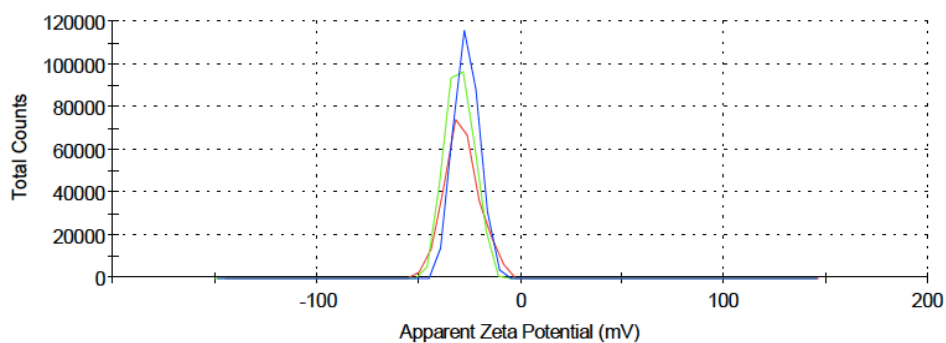
Figure 8.23 Surface zeta potential of InP/ZnS (2) –Gd.5a synthesised with InI_3.
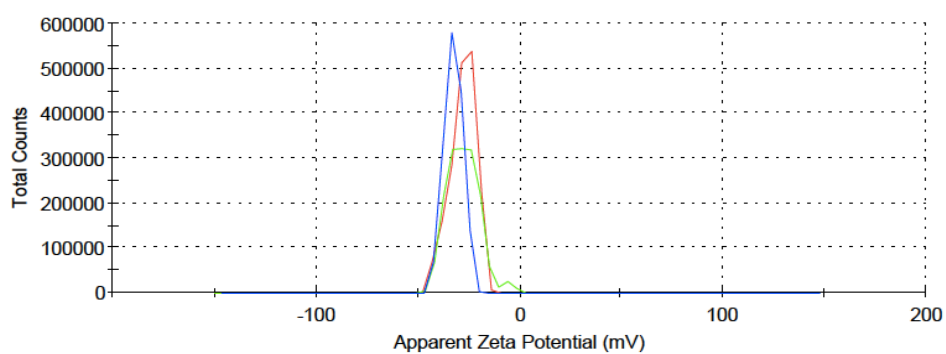
Zeta potential = -28.30 mV
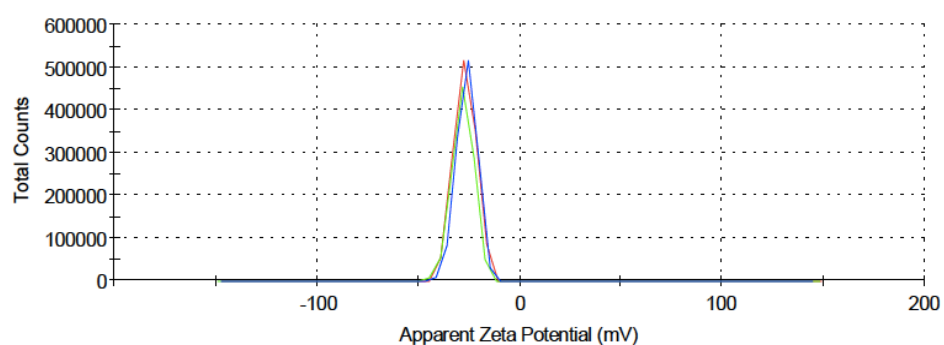
Figure 8.24 Surface zeta potential of InP/ZnS (2) –Gd.5b synthesised with InI_3.

Zeta potential = -27.0 mV
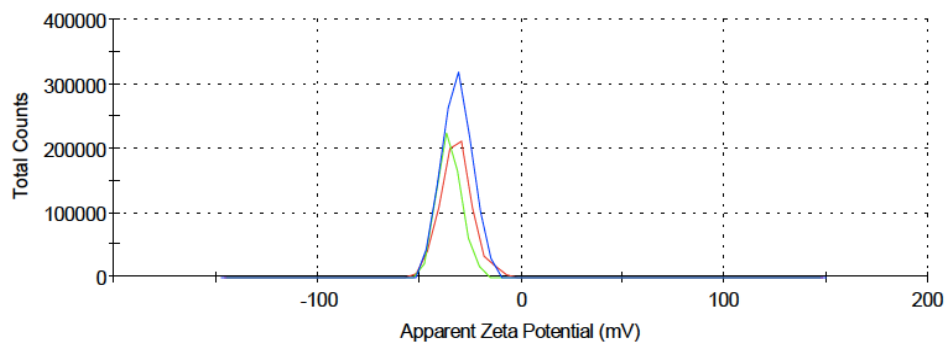
Figure 8.25 Surface zeta potential of InP/ZnS (2) –Gd.5c synthesised with InI3.

Zeta potential = -32.70 mV

Figure 8.26 Surface zeta potential of InP/ZnS (2) –Gd.5a synthesised with InCl₃.

Zeta potential = -27.63 mV

Figure 8.27 Surface zeta potential of InP/ZnS (2) –Gd.5b synthesised with InCl3.

Zeta potential = -31.13 mV

Figure 8.28 Surface zeta potential of InP/ZnS (2) –Gd.5c synthesised with InCl$_3$.

Zeta potential = -28.73 mV

Figure 8.29 Surface zeta potential of InP/ZnS (2) –NHS – mAb (mAb – A5.158) synthesised with InI$_3$. Zeta potential = -27.9 mV
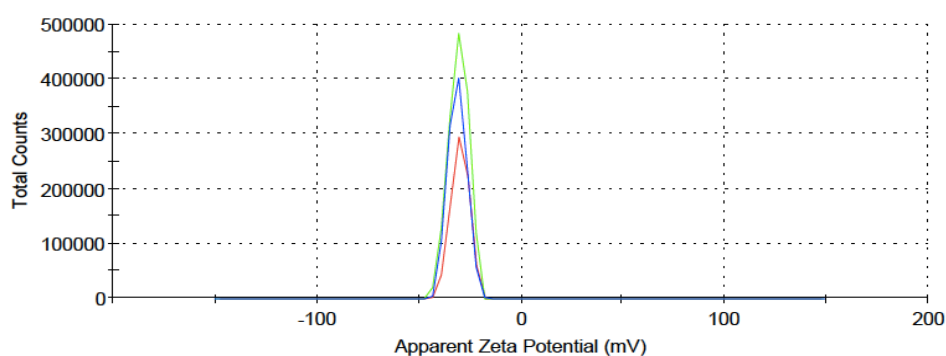

Figure 8.30 Surface zeta potential of InP/ZnS (2) –NHS – mAb (mAb – 39.10) synthesised with InCl$_3$. Zeta potential = -31.2 mV
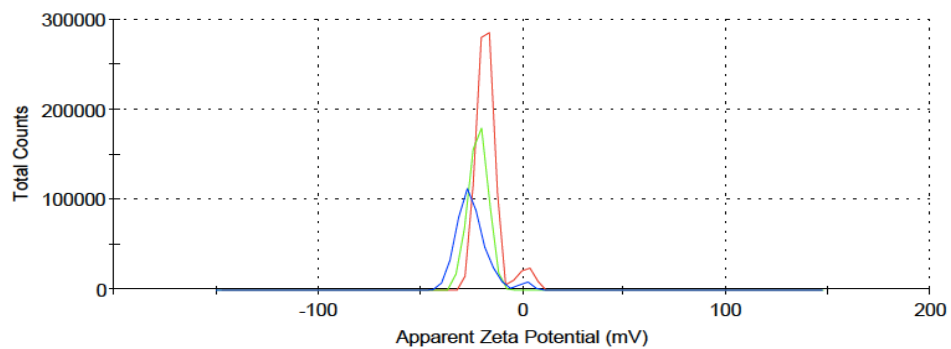
Figure 8.31 Surface zeta potential of InP/ZnS (2) –NHS – probe (mAb – A5.158) synthesised with InI_3. Zeta potential = -24.4 mV
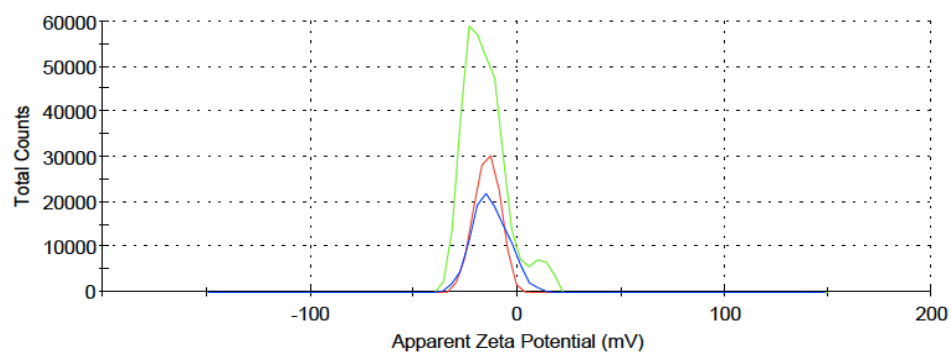

Figure 8.31 Surface zeta potential of InP/ZnS (2) –NHS – probe (mAb – A5.158) synthesised with $InCl_3$. Zeta potential = -14.7 mV